UNIVERSITÀ
DEGLI STUDI
FIRENZE

DIEF
DIPARTIMENTO
DI INGEGNERIA
INDUSTRIALE

Università degli Studi di Firenze
School of Engineering
DIEF - Department of Industrial Engineering of Florence

PhD School: *Energetica e Tecnologie Industrali Innovative*
Scientific Area: ING/IND 09

A CLOSE INVESTIGATION ON THE AEROTHERMAL BEHAVIOUR OF MODERN AEROENGINE COMBUSTORS

PhD Candidate: ING. GIANLUCA CACIOLLI

Tutor: PROF. ING. BRUNO FACCHINI

Academic Relator: DR. ING. ANTONIO ANDREINI

Industrial Relator: ING. FABIO TURRINI

PhD School Coordinator: PROF. ING. MAURIZIO DE LUCIA

XXV PhD School Cycle - 2010-2012

To my family,
the greatest gift I've received and
that I wouldn't have dared to ask for

Acknowledgements

In these years, lots of people have come across my life and have left a mark on it. My feelings, my thoughts, my wishes and, generally, the person I am now, are the result of the meeting with those people and I do want to take this opportunity to thank them. Surely, these few lines will not be enough to express my gratitude for you all.

First of all, I would like to thank Prof. Bruno Facchini, a guide and a father for me during my time at the University: thank you very much for your inestimable support, motivation and patience of these years.

I wish to express my warmest thanks to Fabio Turrini: your considerable experience and your practical way of thinking have been of great value for all my work.

A special thanks is devoted to Antonio and Lorenzo, my mentors in these years: you have always found time to teach me and to give precious advices. If Bruno was my father, you were my elder brothers. Thank you for your friendship, too!

Many thanks to my PhD-mates that, in these years, shared with me not only wonderful working experiences, but also a friendly spirit of mutual help. First of all, I want to thank my friend Lorenzuccio: I worked very well with you and we had a very fruitful (and funny) collaboration. Above all, thank you for your patience with me! Special thanks to my close "travel buddies" Francesco (Maio), Luca (Lucuccio) and Andrea: it was really a pleasure to work with you, sometimes suffering, but mostly having a good time all together. Furthermore, I want to warmly thank Francesco (Fransis) for his indispensable help during the Newac campaign

and also for the nice (sometimes delirious) moments we had in the Lab-Colonne. Many thanks also to Alessandro, Alessio (Bonini), Leonardo, Lorenzo (Winkleruccio), Tommaso (Fondelli) and Riccardo (Ferraro) for the time we spent together "squeezed" in our office. Special thanks to the remaining "inhabitants" of the glorious Lab-Colonne, Marco and Daniele, to the Ergon guys Cosimo, Mirko and Riccardo and, not less important, to Carlo and Luca (Inno).

How could I forget my colleagues of the THT-Lab? Many thanks to Riccardo and Tommaso for the precious help, which has been essential in the last month. Thank you also for pleasant time spent working together in the middle of nowhere (however close to the Chinese!). I want also to express my gratitude to Charlie, our "little" French guest: thank you very much for our close international cooperation for the realization of the Sector and, above all, for the time spent together to fix every "problem of the day" in the THT-Lab. A special mention is dedicated to Alessio (Picchiuccio): we have worked together side by side for all these years and, sincerely, I really feel lucky for this. I am sure that, without you, everything would have been much harder, if not even impossible, and definitely less funny. Thank you very much for your help and, above all, for your friendship.

My gratitude is also for all my great old friends: it is amazing to realize how our relation becomes stronger as time passes by. Just to mention some of you: Filippo, Marco, Iari (we grown up together like brothers), Bigo, Milo and Simo (great friends), Zizi and Gaia (dear friends, almost sisters). Many thanks to you for everything we share in our life; thanks also to all those people I met and that are coming into my mind right in this moment.

I want to thank my family for all the support and the love they have been giving to me since I was born: thank you Mum and Dad for having tough me to understand what really matters, thank you Niki for being the best sister ever, and thank you Dof for having shown me the Truth. Many thanks also to my second family, Giuseppe, Roberta, Lorenzo and Marta, for their love and for having treated me as a real son/brother. My

thoughts are also to all my grandparents, my relatives and my relatives in-law: thank you very much for your love to my family and me.

A final thanks to my wife, Valentina: everyday you lights my heart and touches my soul, and you are the reason why each single day of my life shines. Thank you very much for your support and help during these years of Ph.D, especially for the last hard months: what would I be without you?

This Ph.D thesis was carried out within the European research projects "NEW Aeroengine Core concepts - NEWAC" (Grant Agreement FP6-030876) and "Full Aerothermal Combustor-Turbine interactiOn Research - FACTOR" (Grant Agreement FP7-265985). I gratefully acknowledge both consortia for the permission to publish and especially for the opportunity to take part in such a challenging work.

"The proof of your faith, being more precious than gold
that perisheth though it is proved by fire to make it pure,
may be found unto praise and glory and honour
at the revelation of Jesus Christ"
First epistle of Peter, 1,7

Abstract

The high level of forecast growth of annual air traffic led the introduction of severe legislation limits for polluting emissions from aeroengine gas turbines. Currently, lean combustion systems are considered the most effective technology that guarantees significant pollutant reductions and, at the same time, allows to improve the engine performance.

However, the design of efficient and reliable lean burn combustors requires very detailed knowledge about parameters influencing new cooling system performance and, in addition, about the mixing process between the mainflow and the coolant that occurs inside the chamber. Furthermore, it is necessary to fulfil the lack of experimental data on these innovative combustors, in view of validating advanced computational modelling and increasing the industrial experience.

This research study is aimed at deepen the comprehension and the knowledge of some phenomena involved in the lean combustor and, moreover, at collecting new detailed experimental data, valuable in benchmarking advanced computational codes and updating the combustor design tools.

Initially, the analysis is carried out by means of an experimental survey on a simplified geometry which represented of a real effusion-based combstor cooling arrangement (3:1 scaled); afterwards, the focus moves to the entire combustor: an engine-representative rig (1:1 scaled), made up of three annular sectors of a lean combustor architecture, provided with an effusion cooling system, is set up to investigate the generation of hot streaks inside the chamber due to the interaction between the main-

flow and the coolant.

The experimental survey fulfils some lack of experimental data available in literature concerning the effects of some operative parameters on the performance of an effusion system; moreover, the high TRL (Technology Readiness Level) of the combustor simulator allows to collect a wide database of detailed measurements, obtained with several experimental techniques, that characterizes the generation of the hot streaks and their transport through the combustor chamber.

The extensive investigation carried out in this study contributes to increase the comprehension and to provide experimental data on the effusion cooling behaviour and on the mixing process inside a lean burn combustor.

Contents

List of Figures

List of Tables

Nomenclature

Letters

A	Area	$[m^2]$
BR	Blowing Ratio	$[-]$
C	Concentration mass fraction	$[-]$
C_d	Discharge Coefficient	$[-]$
D, d	Hole diameter	$[m]$
DR	Density Ratio	$[-]$
HTC	Heat transfer coefficient	$[W/(m^2K)]$
I	Momentum flux ratio	$[-]$
L	Length	$[m]$
Le	Lewis Number	$[-]$
m	Mass flow rate	$[W/mK]$
Nu	Nusselt number	$[-]$
$NHFR$	Net Heat Flux Reduction	$[-]$
p, P	Pressure	$[Pa]$
P_T	Total Pressure	$[Pa]$
Pr	Prandtl Number	$[-]$
q	Area Specific Heat flux	$[W/m^2]$
R	Gas constant	$[-]$
Re	Reynolds number	$[-]$
s	Thickness	$[m]$
S_n	Swirl number	$[-]$
S_x	Streamwise pitch	$[m]$

S_y	Spanwise pitch	$[m]$
Sc	Schmidt number	$[-]$
St	Stokes Number	$[-]$
T	Temperature	$[K]$
T^*_{aw}	Imposed adiabatic wall temperature	$[K]$
T_N	Normalized Temperature	$[K]$
Tu	Turbulence	$[\%]$
V, v	Velocity	$[m/s]$
VR	Velocity Ratio	$[-]$
W	Molecular weight	$[kg/kmol]$

Greeks

α	Hole inclination angle, Swirl angle	$[deg]$
β	Pitch angle	$[deg]$
δ^*	Displacement thickness of the boundary layer	$[m]$
η_{aw}	Adiabatic Effectiveness	$[-]$
η_{ov}	Overall Effectiveness	$[-]$
γ	Ratio of specific heat	$[-]$
λ_{PVC}	Conductivity of Polyvinyl Chloride	$[W/(m \cdot K)]$
μ	Dynamic viscosity	$[Pa \cdot s]$
ϕ	Equivalence ratio	$[-]$
ρ	Density	$[kg/m^3]$
θ	Dimensionless temperature, azimuth angle	$[-], [deg]$

Subscripts

an	Annulus
aw	Adiabatic wall
$c; cool$	Coolant
$conv$	Convective
eff	Effusion

fg	Foreign gas
is	Isoentropic
j	Jet
$main$	Mainstream, gas side
$ref, 0$	Reference condition
sl	Slot
sw	Swirler
t	Turbulent
w	Wall
30	Combustor inlet
40	Combustor outlet

Acronyms

$ACARE$	Advisory council for Aeronautical Research in Europe
$CAEP$	Committee on Aviation Environmental Protection
CO_2	Carbon Dioxide
CS	Combustor simulator
CVP	Counter-rotating Vortex Pair
DP	Design Point
$FACTOR$	Full Aerothermal Combustor-Turbine interactiOn Research
FAR	Fuel-Air Ratio
FDM	Finite Difference Model
FRT	Fast Response Thermocouple
HP	High Pressure
HS	Hot Streak
HWA	Hot Wire Anemometry
$ICAO$	International Civil Aviation Organization
ITD	Inlet Temperature Distortions
LDI	Lean Direct Injection
LE	Leading Edge

LES	Large Eddy Simulation
LP	Lean Premixed
LPP	Lean Premixed Prevaporized
$NEWAC$	New Aero-Engine concepts
NGV	Nozzle Guide Vane
NO_x	Nitrogen oxides
OPR	Overall Pressure Ratio
$OTDF$	Outlet Temperature Distribution Factor
$P40, P40+$	Plane 40, Plane 40+
PIV	Particle Image Velocimetry
$PERM$	Partially Evaporated and Rapid Mixing
PS	Pressure Side
PSP	Pressure Sensitive Paint
$PMMA$	Poly-Methyl Methacrylate
PVC	Processing Core Vortex
$P40$	Plane 40
$RANS$	Reynolds Averaged Navier-Stokes equations
$RTDF$	Radial Temperature Distribution Factor
RQL	Rich-Quench-Lean combustor
SS	Suction Side
TBL	Turbulent Boundary Layer
TE	Trailing Edge
TIT	Turbine Inlet Temperature
TLC	Thermochromic Liquid Crystal
TRL	Technology Readiness Level
TS	Traverse System
UHC	Unburned Hydro-Carbons
ULN	Ultralean Low NO_x

Introduction

"Caution: cape does not
enable users to fly"
Warning label on Batman costume

The development and the spreading of the gas turbine engine as an aircraft prime mover has been so rapid that it is difficult to appreciate that prior to the 1950's very few people had heard of this method of aircraft propulsion. The possibility of using a reaction jet had interested aircraft designers for a long time, but initially both the low speeds of early aircraft and the unsuitably of a piston engine for producing the large high velocity airflow necessary for the "jet" presented many obstacles.

In 1913 a French engineer, René Lorin, patented a jet propulsion engine: actually it was a "ram jet" and, at that period, it was impossible to be manufactured or used, since suitable heat resisting materials had

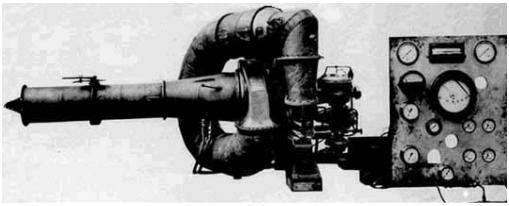

Figure 1: First turbojet engine (F. Whittle, 1937)

(a) Rolls-Royce Trent XWB (b) General Electric GE90 115-B

Figure 2: High-bypass ratio multi-shaft turbofan engines

not been developed yet and, in the second place, jet propulsion would have been extremely inefficient at the low speeds of the aircraft of those days.

Dr. Hans von Ohain and Sir Frank Whittle are both recognized as being the co-inventors of the jet engine. Each worked separately and knew nothing of the other's work. Hans von Ohain is considered the designer of the first operational turbojet engine. Frank Whittle was the first to register a patent for the turbojet engine in 1930 (figure 1). Hans von Ohain was granted a patent for his turbojet engine in 1936 and his jet was the first to fly in 1939. Frank Whittle's jet first flew in in 1941.

In the following decades, the development of well performing and high specific power engines reached insurmountable, for those times, limits. Engineers had already guessed the huge potential of a reaction jet but, as mentioned before, piston engines were completely unsuitable for such a purpose.

Gas turbine engines rapidly became the standard choice for aircraft propulsion and, even though the operating principles have kept substantially unchanged from the prototype that Whittle and von Ohain invented, a lot of, sometimes outstanding, developments and improvements have been made. Figure 2 shows two examples of modern aeroengine architecture, which includes the use of a turbofan at the intake to obtain high by-pass ratio, and the use of multi-shafts to take the advantage of

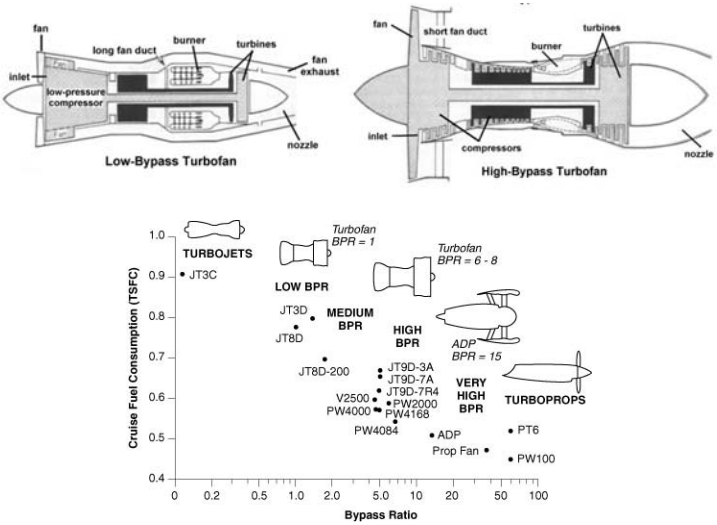

Figure 3: Evolution of turbofan engines[1]

various rotational speeds of the shaft for different parts of the engine.

The advent of gas turbine engines represented a revolution for aero-propulsion: higher flight speeds, increased efficiency, better thrust to weight ratio and reduced sizes were among their major appeals. As stated by Lefebvre [1], developments in the art and science of gas turbines have traditionally taken place gradually and continuously, rather than through dramatic change. However, during the last two decades the more demanding request of engine improvements in overall efficiency and power output, as well as the reduction of weight and fuel consumption, caused a rapid acceleration in the development of more performing engines. These requirements has driven to a complete revision even of the architecture and the design concepts, leading to the several innovations which now represent the status of modern aeroengine. The sketch in figure 3 illustrates a comparison between the low and high by-pass ratio turbofans: even if the low-bypass turbofan is more compact, the

[1] *http://www.aerospaceweb.org/question/propulsion/q0033.shtml*

trend of evolution is directed to high-bypass turbofan which can produce much greater thrust, it is more fuel efficient, and it is much quieter. The picture highlights also some of the main features of high-bypass engine, as the previous mentioned multi-shafts (in this example, two compressors and the fan of the high-bypass turbofan the are driven at different speeds by two turbines) and the compact burner, which substitutes older arrangements like the can or can-annular combustors.

Context and Motivations

The demand of more efficient engines, with reduced specific fuel consumption and increased specific power output, is directly related to the possibility to realize compressors with high compression ratios and high efficiency, and to build components capable to withstand high temperatures; in fact, for a conventional gas turbine cycle, the thermal efficiency is mainly a function of the overall pressure ratio (OPR) and the turbine inlet temperature (TIT). This is illustrated in figure 4, which plots the trend of evolution during the last decades of the specific core power output production (which is related to the engine specific thrust) as a

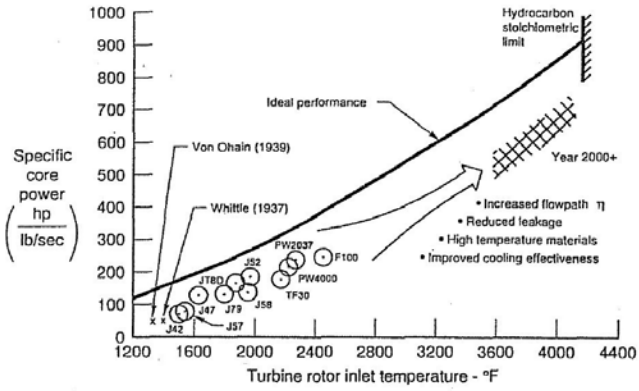

Figure 4: Trend in TIT: effects on cycle power output [2]

function of turbine inlet temperature.

OPR and TIT directly affects the design of the combustor and the high pressure turbine, which are the most critical components from a thermal point of view: in fact, an increase of OPR leads to an increase of combustor inlet temperature, which in turns reduces the cooling capabilities of air for combustor liners and tubine vanes, blades and endwalls. Moreover, the enhancement in OPR causes a direct increase of radiative thermal loads in the combustor, and the request of higher TIT implies higher thermal stresses on all the hot components of the engines. Therefore, the design of more efficient cooling systems becomes mandatory, as well as an optimization of the mixing between the hot gases and the cooling flows in the combustion chamber in view of the impact on the high pressure turbine.

The enhancements of overall pressure ratio and turbine entry temperature have to face not only with maximum material temperatures, but also with the increasing of polluting emissions, whose production rate is directly related to the combustor working conditions. Actually, parallel to the request of improving the overall efficiency of the aircraft, the issue of atmospheric pollution by combustion products has escalated appreciably in public importance, and it has led to the promulgation of increasingly stringent regulations for limiting polluting emissions of aircraft gas turbines. To meet these requirements, a complete review of the design guidelines of gas turbine combustors has become an outstanding issue, being this component the core of the engine where the combustion process takes place and, consequently, where the pollutants are generated. The introduction of new concepts and technologies for ultralow emission combustors, along with concomitant developments in fuel preparation and wall cooling techniques, and the consequent need of testing and validating the innovative solutions, are therefore the challenges to be faced.

Within this scenario, lots of European projects have been funded during the last years with the aim of identifying the technology routes to environmentally friendly and economic propulsion solutions. The research presented in this study was carried out within the context of sev-

eral EU projects, mainly the *NEWAC* (NEW Aeroengine Core concept) Integrated Project (Grant Agreement FP6-030876) and the *FACTOR* (Full Aerothemal Combustor-Turbine interactiOn Research) Collaborative project (Grant Agreement FP7-265985). The leading thread of this thesis is the investigation of some features of new aeroengine combustors, with the aim of deepening the knowledge on their operation and moreover giving indications on how to update the current design practices.

More specifically, after a general introduction to gas turbine combustors for aeroengines (Chapter 1), the first part of the work (Chapters 2 - 4) will deal with effusion-based liner cooling systems for low emission combustors: through numerical and experimental investigations, the study will be aimed at pointing out indications and guidelines for the design of such kind of cooling technology. Afterwards, the effusion system will be integrated within the rest of the module and the investigation will be extended to the entire lean burn combustor (Chapters 5 - 8): the attention will be focused on the generation of hot streaks due to the interaction between the mainflow and the effusion coolant, in view of their impact on the thermal design of the high pressure turbine.

Chapter 1

Combustor for Aeroengines

"Oh, she doth teach the torches to burn bright!"
W. Shakespeare, Romeo & Juliet

Combustors are the "burning heart" of gas turbines; this chapter will give a general overview on combustors for aircraft propulsion and their typical layout integrated within the rest of the engine. The focus of attention will be then moved to their trend of evolution in the last decades and, moreover, to the causes that are leading the design choices of novel combustors; as it will be explained, the requirements concerning an increase in engine performances go together with the need of reducing polluting emissions from the combustion process, especially in terms of NO_x . This aspect is driving the development of combustors towards the lean-burn combustion technologies, which now represents the most promising solution to achieve the main goals of aeroengine gas turbines development.

Following this brief introduction to combustors for aircraft applications, the purpose of this work will be finally presented.

1.1 Combustor System Layout

Aircraft propulsion is an interesting application of Newton's third law of motion and momentum principle. The aircraft engine expels a jet of hot gases from its tail: this is say, an action force. The jet of hot gases exerts a force on the jet engine, propelling it forward; this is the reaction force. From the momentum point of view, the hot gases acquire momentum in the backward direction and the aircraft acquires an equal amount of momentum in the forward direction. A jet engine produces thrust by ejecting a large amount of air backwards one in the form of a large air slipstream at comparatively low speed and the other in the form of a jet of gas at very high speed. The types of jet engine, whether ram jet, rocket, gas turbine, turbo/ram jet, etc., differ only in the way in which the engine supplies and converts the energy into power thrust for flight.

Figure 1.1 depicts a scheme of a modern gas turbine engine for aircraft propulsion: air drawn by the fan and is splitted before entering the compressor. Depending on the by-pass ratio, the main amount of air is directed to the external part of the engine and it does not take part to the process. The pressure of the remaining mass flow is risen by several

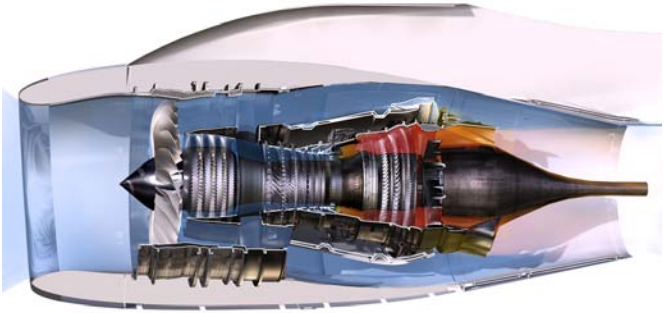

Figure 1.1: Sketch of a typical turbofan jet engine (PowerJet SaM146[1])

[1] *http://superjet.wikidot.com/wiki:rukovoditel-powerjet-kloda-pulan-dal-intervu-vladimiru*

stages of the axial compressor and then it is driven to the combustor chamber: here, air is mixed with fuel and the chemical energy of the resulting mixing is converted to thermal energy of combustion products and excess of air. The enthalpy, i.e. the temperature, of air raised by the combustion process in the combustor is then is converted in mechanical energy by the following stages of the turbine; the power generated by the turbine is used to drive the compressor and the fan. Finally the exhaust gases mix with the cold air bypassed by the fan in a converging nozzle to generate the jet that gives the thrust to the entire aircraft.

Despite the fact that combustion chambers are located in the core of of the Brayton-Joule cycle, (highest levels of temperature, pressure, inlet velocity, etc.), historically they always had higher efficiency (often approximated to 100%) with respect to other components. However, combustors have been the object of constant improvements in order to reduce pollutant emissions and increase the component's life [1].

Starting from its primary purpose, the simplest scheme for a combustor chamber would be made up of as a straight duct linking the compressor exit to the turbine entry (figure 1.2(a)). If enough fuel were injected inside such a channel, a coarse mixing with air would be achieved and the combustion process would take place. Unfortunately this simple configuration is unusable because the high air velocity at the inlet of the combustor would cause too high pressure loss and it would make impossible to maintain anchored the flame. In addition, this simple configuration

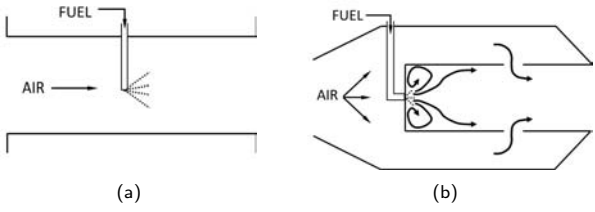

Figure 1.2: Developments in combustor chamber concept

would require a continuous introduction of heat to maintain the chemical process; moreover, not all the mass flow from the compressor should be involved in the reaction since the Fuel-Air Ratio (FAR) must be kept within the flammability limits of the mixture to avoid the extinction of the flame. These basic considerations directly lead to the configuration shown in figure 1.2(b): a diffuser located at the combustor inlet reduces the velocity of air, which is then split before entering the flame tube. Only a portion of the mass flow is directly mixed with the fuel to guarantee a suitable value of FAR, while the rest of it is first used to cool the liner, a metal sheet that bounds the burning region, and then added to the burned gases to complete the chemical reactions and lower the main-flow temperature. In addition, a part of the hot gases is recirculated inside the combustor chamber itself to continuously supply heat for the maintenance of the combustion.

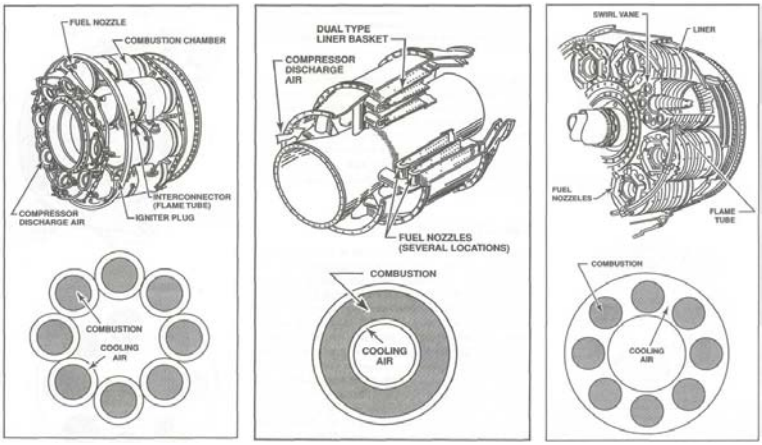

Figure 1.3: Geometrical arrangements for combustor: a) Can, b) Annular, c) Tubo-annular[2]

[2] *http://dc304.4shared.com/doc/RovTA9ri/preview.html*

The geometry of a combustion chamber is dictated also from the needs of the rest of the engine. Historically, three different configurations of gas turbine combustor have been employed (figure 1.3): can or tubular, annular and tubo-annular . Each configuration has peculiar features and drawbacks, but in the field of aircraft engines the annular layout has become the most effective choice since the '60s: despite the higher buckling load on the outer liner, the difficulties in achieving a uniform distribution of fuel around the annular space to guarantee combustion stability for all the engine operating conditions, and, consequently, the marked temperature non-uniformities at the outlet section, annular combustors offer a compact layout with maximum utilization of available volume, reduced weight and minimum pressure loss. Furthermore, light-around problems, i.e. the propagation of the entire circumference of the combustor from sparse igniter, are minimal [3].

Figure 1.4 shows a cross section of typical annular combustor and indicates the location the main components:

a) *Diffuser*: basically it consists of a diverging duct that connects the compressor outlet guide vane to the core of the burner. It is aimed at lowering the velocity of the air flow to reduce as much as possible the pressure losses across the combustor due to friction and to recover the dynamic pressure; the objective of its aerodynamic design is the minimization of losses related to pressure recovery (flow detachment and generation of turbulent shear layer and zones of recirculating flow due to the adverse pressure gradient).

b) *Cowl*: it is a shaped structures that, together with the diffuser, split the mass flow from the compressor in the two cooling and a main flows, directed respectively to the two annuli and to the dome. Similarly to the diffuser, the cowl must minimize the pressure loss of the mainstream.

c) *Dome*: it is the front end of the combustor and it acts as a shield for the injectors from a direct contact with hot burning gases and from the radiative load from the flame. It is subjected to heavy

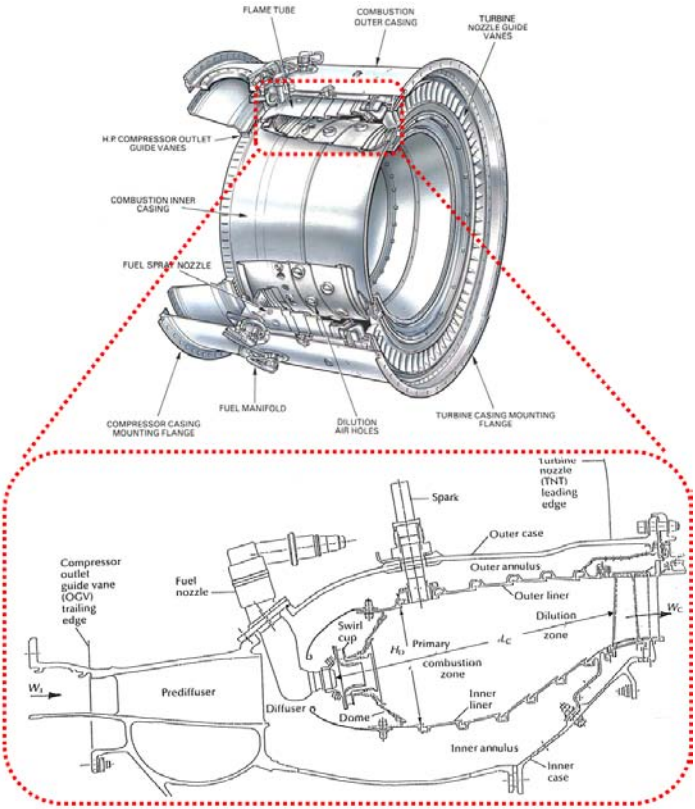

Figure 1.4: Example of an annular combustor chamber (RR-RB211 [4]) and detailed view on a general layout (GE CF6-80C [3])

thermal loads and it needs to be cooled.

d) *Casing*: structural shell of the combustor that carries the thrust load. It bounds the internal and external annuli, which are the passages for the liner cooling air.

e) *Inner/Outer liners*: liners are made up of a thin metal sheet and they protect the casing and the power shaft from the burning gas.

Furthermore, they provide air for the control of the combustion all along the flame tube; "fresh" air is used also to keep them cooled through several cooling techniques.

f) *Fuel injectors*: injectors delivers fuel to the chamber and promotes the fuel/air mixing. In addition, they set up dominant flow structures in the combustion chamber, mainly the recirculation zone, that provides the dominant flame stabilization mechanism. Furthermore, the aerodynamics of the injector affects the formation of polluting emission and, through the flow field generated in the flame tube, of the heat load on the liner walls. Finally, it directly influences the thermal field at the outlet of the combustor, and consequently its impact on the first stages of the turbine.

g) *Flame tube*: bounded between the liners, the flame tube is where the combustion processes take place. Commonly it can be divided two zones: in the primary combustion zone most of the chemical reaction are carried out, while in the dilution zone a rapid mixing with a large amount of air lowers the gas temperature and completes the reactions.

h) *Spark*: located close to the exit of the swirlers, it is the heat source to start the ignition of the fuel-air mixture and, if necessary, to help the sustenance of the chemical reactions.

Since the advent of gas turbines in aeronautical propulsion, each component of the combustor was developed and improved following a natural process of optimization, which was driven by requests such as the increase of efficiency, the reduction of the weight and the sizes, the reduction of fuel consumption, the increase of the turbine inlet temperature (TIT), i.e. the increase of temperature in the chamber, the increase of the stability of the combustion in different operating conditions, etc. This trend of evolution had a radical change around the 90's, when the issue of atmospheric pollution by air transport escalated appreciably in public importance and led to the promulgation of increasingly stringent regulations for limiting pollutant emissions for aircraft gas turbines. Legislation

limits defined by ICAO-CAEP and ambitious pollutant reduction target set by ACARE made it necessary to completely review the standard design procedures for combustors, starting even from the design concepts and the architecture of this component.

1.2 Evolution of Combustor Concept

Global air transport moves over 2.2 billion passengers annually and it is forecast to grow at an average annual rate of around 5% in the next decades. As a result, the aviation industry is facing a massive challenge to satisfy this demand for increased air travel in an economic and safe way, channelling the effort of the research to develop more powerful and fuel efficient engines. However, this high level of growth introduces also the need to keep under control the environmental impact of air transport, especially in terms of polluting emissions. The aviation industry in Europe has long recognised this challenge and in 2001 the Advisory Council for Aeronautical Research in Europe (ACARE) established the following ambitious targets for 2020 (compared to 2000):

- reduction of fuel consumption and CO_2 emissions by 50% per *pkm*
- reduction of NO_x emissions by 80%
- reduction of perceived noise by 50%
- reduction of the environmental impact of the manufacture, maintenance and disposal of aircraft and related products

Unfortunately, in some aspects, satisfying the requirement of increasing engine performance is in conflict with previous objectives, particularly the decreasing of polluting emissions: as an example, the demand of having more fuel efficient engines can be fulfilled by improving the thermal efficiency of the core engine through an increase of the overall pressure ratio (*OPR*) and the *TIT*. Both these measures have a negative effect on the production of nitric oxides: according to the Zeldovich mechanism, which is mainly the responsible for the formation of NO_x emitted by

common aero engines [5], the nitric oxides production rate depends exponentially on the temperature. The combustor pressure, especially for conventional burners, has an effect on the NO_x production rate mainly due to the effects of the homogenization of the fuel air mixture.

As a results of the target set by ACARE, serious regulations on the production of these pollutants have been emitted by governments in the last decades and in the near future limits allowed to certificate turbine engine are expected to become stricter and stricter. As a consequence, the need of reducing emissions, especially in terms of NO_x , became the driving force that has been leading the evolution of combustors for the last twenty years.

1.2.1 Rich-Quench-Lean Combustors

The state of the art for low-NO_x combustors are represented by the so called RQL (*Rich Quench Lean*) scheme: in fact this configuration allows the control the polluting emissions and, at the same time, it guarantees an extremely wide stable operation range from idle to maximum power.

A sketch of a RQL arrangement is depicted in figure 1.5(a): fuel is directly injected in the "rich-burn" zone where it mixes via turbulent and molecular diffusion with part of the air flow from the compressor; this results in equivalence ratios (ϕ) higher than stoichiometric at high

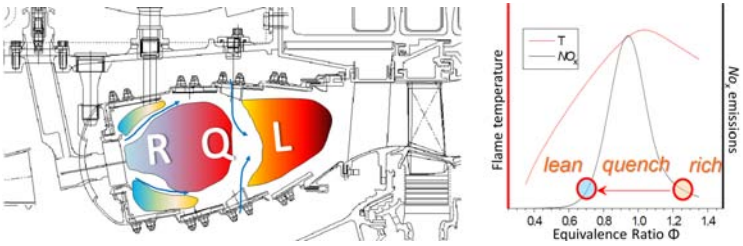

(a) RQL combustor scheme (RR Trent XWB) (b) NO_x formation chart

Figure 1.5: Rich-Quench-Lean combustor concept

power (ϕ=1.2-1.6) and acceptable lower values at idle [6]. In addition, rich burn conditions minimize the production of nitrogen oxides due to the relative low temperatures and low population of oxygen containing intermediate species. This "primary" zone is aimed also at generating a recirculating flow that anchors the flame and provides sufficient resident time for fuel-air mixture to carry on the combustion process.

The effluent emanating from the rich primary zone will be high in the concentration of partially oxidized hydrocarbon species, hydrogen, and carbon monoxide, which are oxidized between the primary and the dilution zones: here a massive amount of air is injected through wall jets (dilution holes) to favour a rapid mix with the partially burned gases, "quenching" the chemical reactions and creating "lean-burn" conditions (ϕ=0.5-0.7) prior to the exit of the combustor.

Figure 1.5(b) shows the emission characteristics of RQL combustor; the critical passage for the production of NO_x takes place during the switching from rich to lean combustion: in fact, if the mixing between air from the dilution jets and the burning gases is not quick enough, local values of $\phi \approx 1.0$ may occur with the consequent enhancement of the thermal NO_x production rate. This intrinsic characteristics of the operation of RQL combustors represents a severe limitation in optimizing the polluting emissions. In addition: the application of cooling technique based on the generation of a protective film (film cooling) requires extra care because also cooling air injections may produce locally stoichiometric conditions with high temperatures that may counteract the low NO_x target; the primary zone generates a large amount of soot which radiates heat to the walls aggravating the cooling problem; the quench zone requires a very fast mixing to minimise residence times near stoichiometric equivalence ratios and high temperatures; finally, the lean-burn zone needs to operate sufficiently hot to burn out soot, CO and UHC from the primary zone exhaust [7].

These aspects led the research to find new strategies for NO_x reduction; several alternatives were proposed, but the most promising approaches for the significant improvement needed to meet the ACARE's

target are all based on the lean-burn technologies. To introduce these new technologies, the architecture of the combustor itself needs to be reviewed and adapted to satisfy new requirements.

Before going into details and highlighting the characteristics of lean-burn combustors, it is worth mentioning the main features of the RQL arrangement as a touchstone:

- *Air distribution*: most of the air from the compressor, roughly 55-65%, is directed towards the outer and inner annuli; a portion of this mass flow is then injected inside the combustor chamber through several holes or slots distributed along the liner for cooling purpose, while a significant part is introduced through primary and dilution holes, necessary for the combustion process. The remaining part of air from the compressor is directed to the cowl: roughly its 60% is sent to the injectors, while the rest is used to cool the dome.

- *Fuel injection*: fuel is directly injected in the combustion chamber where it evaporates and mixes with air by means of turbulent and molecular diffusion, resulting in a diffusive flame. Injectors are requested to promote the swirling flow that anchors the flame and helps the mixing. As it will be explained further on, injectors for lean-burn combustors have a more active role in fuel preparation.

- *Liner cooling*: cooling of the liner is usually achieved using forced convection in the annulus and through the injection of film cooling air by means of holes or slots along the metal walls. Since a large amount of air is available, the design of the cooling arrangement is, paradoxically, mainly driven by other needs than cooling, such as prevention of stoichiometric regions due to the injection of film cooling air.

Given these characteristics, the possibility to switch directly to a lean burn combustion is not feasible; as an example, the idle condition and the weak extinction limits prohibit lean flames at higher power settings because with fixed geometry the air split between the primary and the

downstream secondary and dilution zone is constant over the operating range. Consequently, as stated before, a complete review of the main features of combustors became mandatory to meet the requirements dictated by new low-NO_x technology.

1.2.2 Lean-Burn Combustors

The idea of a lean burn combustor is to operate with an high excess of air to avoid stoichiometric conditions, to keep a lower temperature level inside the combustor and thus to inhibit the formation of NO_x . Unfortunately, moving to lean mixture, the production of CO and UHC rises because the low burning temperature increases the conversion times of these species, that become of the same order of flow residence times in the flame tube [8]. The dependency of the polluting emission rate with FAR is illustrated in figure 1.6; the figure indicates that the operating range in which a lean combustor can work with low emissions and without occurring in flame extinction is quite narrow. The issue becomes even more critical considering that engine is subjected to different operating regimes, from the idle to the take off conditions, and that the efficiency, the stability and the low polluting emissions of the combustion process

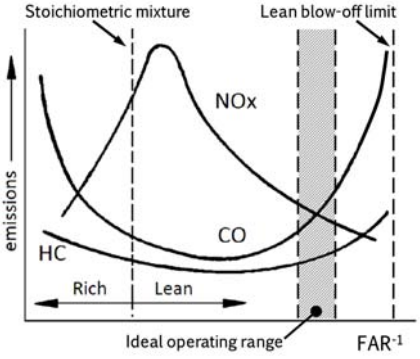

Figure 1.6: Dependency of NO_x, CO and UHC emission on the FAR

must be always guaranteed through the whole Landing-Take Off (*LTO*) cycle.

A rather simple method to overcome the operating range problem of the conventional combustor is fuel staging. It is accomplished by turning off individual or groups of burners, and thus increasing fuel flow and equivalence ratio in the remaining burners. In a staged combustor two separated zones are designed to optimize certain aspects of combustion performance: the first zone operates at fairly high equivalence ratio (slightly lower than stoichiometric) to achieve high combustion efficiency and to minimize the production of CO and UHC. This "rich" zone guarantees the stability of combustion during idle and low power conditions. At higher power level, it acts as a pilot source of heat for the second "main" combustion zone, which is supplied with premixed fuel-air mixture; in this way, the engine globally works in lean conditions, minimizing the NO_x emissions and smoke; moreover, the combustion process results efficient and stable for a wide range of operative conditions. An example of an axially-staged approach was developed in the CLEAN combustor (*Component vaLidator for Environmentally Friendly Aero Engine*) within the EU research program EEFAE (*Efficient and Environmentally Friendly Aircraft Engine*) [9]: the main dome of the combustor, depicted in figure 1.7(a), is designed to achieve the best possible lean premixed pre-vaporized combustion thanks to a so-called *LPP* injection system (see below).

Nevertheless, this type of combustors slightly deteriorates CO and UHC emission levels in comparison with a single annular chamber, particularly at low regime [9]. Furthermore, the weight and complexity of the system are increased; in addition, the geometrical complexity of these combustors have relatively large surfaces to be cooled, leaving, for a given cooling technology, less air available for the lean injectors and so limiting partially the expected gain in NO_x emissions. This drawback can be overcome with advanced cooling systems but to detriment of costs.

New single annular technology with fuel staging has been explored with the GE-TAPS (Twin Annular Premix System), a concept already

(a) CLEAN Axially-staged Combustor

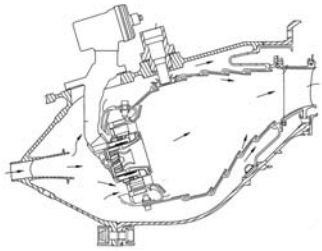

(b) GE TAPS combustor

Figure 1.7: Examples of fuel staging combustor arrangements

tested on CFM56 engines (fig. 1.7(b)). The idea is to combine the two domes into one with fuel staging using two fuel manifolds. Emission performance characteristics have shown this approach to be highly promising, making it possible to reduce all types of emissions compared with a double annular combustor. However, CO and UHC emissions remain higher than on a conventional single annular combustor and they still have some operability constraints. In addition, as they are more complex compared to conventional air-blast fuel spray nozzles, a significant proportion of the combustor cost will now be related to these internally staged injectors.

Despite some drawbacks, GE-TAPS overcame many limitations related to staged combustor; therefore the focus of the research has moved to the definition of new single annular combustor architectures with lean injectors internally staged. Such architectures, named ULN (*Ultra Low* NO_x), offer the highest potential to keep penalties on weight and cost associated with the introduction of lean low emission combustion technology at acceptable levels.

The first key strength for an effective and well performing low NO_x combustor is in the design of the lean burn injection system: air quantity needed for emission abatement is expected to be 60% to 70% of the combustion air ($\approx$ 50% more than RQL arrangements). With this level of FAR in correspondence of the injector, operability including ignition, al-

titude re-light, pull-away, weak extinction stability and thermo-acoustics will be a serious problem which needs to be carefully taken into consideration during ULN combustor development [10].

Generally speaking, different aeroengine sizes, maximum OPR and related core loadings usually imply very different engine cycles in terms of combustor inlet pressures and temperatures, as well as nominal FAR. It comes straightforwardly that these operating parameters have an outstanding impact on low NO_x injector performance. In addition, the goal of achieving an efficient and clean combustion is even more critical since aeroengine combustors employ liquid fuels. Actually, to achieve low-emission combustion, a complete evaporation of the fuel is fundamental: the liquid must be atomized into small droplets and then suitably distributed in an air stream in order to obtain an optimal level of mixing among the air, fuel, and combustion products inside the combustion zone. Once the geometry of the injector is fixed, the combustor working pressure has a strong impact on the performance of the fuel atomization and mixing and, consequently, on the efficiency of the entire combustion process.

As a consequence of previous considerations, ULN technology including fuel preparation, fuel placement and the formation of two combustion zones strongly interacting each other (pilot and main) is very difficult to scale to various engine sizes, due to several nonlinear effects. To overcome this issue, the attention was focused on different combustion technologies depending on the size and the operating conditions of the engine, e.g. the OPR; as an example, figure 1.8 reports the main injection systems developed within the NEWAC research project [10]:

- *LP(P)*: small engines operate at low OPR levels, but their combustors have to face problems related to low volume-to-surface ratios: since combustion temperatures are roughly the same, this leads to a relatively higher air consumption for cooling than large combustors. This kind of engines allows the implementation of LP(P) technology (*Lean Premixed Prevaporised*): it is based on the action of two air flows, one devoted to the fuel atomisation and the second dedicated

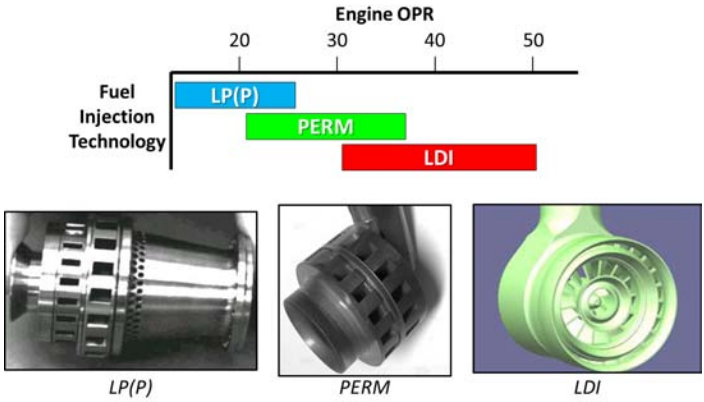

Figure 1.8: Ultra Low NO_x fuel injector technologies

to the mixing and fuel evaporation. The combination of the two acts also as a promoter for the flame stabilisation in the combustion chamber.

- *PERM*: LPP injectors cannot be mounted on high OPR engines due to their inherent risk for auto-ignition and flashbacks that may lead to integrity problems of both the burners and the combustor. The design of PERM injectors (*Partially Evaporated and Rapid Mixing*) overcomes this risk: the concept is based on swirler technology development and it is addressed to achieve partial evaporation inside the inner duct and a rapid mixing within the combustor, optimising the location of the flame and the stability of the lean system.

- *LDI*: this kind of injection system is suitable for very high OPR engine. LDI (*Lean Direct Injection*) concept is based on a controlled premixing: concentric internally staged fuel injection with optimised pilot and main stage flame structure are used to control their interaction for low NO_x and weak extinction stability.

With respect to RQL injectors, the aerodynamics of these new technologies has to be completely review; moreover, fuel preparation, stabi-

lization of the combustion process, stability control system for the pilot and main injection circuits to restrict the flame temperature and to maintain combustor operability, control of thermo-acoustic and combustion instabilities, thermal management to prevent fuel coking, are only some of the issues to be taken into account for the design of the new combustion systems.

Once the lean burn combustion has been identified as the most effective strategy to achieve significant NO_x emissions, and new suitable injection technologies have been characterized, a review of the entire combustor arrangement becomes of outstanding importance both to fulfil the new specific requirements and, no less important, to obtain an efficient integration with the following high pressure turbine module.

1.3 Research Objectives and Thesis Outline

This chapter presented an overview of the trend of evolution of combustors for aeroengines. New combustion systems are required to satisfy the ambitious objectives related to the reduction of polluting emissions; in the current scenario, lean combustion systems are considered the most effective technology for a significant NO_x reduction in future aero-engines. The introduction of these innovative systems rises the necessity of a complete review of the main features of combustors to meet the requirements of new ULN engines; in particular, in addition to new injection systems, the main aspects that require major investigations aimed at deepening their knowledge for a reliable design and integration within the engine are:

a) Cooling systems

As mentioned before, to obtain a lean combustion, air distribution among the cowl and the annuli is completely changed with respect to RQL: up to 70% of the overall air mass flow is utilized for fuel preparation and the initiation of lean combustion, at the expense of cooling air, which is severely reduced. Indeed, one goal in future combustor development is the improvement of the cooling performance and the reduction of the

amount of coolant by about 50% [11].

Furthermore cycle parameters as combustor pressure, inlet temperature, and exit temperature are continuously rising which leads to an increase of the thermal load at the combustor walls. At the same time the cooling potential is reduced since the cooling air temperature increases due to higher pressure ratios. For these reasons, lean combustors require very efficient cooling to cope life targets.

Within this scenario, *effusion cooling* is one of the most promising solution, as the growing number of studies on this topic shown. However, to have a full comprehension of the effusion behaviour, very detailed information about parameters influencing the cooling performance are required, and in the case of lean combustion much more exhaustive than available at the moment.

b) Combustor-turbine interaction

The combustor-turbine interface is a critical area of the engine. Combustor designs, particularly for aeroengines, typically have film holes or slots that provide cooling along the liners; the coolant that is injected out of the liner produces highly non-uniform temperature and pressure radial/tangential profiles which leave the combustor and enter into the turbine; such non-uniformities are commonly named *hot streaks*.

Despite the tight link between the combustor and the turbine due to these non-uniformities, historically the design of the two modules relied on separated approaches and the gap of knowledge on the mutual interaction was bridged by the industrial experience. The introduction of new injectors and new cooling systems for lean combustors changes completely the development of the flow field inside the chamber with respect to RQL. In particular, the absence of dilution holes reduces the mixing process between the burning gases and the cooling flows, enhancing the temperature distortions and the degree of swirl of the mainflow at the turbine inlet; furthermore, new cooling arrangements based on a homogeneous film cooling distribution along the liner, such as effusion system, generate a coolant layer whose thickness increase row by row towards the

combustor exit without a significant mixing with the mainstream. These effects have both a strong impact on the resulting hot streak distribution which, in turn, directly affects the aerodynamics, heat transfer, loading, life, secondary loss, and, therefore, the overall efficiency of the high pressure turbine [12].

The lack of confidence in the prediction of combustor-turbine interaction and the poor industrial experience on new lean burn combustors lead to apply extra safety margins on the design of the components of the engine that are subjected to the highest thermal loads: however, this conservative approach, which is necessary to avoid failures of these components, drastically limits the potential for lower specific fuel consumption and CO_2/NO_x emissions. As a consequence, the understanding of combustor-turbine flow field interactions and, above all, the possibility of collecting reliable experimental data on hot streaks are mandatory to preserve hot components life and performance when optimising the design of new HP turbines and combustors of lean burn engines.

The two previous paragraphs introduced the research area of this work: the study, focused on these two aspects of a lean burn combustor, is aimed at deepening the knowledge of the involved phenomena and at collecting new detailed experimental data. The test rigs and the experimental procedures developed in this work, as well as their integration with numerical activities, are directed to provide useful information for the design of a low emission combustor, as well as to indicate general guidelines to update the current design tools.

Initially, the focus will be on cooling systems for lean burn combustors: after a general introduction on the topic (Chapter 2), a short chapter will introduce the enhancement of a 1D numerical tool for the design of combustor cooling systems (Chapter 3). This numerical code will be recalled at the end of the following chapter (Chapter 4): this section will be dedicated to an extensive investigation of an effusion cooling system and its integration with other features of a combustor. An experimental survey will be carried out on a simplified effusion geometry integrated with re-

alistic supporting elements (3:1 scaled); afterwards, the wide obtained experimental database will be exploited by the previously mentioned 1D code both to deepen the analysis, and to increase the fidelity on the effusion technology.

Once assessed the efficiency and the reliability of the effusion cooling, the system will be integrated in the combustor and the experimental analysis will be extend to the whole flow field inside the chamber. In order to obtain engine-representative data, such kind of analysis requires that the geometry of the test rig is close to a real combustor and tested in a relevant environment; therefore, with respect to the analysis on effusion cooling geometry, an important step in TRL [13] of the experiment is necessary, which is raised from ≈ 3 to ≈ 4 .

After a preliminary excursus on the hot streaks and on test rigs in literature dedicated to their study (Chapter 5), the development and the installation of a non reactive annular three sector test rig will be described (Chapter 6). The combustor simulator, manufactured in a 1:1 scale, allows to perform exhaustive experimental analyses to have a full investigation on the generation and the transport of hot streaks. The purpose of this investigation is to collect an experimental database documenting the thermal and flow characteristics in the lean burn representative combustor simulator, cooled by an effusion system. Chapter 7 will present the measurement techniques employed in the experimental survey, whose details and main results will be described in Chapter 8. Specifically, the investigation is aimed at characterizing the aerothermal field and the resulting hot streaks at the combustor exit; in addition, the analysis is focused also on the influence of the effusion cooling flow on the temperature and velocity non-uniformities at the outlet section of the chamber.

This wide experimental database is valuable in benchmarking computational predictions. With a greater understanding of these phenomena, designers will better able to predict the behaviour and the characteristics of hot streaks in a lean burn combustors and, in the long term, to optimize its design in view of the interaction with the high pressure turbine.

Chapter 2

Combustor Cooling

"Nothing burns like the cold."
G. R.R. Martin, A Game of Thrones

In order to perform a lean combustion, a large amount of air mass flow from the compressor is used for the fuel preparation: as a consequence, lean combustion requires a strong reduction of air available for cooling purposes. With reference to the burner mass flow, the fraction of the cooling air has to be reduced from up to 50% in conventional combustors to roughly 30% in lean combustors [14]. In addition, to improve the performance of the engine the pressure ratio is usually increased as well, resulting in an higher cooling air temperature at the inlet of the combustor. When considering all these aspects, it becomes clear that there is a great need for more efficient cooling technology. Among the different cooling solutions, the one that offers the most attractive characteristics to fit the requirements of new lean burn combustor is the effusion cooling.

After introducing the issues concerning the combustor cooling, this chapter will provide an overview on effusion cooling technology and on how it has been studied in literature for the last decades.

2.1 Cooling System Arrangements

Although the mechanical stresses experienced by combustor chambers are small in comparison with those affecting many other engine components, liner and flame holding segments are called to withstand high temperature and steep thermal gradients that threaten the structural integrity of the whole module. To ensure a satisfactory liner and dome life, it is important to keep temperature down to an acceptable level. Definitions of "acceptable" are almost arbitrary, but according to Lefebvre [1] for nichel-based alloys in common use the maximum operating temperature should not exceed 1300K against flame temperature that can reach and usually exceed 2000K. Therefore, it is clear that the design of a combustion chamber cannot exclude a correct layout of an effective cooling system.

The following paragraphs deal with the cooling systems of the two main critical components of the combustor chamber, which are the dome and the liner. If the impingement cooling has been long recognized as the most performing arrangement for the dome cooling, as far as the liner is concerned the research is still on going, especially in view of the strong reduction of coolant availability in lean burn combustors. One of the most promising solution able to guarantee an effective liner protection with small coolant consumption is the effusion cooling, which will be the major topic of this chapter.

2.1.1 Dome Cooling

The dome is aimed at holding the fuel injectors and above all at protecting them from the severe radiative and convective heat loads from the burning gas. Therefore, this component is subjected to high thermal gradients and it requires a very effective cooling.

Jet impingement is the cooling method that has the most significant potential to increase the local heat-transfer coefficient among all heat-transfer enhancement techniques. However, as it will be explained below, the construction of this flow arrangement weakens the structural strength

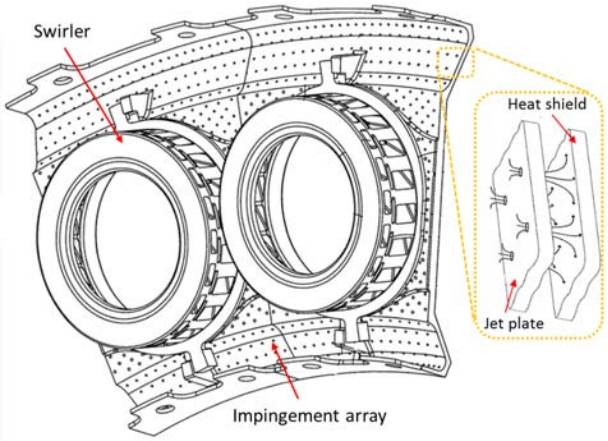

Figure 2.1: Impingement arrangement for dome cooling[1]

of the component and moreover it requires higher pressure with respect to other technique [2]. These considerations support its use for dome cooling, where pressure level and structural issues are less important than in other components. With respect to other impingement applications in gas turbine cooling , like blade leading edge and endwalls, dome impingement cooling is often applied to quite large surfaces.

Regular arrays of impingement jets are quite commonly used within combustors dome to provide relatively uniform and controlled cooling of the back surface of the *heat shield*, which is the metal sheet of the dome exposed to the flame: part of the air that accesses the cowl does not take part to the combustion process and it is used to feed the impingement array (figure 2.1). Such regular array is generally directed against the back surface of the heat shield by means of a sheet metal baffle plate (*jet plate*) that is fixed in position relative to the dome surface.

One of the milestone available in open literature focused on impingement cooling was done by Florschuetz et al. [15]; besides a comprehensive analysis of the phenomenon, the authors present a correlation that is still

[1] *http://www.strutpatent.com*

commonly employed in technical community as a term of comparison to validate new results. However, it is important to remark that the work of Florschuetz et al. was mainly dedicated to blade and vane cooling arrangements, which typical present higher values of pressure drop across the jet plate with respect to combustor domes. More recently, a deep investigation on impingement cooling from regular and sparse arrays for combustor cooling applications was carried out by Surace [16].

For a more effective protection, in some application a TBC is employed to the external surface of the dome to provide a very low conductive layer and thus increase the thermal insulation of the heat shield. Except for this further device, impingement is still the main cooling technique adopted for the dome. With the exception of a geometrical optimization of the array aimed at reducing the air consumption and increase the cooling effectiveness, this method almost remained unchanged switching from RQL to Lean-Burn combustors.

2.1.2 Liner Cooling

Forced convection inside the annulus is the basic method to cool the liner. However, the high temperatures and thermal gradients that burden on this component make the forced convection alone not suitable for combustion chamber cooling. Consequently, efforts were spent to integrate systems able of increasing heat transfer surfaces and coefficients that were historically developed for blade cooling. Among them, the most practical to use for liner cooling purposes should be ribs: indeed, they allow both an augmentation of the heat transfer surface and an increase in heat transfer coefficient due to the high turbulent and unsteady flow field they promote. Ribs have been widely investigated in literature, mainly for blade cooling, and, as a rule of thumb, their use permit an increase in HTC of 2-3 times with respect to the smooth surface. Studies on the application of further combustor cooling methods are available in literature, such as impingement cooling [16] or alternative arrangements obtained combining different techniques [17, 18]. Nevertheless, due to the additional manufacturing costs and the increase of the complexity of the

system, both simple configurations, and innovative arrangements based on the use of ribs have found difficulties to be integrated in the combustor.

The most widely used technique to control the liner temperature is film cooling. It is implemented by injecting relatively cold air bled from the annulus on liner inner side through holes or slot, thus creating a protective film that shields the liner from a direct contact with hot gases. In its basic design, film cooling makes use of a number of annular 2D slots injecting the coolant axially along liner hot surface; the film cooling is gradually destroyed downstream the injection point by the turbulent mixing with hot gas flow, so the normal practice is to repeat a succession of slot along the liner length. Mechanical robustness and low weight are

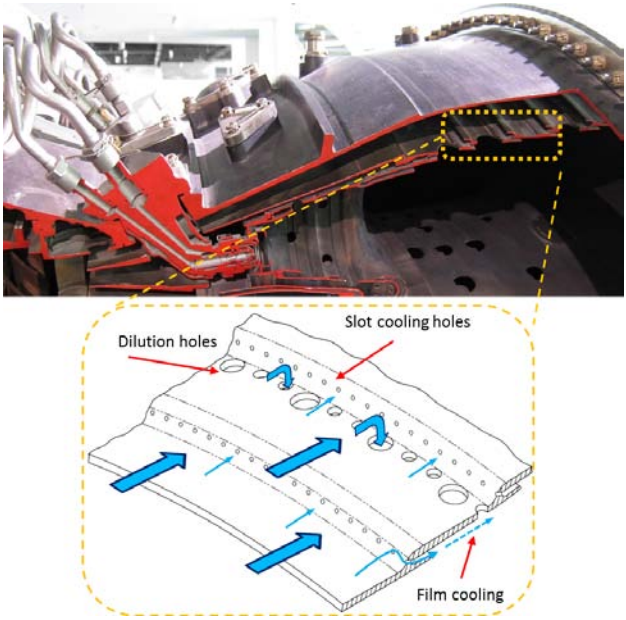

Figure 2.2: Example of liner cooling arrangement (P&W JT9D)[2]

[2] *http://en.wikipedia.org/wiki/Combustor*

the mayor advantages of such a technique which has found widespread application in both industrial and aircraft gas turbines. An example of slot cooling configuration is displayed in figure 2.2; the picture shows also the dilution holes located in some sections of the liner: these holes are necessary to complete the combustion process in a RQL combustor but they do not contribute to film cooling.

Due to the intensive use of film cooled solutions in the years of combustors development, a great number of theoretical and experimental studies are available in literature. A full description of the flow field behaviour downstream from a slot injection was given by Stollery and El-Ewany [19]; according the authors, three separated regions can be identified: the first comprising a potential core in which wall temperature is very close to that of the coolant, followed by a region where the velocity profile is similar to that of a wall jet, which finally evolves into a third zone where flow conditions become similar to a turbulent boundary layer. The main parameter governing the extension of these zones is the coolant-to-mainstream velocity ratio; however for combustor applications, which are characterized by highly swirled and turbulent gas flow fields, a high dependency on region extension from the swirl number and the turbulence level of free-stream and coolant was found respectively by Yang et al. [20] and Simon [21].

The demand for more powerful and efficient engines makes the need of developing more performing cooling systems increasingly important. According to Lefebvre [1], the main reasons are:

a) *Increase of OPR*: the increase of the overall pressure ratio allow to obtain substantial reductions in engine fuel consumption. Unfortunately, increasing the OPR raises the radiative heat transferred to the liner walls; in addition, increasing the pressure ratio causes an increase in combustor inlet temperature, thus reducing the capability of the annulus air to cool the walls.

b) *Increase of TIT*: turbine inlet temperature directly affects the over-

all efficiency of the engine; therefore the necessity of increasing TIT calls for improvements in combustor pattern factor in order to maintain the integrity of the hot sections downstream. Since film-cooling air flows along the liner wall, it makes no contribution to mixing. Thus, reduction in wall cooling consumption gives a direct contribution to pattern factor improvement.

c) *Increase of durability*: as noted by Dodds and Bahr [3], as combustor operating temperatures have increased, component durability and life expectations have also risen and thus the engine operating time before combustor maintenance has exponentially grown.

d) *Introduction of new combustion technologies*: as indicated in chapter 1, regulations governing NO_x pollutant emissions have become increasingly stringent and lean burn technologies have been identified as the most promising to meet the new legislation limits; such technologies need to highly increase air amount necessary to combustion, at the expense of air available for liner-wall cooling. Furthering this trend was the knowledge that reductions in film-cooling air are highly beneficial in lowering the emissions of carbon monoxide and unburned hydrocarbons.

Following these consideration, the need to find out alternative solutions to the typical slot cooling configuration has become mandatory. Among them, the most promising method that allow to have an efficient liner cooling at the expense of a reduced amount of coolant consumption is the *effusion cooling*.

2.2 Effusion Cooling

Effusion cooling represents a compromise between the well-known technique of full coverage film cooling, widely used in nozzle and vanes, and the transpiration cooling [2], the best efficient cooling solution based on porous and no-metallic materials, but which is still not compatible with the current reliability standard. The effusion cooling is realized

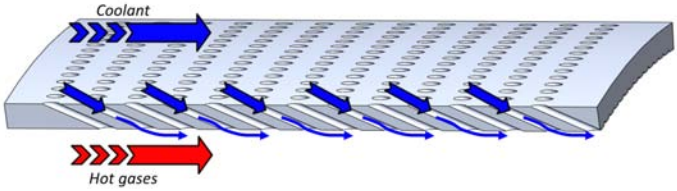

Figure 2.3: Effusion cooling scheme.

drilling over the liner surface a dense array of closely spaced cylindrical holes characterized by a very small diameter of about few tenths of millimeter (see figure 2.3). These holes have also a small injection angle (usually about 30°) relative to the nominal main flow direction. It is possible to reach angles of 10°-11° [22] in order to obtain a better wall protection with the film, but highly increasing the cost of the manufacturing. These geometrical features point out the two main characteristics of this cooling technique:

- the dense array of holes allows an homogeneous film cooling protection, which is guaranteed by the constant injection of coolant all along the liner length and by the consequent film superposition row by row;.

- holes are characterized by a quite high length-to-diameter ratio (L/D), that allows to strongly increase the heat transfer surface: in fact effusion cooling system permits to lower the wall temperature mainly through the so called *heat sink effect*, which is the homogeneous wall cooling due to the heat removed by the forced convection of the coolant flowing through each holes [23, 24].

Even if effusion systems do not guarantee the excellent film protection achievable with 2D slots (at least in the first part of the liner) and their manufacturing are quite more expensive, this new cooling methodology allows to overcome the some limitations of the classical arrangements that make it very attractive for lean burn combustors. First of all, it allows to obtain very efficient cooling performance at the expense of a

reduced coolant consumption rate with respect to 2D slot, which are considered to be highly wasteful of air [25]; this aspect is fundamental in lean burn combustors, in which only a small part of air is aimed at liner cooling purpose. Furthermore, the effusion system permit to overcome a general limitation of film cooling, which is related to the degradation of protection receding from the injection point: in the typical 2D slot configuration, to avoid too many injection points and to guarantee a reasonable effect before the film decay, a large amount of air flown through each slot, causing over-cooling on regions just downstream its exit. On the contrary, an effusion system allows a more homogeneous cooling of the liner through its fine array of small holes uniformly distributed all over the wall surface. Finally, the use of slot cooling in lean burn combustors would introduce a further technological issue: to guarantee the good operation of this system with reduced cooling mass flow, the height of the slot should be shorten in such a way that, in presence of strong thermal dilatations, it would be very challenging to guarantee the good passage area for the coolant.

Before going into details about the behaviour of this cooling technique, a brief description of the "jet in cross flow" phenomenon will be given in the next section; following, an overview of the main parameters that affect film cooling will be provided, with a special attention on those related to effusion systems.

2.2.1 Jet in Cross Flow

The physics of the flow developed in the effusion cooling is determined by the interaction between the cold jets coming out from the holes and the mainstream hot flow. In literature, this phenomenon is the so call "jet in cross flow". This interaction creates a flow field in the zones immediately downstream of the jets characterized by several large scale vortical structures [26]; all these structures are inherently unsteady and anisotropic [27].

The principal structures of vortices are depicted in figure 2.4:

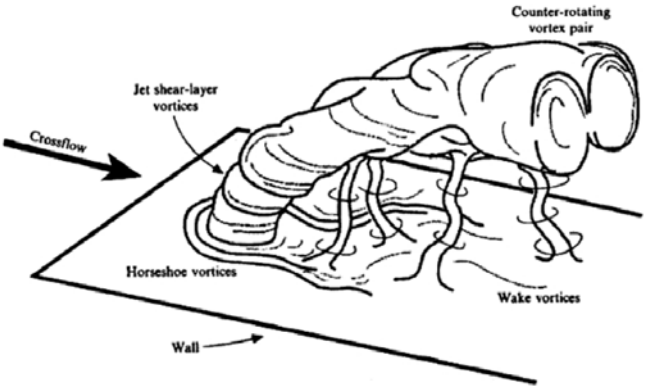

Figure 2.4: Jet in crossflow [26]

- jet shear-layer vortices;
- counter rotating vortex pair (CVP);
- horse-shoe vortices;
- wake vortices.

The jet shear-layer vortices dominate the initial portion of the jet and they are the results of the instability in the annular layer close to the plate. This layer is subjected to shear stress and tends to separate at the hole exit, leading to the formation of ring vortices around the jet: these vortices are transported downstream together with the jet.

The counter-rotating vortex pair (CVP) are generated in the hole interior; downstream the hole exit, these vortexes are strengthened by the interaction with the cross flow, which bends the jet and causes strong shear stresses on its sides. They entrain surface fluid into the jet center, resulting in the typical kidney-shaped structure; their development goes on in the area downstream of the jet and, indeed, their action becomes dominant in the regions far from injection. These flow structures deeply

influence the film cooling, since they are responsible for the mixing between the jet and the crossflow: depending on the fluidynamic conditions of the two flows, their interaction can promote a lateral spreading of the jet and hence a better protection of the wall or inhibit the formation of the film layer. In fact, the CVP orientation tends to promote the lifting of the jet (figure 2.4), generating a zone where the entrainment can either help or damage the film cooling generation. Although the presence of CVP is widely documented in literature, there is not a unique and universally recognized discussion about the causes of its formation. Moreover, as mentioned before, each structures of motion, including the CVP, are strongly affected by the actual physical conditions and it is conceivable that different mechanisms may contribute in several ways and different operating conditions to their formation. The most important theories about the formation of CVP are presented by Andreopoulos [28] and by Walters and Leylek [29].

Horseshoe vortices are generated upstream of the hole leading edge and the jet shear-layer vortices. The formation of these flow structures is similar to that observed upstream of a solid obstacle, such as a cylinder or an airfoil leading-edge: when the boundary layer meets an obstacle (of any kind), an adverse pressure gradient is generated, leading to the formation of the horseshoe vortices. These vortices wrap around the base of the jet travelling downstream with vorticity counter to the CVP [28]; such vortices are, in some cases, responsible for the spreading for the coolant spreading on the side of hole exit.

The wake vortices are flow structures where the mean component of vorticity is directed normal to the plate. These vortices are characterized by an evident unsteadiness and by the typical mechanism of vortex shedding. Experimental investigations by Fric and Roshko [26] show that the wake vortex formation is caused by the separation in the boundary layer of the plate immediately behind the jet (figure 2.5). Their investigations show that the two components of the crossflow turning around the jet,

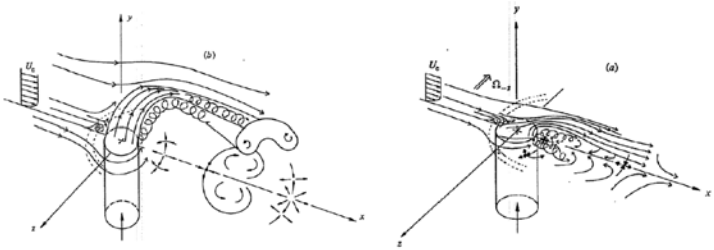

(a) High velocity ratio (VR=2.0). (b) Low velocity ratio (VR=0.5).

Figure 2.5: Jet penetration at different velocity ratio [26].

crash behind it and they lead to the formation of separation bubbles. These vortices are then lifted by the jet and dragged downstream. The formation of the wake vortex is therefore affected by the main jet lifting.

As far as the jet penetration is concerned, its occurrence largely depends on both the injection angle and the local jet-to-mainstream velocity ratio: at large angles and velocity ratios (figure 2.5(a)), the jet lifts off, while for lower values (figure 2.5(b)) the jet bends over quickly and attaches to the wall. After the completion of the jet bending, pressure forces are small and the jet follows the local flow. As soon as the coolant exits the hole, turbulent mixing process causes the coolant mixing with the free-stream. Neighbouring jets can merge giving a blanket of coolant at some distance downstream; the distance is dependent on the jet spacing. Similarly, coolant from an upstream row of jets can help to form a blanket of coolant, depending on the spacing and the staggering of the jet rows.

2.2.2 Geometrical Parameters

Literature studies on full-coverage film cooling often refer to a simplified configuration of effusion geometry usually addressed as a multi-perforated plate which is the simplest possible geometry. Such geometry

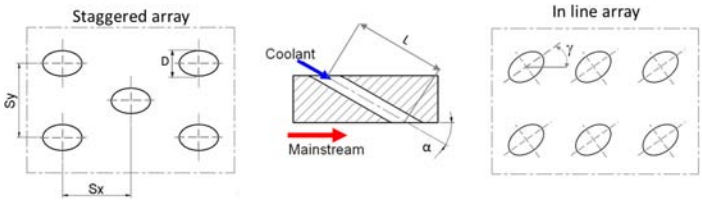

Figure 2.6: Main geometrical parameters for an effusion arrangement.

is reported in figure 2.6 together with indications of main geometric parameters: the hole diameter (D) and length (L), the streamwise and spanwise pitches (S_x and S_y), the effusion angle (α), which is the angle between hole axis and its projection on the surface, and the compound angle (γ), defined as the angle between the projection of hole axis on surface and the direction of main flow.

Geometrical features that are usually introduced to optimize the behaviour of film cooling holes for blades and vanes, as the fan shaped holes or laidback holes, are not adopted for effusion holes: in fact, despite the advantages achievable with such kind of geometrical arrangement, their adoption for the huge amount of effusion holes expected on a liner would introduce a not affordable manufacturing cost.

The selection of the effusion geometrical parameters is mainly dictated by a trade off between the manufacturing costs and the cooling performance. At the status of the art, combustor manufacturers are oriented towards: $\alpha = 30° - 60°$; $\gamma = 0°$ (no compound); $L/D = 3 - 6$. Concerning S_x/D and S_y/D, they are quite variable from engine to engine.

2.2.3 Operating Parameters

Many dimensionless parameters have been introduced in literature to describe the behaviour of film cooling by taking into account the operating conditions of the two flows involved in the phenomenon, which are

the coolant and the mainstream. They are known as:

$$Blowing\ Ratio: \qquad BR = \frac{(\rho \cdot v)_{cool}}{(\rho \cdot v)_{main}} \tag{2.1}$$

$$Velocity\ Ratio: \qquad VR = \frac{v_{cool}}{v_{main}} \tag{2.2}$$

$$Density\ Ratio: \qquad DR = \frac{\rho_{cool}}{\rho_{main}} \tag{2.3}$$

$$Momentum\ Flux\ Ratio: \qquad I = \frac{(\rho \cdot v^2)_{cool}}{(\rho \cdot v^2)_{main}} \tag{2.4}$$

The velocity ratio, defined in equation 2.2, is used in literaure to distinguish the particular regime of jets injected from the cylindrical holes: it is usual to assume that for VR > 0.8 jet lift-of from surface appearing as penetrating in the main flow [2].

In modern aeroengine combustor, the working conditions of each row of cooling holes are quite variable: this is due (a) to the different regimes of the engine, from idle to take-off, characterized by quite different levels of pressure, temperature and mass flow rate, and (b) to pressure and temperature variations along the combustion chamber in each working condition. Consequently, the variability of the operative parameters is quite wide and general guidelines are difficult to be drawn; however, common range of blowing ratio is BR$\approx 1 - 7$, while for the density ratio DR$\approx 1.5 - 3.0$.

The analysis of the effect of each operative parameter on cooling system performances was the object of many investigations. The large number of parameters and their non-linear interactions in affecting the system working conditions make the characterization of film cooling quite a difficult matter. In fact, to make the subject affordable, researchers usually focus on a subset of parameters and investigate the influence of each one in a well defined range of variation. Generally speaking, it can be said that the main parameter is the blowing ratio BR. Keeping the DR constant and increasing the blowing ratio means to augment the momentum of the jet with respect to the main flow. Studies for a single row of hole showed that the adiabatic effectiveness is positively affected by this ac-

tion till to values of BR of about 1 [30]. Beyond these values the jet deeply penetrates into the cross flow; the coolant tends to move away from the wall preventing the formation of a coolant film on the surface and, consequently, a decay in the protective action of the system occurs.

Finally, the jet Reynolds number defined in equation 2.5 has been taken into account in literature to describe the operating regime of the jet:

$$Re_j = \frac{(\rho \cdot v)_j \cdot D}{\mu} \tag{2.5}$$

This parameter mainly controls the losses through the holes and the heat transfer within the hole. Usually by increasing Re_j both of them are increased. It is evident that the first one affects the performance of the system negatively while the second is a desired effect, since it increases the heat sink effect and helps in lowering the metal temperature.

2.2.4 Performance Parameters

Many parameters are usually accounted for governing the overall performance and effectiveness of the film cooling process. First of all it is worth recalling the Newton equation for the heat flux from a cooled surface, reviewed by Goldstein [31]:

$$\dot{q} = HTC_{main} \cdot (T_w - T_{aw}) \tag{2.6}$$

where the subscript *main* stands for hot gas side in presence of film cooling. The driving potential for this heat transfer is the difference between the surface wall temperature, T_w, and the adiabatic wall temperature, T_{aw}. The adiabatic wall temperature, introduced by Goldstein, would be obtained in the limiting case of perfectly insulated (adiabatic) surface, where heat flux would be zero. The use of the adiabatic wall temperature in equation 2.6, instead of any other reference temperature, yields to a heat transfer coefficient independent of the temperature difference for a constant property flow, as clearly demonstrated by Goldstein [31]. As pointed out by Eckert [32], in case of injection at the free-stream temper-

ature, no differences subsist between adiabatic wall, free-stream and jet temperature: hence heat transfer coefficient may be obtained once free-stream and wall temperatures are known (as will be done in chapter 4).

Adiabatic wall temperature is often presented in dimensionless form as the adiabatic effectiveness:

$$\eta_{aw} = \frac{T_{main} - T_{aw}}{T_{main} - T_{cool}} \tag{2.7}$$

where T_{main} is the mainstream (hot gases) total temperature and T_{cool} is the temperature of flow exiting from the cooling hole.

Despite the wide use of adiabatic wall temperature as driving potential for the actual heat flux over a film-cooled surface, a recent study carried out by Zhao and Wang [33] questioned the appropriateness of its application, especially in experiments under laboratory conditions, where the effects viscous dissipation as a heat source near the wall are negligible. In their work, authors support the validity T_{aw} on the hypothetical zero wall thickness condition and for very low conductive material; on the other hand, in the conjugate wall cases, they showed that T_{aw} is not always higher than wall temperature (T_w), and therefore, it does not always play the role as the driving potential. To overcome this limitation and to obtain a correct estimate of wall heat flux, authors suggest to perform two different test, varying the thermal conductivity of the film-cooled wall. However, evidence supports that adiabatic wall temperature is still be used to correctly predict the heat flux direction.

An other important parameter to be taken into account to predict cooling performance is the previously mentioned HTC_{main}, which is the convective heat transfer coefficient in presence of film cooling on the hot gases side; usually, it is compared with the reference HTC without film cooling (HTC_0).

Being the final aim of an effusion cooling system design the reduction of heat transfer to the surface, which is dependent on both the adiabatic effectiveness and the heat transfer coefficient, both η_{aw} and HTC_{main} are required to determine if the overall heat load from the hot gases to the wall surface is reduced (see also Kelly and Bogard [34]). In this con-

text, Sen et al. [35] suggest to use the Net Heat Flux Reduction (NHFR) to quantify the global heat transfer reduction to a cooled surface; it is defined as the ratio between the heat flux reduction due to film cooling ($\dot{q}$) and heat flux taking place without cooling ($\dot{q_0}$):

$$NHFR = \frac{\dot{q_0} - \dot{q}}{\dot{q_0}} = 1 - \frac{HTC_{main}}{HTC_0} \cdot (1 - \eta_{aw} \cdot \theta) \tag{2.8}$$

θ is the non-dimensional temperature defined as:

$$\theta = \frac{T_{main} - T_{cool}}{T_{main} - T_w} \tag{2.9}$$

The aim of a well performing cooling system is thus to increase NHFR values: this goal is achieved through a reduction in $\mathrm{HTC}_{main}/\mathrm{HTC}_0$ and an enhancement in η_{aw}. Unfortunately, increased mixing in the boundary layer due to coolant injection and the development of renewed thermal boundary layers underneath the jets cause a significant mainstream heat transfer coefficient augmentation [34]. Adiabatic effectiveness has then to be high enough to compensate for this heat transfer coefficient enhancement, otherwise overall heat load abatement will not be attained.

Despite previous considerations, NHFR is not properly representative for an effusion cooling system since its definition (eq. 2.8) does not explicitly take into account the heat sink effect, which instead plays an important role in this type of cooling technique. To overcome this aspect, one further parameter is used in literature to indicate the overall cooling capability of a cooling system: it is the overall effectiveness [36], defined as:

$$\eta_{ov} = \frac{T_{main} - T_w}{T_{main} - T_{cool}} \tag{2.10}$$

Since the definition includes the actual wall temperature, this parameter takes into all the contribution to wall cooling, which are both the film protection and the heat sink effect; for this reason, this latter parameter is suitable to give information about the overall performance of an effusion system.

Bunker [37] presents a cooling design method which is divided into

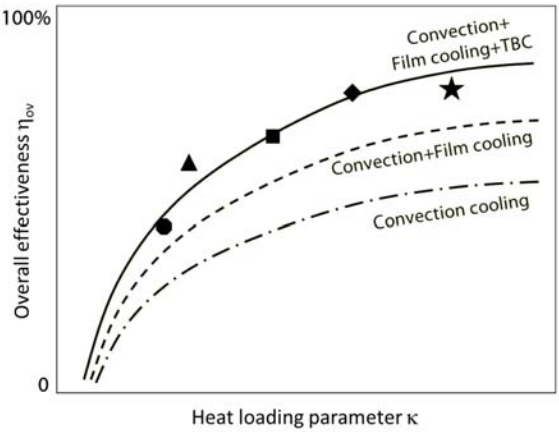

Figure 2.7: Curves of cooling technologies performances [37]

four levels (0-3). Level 0 is the preliminary cooling design analysis in which the cooling design is completely wrapped up in a single set of performance characteristic curves, known as "Cooling Technology Maps". As an example, figure 2.7 shows a generic cooling performance chart for a turbine airfoil. The technology curves shown on this chart present the overall cooling effectiveness versus a heat loading parameter (κ). The symbols represent various engine data points for different designs. The heat loading parameter relates the overall hot gas heat flux which is transferred to the wall to the overall coolant capacity that acts as a heat sink; it is defined as

$$\kappa = \frac{m_{cool} \cdot c_{p,cool}}{2 \cdot HTC_{main} \cdot A_{main}} \tag{2.11}$$

The curves proposed by Bunker can be used in a preliminary design phase in order to examine the expected cooling performance with respect to the working conditions. However, curves were obtained for blade cooling applications and their extension to effusion systems is not straightforward: in fact, coolant penetration and hence the cooling performance are

influenced by many different parameters which may have significant local variations depending on operating conditions and geometry. This complicates a proper comparison and evaluation of different cooling schemes and airspray nozzle designs. Based on the definition given by Bunker for a turbine airfoil, Wurm et al. [38] presented a dimensionless cooling efficiency that allows a significant reduction of data for characterizing the cooling performance within combustion chambers.

2.3 Literature Review of Effusion Cooling for Combustor Liners

Studies on film cooling have been performed by many authors since the 60's: a specific summary of the investigations aimed at understanding the influence of geometrical and operative parameters on this phenomenon is beyond the scope of this short review. Attention will be focused to relevant past studies concerning effusion cooling for combustors liner.

Martiny et al. [39] evaluated row by row adiabatic effectiveness (via IR-thermography) and performed flow visualizations (by means of Schlieren photography) on an effusion cooled plate with a very shallow injection angle of 17°; their study included also different flow patterns for the investigated blowing ratios, with varied from 0.5 to 4.0. They noticed that in the starting region of a cooling film, at blowing ratio of 0.5 (figure 2.8(a)),

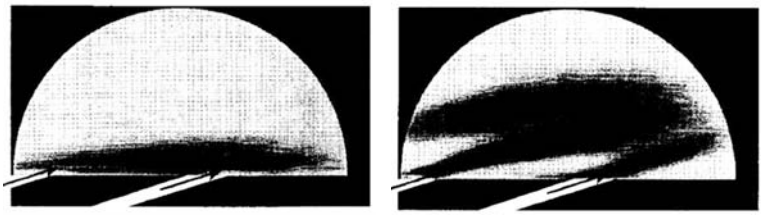

(a) Flow pattern BR=0.5 (b) Flow pattern BR=4.0

Figure 2.8: Schlieren flow traces, 2^{nd} and 3^{rd} effusion row observed [39]

jets remain attached to the wall and for higher values of blowing parameter a closed cooling film is prevented by the jets lifting-off from the surface (figure 2.8(b)). Nevertheless, even in cases of complete penetration, cooling benefits, in terms of adiabatic effectiveness, are still visible: they are ascribable to the massive coolant injection, which increases row by row and reduces main flow temperature in the mixing zone. The same facilities and test samples were employed by Martiny et al. [40] while developing an analytical model for the calculation of wall temperature of an effusion cooling array: by means of a parametric study, they investigated the dependencies of dimensionless quantities on the overall effectiveness.

Many studies of full coverage film cooling have been focused on measuring or estimating the film effectiveness generated by coolant jets and the heat transfer of effusion cooling. A detailed experimental investigation on hot side heat transfer associated to an effusion solution is the one due to Kumada et al. [42]; even if their work is not too much recent, authors present a precious effort in correlating the wall heat transfer coefficient variation with the jets fluid dynamics that will be widely used until nowadays. Scrittore et al. [41] investigated an effusion cooling scheme through flowfield measurements and adiabatic wall temperatures. Of particular interest was the considered range of blowing ratio, from 3.2 to 5.0, which is closer to the one that could be found in typical applica-

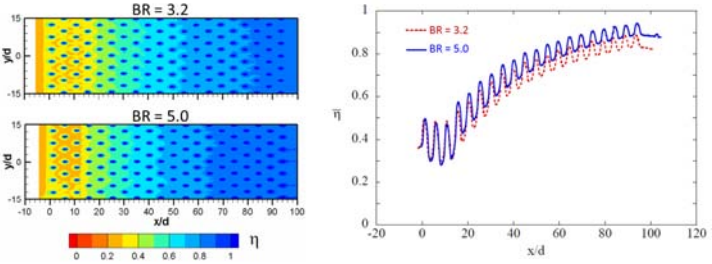

(a) Adiabatic effectiveness maps (b) Spanwise averaged effectiveness

Figure 2.9: Effusion cooling effectiveness for a combustor liner [41].

tions for combustor liners; furthermore, authors studied a cooling scheme close to a real engine one, that contained twenty rows of cooling holes with equally spaced holes in both streamwise and spanwise directions ($S_x/D = S_Y/D = 4.0$). They measured adiabatic effectiveness of this full coverage scheme, finding the attainment of a fully developed effectiveness region at the 15^{th} row and a very low effect of blowing ratio on cooling performance (figure 2.9). They also observed a fundamental independence of penetration height for the cooling hole rows on the momentum flux ratio for the range that was considered at the fully-developed condition. Finally, they also confirmed the hypotheses proposed by Schulz [43]: measuring velocity planes around the holes, he found jet separation just downstream of the hole trailing edge and, moreover, the presence of CVP which served to entrain hot mainstream flow toward the surface at the plate leading edge. Downstream, however, this effect serves to mix the accumulated coolant flow and provides a more uniform surface temperature across the pitch. The cooling effectiveness of the film layer increases asymptotically at the same rate for both blowing ratios, with only little improvement for the higher blowing ratio with respect to the lower blowing ratio.

Scrittore et al. [44] performed also a flow field investigation to better understand the influence of dilution jets on effusion film development; results showed how the coolant was transported from the film-cooling layer in the near wall region to the free-stream and downstream from

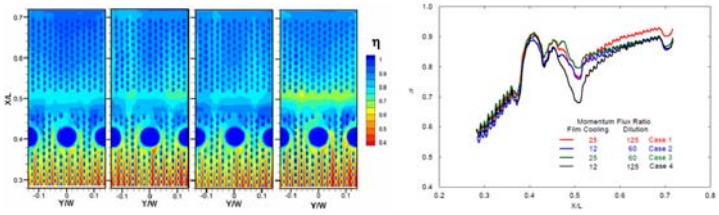

(a) Adiabatic effectiveness maps (b) Spanwise averaged effectiveness

Figure 2.10: Film cooling effectiveness near combustor dilution hole [44].

the dilution jets. Furthermore, the presence of the dilution jet caused an high increase of turbulence level: such an effect resulted in an increased spreading of the film-cooling jets. Increasing dilution blowing ratio resulted in a degradation of film cooling. Examples of such results are shown in figure 2.10.

Metzger et al. [45] studied the variation of heat transfer coefficient for full-coverage film cooling scheme with normal holes, founding an augmentation of 20-25% in the local heat transfer with blowing ratio 0.1 and 0.2. Crawford et al. [46] experimentally determined Stanton number for an effusion cooling geometry. Martinez-Botas and Yuen [47] measured heat transfer coefficient and adiabatic effectiveness of a variety of geometries in a flat plate to test the influence of the injection angle by varying blowing ratio from 0.33 to 2.0. They measured the variation of the heat transfer coefficient h with respect to a reference case h_0; results show that there is a maximum of h/h_0 close to the hole and further downstream with highest heat transfer augmentation for 30° injection angle.

Kelly and Bogard [34] investigated an array of 90 normal holes and found that the largest values for h/h_0 occur immediately downstream of the film cooling holes and the levels of h/h_0 are similar for the first 9 rows. They explained that this could be due to an increase in the local turbulence levels immediately downstream of the holes, created by the interaction between the cooling jet and the mainstream flow. Another reason could be the creation of a new thermal boundary layer immediately downstream of the cooling jets. None of the previous studies investigates the effect that a high blowing ratio has on adiabatic effectiveness, heat transfer coefficient, and Net Heat Flux Reduction. As reported by the authors, increases in heat transfer coefficient due to high blowing ratios could potentially be replaced by an increase in heat transfer coefficient due to high mainstream turbulence.

Ceccherini et al. [48] measured the overall effectiveness and Facchini et al. [49] estimated the heat transfer coefficient at variable blowing ratios on the same real engine cooling scheme to evaluate the combined effects of slot, effusion, and a large dilution hole; they found that an increase

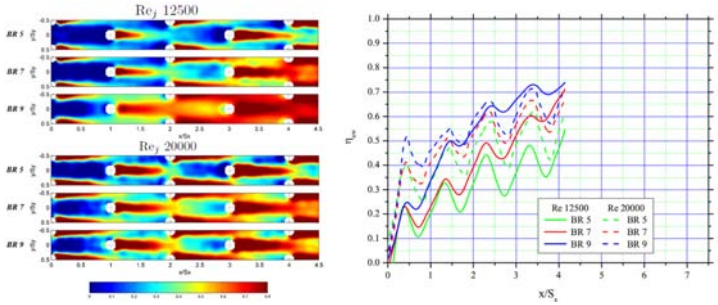

(a) Adiabatic effectiveness maps (b) Spanwise averaged effectiveness

Figure 2.11: Adiabatic effectiveness for an effusion geometry [51].

in VR makes jets become more and more penetrating in the main flow and they behave as an obstacle against film development, lowering the effectiveness values. On the contrary, they found that high BR values enhance the heat transfer phenomenon: in fact, the high jet velocity that draws hot gases from mainstream flow on the liner surface alters the local boundary layer on the effusion surface causing an increase of HTC. Facchini et al. [50] investigated also the influence of a recirculating area in the mainstream on the same geometry: they highlight that the presence of the recirculation impedes the creation of the film layer, leading to a general reduction of the effectiveness but without having significant effects on the heat transfer coefficient.

A deep experimental investigation on effusion cooling for combustion chamber liners and high-pressure vane endwall applications was performed by Toni [51]. Several geometries were investigated with the aim of highlighting the impact of the geometrical arrangement and the operating conditions on the performance of this cooling system; figure 2.11 shows an example of adiabatic effectiveness results obtained by means of Thermochromic Liquid Crystal (TLC) technique on a single geometry tested at different blowing rate. An exhaustive study on the cooling system preliminary design for modern lean burn combustors was provided by Ceccherini [52]: a one-dimensional analysis on combustor liner cooling

system was carried out, highlighting the ability to improve the performance of effusion. Furthermore, CFD investigations where performed as well as experimental surveys in order to give more details of the behaviour of effusion cooling and its practical implementation in engine-like cooling schemes.

More recently Ligrani et al. [53] presented film effectiveness and heat transfer results for full coverage film cooling arrangements with streamwise pressure gradient; they studied the effect of the blowing ratio and the influence of dense and sparse hole arrays on the thermal effectiveness, giving an extensive overview of the behaviour of this system subjected to several operating conditions. Experiments under conditions of very high freestream turbulence up to 25% were conducted by Martin and Thorpe [54] on an effusion test plate with angled hole array and staggered pattern, varying blowing ratios from 0.3 to 1.5. They found that when freestream turbulence is increased the spatially averaged effectiveness can increase by as much as 85% at BR = 1.4 due to the spanwise spreading of coolant and turbulent transport of coolant back towards the plate surface.

Despite many studies deal with the investigation of the effusion cooling performance, most of them were conducted by using air as coolant and mainflow, precluding the possibility to point out the effects of density ratio between the two flows. Density ratio is, however, a key parameter for the design of a liner cooling system, mainly because of the actual large temperature difference between coolant and burned gases inside the core of the combustor. Ekkad et al. [55, 56] measured effectiveness and heat transfer coefficient distribution over a flat surface with one row of injection holes inclined streamwise at 35° for several blowing ratios and compound angles; tests were carried out by using air and carbon dioxide as coolant, finding that both heat transfer and effectiveness increase with blowing ratio. They also pointed out the effects of density ratio, showing how these effects are more evident with increasing the compound angle and the momentum flux ratio. This experimental survey was, however, oriented for turbine blade applications rather than combustors. More

recently, Lin et al. [57, 58] investigated both experimentally and numerically adiabatic film cooling effectiveness of four different 30° inclined multihole film cooling configurations; the survey, which was specific for combustor liner applications, was performed by using a mixture of air and CO_2 as coolant, but it was mainly focused on studying the influence of hole geometrical parameters and blowing ratio on film cooling rather than on the effects of density ratio. Andreini et al. [59] performed a CFD analysis on the a test article which replicated a slot injection and an effusion array; they simulated the behaviour of the cooling system both with air and CO_2 . Numerical results show that the entity of local heat transfer enhancement in the proximity of effusion holes exit is due to gas-jets interaction and that it mainly depends on effusion velocity ratio; furthermore, a comparison between results obtained with air and with CO_2 as coolant pointed out the effects of density ratio, showing the opportunity to scale the increase in heat transfer coefficient with effusion jets velocity ratio.

2.4 Concluding Remarks

At the present point of the work, a choice has already been made concerning the cooling techniques which seemed to be the best performing and which can fit the requirements of lean burn combustors: impingement for dome cooling, already extensively used, and effusion cooling for liners.

Even though several notable studies are available in literature on effusion configurations, there are still some aspects that are worth to be further investigated; among them, there is a lack of experimental data concerning the influence of the density ratio on the cooling performance of the effusion system and, more generally, on how this technology works when it is integrated with other typical features of a combustor liner, such as slot film cooling and dilution holes. Furthermore, it is necessary a process of synthesis of the data in order to update the design tools employed for the combustor liners.

To complete the scenario of the past studies about the combustor issues of this research, a literature review concerning the hot streaks and the effects of the combustor-turbine interaction was carried out. However, this topic will be discussed in Chapter 5 to facilitate the readability of this dissertation.

Chapter 3

Enhancements in a 1D Thermal Procedure for Combustor Cooling Analysis

"Simplifying doesn't always mean cutting something. Sometimes, it means organizing that something better."
Anonymous

A reliable thermal design of a combustion chamber is a vital task to improve actual capabilities and accomplish the desired compromise among the distinct needs arising from modern engines.

This chapter will present the developments of a in-house one-dimensional thermal procedure for the design of a combustor chamber cooling system and the estimate of liner wall temperatures. The procedure is provided with a wide database of correlations available in literature, including all those reported in the works reviewed in Chapter 2 about the effusion cooling.

After an introduction to the main features of the code, this chapter will illustrate a brief description of the major recent improvements; the

procedure will then used for the thermal analysis of a real effusion-based combustor cooling schemes, that will highlight the good accuracy of this numerical tool and its effective capability in predicting the performance of such kind of cooling system.

The procedure will be further recalled in Chapter 4, where it will be employed to deepen an experimental investigation on an effusion-based cooling arrangement, and also in Chapter 7, where it will be used as the design tool for the cooling system of a probe for optical measurements in harsh temperature conditions.

3.1 1D Thermal Procedure

One-dimensional codes are still a fundamental tool for the design of complex systems, such as cooling schemes for combustor chambers or turbine blades. They are based on the use of engineering simplified models that are linked each other to represent the whole combustor cooling system; such type of codes are characterized by a wide library of elements used to describe the different parts of the system, from simple models to represent an orifice or a straight pipe to more complex models used to represent cooling arrangement, such as impingement or effusion cooling. Each model solves the one-dimensional form of the Navier-Stokes equation and it includes dedicated correlations to describe pressure loss, heat exchange, mass flow split, etc. of a specific part of the combustor. To provide a complete analysis of the cooling system, the solution of the fluid network must be coupled with further estimates of the heat loads on the critical parts of the chamber, with the aim of setting the boundary conditions to solve the thermal conduction through the metal: the output of this calculation is the temperature distributions along the liner walls, which can be used to assess the performance of the combustor cooling arrangement under investigation.

The main strength of such type of 1D codes lies in the short time needed to model the system and to run the simulation: this aspect makes them a powerful tool especially in the preliminary stages of the design procedure, usually aimed at testing several arrangements at various working conditions to identify the most promising solution and to draw the guidelines for the following more detailed investigations. In addition, thanks to their ability of easily set boundary conditions and manage with complex geometries, they may also be used to perform design of experiment (DOE) calculations in order to indicate useful correlations or trends and the relative importance of the operating parameters. On the other hand, the use of this kind of tools has to take into account some native limitations of the one-dimensional approach: these meanly deal with both the impossibility to describe with high accuracy a fully three-dimensional

flow, like swirling flows in the combustor chamber or cold recirculating flows at the end of the annulus, and with the uncertainty of empirical correlations, which is commonly lower than 10% only within their (usually narrow) range of validity.

Previous considerations briefly highlighted the importance of 1D codes for the liner cooling design. In particular, this is even more essential for an impingement or effusion based system: in fact, such dense arrays of small holes implies a significant computational cost if the cooling holes are all included in a simulations with three-dimensional CFD codes and, therefore, the time needed for a sensitivity analysis to geometrical parameters or working conditions would become unbearable. Even if many efforts have been made to develop lower order approaches aiming at reducing the number of mesh elements, such as those based on localized mass sources in the region of hole discharge [60], 1D codes still remain the first choice for the preliminary design phases. It becomes hence mandatory to update these tools including models for effusion arrangements, being it the core of lean burn combustor cooling systems. In addition, since in these system an important contribution to wall cooling comes from the heat sink effect, an update of the conjugate approach to solve simultaneously heat convection and conduction through the liner thickness is necessary, too.

3.1.1 Therm1D

The previous section highlighted the necessity to develop specific 1D tools for the design of cooling systems for novel combustor; focusing on new lean burn concepts, this need becomes even more critical due to the different and usually non linear phenomena that occurs in the combustor.

With the aim of achieving this goal, a one-dimensional thermal procedure, named *Therm1D*, was developed, inspired by a well proved approach to similar problems for the analysis of blades and vanes cooling systems. This tool is capable of calculating radiative and convective heat loads on gas side, while, on the cold side, it estimates convective heat transfer associated to different cooling schemes; the final aim is the

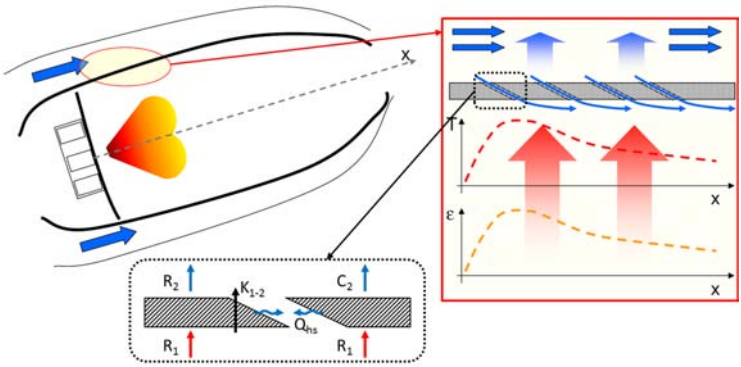

Figure 3.1: Concept view of 1D thermal design methodology

prediction of the temperature reached by the elements of a combustion chamber which are subjected to the highest thermal load.

The thermal procedure is based on the well known approach proposed by Lefebvre [1] and later improved by Kretschmer and Odgers [61] and De Champlain et al. [62]. As conceptually described in figure 3.1, the procedure is based on the balance among different mechanisms of heat transfer: radiative and convective heat loads on gas side (R_1 and C_1), radiative heat transfer toward the casing (R_2) and heat transfer between metal and coolant (C_2). Energy balance in steady state condition implies that (neglecting heat conduction in axial direction):

$$R_1 + C_1 = R_2 + C_2 = K_{1-2} \tag{3.1}$$

Heat conduction inside the metal (K_{1-2}) and then its final temperature distribution is obtained by using a 1-D Finite Difference Model (FDM) of the component with an in-house code, built-in inside the whole procedure, and then calculating the metal conduction as far as hot and cold side boundary conditions are known. Hot side heat loads (both convective and radiative) are modelled in detail and evaluated from a given description of the flame in terms of FAR, temperature, hot gas velocity and pressure. In addition, heat sink effect (Q_{hs}) is evaluated by apply-

ing to the FDM model, for each row, heat removal given by the mean heat transfer coefficient and adiabatic wall temperature inside the cooling holes.

After this brief introduction, some details on the main codes that are involved in the procedure will be given in the following. The procedure is composed of three main parts: *Icons1D* (Internal COoling Network Solver), a fluid network solver for heat transfer evaluation on the interfaces between the metal and the coolant, *Cowl*, that estimates the radiative and convective heat loads on the gas side and radiative heat transfer between the liner and the casing, and the thermal solver, that computes the heat conduction through the metal and finally provides the wall temperature distribution.

The analysis of the coolant fluid network is performed using a one-dimensional steady code, *Icons1D*, developed starting from a in-house code (*SRBC*) successfully used in several works [63, 64, 65]. The representation of a cooling system consists of a fluid network made up connecting basic components, each one dedicated to model a particular region of the combustor. Specifications of the geometrical characteristics of a single component, such as holes diameter, pitch, length, roughness, inclination angle and so on, can be custom selected. Coolant is considered a perfect gas subjected to wall friction and heat transfer, and flow field is solved in subsonic regime, using correlations to determine HTC, friction factor, cooling effectiveness, etc. The user can specify boundary conditions for the fluid network in terms of inlet and outlet pressure or mass flow rate, depending on design specifications. Through the resolution of the fluid network, *Icons1D* provides coolant side boundary conditions for thermal calculation; in addition, it estimates also the heat sink effect of cooling holes.

Heat load on the gas side and radiative heat exchange between the liner and the casing are estimated by *Cowl* following the approach suggested by Lefebvre [1] and more recently improved by Andreini et al. [66]; afterwards, cold side and hot gas side boundary conditions are read by the thermal solver for the resolution of the Fourier law within the metal

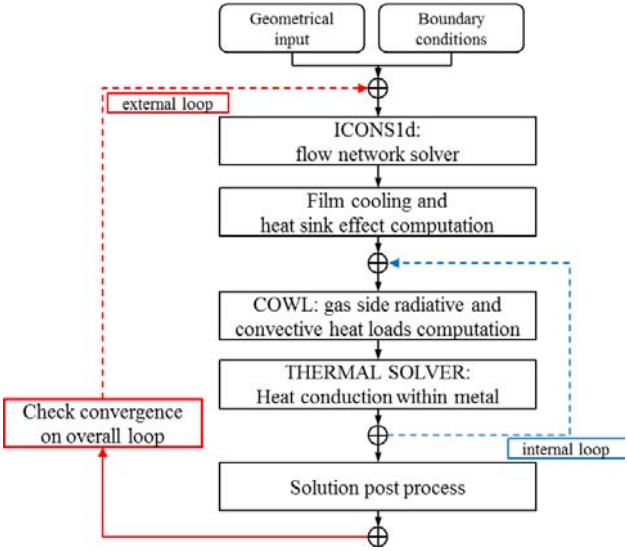

Figure 3.2: Therm1D: procedure flow chart

and the wall temperature is finally calculated. Since the mass flow rate and pressure drop is wall temperature dependent, an iterative overall procedure is required; in addition, an internal loop is included to speed up the convergence of the procedure. Convergence is achieved when differences in temperatures, pressures and mass flow remain unchanged or below an error set by the user.

To have a better comprehension of the overall procedure and to clearly describe the connections among the different involved codes, a schematic flow chart is reported in figure 3.2. Further details on the procedure can be found in [66, 67].

3.2 Application to an Effusion-based Combustor Cooling Scheme

Therm1D is a well proven tool which has been in-house developed and upgraded during the last ten years. During the assessment of this numerical tool, attention has been continuously paid to the development of a versatile instrument capable of investigating main design parameters of cooling arrangements suitable for the modern combustors. In particular, in the latest years new developments in combustor architecture has risen the need of having a more flexible tool able to easily manage complex geometries; in addition, new cooling techniques introduced the need to develop new 1D models able to describe these configurations and, therefore, to test innovative combinations of several cooling methods. If, on one hand, this task has been accomplished by introducing new models [52] and related new correlations [68], on the other hand a complete review of the native method to handle the description of the geometry has been required to investigate new liner and combustor chamber configurations. This need leads to a refurbishment of the procedure; following, a brief list summarizes the main new features that were introduced in the code within this work to meet the requirements mentioned above:

- the capability to model complex geometries using a more "user friendly" approach was introduced: the combustor is now represented writing the coordinates of points that describe the geometry of the liners and the annuli. Flow passage areas, wet surfaces and liner feature are automatically computed, while in the previous version of the code the user was requested to insert all these information as input data. This new features makes the realization of the flow network and the modelling of the metal parts easily to be managed, for instance with the help of a cad model. As an example, figure 3.3 depicts a cross section of a reference combustor test rig (see Appendix A), with a detailed view of the dome cooling system: the picture includes also a sketch of the flow network built in this complex area of the combustor, whose realization was easily done

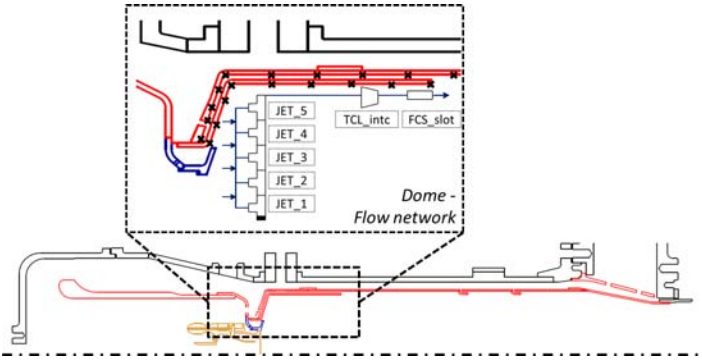

Figure 3.3: Example of Therm1D geometrical representation of a combustor liner and the related cooling system flow network

with the assistance of the 2D cross section of the cad model.

- the possibility to describe complex geometries made up of several metal parts, like multiple liners, heat shield, double walls inside the annuli, etc., was introduced Following this update, *Icons1D* and *Cowl* were updated as well in order to include both the coolant heat exchange and friction with several metal parts at the same time, and the radiative heat exchange between liners viewing each other.

- possibility to simulate the behaviour of the whole combustor (inner and outer liners/multiliners, cowl, dome and heat shield) in a single run: this new feature allows to model the entire system with a single fluid network and thus to have an estimate of the flow split within the combustor.

- a complete review of the appearance of the operative files was carried out: input file are better organized with the aim of making the setting of the boundary conditions simpler and quicker; analogously, new output files allow a quicker comprehension and a more rapid access to post processed data.

As mentioned before, *Therm1D* has been widely tested over the last ten years; the new updates were initially checked with the use of previous test cases and, once validated, the procedure was successfully employed for the analysis of new combustors. The next paragraphs will shortly illustrate the application of procedure to a real combustor geometries, based on effusion cooling system and designed by *Avio Aero* within European projects.

3.2.1 Analysis of the NEWAC combustor

Figure 3.4 depicts a sketch of the combustor developed by *Avio Aero* in collaboration with the *Department of Energy Engineering "S. Stecco"* within the NEWAC European project: it is a lean burn combustor based on the PERM injection system. The image, extracted from the work of Andreini et al. [69], shows the contours of non-dimensional velocity on a meridian plane of the combustor: the main features of the flow field in the chamber are highlighted, especially the large central recirculation zone and the vortex breakdown of the jet coming from the injector.

As far as the cooling system is concerned, air entering the dome crosses a jet plate and cools down the heat shield through an impingement arrangement; the exhaust air is channelled towards the external bounds of the chamber and it is injected from a slot tangentially to the liner hot wall: this configuration allows to generate an effective film cool-

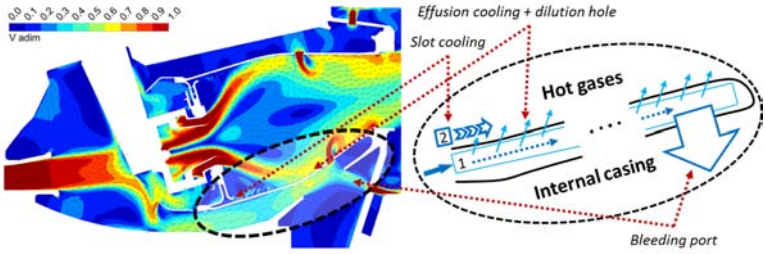

Figure 3.4: Sketch of NEWAC combustor and flow network modelling (adapted from [69])

ing layer which protects the first part of the inner and outer liners from hot gases. Liners are cooled by an effusion system, made up of a dense array of homogeneous holes which cover the whole surface exposed to the burning gases. Part of the air flowing through the two annuli is bled from bleeding ports located on the casing and it does not contribute to liner cooling (bled air is directed to the first vane cooling system); in addition, a row of dilution holes is located in the second half of the chamber: it is aimed at completing the combustion process and moreover to establish the desired temperature profile at the inlet of the turbine.

A detailed analysis of NEWAC combustor cooling system was carried out by Ceccherini [52]; in his dissertation, the author performs both the preliminary design, and the following optimization of the geometrical parameters using *Therm1D* as the main design tool. His work was considered a suitable test case to check the new features of the procedure: in fact, it is characterized by a quite complex geometry of the two shaped annuli and, at the same time, by a quite simple flow network. In this way, it was possible to test the capability of the new geometrical representation and to have quick comparisons in term of well proven results. Within this context, details on the flow network and on the setting up of boundary conditions will not be provided and only a few topics will be recalled. Readers can find further information in the dissertation quoted above.

Figure 3.4 sketches the fluid network used to represent the cooling system; a single model ("*1*" in the picture) is used to describe the annulus passage and the liner cooling system: effusion holes are described in the model row by row, specifying the position and the geometrical characteristics. From such a set of data, coupled with boundary conditions, the model is able to evaluate the mass flow through each row of film cooling holes as well as exiting thermofluid-dynamic conditions once the average temperature of holes surface is known. Holes pressure loss can be modelled by the use of correlations for constant section channels; however, in the case of small length-to-diameter ratios, the use of a discharge coeffi-

cient (C_d) is needed to take into account the losses at inlet, inside and at the outlet of the hole; such a coefficient is mostly dependent on geometry and fluid-dynamic conditions and it was evaluated according to Hay and Lampard [70]. Knowing the mass flow rate through each row and the wall temperature of holes, the model estimates also the heat transfer coefficient and consequently the heat removed by sink effect. All the geometrical information in therms of description of the different heights of annulus passage, liner shape and holes position on the liner were provided inserting the coordinates of a set of points extracted from a cad model.

The flow network of the dome was not reproduced in this work; however, the presence of the dome cooling system was taken into account inserting a dedicated model ("*2*" in the picture) which acts as a slot cooling generator. This model is capable of being included in a more complex network but it also gives the possibility of just simulating the effects of the slot film cooling on the computation. The geometry of the slot passage and the coolant mass flow rate were specified, together with the correlation to compute the film adiabatic effectiveness. The model allows the use of several correlation, whose behaviours are depicted in figure 3.5 for two values of blowing ratio:

- Goldstein and Haji-Sheikh's correlation [71] has not any theoretical limit in terms of BR; its major fault consists in the fact that it does not consider lip thickness of the slot.

- The correlation proposed by Lefebvre [1], instead, takes into account slot thickness and presents two approaches: Turbulent Boundary Layer model (TBL) [19] and Wall Jet model (WJ) [72], which were developed for $0.5 < BR < 1.3$ and $1.3 < BR < 4.0$ respectively. When the slot height-to-lip thickness ratio is quite low, it has to be noted that the effect of such a parameter is not negligible.

- The interesting aspect of the correlation proposed by Simon [21] is its sensitivity to mainstream and coolant turbulence intensity level. However, as illustrated in figure 3.5, the behaviour of this correlation is highly affected by this parameter which, unfortunately, is

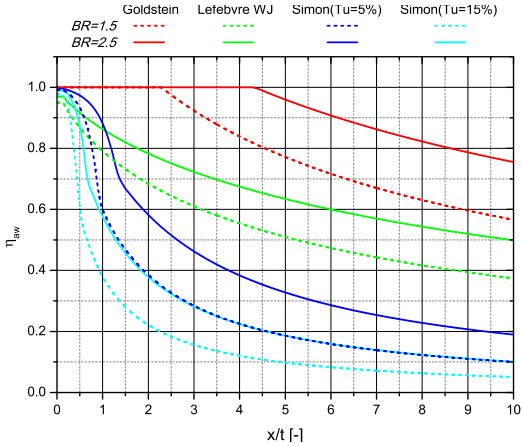

Figure 3.5: Sensitivity analysis on slot film cooling correlations

quite variable in a combustor chamber and thus is hard to be estimated with accuracy.

After the sensitivity analysis carried out by Ceccherini, the correlation proposed by Lefebvre was selected. Concerning the effusion holes, the correlation proposed by L'Ecuyer and Soechting [30] was chosen. The superposition principle proposed by Sellers [73] is taken into account to predict the performance of multiple film cooling rows. As well known, superposition principle is not able to properly take into account the mixing of coolant occurring in the interaction between subsequent jets; due to this interaction, the influence of injection from a row does not extend indefinitely downstream but only for a certain length (i.e. a given number of rows). Therefore, adopting the approach proposed by Andreini et al. [74], the effectiveness *superposition length* was specified for each row of cooling holes. Film cooling superposition includes also the slot cooling from the dome, whose contribution in terms of superposition length was considered active up to the location of the dilution hole ($\approx x/L = 0.53$).

Figure 3.6(a) illustrates the adiabatic effectiveness distribution along the inner liner with and without the slot cooling: it is possible to appre-

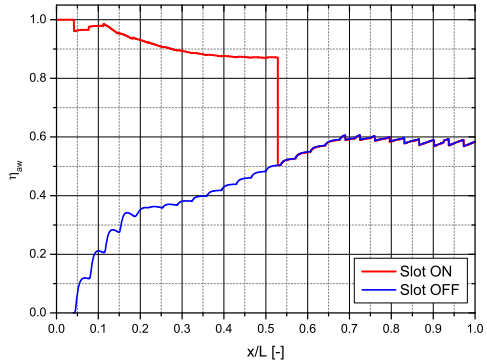

(a) η_{aw} distribution (Inner liner)

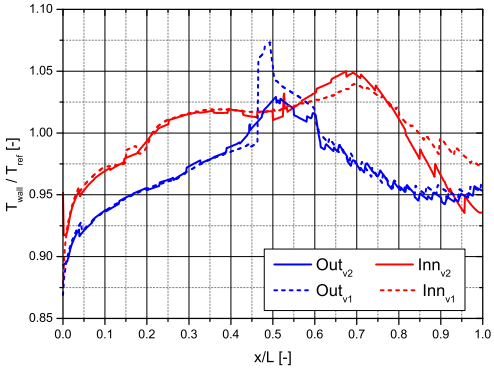

(b) Temperature along the liner walls

Figure 3.6: Results from NEWAC combustor analysis

ciate the effects of film cooling superposition, which allow an increase of the wall protection row by row up to an asymptotic value. In addition, it is worth noting that without the slot cooling, effusion system does not guarantee a sufficient protection of the first part of the liner. These considerations will be confirmed by the experimental investigation described

in chapter 4.

Figure 3.6(b) shows a comparison between the trend of the wall normalized temperature of the two liners for a reference working condition of the combustor, obtained with the previous (subscript "*v1*") and the new (subscript "*v2*") version of the code: these results, as well as the mass flow distribution along the liner, the pressure distribution, etc., indicate a very good agreement with data presented by Ceccherini. The slight discrepancies at the end of the inner liner are due to the emphasized curvature of the annulus in this region, whose geometrical representation is quite different between the two versions of the code; finally, improvements in heat sink effect treatment lead to, in certain locations, smoother results with respect to the previous code.

Finally, the procedure was employed to simulate the behaviour of the NEWAC combustor cooling system subjected to real aircraft take-off conditions (maximum load). Hot gas boundary conditions are set by means of a one-dimensional distribution of pressure, temperature, velocity, FAR, etc., that describe the flame behaviour along the liner. Such kind of boundary conditions are difficult to be set with high accuracy since the complex flow and thermal fields within the combustor chamber are strongly three-dimensional and non uniform; furthermore, the combustion process introduces unsteady effects and the resulting flow can hardly be represented through a one-dimensional distribution without using further numerical tools. To overcome this limitation, the thermal procedure must be coupled with an external code, which should preferably be a one-dimensional code, like the Chemical Reactor Model (CRM) used recently by Andreini et al. [67] in their work, or a CFD code. Concerning this analysis, the hot gas boundary conditions were extracted by the RANS calculations performed by Andreini et al. [69].

Estimated wall temperature are shown in figure 3.7 as a function of a non-dimensional abscissa; numerical results, normalized with a reference temperature, are compared with data collected by *Avio Aero* during an experimental campaign on a combustion test rig; measured wall temperatures were obtained by means of several thermocouples welded on the

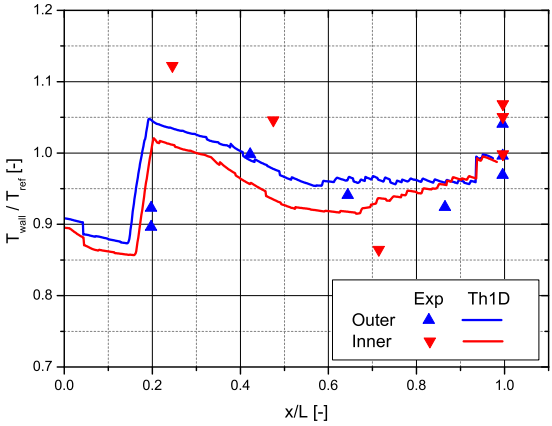

Figure 3.7: NEWAC metal temperature: exp. vs Th1D

liners. It is worth pointing out that some thermocouples are located also at different circumferential positions, so as to make possible the evaluation of the temperature variation in circumferential direction.

Due to the discrete injections of fuel related to the annular configuration of the NEWAC combustor, a strong variation of metal temperature is expected in tangential direction; this phenomenon makes the comparison among numerical results and discrete thermocouples as well as intrinsic tangential averaged results of 1D methodology a complex task. Nevertheless is important to point out how *Therm1d* results reasonably match the trend of the experimental data along the entire extent of the component, with an overall acceptable agreement at least on the outer liner. In addition, it is necessary to take into account the uncertainty related both to hot gas boundary conditions, and to metal temperature measurements: indeed, in this type of full annular tests, the accuracy of the experimental data is not only related to the accuracy of the thermocouples, but also to possible mismatches in their location with respect to the injection system and therefore the flame position.

Several analysis on an effusion-based cooling systems were performed to test the accuracy of the new procedure. For the interested reader, a further study is presented in Appendix A; the cooling arrangement of this combustor is characterized by a much more complex geometry with respect to the one presented above, in order to have a severe test to assess the capability of the new version of the procedure in terms of geometry handling.

3.3 Concluding Remarks

This chapter presented the latest upgrades of a in-house thermal procedure, named *Therm1D*, dedicated to the conjugated fluid-metal calculation for combustor cooling systems. The new features, developed within this work, allow an easier management of the description of the geometry of a combustor and, consequently, they permit to model and simulate complex cooling configurations.

The application of the procedure to a real engine effusion-based cooling schemes was illustrated. The annular NEWAC combustor was used to make comparisons between the new version of the procedure and the old one, whose accuracy was shown in several works available in literature. Results highlighted that the code is reliable and able to predict with good accuracy the performance of an effusion cooling system, as pointed out also by a comparison with experimental results. Therefore, *Therm1D* shown to be a useful design tool, capable to easily set up a conjugated calculation and give important indications since the early stages of the design process.

Thanks to the flexibility of the procedure, *Therm1D* will be used to deepen an experimental analysis of a combustor cooling configuration in the last part of Chapter 4: experimental data will be employed within numerical simulations to overcome some limits of the set up of the test campaign, e.g. the absence of the radiative heat load, with the aim of obtaining further information and increase the fidelity on the effusion technology.

Furthermore, the thermal procedure will used in Chapter 7 for the design of the cooling system of a special probe for optical measurements inside a combustor simulator test rig.

Chapter 4

Analysis of the Cooling Performance of an Effusion-based Combustor Liner Cooling System

"Colour is the overpowering of black;
white - the final victory over black"
Dejan Stojanovic

The main objective of the present chapter is the analysis of the interactions between an effusion and a slot cooling systems; the survey will be carried out by means of an extensive experimental campaign, focused on fulfilling a lack of experimental data available in literature concerning the effects on the effusion cooling performance of:

- coolant-to-mainstream density ratio;
- high penetration regimes of the cooling jets;
- interaction among the effusion system and other typical features of a combustor liner, such as the dilution hole and the slot cooling.

The test campaign will be led on a flat plate test sample, installed in a square duct wind tunnel; homogeneous inlet conditions will be imposed on the mainstream side. The geometry of the test sample reproduces, on a 3:1 scale, the cooling system of the NEWAC combustor, studied in by means of *Therm1D* in § 3.2.1.

The exhaustive survey will be presented in this chapter, starting from the measurement technique, the description of the experimental set up, and the post processing procedure. The main outcomes of the campaign, which are the distributions of heat transfer coefficient and adiabatic effectiveness, will be shown in details; moreover, experimental data will be exploited to carry out two further numerical analysis that will deepen the knowledge of the effusion and that will allow to make some considerations on its modelling in a numerical design tool.

4.1 Thermochromic Liquid Crystals

Thermochromic Liquid Crystals (*TLC*) are temperature indicators which reflect different colors depending on their local temperature; this behaviour is based on the selective reflection of certain wavelengths by the crystal structure of the material. Usually clear or slightly milky in appearance, liquid crystals change in appearance over a range of temperature called the "color-play interval" [75]; within this range, they reflect light in the visible colour spectrum, while outside their activation range they look transparent.

Their working principle is briefly described: incoming light rays hit the layers of liquid crystals and reflect back out again, with outgoing rays interfering (adding together or subtracting from one another) to produce light of a particular color through what's called *Bragg diffraction* (Bragg scattering). The color of the reflected light depends on how closely the crystals are together. Heating up TLC modifies the spacing between them, altering the amount of interference and changing continuously the color of the reflected light from black, through red (lowest activation temperature) and all the colors of the spectrum to blue and back to black again. More details on the working principle and properties of thermochromic liquid crystals can be found in [75, 76, 77].

Liquid crystal coating as a surface temperature indicator has been widely used, especially in the gas turbine community; one of the most appealing benefits of the TLC method is that it provides detailed temperature distributions on the entire surface of interest rather information on discrete points; in addition, TLC are not intrusive, having a negligible interaction with the flow. On the other hand, such method suffers from issues mainly due to the limited temperature range of activation and the sensitivity of crystal response to the illumination source and the camera position.

Depending on the width of temperature activation band, TLC can be employed in different techniques; in the present study, the steady-state, hue-capturing method is adopted.

4.1.1 Calibration

A robust TLC color-temperature response calibration is necessary for high accuracy measurements. When temperature is measured with the TLC, extra care has to be taken to fix all the conditions identical to the calibration to avoid the color variation problem due to the lighting/viewing arrangement. The TLC calibration has been conducted following the steady state gradient method proposed by Chan et al. [78]. The calibration set up, sketched in figure 4.1, is made up of a $4.5mm$ thick aluminium rectangular plate, sprayed with black background paint and then TLC, which houses seven thermocouples. One of its edges is heated by an electric heater, while the other is cooled by air. The whole apparatus is placed into an insulating basis.

A linear temperature gradient will appear on TLC surface: once steady conditions are reached, a single picture is sufficient for a precise measurement of color-temperature response, with the latter parameter measured through thermocouples. A digital camera (Sony XCD-SX90CR) is used to capture color images (1280×960 pixel) from the TLC painted surface; the illuminating system (Shott-Fostec KL1500 LCD) uses an optical fiber goose-neck to ensure an uniform illumination on the test surface and allows to keep both color temperature and light power constant. This arrangement allows an entire TLC hue-temperature calibration curve to be computed from a single image. However, several tests have been carried out, so as to increase global precision; moreover the calibration has been checked directly on the test article before each experiment.

Temperature requires to be associated with a measurable scalar representing the color of the TLC painted surface at every pixel if quantitative measurements are to be performed. The Hue angle is maybe the most employed parameter as far as wide band crystals are considered; it is defined in a polar chromaticity space by the intensities of the red, green and blue primaries (R, G and B values). Such color spaces are not unique and literature is prodigal of Hue definitions [79]; the following one, equation 4.1, is suggested because of its computational simplicity and, in particular,

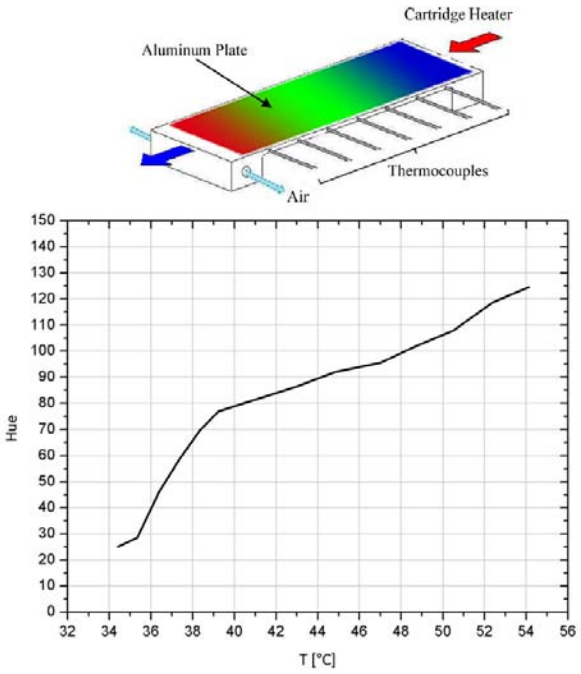

Figure 4.1: Set up for TLC calibration and calibration curve

for its lowest average uncertainty [80]:

$$Hue = arctan\left[\frac{\sqrt{3}(G-B)}{2R-G-B}\right] \tag{4.1}$$

The choice of hue as the color detector is due to the fact that this parameter is less sensitive to measurement conditions (e.g., light intensity) with respect to others; moreover, as it is shown in the calibration curve of figure 4.1, its dependency from temperature is monotonic inside the activation range of TLC [81].

4.2 Experimental Set Up

The experimental survey that will be presented in this chapter was aimed at investigating the effects of coolant-to-mainstream density ratio on the performance of a combustor cooling system composed by an effusion array and a slot cooling. In fact, as mentioned in 2.3, despite many studies deal with the investigation of the effusion cooling performance, most of them were conducted using air both as coolant and mainflow, and with reduced temperature difference between the two flows, precluding the possibility to point out the effects of the DR. In order to reproduce a representative value of combustor density ratio, in this study tests were carried out by feeding the cooling system with carbon dioxide (CO_2),while air was used in the main channel; the test plate was tested imposing several values of blowing and velocity ratios within the range of typical modern engine working conditions. To highlight the effects of density ratio and, as a consequence, to distinguish between the influence of blowing ratio and velocity ratio, tests were replicated by using air both as coolant and mainstream and results were compared.

The test rig, depicted in figure 4.2, consists of an open-loop suction type wind tunnel which allows the complete control of three separate flows: the hot mainstream, the slot cooling, and the effusion cooling flows. The vacuum system is made up of two rotary vane vacuum pumps with a capacity of $900 m^3/h$ each dedicated to the extraction of the mainstream mass flow. The mainstream flow rate is set up by guiding the speed of the pumps and using a calibrated orifice located at the beginning of the wind tunnel (throttle). The mainstream temperature is set up by using a $24.0 kW$ electronically controlled electric heater, placed at the inlet of the rig.

Slot and effusion coolant flows reach the test rig crossing two different lines that connect the wind tunnel with a pressure tank which stores the cooling fluid up to a maximum pressure of $1 MPa$. Flow rates are set up by throttling two separated valves. Heaters for a total power of $1.5 kW$

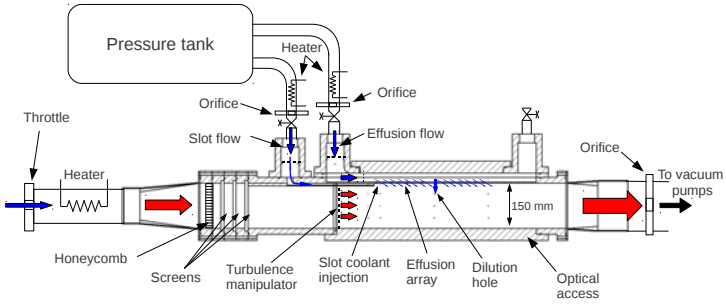

Figure 4.2: Sketch of the test rig

are placed along the lines which connect the tank to the rig in order to set the desired inlet coolant temperature.

Mass flow rates are measured at three different locations of the rig: one calibrated orifice measures the flow rate blown by the pumps according to the standard EN ISO 5167-1, while two orifices measure the slot and the effusion mass flow rates. Two pressure scanners Scanivalve DSA 3217 with temperature compensated piezoresistive relative pressure sensors measure the static pressure in 32 different locations with a maximum accuracy of $7.0Pa$. Several T-type thermocouples connected to a data acquisition/switch unit (HP/Agilent 34970A) measure the mainstream and the coolant static temperatures.

The main channel has a constant cross-section of $100\times150mm$ and is $1000mm$ long. In the first part of the channel the mainstream flow crosses a honeycomb and three screens which allow to set an uniform velocity profile. A $6.0mm$ square hole grid (hole pitch $7.6mm$, plate thickness $0.7mm$) is placed $125mm$ upstream the slot coolant injection: according to correlations proposed by Roach [82], this grid sets the turbulence level at $x/S_X = 0$ at about 5%, with macroscopic length scale of $2.8mm$.

4.2.1 Geometry of the Test Sample

The test article is completely made of transparent PMMA to guarantee the required accesses for optical measurements; effusion test plate is located on one of the lateral walls of the wind tunnel an it is made of PVC.

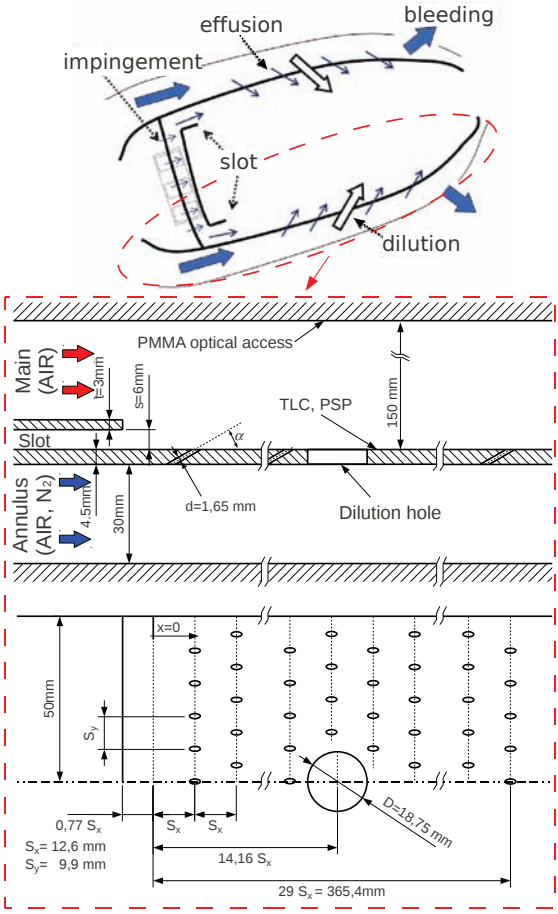

Figure 4.3: Geometry of the test sample

Figure 4.4: Liner cooling system of NEWAC combustor (curtesy of Avio Aero)

Figure 4.3 summarized the main geometrical characteristics of the test sample: it is representative of the geometry of the cooling system of the NEWAC combustor, previously studied by means of *Therm1D* (§ 3.2.1); a picture of the liner of the real prototype is displayed in figure 4.4.

A brief description of the geometry of the test sample is provided here: the slot coolant representing the starter film cooling is injected in the mainstream from a $6.0mm$ high channel, with a lip thickness of $3.0mm$; the effusion array and the dilution hole are fed by an annulus with a rectangular $30.0mm$ high and $120.0mm$ wide cross section.

The effusion geometry consists of a staggered array of 272 circular holes (d=$1.65mm$), with an inclination angle of α=30°, drilled in a $4.5mm$ thick plate and with a length to diameter ratio of L/d = 5.5. The spanwise and the streamwise pitches are, respectively, $S_x = 9.9mm$ and $S_y = 12.6mm$; the first row is located $22.25mm$ ($1.77S_x$) after the slot injection, while the last row $375mm$ downstream. The origin of the coordinate system ($x = 0$) was set in order to have $x/S_x = 1$ at the first row and $x/S_x = 29$ at the last row, while the slot injection is located at $x/S_x = -0.77$. The dilution hole (D=$18.75mm$) is located immediately after the 14^{th} row, at $x/S_x = 14.16$.

4.2.2 Measurement Technique and Test conditions

Measurements were carried out by setting the desired operating condition of mainstream and cooling flows and using a digital camera (Sony XCD-SX90CR) to record the temperature distribution from the TLC painted surface; color bitmap images (1280×960 pixel) were acquired after reaching the steady state conditions. Wide band TLC 30C20W paint, active from $\approx 30^\circ$ to $\approx 50^\circ$, were used to cover the whole temperature range of the plate with a single image. The illuminating system (Shott-Fostec KL1500 LCD) uses an optical fiber goose-neck to ensure a uniform illumination on the test surface and it allows to keep both color temperature and light power constant.

The experimental survey was formed by two main campaigns: the first campaign was aimed at measuring the heat transfer coefficient over the effusion plate, which was tested by imposing values of blowing ratio and velocity ratio within a typical range of an aeroengine combustor. Afterwards the same fluid conditions were replicated in the second campaign in order to estimate the adiabatic effectiveness of the film cooling generated by the system.

In modern combustor the temperature differences between the cooling air and the hot gases lead to a coolant-to-mainstream density ratio which usually falls within the range 1.5-3.0. To reproduce the effects of DR in a low temperature lab-scaled facility two main approaches are adopted in literature: cool down the cooling flow or use a foreign gas with a molecular weight greater than the air one. In this work measurements were carried out by feeding the cooling system with carbon dioxide (CO_2): including the typical temperature differences required to perform experiments with TLC paints, the use of this foreign gas leads to a $DR \approx 1.7$.

To highlight the effects of density ratio, the test matrix was duplicated and each fluid dynamic condition of the campaign was tested twice: the cooling system was first fed with air and then with CO_2 , while air was used for the mainflow. The main investigation parameter imposed during the tests is the average blowing ratio, defined as follow:

$$BR_{eff} = \frac{1}{N_{row}} \cdot \sum_{k=1}^{N_{row}} BR_k \tag{4.2}$$

The BR_{eff} represents the mean value of the blowing rate of the effusion rows, evaluated excluding the contribution of the dilution hole. BR_k, the blowing rate of the k^{th} row, is estimated using the actual mass flow rate through the holes and the correspondent mainstream mass flow (inlet mainstream mass flow and coolant mass flow injected by the previous $(k\text{-}1)^{th}$ rows):

$$BR_k = \frac{Cd_k \cdot (4 \cdot m_{is,k}/(\pi d^2))}{m_{main,k}/A_{main}} \tag{4.3}$$

A_{main} is the mainstream channel cross-section and d is the diameter of effusion holes. In the 4.3 the amount of coolant crossing each effusion row was defined using the isentropic coolant mass flow ($m_{is;k}$) and the hole discharge coefficient of the k^{th} row defined as follows:

$$Cd = \frac{m_{real}}{m_{is}} = \frac{m_{real}}{p_{Tc}\left(\frac{p_{main}}{p_{Tc}}\right)^{\frac{\gamma+1}{2\gamma}} \sqrt{\frac{2\gamma}{(\gamma-1)RT_{Tc}}\left(\left(\frac{p_{Tc}}{p_{main}}\right)^{\frac{\gamma-1}{\gamma}} - 1\right)} \frac{\pi}{4} d^2} \tag{4.4}$$

Similarly, the blowing rate of the dilution hole can be calculated as:

$$BR_{dil} = \frac{Cd_{dil} \cdot (m_{is,dil}/\pi D^2/4)}{m_{main,14}/A_{main}} \tag{4.5}$$

Starting from the cooling and mainstream mass flows and the several pressure values measured along the annulus and in the main channel, an automatic procedure uses the previous equations to estimate the average effusion blowing ratio (BR_{eff}). The overall isentropic mass flow rate of coolant, calculated row by row, and the measured mass flow were employed to estimate a mean value of the effusion discharge coefficient, which was then used to calculate the actual mass flow through each row and consequently the blowing ratio (4.3). It was estimated that $C_d \approx 0.73$ almost constant for all the tested conditions, while in the procedure C_{dil} was imposed equal to 0.6 [1]. This approach allows to take into account the variation of the effusion hole exit velocity along the annulus, due

to both the decrease of pressure towards the end of the annulus, and the increase of the actual main mass flow due to the multiple coolant injections row by row; both these effects lead to a decrease of actual BR_k row by row that, through this approach, can be taken into account during the data post process: as an example, considering the BR_{eff}=3 case, the blowing rate drops from BR_1=3.3 of the first rows (+10% respect to the mean value) to BR_{29}=2.8 of the last rows (-7% respect to the reference value). Similar variations were found for all the tested flow conditions.

An other important working parameter for this test campaign was the slot blowing ratio:

$$BR_{sl} = \frac{m_{sl}/A_{sl}}{m_{main}/A_{main}} \tag{4.6}$$

where A_{sl} is the slot cross section.

For a better comprehension of slot and effusion influence on the cooling performance, some tests were performed activating only the effusion cooling flow; when the two cooling systems were tested together, the slot flow was set in order to keep a constant value of $BR_{sl} \approx 1.5$. Mainstream absolute pressure was kept constant at about $p_{main} = 50000\ Pa$ ($Re_{main} \approx 75000$, $Ma_{main} \approx 0.04 - 0.05$), while coolant pressure was varied to ensure the desired values of coolant velocity inside the holes. As far as the similitude between the tests and the real engine conditions is concerned, the attention was focused more on the effusion operating parameter, such as BR_{eff}, and the geometrical scaling of the real combustor rather than in the mainstream non dimensional numbers. In fact, mainstream conditions of a combustor are pretty different from the one simulated in this test rig, especially in terms of velocity flow field and turbulence level; hence, also the non dimensional number of this campaign are not completely representative for a combustor. In any case, the mainstream similitude would have been match only employing a real swirler, which was beyond the aim of this study.

For sake of clarity, the test matrix was summarized in table 4.1: the effusion plate was first tested using air as coolant, and then using CO_2 ;

Table 4.1: Test matrix

Flow Type (Coolant / Mainstream)	BR_{eff} (VR_{eff})	VR_{eff} (BR_{eff})
AIR / AIR	1.5 (1.5)	-
	3.0 (3.0)	-
	5.0 (5.0)	-
	7.0 (7.0)	-
CO_2 / AIR	1.5 (0.9)	1.5 (2.6)
	3.0 (1.8)	3.0 (5.1)
	5.0 (2.9)	5.0 (8.5)
	7.0 (4.1)	7 (11.9)

4 different BR_{eff} and 4 different VR_{eff} were investigated. The full test matrix was made up of 48 experiments: each point of table 4.1 was tested twice, feeding or not feeding the slot cooling system (8 AIR/AIR and 16 AIR/CO_2 experiments). The resulting 24 experiments matrix was finally performed twice in order to measure HTC and adiabatic effectiveness. When air is used both as cooling and mainstream flows, the temperature differences of the experiments lead to a density ratio of DR≈1.1 and, as a consequence, tests carried out by imposing the desired values of VR coincide with tests with the correspondent values of BR imposed. It is important to underline that, referring to the classification introduced by L'Ecuyer and Soechting [30], the effusion jets work within the penetration regime ($VR_{eff} > 0.8$) in all testing conditions.

Details on the two different techniques used to measure the heat transfer coefficient and the adiabatic effectiveness will be given in the following section.

4.3 Data Analysis and Post Process

In this section the experimental method and the post process procedure will be described. Generally speaking, the preparation of the test plate is the same for both the HTC and η_{aw} measurements: crystals are thinned with water and sprayed with an airbrush on the test surface; pre-

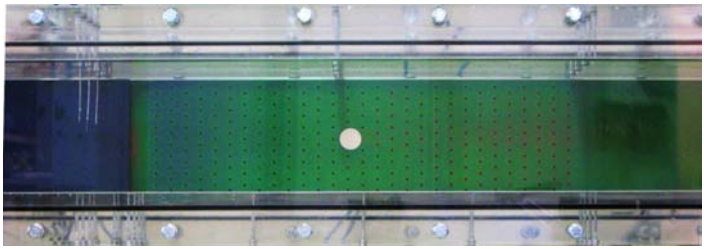

Figure 4.5: TLC appearence on the test sample

liminary, a black background paint was applied on test sample to increase the colour contrast between the TLC and the background; illuminating system was set up to reproduce the same conditions of the calibration, and, in addition, the calibration has been checked directly on the test article before each experiment. An example of how the test sample looks like once the TLC are activated is displayed in figure 4.5 (the slot is in correspondence of the blue surface on the left).

Once the steady state conditions were reached, the digital camera was used to capture color images from the TLC painted surface; the image was then processed and the surface temperature (T_w) was locally estimated by means of the calibration curve. Afterwards, different approaches were adopted to evaluate the heat transfer coefficient and the adiabatic effectiveness. Details on the data post process will be explained in the following.

4.3.1 Heat Transfer Measurements

Heat transfer coefficients were determined by a steady state technique, using TLC paint to measure the wall temperature from a heated surface. The heating element was a 25.4 μm thick Inconel Alloy 600 foil; it was laser drilled with the same array pitches of the PVC plate, and then applied on the test plate with a double sided tape. Surface heat flux was generated by Joule effect, connecting the Inconel sheet to a DC power

supply (Agilent® N5763A) through two copper bus bars fixed on lateral extremities of the back side of the test plate; a picture of the apparatus is displayed in figure 4.6.

The mainstream heat transfer coefficient is defined as:

$$HTC_{main} = \frac{q_{conv}}{T_{aw} - T_{main}} \tag{4.7}$$

where T_{main} is the mainstream static temperature, measured by means of three thermocouples located one pitch upstream the slot injection. Since tests were carried out at isothermal conditions of the two flows and the Mach numbers were low, the adiabatic wall temperature of the mainstream (T_{aw}) can be approximated with the wall temperature measured by means of TLC (T_w). q_{conv} represents the heat rate exchanged by convection between the effusion plate and the mainstream flow. Due to the presence of the effusion and dilution holes, heat generated by the Inconel foil is not uniform on the surface of the plate; in addition, despite the low thermal conductivity of the PVC, test sample is not ideally adiabatic and the two main source of heat losses, to both the conduction through the plate, and the convective heat removed by coolant both in the annulus

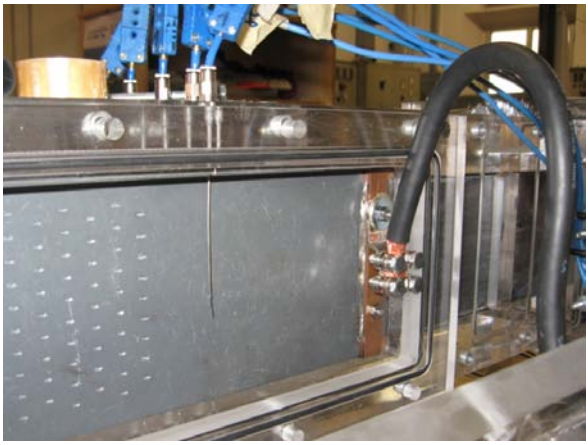

Figure 4.6: Position of the bus bars on back surface of the test plate

and inside the holes, have to be taken into account. As a consequence, in order to have an accurate evaluation of the net heat flux transferred from the surface to the mainstream, q_{conv} was estimated implementing an iterative procedure based on a complete 3D thermal-electric FEM simulation. The procedure evaluates the non uniform heat locally generated on the surface, allowing to obtain an accurate estimate of q_{conv};

- Colburn correlation $Nu = 0.023 Re^{4/5} Pr^{1/3}$ was used to set the heat loads on the cold side; non-dimensional number distributions were calculated with the hydraulic diameter of the annulus and taking into account the mass flow reduction due to the coolant extraction from the effusion plate;

- heat loads inside the hole were estimated through the Colburn correlation, too; Reynolds number inside the holes was calculated considering the variation row by row of the actual mass flow rate crossing the holes;

- on the hot gas, a convective heat load was applied using the HTC_{main} of the previous iteration;

- the PVC plate was modelled with thermal elements, while for the Inconel sheet thermal-electric elements were used for a total amount of $9 \cdot 10^5$ elements (figure 4.7(a)); the same DC voltage difference used for the tests was applied on the boundaries, in correspondence of the copper bus bars.

Outputs from the FEM calculation (e.g. figure 4.7(b)) allow a fine estimate of HTC_{main} for each pixel of the digital image acquired during the test; results from this calculation are then used to update the hot gas side boundary conditions for the subsequent FEM run and, therefore, to iterate on HTC_{main} until the convergence is reached. Heat losses are taken into account too: depending on the fluid dynamics conditions of the tests, they are approximately 2% - 5%.

This iterative procedure was developed by Facchini et al. [49]; a source of uncertainty consists of using the Colburn correlation for the estimate

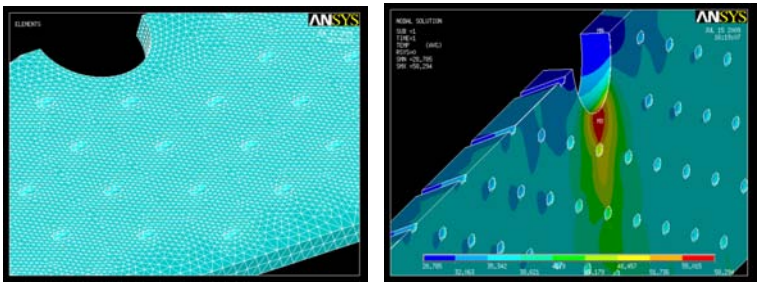

(a) FEM model (b) Example of q_{conv} distribution

Figure 4.7: FEM model for the estimate of HTC_{main} [49]

of the cold side heat transfer coefficient. Actually, the work of Byerley [83], recently reviewed and extended by Andreini et al. [84, 85], highlighted that the bleeding of coolant from film cooling holes significantly enhances the HTC in the proximity of the entrance of the hole itself: this phenomenon is due to a reduction in boundary layer thickness caused by bleeding off the upstream boundary layer, that increased proportionally to bleed rate. Therefore, to assess the impact of using a simplified correlation such as the Colburn one, Facchini et al. carried out a series of FEM simulations to investigate the effect of the uncertainty of the cold side heat load on the final results of mainstream HTC: enhancing the load on coolant side and holes interior of 50%, they found that the variation of the HTC_{main} was about 5-6%, anyway inside the relative error committed on the calculation of the mainstream HTC. Further details on this sensitivity analysis and on the entire procedure for the estimate of HTC_{main} can be found in the work of Facchini et al.

Heat transfer experiments were carried out with coolant and mainstream at room temperature. Likewise effectiveness measurements, the mainstream absolute pressure was kept constant at about p_{main}=50000 *Pa*, while coolant pressure was varied in order to ensure the desired values of BR_{eff} and VR_{eff}.

According to Jones [86], the use of a foreign gas requires a special cor-

rection during the post process of the experimental data (both for heat transfer and effectiveness measurements); this correction allows to take into account the difference in specific heat and thermal conductivity between the foreign gas (CO_2 in this campaign) and the actual cooling flow of a real application (air). The author assesses that a little correction is necessary in the case of CO_2 injection; in particular, the correction becomes smaller with increasing the coolant velocity (high BR-VR), due to the fact that the transport of species, momentum and enthalpy becomes mainly dependent on the turbulent flow field rather than on the concentration gradients and the viscosity. Concerning the results of this campaign, whose tests were performed at high BR-VR, it was estimated that the entity of this correction is almost negligible and falls within the error due to the experimental uncertainties.

4.3.2 Adiabatic Effectiveness Measurements

Effectiveness measurements were carried out by heating both the coolant and the mainflow, in order to obtain temperature of about 300 K and 350 K respectively. Likewise HTC measurements, the mainstream absolute pressure was kept constant at about p_{main}=50000 Pa, while coolant pressure was varied in order to ensure the desired values of coolant velocity.

The definition of adiabatic effectiveness is here recalled:

$$\eta_{aw} = \frac{T_{main} - T_{aw}}{T_{main} - T_{cool}} \tag{4.8}$$

Three thermocouples, normal to the flow, located at $-1.77x/S_x$ acquired mainstream temperature T_{main}; three additional probes were dedicated to the coolant and inserted into the annulus, at $x/S_x = 0; 14; 29$.

Once the image of the test plate coloured by TLC was acquired, the temperature distribution estimated by means of the calibration curve was post processed in order to get the adiabatic wall temperature (T_{aw}); in fact, the following heat losses had to be taken into account:

1. Heat transfer due to convection between the mainstream and the effusion plate;

2. Conduction across the effusion plate; in fact, despite the low thermal conductivity of PVC ($\lambda_{PVC} = 0.145 W/mK$), test plate cannot be considered adiabatic;

3. Convection between the effusion plate and the coolant, both in the annulus and inside the holes.

Therefore, T_w distribution was post-processed using a 1D correlative procedure:

$$T_{aw} = T_w + \frac{Q_{loss}}{HTC_{main}} \tag{4.9}$$

Values of HTC_{main} were measured in the dedicated experimental survey, while Q_{loss} was estimated with the following equation:

$$Q_{loss} = HTC_{comb} \cdot (T_w - T_{cool}) \tag{4.10}$$

HTC_{comb} was calculated combining the resistances of the conduction across the PVC and the convection with the coolant flow both in the

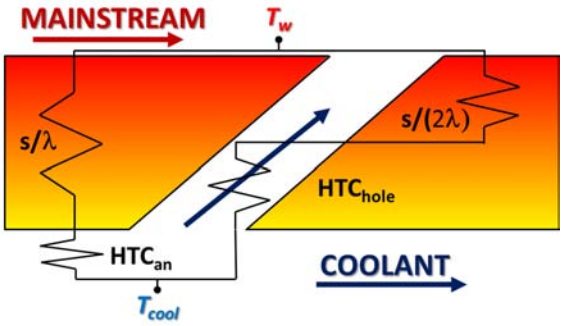

Figure 4.8: 1D model of heat transfer through the test plate

annulus and inside the holes (figure 4.8):

$$HTC_{comb} = \left(\frac{1}{HTC_{an}} + \frac{s}{\lambda_{PVC}} \right)^{-1} + \left(\frac{1}{k_h \cdot HTC_{hole}} + \frac{s}{2\lambda_{PVC}} \right)^{-1} \tag{4.11}$$

HTC_{an} and HTC_{hole} were estimated using the Colburn correlation $Nu = 0.023 \cdot Re^{0.8} Pr^{1/3}$, calculating the Reynolds and the Nusselt numbers with the hole diameter and with the annulus cross section hydraulic diameter respectively; a corrective coefficient (k_h), which represents the ratio between the surface of the hole (πdL) and the area of the annulus associated to one hole ($S_x \cdot S_y$), was applied to HTC_{hole}.

A preliminary sensitivity analysis to HTC_{comb} was performed to estimate how the uncertainty due the use of the Colburn correlation affected the final evaluation of η_{aw}. The analysis pointed out that a variation of both HTC_{an} and HTC_{hole} of 20% alters HTC_{comb} of only 6%: this can be explained considering high thermal resistance of the conduction with respect to the convection. The impact of this variation on adiabatic effectiveness is even smaller: as an example, considering $BR_{eff} = 3$ case, a 20% variation in HTC_{an} and HTC_{hole} roughly affects the effectiveness of 5% for $\eta_{aw} = 0.3$ and 1% for $\eta_{aw} = 0.6$.

Finally, it is worth noting that η_{aw} is evaluated using a constant value of T_{cool}, which is the temperature measured with thermocouples at the inlet of the annulus. However, the low velocity of the coolant inside the annulus and, as a consequence, the small heat transfer coefficient, allow to neglect the temperature rise; however, the measured temperature rise between the inlet and the outlet of the annulus was less than $1K$ for all the testing conditions.

4.3.3 Effect of Heat Conduction on Effectiveness Data Post-Process

Local values of adiabatic effectiveness evaluated by means of the TLC techniques suffer from the heat conduction through the test plate; since the post-processing procedure employed in this survey takes into account

these thermal effects through a one-dimensional approach, a preliminary study was performed to deepen the effect of the heat conduction on film effectiveness.

To assess the accuracy of the 1D post-processing procedure to evaluate the heat flux through the plate, and therefore to obtain the adiabatic wall temperature, a 3D FEM analysis was performed using the commercial code *ANSYS® Mechanical 14.0*. The domain reproduces a portion of the multiperforated plate; the conductivity was set equal to the conductivity of the real test sample (λ_{PVC}). The imposed boundary conditions were:

- forced convection on the hot gas side (HTC_{main}, T^*_{aw})
- forced convection on the annulus side (HTC_{an}, T_{cool})
- forced convection inside the holes (HTC_{hole}, T_{cool})
- adiabatic lateral surfaces (*spanwise direction*)
- translational periodicity on the front and back surfaces (*streamwise direction*)

All the boundary conditions were set referring to the $BR_{eff} = 7$ case, as it can be considered the most critical test from a thermal point of view: in fact it is the case with the highest coolant velocities, that is the highest heat transfer coefficients both in the annulus and inside the holes.

Since the performance of the cooling system, i.e. the film cooling distribution, changes from the first to the last rows, two different simulations were performed in order to have a complete characterization of the thermal behaviour of the plate. *Test A* simulates the first three rows: assuming a constant value of $\eta_{ad,FEM} = 0.0$, the adiabatic wall temperature on the hot gas side was imposed equal to the hot gas temperature measured during the experiments ($T^*_{aw} = T_g$). *Test B* reproduces the behaviour of the rows downstream the dilution hole (e.g. rows 19^{th}-21^{th}): here the imposed adiabatic wall temperature (T^*_{aw}) was evaluated assuming a constant value of $\eta_{ad,FEM} = 0.66$.

Results of the simulations were post-processed obtaining the temperature distributions over the hot gas side surface of the plate. Temperatures

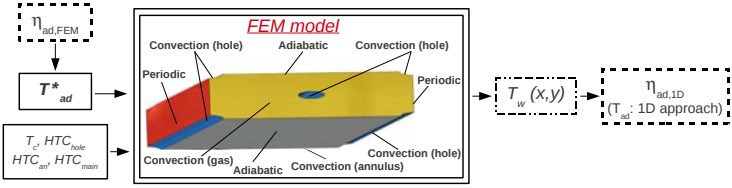

Figure 4.9: Procedure to evaluate the accuracy of the 1D post-processing procedure

were then used to evaluate the adiabatic wall temperature and the film effectiveness over the plate through the 1D post-processing procedure ($\eta_{ad,1D}$): since the FEM simulations were carried out assuming a specific value of adiabatic effectiveness ($\eta_{ad,FEM}$), the deviation between the target value and $\eta_{ad,1D}$ gave indication about the approximation related to the use of a 1D approach. The procedure described above is sketched in figure 4.9.

Results of the analysis are summarizes in figure 4.10; focusing on *Test A*, plot of figure 4.10(a) shows that the spanwise averaged distribution of $\eta_{ad,1D}$ fluctuates around the target value $\eta_{ad,FEM} = 0.0$ within a range which is roughly ± 0.1. As expected, the highest discrepancy are located immediately upstream the exit of the holes, where the heat sink effect is more emphasized. The averaged effectiveness value over the whole surface of the model was $\eta_{ad,1D} = -0.014$. The adiabatic effectiveness distribution map, displayed in figure 4.10(a), highlights that under the most critical conditions from a thermal point of view (BR_{eff}=7, $\eta_{aw} = 0.0$, i.e. the highest Reynolds numbers inside the holes and the highest temperature gradients between the surface and the coolant), the 1D approach used to evaluate the adiabatic wall temperature is quite accurate, despite some discrepancies, especially around the exit of the holes.

Concerning *Test B*, plot of Fig. 4.10(b)c shows that the spanwise averaged distribution is quite close to the expected value; the highest errors are still located upstream the hole exit, but in this case the deviation

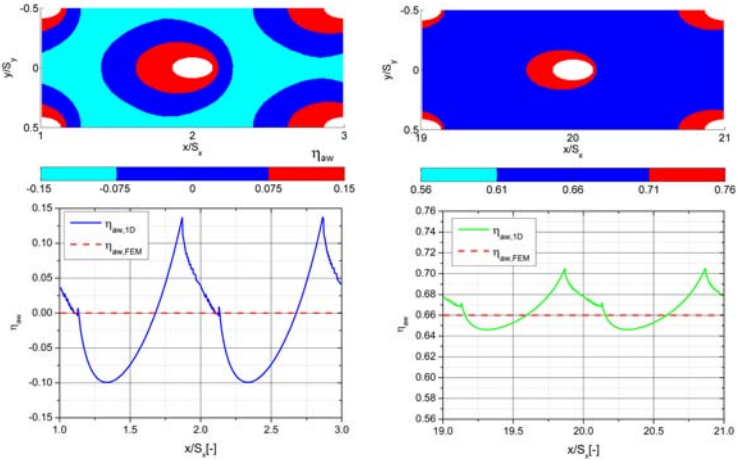

(a) Test A ($\eta_{aw,FEM} = 0.0$) (b) Test B ($\eta_{aw,FEM} = 0.66$)

Figure 4.10: Results of the FEM analysis for the estimate of η_{aw}

from $\eta_{ad,FEM} = 0.66$ is always less than ± 0.05. The averaged effectiveness value over the whole surface is $\eta_{ad,1D} = 0.667$. Focusing on 2D map, it can be noticed that the highest errors are inside a halo around the exit of the holes; the maximum extension is however less than one diameter in the streamwise direction.

Concluding, the previous analysis pointed out that the 1D post-processing procedure allows to estimate the adiabatic effectiveness with good accuracy, despite some limitation around the exit of the holes, where the heat sink effect is more pronounced and the thermal conduction is highly three-dimensional.

4.4 Uncertainty analysis

Uncertainties associated to direct measurements inevitably affect the evaluated quantities values, that are obtained by properly combining the former ones (e.g. flow rates, adiabatic effectiveness, heat transfer coef-

ficients, discharge coefficients, etc.). The average experimental uncertainty can be computed following the standard ANSI/ASME PTC 19.1 [87] based on the Kline and McClintock method [88].

If G is the quantity of interest, known function of n independent variables, g_i, in their turn influenced by a partial absolute uncertainty $\pm\Delta g_i$, it is straightforward to write the following equations:

$$G = f(g_1, g_2, ..., g_n) \tag{4.12}$$

$$G \pm \Delta G = f(g_1 \pm \Delta g_1, g_2 \pm \Delta g_2, ..., g_n \pm \Delta g_n) \tag{4.13}$$

The absolute error on G may be computed as in equation 4.14:

$$\Delta G = \sqrt{\left(\Delta g_1 \frac{\partial f}{\partial g_1}\right)^2 + \left(\Delta g_2 \frac{\partial f}{\partial g_2}\right)^2 + ... + \left(\Delta g_n \frac{\partial f}{\partial g_n}\right)^2} \tag{4.14}$$

It is evident that the accuracy depends both on the single measurements value and on their uncertainty.

In case of relationship between G and g_i as in equation 4.15:

$$G = g_1^a \cdot g_2^b \cdot ... \cdot g_n^m \tag{4.15}$$

the overall percentage error in G evaluation, due the single percentage error in each g_i, can be calculated as:

$$\frac{\Delta G}{G} = \sqrt{\left(a\frac{\Delta g_1}{g_1}\right)^2 + \left(b\frac{\Delta g_2}{g_2}\right)^2 + ... + \left(m\frac{\Delta g_n}{g_n}\right)^2} \tag{4.16}$$

The estimate of the uncertainties of the measured or calculated quantities were performed starting from the information given by the manufacturer of the instrumentation and applying the previous equations. The piezoresistive relative pressure sensors, used to measure the static pressure in different locations of the test rig have an uncertainty of $\pm 7.0 Pa$, while the T type thermocouples have an uncertainty level of about $\pm 0.5 K$. The mainstream and the effusion mass flow rates were measured with an uncertainty of $\pm 2\%$ and $\pm 4\%$ respectively. The mean values of Blowing and Velocity ratios were estimated with an uncertainty level of $\pm 5\%$.

Table 4.2: Uncertainty analysis (95% level of confidence)

	Variable	Meas. Technique	Uncertainty	Units
d	Hole Diameter	-	±2%	$[-]$
T	Temperature	T/C with cold junction	±0.5	$[K]$
P	Pressure	Pressure scanner	±7	$[Pa]$
$\dot{m}_{cool}$	Cooling mass flow	Orifice	±4%	$[-]$
$\dot{m}_{main}$	Main mass flow	Orifice	±3%	$[-]$
BR	Blowing Ratio	-	±5%	$[-]$
VR	Velocity Ratio	-	±5%	$[-]$
HTC	Heat Transfer Coefficient	TLC	±10	$[W/m^2K]$
η_{aw}	Adiabatic Effectiveness	TLC	±0.05	$[-]$

As far as the uncertainty of heat transfer coefficient and adiabatic effectiveness measurements is concerned, it was estimated to be respectively $\pm 10 W/m^2K$ and ±0.05 related to the spanwise averaged values. These estimates include the effects of calibration and data post-processing. Tests were repeated several times in order to confirm the repeatability of the results.

Table 4.2 summarizes the contributions to the uncertainties for each parameter as well as the absolute or percentage error; all the experimental uncertainty estimates are based on 95% confidence levels.

4.5 Experimental Results

Experimental results for the two test campaigns will be presented in the next sections; detailed 2D maps and spanwise averaged trends will be provided for only one reference condition, since the relative behaviour of the test plate subjected to the other conditions is almost the same. The results of the whole test will be summarized showing a single averaged value for each test condition; however, averaged values gives important information to the designer since they can be used to know how the system works varying the operating point, and thus to choose the best one on the base of other constrains.

4.5.1 Heat Transfer Coefficient

Figure 4.11 shows heat transfer coefficient maps for the experiments carried out by imposing BR_{eff}-VR_{eff}=3 (due to the small coolant to mainstream density ratio, $VR_{eff} \approx BR_{eff}$ in AIR tests); results are displayed dividing the local HTC_{main} by a constant reference value (HTC_{ref}). In white areas close to the dilution hole HTC was not measured because the local low/high surface heat generation did not allow TLC paints working properly within their activation range. Maps displays the overall trend of HTC, showing that it increases up to the 14^{th} row and then remains nearly constant. Differences between tests with and without slot are restricted to the first 2-3 rows, where coolant coming out from the slot mitigates the heat transfer; after the 5^{th} row, the presence of the slot flow does not alter significantly the behaviour of the effusion cooling.

HTC contours are very similar to those presented by Kumada et al. [42], the main difference being the absence in Kumada's test of an high heat transfer zone just downstream the hole exit, probably due to the lower blowing ratio investigated (0.3 - 0.7).

Imposing the same mainstream conditions of all the other exper-

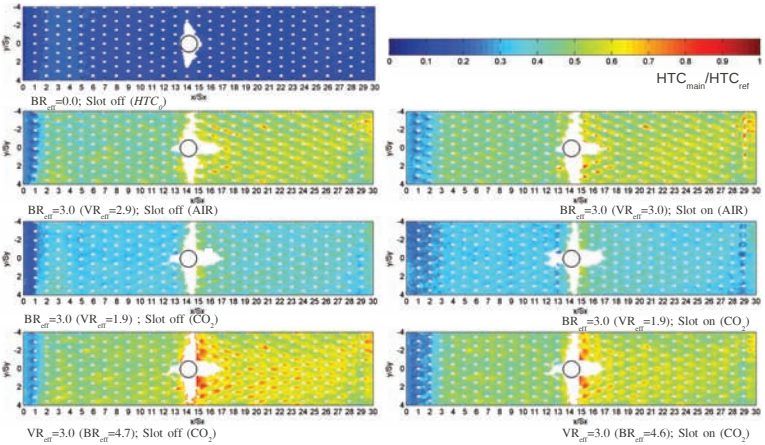

Figure 4.11: Heat transfer coefficients maps ($BR_{eff} - VR_{eff} = 3$).

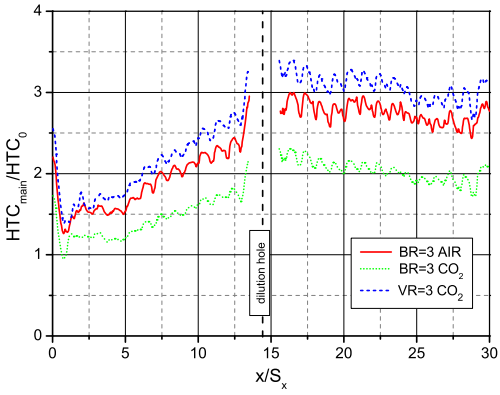

(a) Effusion

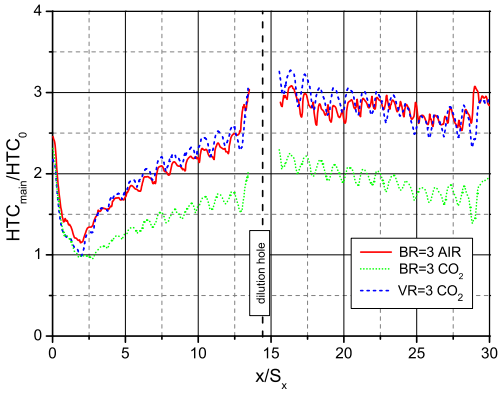

(b) Effusion + Slot

Figure 4.12: Spanwise averaged HTC/HTC_0 ($BR_{eff} - VR_{eff} = 3$).

iments, a reference test was carried out in order to evaluate the heat transfer coefficient without film cooling (HTC_0); map of HTC_0 is displayed in figure 4.11. Values of HTC_0 were spanwise averaged and the resulting trend along the centerline was used as the reference in figure 4.12 and 4.13.

Figures 4.12(a) and 4.12(b) show trends of spanwise averaged heat

transfer coefficient along the plate with effusion coolant only and with both slot and effusion flows for BR_{eff}-VR_{eff}=3; data are plotted in term of (HTC_{main}/HTC_0) in order to highlight the increase of heat transfer due to coolant injections. First of all, a double heat transfer peak can be observed downstream the exit of the holes: the presence of two peaks of different strength was reported also in the work of Kumada et al. As early pointed out by Kelly and Bogard [34], the increase on the heat transfer coefficient downstream the hole exit is strictly related to the generation of a new thermal boundary layer (*TBL*). In their numerical investigation, Andreini et al. [59] showed that, such a new TBL, is not only due to mass injection from the effusion hole but also by the induced three dimensional vortical structure originated by the jet in crossflow phenomenon. In particular, they showed that when the CVP of two subsequent holes interact, in proximity of the exit of the downstream hole, a momentum exchange takes place; due to this interaction, the flow near the wall is deviated and accelerated in the spanwise direction, making the TBL thinner and thus increasing the heat transfer with the surface.

From an overall point of view, figure 4.12(a) shows that HTC remains constant in the first five rows, even if it is enhanced compared to the reference case ($HTC_{main}/HTC_0 > 1$); after the 5^{th} row, it increases up to the dilution hole, where it reaches an asymptotic value. The beginning of the rising trend of HTC is brought forward to the 2-3^{th} row in presence of the slot cooling flow (figure 4.12(b)); however, as it was already shown in the maps, after the 5^{th} row the slot flow has only a slight influence on the heat transfer.

The attention will be now focused on the effects of density ratio; results displayed in figure 4.12 shows that for a constant blowing ratio, heat transfer decreases with increasing the density ratio; on the other hand, results of tests carried out by imposing the same value of velocity ratio are almost coincident. Maps and trends are here shown only for one point of the test matrix, which significantly represents the typical behaviour of the system in each testing condition. A more detailed description of the behaviour of heat transfer coefficient over this effusion

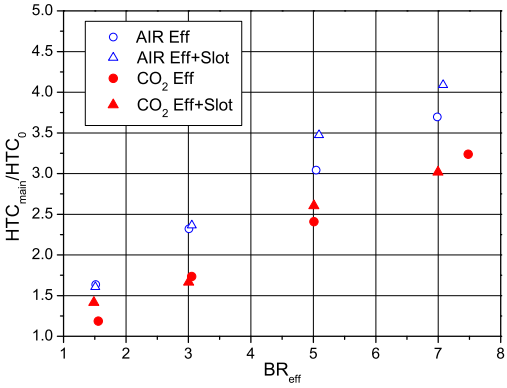

(a) HTC/HTC_0 *vs* BR_{eff}

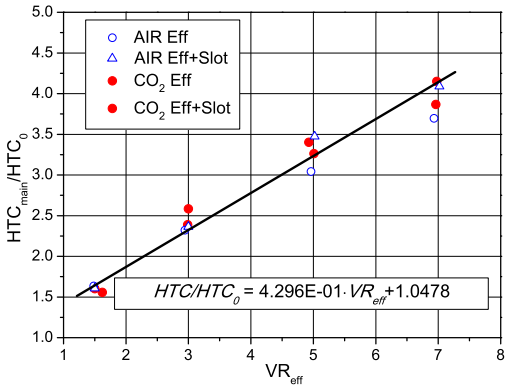

(b) HTC/HTC_0 *vs* VR_{eff}

Figure 4.13: Averaged values of heat transfer coefficient

plate can be found in [49]. Results of the full test matrix are summarized in figure 4.13: it shows the average value of HTC_{main}/HTC_0 of the whole plate with and without the slot flow, plotted versus the actual BR_{eff} (4.13(a)) and VR_{eff} (4.13(b)). Figures clearly display how the HTC linearly increases with increasing *BR-VR*; furthermore, it is possible to highlight that air tests are in good agreement with CO_2 tests

with the same velocity ratio (figure 4.13(b)). This means that, within the effusion jets penetration regime, VR acts as the driving parameter of the phenomenon instead of BR; this confirms the results numerically found by Andreini et al. [59]. Figure 4.13(b) includes also the equation of the linear fitting of the experimental data: the maximum estimated relative error was around 10%, while the averaged value was around 4.5%. Even if the outcomes of the campaign are affected by a low turbulence level with respect to an actual combustor, results give useful information about the behaviour of the effusion system and, moreover, show that the use of velocity ratio in a low temperature facility allows to reproduce the effects of DR without employing a foreign gas.

4.5.2 Adiabatic Effectiveness

Figure 4.14 shows the adiabatic effectiveness maps for BR_{eff}-VR_{eff}=3 test points: maps display the effects of effusion injections and moreover how the cooling performance are affected by the interaction with slot coolant.

From an overall point of view, it is possible to highlight that, when only effusion is present, the effectiveness grows row by row until the dilution hole; after the 15^{th} row, the coolant distribution is dominated by the

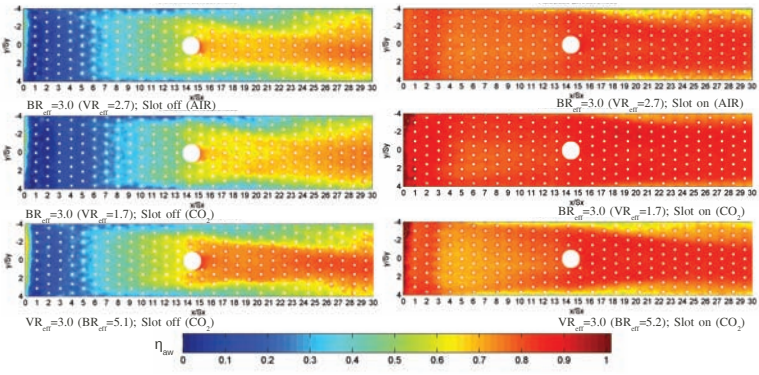

Figure 4.14: Adiabatic effectiveness maps (BR_{eff}-VR_{eff} = 3)

wake generated by the dilution jet: this jet draws cooling flow injected by the effusion holes and generates a high effectiveness wake up to the end of the test plate. In addition, results point out that, without the slot flow, the effusion system does not guarantee a sufficient protection of the first part of the liner by itself. On the other hand, when both the cooling system are active, maps shows that a very efficient protection of the liner can be obtained and the effects of the dilution jet are mitigated.

Figure 4.15(a) shows trends of spanwise averaged adiabatic effectiveness along the plate when only effusion is activated: it is possible to observe how the film cooling superposition increases η_{aw} quite linearly until the 15^{th} row, where the dilution hole is located. As stated before, in the following rows the wake generated by the dilution hole deeply affects the film distribution: a slight decrease of effectiveness can be observed immediately downstream this hole, which however restarts growing from the 20^{th} row until the end of the test plate.

Focusing on the effects of DR, results show that an increase of VR_{eff} leads to a slight increase in η_{aw}; moreover, even if the difference among the curves are quite small, BR_{eff} seems to be the parameter which allows to take into account the effects of density ratio even in air-to-air tests. The limited effect of the blowing rate for an effusion cooling operating at high value of this parameter was found also by Scrittore et al. [89].

The presence of the slot coolant strongly enhances the adiabatic effectiveness; after the first three rows where the η_{aw} remains nearly constant, there is a lower effectiveness area due to the detrimental interaction between the two cooling flows: here the highly penetrating effusion jets partially destroy the high effectiveness film cooling layer generated by the slot [48]. This behaviour can be directly related to the velocity ratio of the jets, which can be used to scale the effects of DR; after the dilution hole, η_{aw} reaches an asymptotic value which can still be related to the velocity ratio.

Figure 4.16 shows the adiabatic effectiveness results for the whole test matrix, plotted versus BR_{eff} and VR_{eff}; each point represents the averaged value of the entire test sample. Focusing on the effusion cooling,

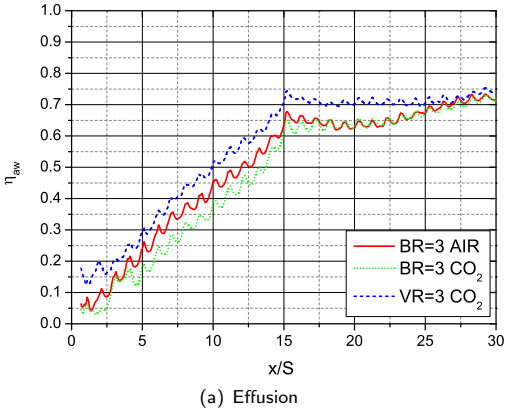

(a) Effusion

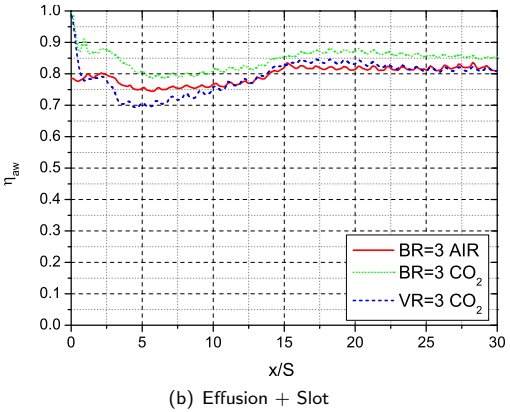

(b) Effusion + Slot

Figure 4.15: Spanwise averaged η_{aw} (BR_{eff}-$VR_{eff} = 3$).

figure 4.16 highlights that this system operates with high effectiveness and stable behaviour for a wide range of working conditions. η_{aw} is only weakly affected by those parameters since the high effectiveness is mainly due to the coolant mass addiction. In fact, even if the penetration of effusion jets increases, η_{aw} does not fall because the large amount of coolant mass flow injected in the mainstream grows row by row and guarantees the good protection of the liner.

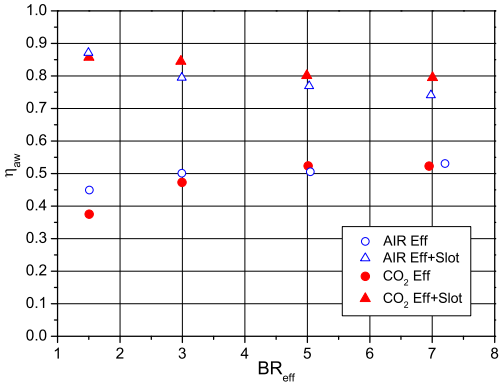

(a) η_{aw} *vs* BR_{eff}

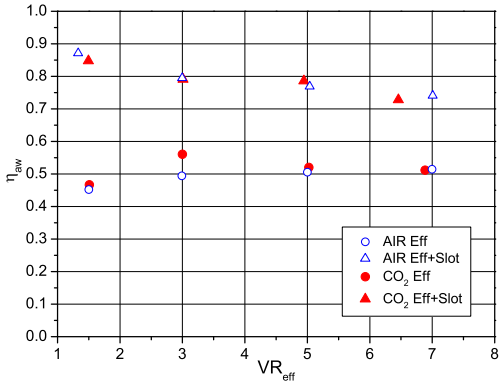

(b) η_{aw} *vs* VR_{eff}

Figure 4.16: Averaged values of adiabatic effectiveness

These considerations are emphasized when the two cooling systems are combined: this configuration allows an effective protection of the liner since the first rows, almost constant through all the tested range of operating conditions. The slight decrease of averaged effectiveness with increasing the blowing rate is due to the high penetration of jets: high-momentum jets act as an obstacle to film development and increase the

initial mixing with the mainstream, thus leading to a detrimental interaction with the slot [48]. However, this behaviour is bounded to the first rows and affects only marginally the good cooling performance of the system. It is important to remember that these results are affected by a reduced turbulence level of the mainstream flow.

As far as the effects of density ratio are concerned, tests without slot flow (circles) confirms the outcomes from the analysis of figure 4.15: experimental results show that within the penetration regime, the effects of coolant to mainstream density ratio are small thus, as commonly found in the literature, BR have to be used to scale the effects of DR.

Concerning tests with both cooling system (triangles), results indicate that η_{aw} decreases with increasing BR-VR (due to the increasing penetration of effusion jets), but only slight differences were found changing the coolant to mainstream density ratio. In fact, the system shows a very effective and almost constant coolant protection for all the tested range and small changes in BR/VR do not strongly alter the performance. However, focusing on tests with the same BR_{eff} (4.16(a)), it it is possible to note that an increase in DR cause a small enhancement in η_{aw}; on the other hand, results indicates that, when the both the slot flow and the effusion are active and the jets work within the penetration regime, VR_{eff} has to be used to take into account the effects of density ratio.

4.6 Exploitation of Experimental Data: Therm1D Analysis

The exhaustive database obtained from the experimental campaign described above was further exploited in several further studies. In particular, the following sections will give an overview of two different works based on the use of *Therm1D* (Chapter 3); they are aimed at validating the correlation used in the code for the estimate film cooling adiabatic effectiveness (§ 4.6.1), and at simulating actual operating condition of an aeroengine combustor and estimate overall performance parameters (§ 4.6.2).

An other interesting application of the database obtained by means of TLC was the validation of an innovative measurement technique for adiabatic effectiveness measurements; Pressure Sensitive Paints (*PSP*) technique is based on the heat and mass transfer analogy and therefore it is not affected by thermal conduction effects that limits an easy use of thermographic methods to obtain the adiabatic wall temperature. This strength of PSP makes this technique particularly suitable to obtain detailed and reliable adiabatic effectiveness data for multiperforated film cooling geometries, as shown by the deep comparative analysis performed by Caciolli et al. [90] using the TLC data presented above. Readers interested in this topic can find details of this work in paper mentioned above.

4.6.1 Check of the correlation available in literature

Adiabatic effectiveness data were used to validate the use of the film cooling correlations available in *Icons1D* for effusion cooling holes. To the author's knowledge, specific correlations for multiperforated plates with a wide validity range in terms of geometry of the holes, fluid conditions, etc., are not available in literature; consequently, the typical approach adopted to deal with multiple rows of film cooling consists of using correlations developed for single row and adding the superposition effect. However, the strong reduction of holes and rows spacing switching from a multirow arrangement, typical of turbine blade, to a combustor effusion arrangement does not directly guarantee that the validity of this method remains unchanged.

Starting from these considerations, this approach was checked through the use of *Icons1D*: the geometry of the test rig was reproduced and one model was employed to simulate the behaviour of the annulus and the effusion holes. In this work, the slot cooling was not modelled and comparisons were carried out with analogous data obtained with only the effusion active; the same fluid dynamic conditions were imposed in terms of inlet total pressure and temperature, and mass flow rate; boundary conditions on the gas side were set using data measured during the test

campaign (mainstream turbulence included); comparisons with tests carried out with CO_2 as coolant were made rising the mainstream temperature in order to obtain the same density ratio of the experiments. Film cooling superposition length [74] was kept constant for all the tests. Since the attention was focused on effusion cooling, comparison will be carried out only up to the 15^{th} row: in fact, as it clearly visible in figure 4.13, downstream this row the film cooling behaviour is dominated by the wake dilution jet, which generates a complex three-dimensional flow field, drawing coolant injected by the adjacent holes and thus altering the behaviour of the effusion system. As a consequence, this phenomenon cannot be reproduce with one-dimensional correlation and comparison between numerical and experimental data will be focused in the part of the liner upstream the dilution hole.

The two main correlations available in *Icons1D* are those suggested by L'Ecuyer and Soechting [30] and Baldauf et al. [91]; as state before, they were both developed for a single row of film cooling holes. The validity ranges of the main operating parameters are summarized in table 4.3. Unfortunately both the correlation were developed for blade film cooling holes and, for example, the range of some parameters such as the blowing ratio are quite lower than typical values for combustor. It is worth noting that the ranges of the experimental database used by L'Ecuyer and Soechting are much wider than the ones used by Baldauf et al. for their correlation, which instead is based on more recent data and moreover it is

Table 4.3: Operating parameters for the investigated correlations

		L'Ecuyer and Soechting [30]	Baldauf et al. [91]
Geometry	α	30°;35°;45°;55°;90°	30°;60°;90°
	S_y/D	2;3	2;3;5
	L/D	D[mm]=2;2.27;11.7;11.8;12.8	6
Hot gas flow	δ^*/D	≈ 0.04-0.63	0.1
	Re_D	3500-52000	6800-14000
	Tu	-	1.5%; 4.0%
Coolant flow	BR	0.1-3.75	0.2-2.5
	DR	0.79;0.85;0.94;1.1;1.5;2.0;4.26	1.2;1.5;1.8

sensitive to the mainstream turbulence level. Outside the validity range, the code extrapolates the behaviour of the correlation.

Figure 4.17 shows comparisons between experimental data and the two correlations for some tests; to asses the sensitivity of the correlations to the density ratio, the analysis was carried out using results from both experiments with AIR and CO_2 . Concerning test at VR_{eff}=1.5, it is possible to observe how the correlation proposed by L'Ecuyer and Soechting is in good agreement with the experiments: in fact, it is able to reproduce the slope of the rising trend of adiabatic effectiveness due to the superposition. On the other hand, comparisons with test at VR_{eff}=0.9 (CO_2) indicate an overestimate of the correlation: according to the definition of L'Ecuyer and Soechting, for this value of velocity ratio the film cooling regime belongs to the penetration regime, just above the threshold of the mixing one (VR=0.8). Since the experimental trend is lower than that predicted by the correlation, it seems that, for the tested conditions, film cooling was still working in the mixing regime.

Moving to the higher values of BR/VR, the correlation is able to reproduce with good accuracy the trends of η_{aw} for the whole investigated conditions, even for values of blowing rate outside its validity range. In addiction, the effects of density ratio are well reproduced, too.

Focusing on the Baldauf's correlation, predictions for BR_{eff}=1.5 are similar to those given by the other correlation in term of accuracy. However, comparisons for higher values of BR show that, outside its validity range, the correlation is completely unsuitable for such kind of cooling system.

Summarising, the comparison between experimental data and numerical prediction shown that the correlation proposed by L'Ecuyer and Soechting, together with the film cooling superposition, is suitable to model the behaviour of an effusion system in terms of adiabatic effectiveness.

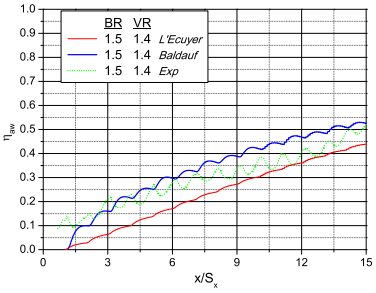

(a) BR_{eff}-VR_{eff}=1.5 (AIR)

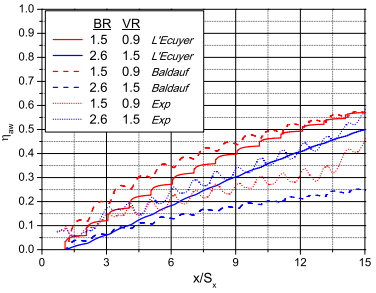

(b) BR_{eff}-VR_{eff}=1.5 (CO_2)

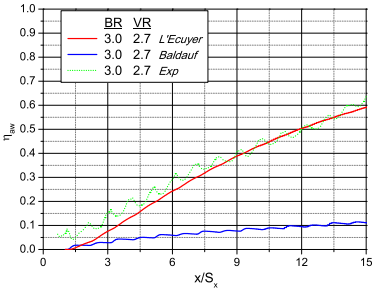

(c) BR_{eff}-VR_{eff}=3.0 (AIR)

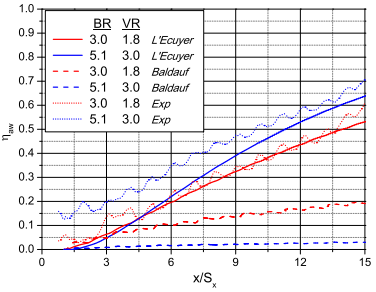

(d) BR_{eff}-VR_{eff}=3.0 (CO_2)

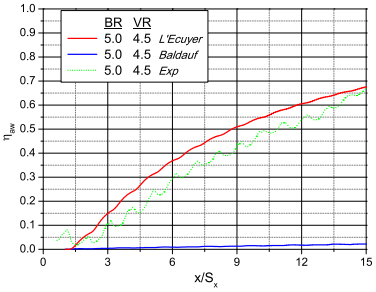

(e) BR_{eff}-VR_{eff}=5.0 (AIR)

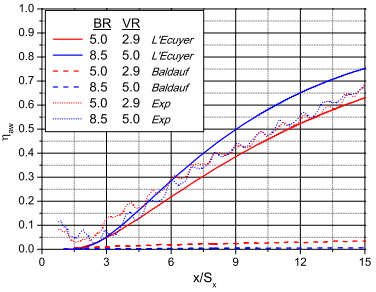

(f) BR_{eff}-VR_{eff}=5.0 (CO_2)

Figure 4.17: Comparison of η_{aw} between exp. data and correlations

4.6.2 Estimate of NHFR and Overall Effectiveness

In open literature [35, 92] NHFR, defined in eq. 2.8, was mainly used to evaluate turbine endwall and blades cooling systems and θ, the dimensionless temperature (eq. 2.9) was set within the range of $\theta = 1.5 - 1.6$. Since the overall effectiveness of a combustor cooling system is generally higher than the one of a turbine airfoil, more recently Facchini et al. [49] updated this parameter to evaluated the NHFR of a cooled liner, imposing a value of $\theta = 1.2$. However, since the heat transfer coefficient and the adiabatic effectiveness are quite variable along the liner, imposing a constant value for the dimensionless temperature limits an accurate estimate of NHFR.

In this analysis, results of the two experimental campaign will be used within *Therm1D* to estimate an engine representative distribution of θ and, therefore, to evaluate the NHFR related to the cooling layout under investigation.

The adopted procedure is sketched in figure 4.18: *Therm1D* was used to set up the cooling fluid network of the test rig, including both the slot and the effusion system; the material properties of the test plate were set equal to the real metal alloy of NEWAC combustor prototype (instead of PVC) to more realistically model the heat conduction through the

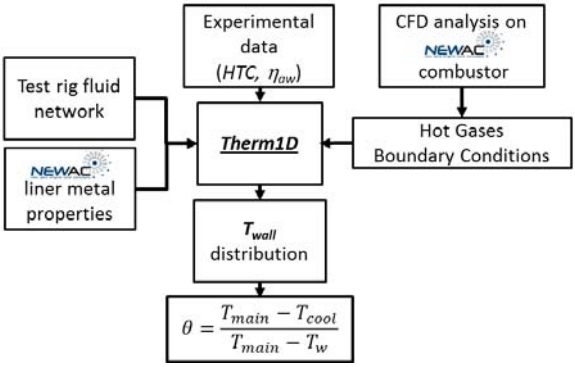

Figure 4.18: Procedure to evaluate θ

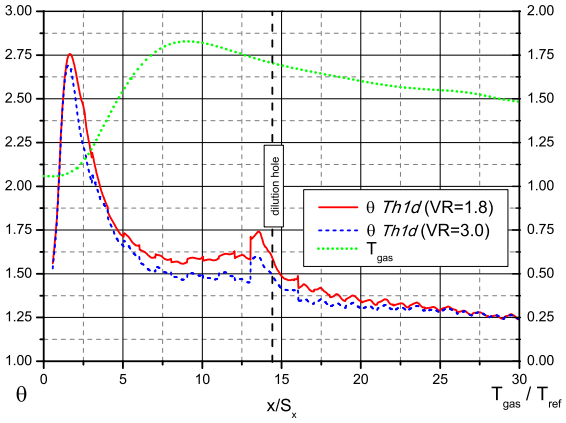

Figure 4.19: Trends of θ and T_{gas} along the liner

plate itself. Moreover, hot gas boundary conditions, taken from previous CFD analysis on the combustor, were imposed in order to to simulate the behaviour of a realistic combustor diffusion flame and, consequently, to estimate realistic the heat loads [66]. As an example, figure 4.19 shows the distribution of mainstream gas temperature inside the core of the combustor (temperatures are normalized with a reference value): it is possible to identify the position of the flame front, which causes the temperature rise downstream the second row. Coolant side inlet pressure was varied in order to set the desired averaged BR-VR through the effusion holes and reproduce the experimental test matrix, while inlet coolant temperature and outlet pressure were kept constant. Instead of using correlation to estimate adiabatic effectiveness and HTC distributions along the plate, experimental data were imposed as boundary conditions: in order to take into account the effects of density ratio due to the temperature difference between coolant and mainstream in the combustor, data were taken only from CO_2 tests, and only from tests with both effusion and slot cooling system.

This procedure allowed to simulate the behaviour of the cooling system under realistic operating condition and to finally estimate the dis-

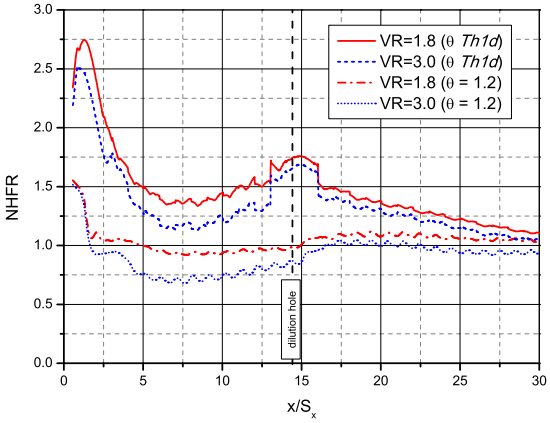

Figure 4.20: Spanwise averaged NHFR distribution

tribution of NHFR along the liner: in fact, each run provided the liner surface temperature distributions (T_w) and the local temperature of the coolant coming out from each effusion row (T_{cool}), including its heating through the hole due to the heat removal by heat sink effect.

Figure 4.19 shows trends of the θ parameter for cases BR_{eff}=3 (VR_{eff} ≈1.8) and VR_{eff} = 3. It is possible to observe how θ varies along the liner as a consequence of both a non uniform mainstream temperature distribution, and of the resulting T_{cool} and T_w; furthermore, it can be noticed that an increase in VR_{eff} leads to a slight decrease of θ.

Figure 4.20 displays trends of NHFR for the two previous test points: results evaluated through *Therm1D* are compared with those estimated by imposing a constant value of $\theta = 1.2$. As a consequence of the θ behaviour, NHFR calculated considering the heat sink effect is much higher than the case with a constant value of θ (the averaged value is almost 30% higher). Obviously *Therm1D* results are highly affected by the hot gases imposed boundary conditions (e.g. the drop after the 2^{th} row is related to the gas temperature rise which represents the flame front), but what is important to highlight is the influence of effusion velocity ratio on NHFR: even if NHFR linearly decreases with VR_{eff}, figure 4.20 points

out that the cooling system always brings to a reduction of the heating flux towards the liner (NHFR> 0).

Despite previous considerations, NHFR is not properly representative for an effusion cooling system since its definition (eq. 2.8) does not explicitly take into account the heat sink effect, which instead plays an important role in this type of cooling technique. To overcome this aspect and give a complete description of the cooling performance of the system, wall temperatures estimated through *Therm1D* were finally employed to calculate also the overall effectiveness of the test plate in real engine conditions. As explained in chapter 2, this further parameter indicates the overall cooling capability of a cooling system (eq. 2.10).

Results estimated through the thermal procedure are shown in figure 4.21: outcomes highlight that, except for very low values of velocity ratio, η_{ov} remains high and almost constant for a wide range of operative conditions. Even if results do not take into account the effects of turbulence, whose level is rather lower than a real combustor, they give useful indications for the designer: in fact, this study points out that the combined effusion and slot system is very effective and robust from a cooling

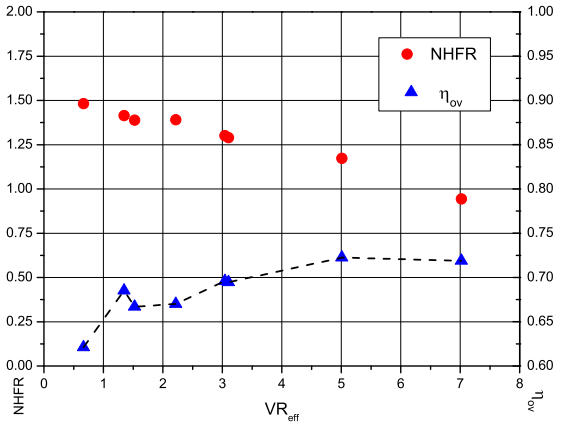

Figure 4.21: Averaged NHFR and η_{ov} vs VR_{eff}

point of view for a wide range of operative conditions. As a consequence, this flexibility of the system allows, during the design phase, to focus its optimization taking into account other requirements, like combustion issues, aeroacoustic or simply off-design working conditions.

4.7 Concluding Remarks

This chapter presented an extensive analysis aimed at deepening the knowledge on the effusion cooling technology and its integration in a typical modern combustor cooling layout. The purpose of the study was to test the system under a wide range of conditions, in order to point out the effects of several operating parameters and to provide useful information for the design of an effusion system.

An experimental study was carried out on a simplified model which represented a real liner cooling arrangement, made up of an effusion cooling plate, a dilution hole and a slot for the starter film cooling. The aim of the survey was to fulfil a lack of experimental data available in literature concerning the effects on the effusion cooling performance of:

- coolant-to-mainstream density ratio;
- high values of blowing ratio, i.e. high penetration of the cooling jets;
- interaction among the effusion system and other typical features of a combustor liner, such as the dilution hole and the slot cooling.

Measurements were performed by means of Thermochromic Liquid Crystals and were aimed at estimating the heat transfer coefficient and the adiabatic effectiveness.

As far as the HTC measurements are concerned, tests pointed out some typical characteristics of the effusion system, such as the peak of heat transfer immediately downstream the exit of the holes [34]; in addition, results showed that the interaction with the slot cooling flow inhibits the heat transfer, especially in the first rows. Concerning the effects of different operating parameters, results indicated that tests carried out

imposing a constant value of VR_{eff}, but with different DR, lead to the same HTC: this evidence suggests that the velocity ratio is the driving parameters of the phenomenon. Finally, as a general results, experiments showed a linear growth of HTC with velocity ratio.

Focusing on the adiabatic effectiveness, results indicated that the η_{aw} of the effusion holes increases row by row due to superposition effects; however, an effective protection of the first part of the liner is achieved only when the effusion is coupled with the slot film cooling. The presence of the dilution hole deeply affects the film cooling distribution: coolant from the surrounding holes and from the downstream rows are dragged by the wake generated of the dilution jet, a phenomenon which alters the progressive growth of effusion adiabatic effectiveness. When the slot cooling flow is active, the interaction with the dilution jet slightly worsen the η_{aw}; however, the film cooling protection achieved by the combined slot-effusion system is very effective, both for high penetration of effusion jets and for different value of density ratio.

The wide database collected with the experimental campaign was exploited to deepen the analysis of the performance of the cooling arrangement by means of the 1D fluid-thermal code *Therm1D*. Initially, data were used to validate the available correlations for effusion cooling; afterwards, experimental results were used to simulate the behaviour of the system under real engine operating conditions: representative thermal loads were applied on the gas side and overall cooling performance parameters were evaluated. This analysis, not feasible in a low temperature facility, allowed to estimate the Net Flux Heat Reduction and the overall effectiveness; results confirmed that the effusion-slot layout guarantee a very effective cooling of the liner for a wide range of engine working conditions.

Concluding, the behaviour of the effusion system integrated with other features of a modern combustor chamber was widely characterized and it reliability and it efficacy were proven; moreover, this study

drawn guidelines for the design of effusion cooling systems and it allowed to increase the fidelity on this innovative technology. However, it is important to underline that the results are obtained under homogeneous mainstream conditions and without taking into account the effects of turbulence, whose level is rather lower than a real combustor. In fact, recent studies (for instance, see [93]) showed that the presence of an engine-representative swirled flow deeply affects the film cooling distribution, and hence significantly bias the performance of the system. Nevertheless, the outcomes of this work provided some general information on the effusion cooling behaviour, which are valid independently from the specific geometry of the mainflow injection device.

Once assessed the efficiency of this cooling technique, the attention will be focused on the entire combustion chamber and, more specifically, in the mixing process between the mainstream and coolant and the generation of hot streaks. In fact, in addition to keep the liner temperature below the critical threshold, an other performance parameter to control and optimize during the design process is the $OTDF$ (Outlet Temperature Distribution Factor), which is fundamental in view of the thermal design of the high pressure turbine. In order to have an engine-representative test, the TRL of the investigation will be raised, and an effusion cooling system will be integrated in a real lean combustor geometry test rig.

Before going into details of this analysis, the next chapter will provide an introduction to the hot streak characteristics, as well as an overview of the test rig available in literature dedicated to their study.

Chapter 5

Literature Review on Aerothermal Investigations on Combustor-Turbine Interaction

"What is past is prologue."
W. Shakespeare, The Tempest

The importance of understanding the impact of hot-streaks, and temperature distortion in general, on the high pressure turbine is a critical issue for the aero-thermal design of the first stage vanes and blades. At the status of the art, there is an lack of reliable experimental data both from operating combustors and from rotating turbine experiments in which a combustor representative inlet temperature profile has accurately been simulated; consequently, turbines are still generally designed starting from an uniform inlet temperature profile, which is often the predicted peak gas temperature. Therefore, there is increasing interest in experiments that attempt to address this deficiency in view of deepening the knowledge of the combustor-turbine interactions and updating the design procedures.

Open literature reports that there are only six main rotating turbine

test facilities for the study of the effects on turbine life, heat transfer, aerodynamics, blade forcing, efficiency, etc., that implements also a combustor (hot-streak) simulators. Moreover, according to the review of Povey and Qureshi [12], three methods are available to simulate the temperature profile: (a) the use of foreign gases to simulate the density gradients that arise due to temperature differences, (b) the use of heat exchanger to generate temperature distortions, and, similarly, (c) the use of cold gas injections to simulate non-homogeneous temperature distributions.

After a brief characterization of the temperature distortions at the combustor exit, this chapter will present a review of the main rotating test facilities described in literature to study the hot streak transport though the turbine; moreover, it will provide a short summary of the main outcomes of previous studies. In the final part of the chapter, the context of FACTOR research project will be introduced, as well as an overview of the main innovations of its rotating test rig for experimental investigations on the combustor-turbine interaction phenomena.

5.1 Combustor Exit Non-Uniformities

The flow field at combustor exit is by nature (i) unsteady because of the turbulent combustion, mixing processes, etc., and (ii) non-uniform on the circumferential distance because of the discrete radial position of fuel injectors and dilution holes, and on the radial direction due to film cooling and core flow mixing. This results in highly three-dimensional unsteady fields at the combustor-turbine interface, both in terms of temperature and pressure. Regarding combustion processes, aeronautics standards require that absolutely no combustion occurs in the turbine, so the mixture is reasonably considered as non-reactive in the turbine [4, 94].

As an example, the measured combustor exit temperature field of a modern Rolls-Royce engine is shown in figure 5.1 [12]: the hot streak issuing from the burner are clearly visible in the central region (apparently

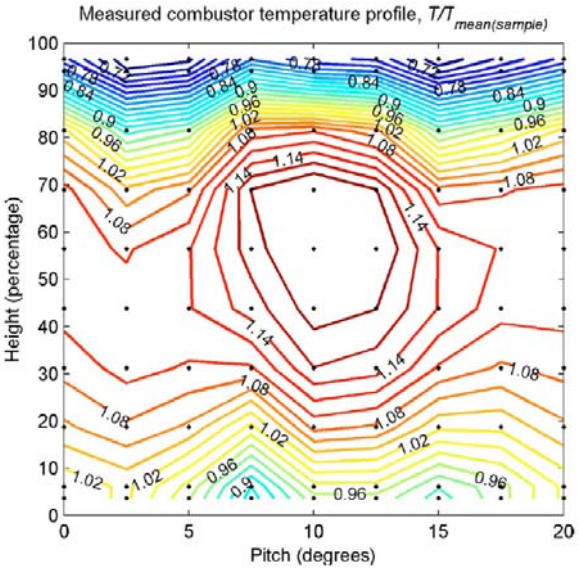

Figure 5.1: Combustor exit temperature field measured across one burner pitch of a modern RR engine operating at an extreme point [12]

centred on the NGV passage). The non-uniformity is definitely more pronounced on the radial direction (blade span) than on the circumferential axis (blade pitch).

Turbine inlet temperature distortions (ITD) can cause changes in the flow field in both the high pressure HP nozzle (NGV) and rotor that affect the aerodynamics, heat transfer, loading, life, secondary loss, and, therefore, efficiency. As demonstrated by Povey et al. [95], the changes in local temperature can cause very large changes in heat transfer rate on both the HP vane and endwall, even when the heat transfer coefficient is effectively unaltered. In addiction, as shown both experimentally and theoretically by Hermanson and Thole [96], a distortion of the inlet total pressure profile causes a strong alteration of the secondary flow development in the vane, leading to strong modification of the flow field and, consequently, of the related heat transfer coefficient. Finally, when both pressure and temperature distortion are present, one would expect corresponding changes in both the local heat transfer coefficient and in local driving gas temperature.

In the HP rotor the effect of ITD is generally more significant: even with uniform HP vane inlet total pressure, in the rotor relative frame ITD causes changes in flow angle, total pressure, total temperature, and Mach number. These modifications cause the well-known temperature segregation effect, which generally causes hot flow to accumulate on the rotor pressure surface and sometimes also a migration of hot flow toward the rotor tip. Secondary flows are therefore induced by ITD, and the associated changes in the heat transfer coefficient and local driving temperature can be significant. A HP rotor designed for a nominally uniform inlet temperature may well prove to be grossly off design when subject to even moderate ITD [12]. The same effects can be observed in the downstream intermediate pressure, or low pressure vane [97] although naturally here the temperature variations will be significantly attenuated.

Despite the significant number of publications, recently reviewed by Povey et al. [95], that consider the effects of ITD by means of experiments

or numerical calculations, it is difficult to draw general conclusions that may be applied to turbine design. In part, this is because of the complex nature of a flow field in which a number of interrelated phenomena are essentially competing, some of which may be more or less pronounced for a given turbine; in part, it is due to the lack of reliable data from real combustor or rotating turbine experiments on non-uniform turbine inlet profile; finally, the intensity of simulated profiles differs up to an order of magnitude between some tests, which indicates that there is no standard test-case profile.

Open literature reports that several rotating test facilities were developed in the last 30 years aimed at investigating the impact of *ITD* on the turbine: a review of the main hot streaks rigs is proposed, along with the available instrumentation used for each experiments. This will allow an easier comparison with the FACTOR project innovative test rig, which is designed to set a reference test case for the topic discussed above.

5.1.1 Temperature Distortion Characterisation

Quite a lot of different factors are used to quantify the degree of non-uniformity of the temperature field at the turbine inlet. Povey and Qureshi [12] propose the definition the *temperature distribution (or distortion) factor TDF*. The overall TDF (OTDF[1]) measures the divergence of the hottest point in the flow (hot streak) to the mean temperature; it is therefore a single value, defined as:

$$OTDF = \frac{T_{40,max} - \overline{T}_{40}}{\overline{T}_{40} - \overline{T}_{30}} \tag{5.1}$$

According to the standard convention adopted in literature, subscripts *30* and *40* are referred respectively to combustor inlet and outlet sections.

Similarly, the radial TDF (RTDF[2]) measures the non-uniformity of

[1] Or *pattern factor in the USA.*
[2] Or *profile factor in the USA.*

the flow field averaged on the circumferential direction:

$$RTDF = \frac{Max(\langle T_{40}(r)\rangle_\theta) - \overline{T}_{40}}{\overline{T}_{40} - \overline{T}_{30}} \tag{5.2}$$

$\overline{T}_{30}$ and $\overline{T}_{40}$ respectively refer to the mean temperature (usually area-weighted or mass-weighted) at combustor inlet and outlet. $Max(\langle T_{40}(r)\rangle_\theta)$ is the maximum value of the circumferentially-averaged temperature.

When a more local definition of the profile is required, one may define the *local* OTDF (2-D field) and *local* RTDF (1-D radial profile), [12]:

$$LOTDF(r,\theta) = \frac{T_{40}(r,\theta) - \overline{T}_{40}}{\overline{T}_{40} - \overline{T}_{30}} \tag{5.3}$$

$$LRTDF(r) = \frac{\langle T_{40}(r)\rangle_\theta - \overline{T}_{40}}{\overline{T}_{40} - \overline{T}_{30}} \tag{5.4}$$

In the context of non-reactive test rigs, these definitions are not easy to use. Therefore, alternate definitions of eq. (5.3) and eq. (5.4) are preferentially used to describe the flow in plane 40 only [12]:

$$LOTDF'(r,\theta) = \frac{T_{40}(r,\theta)}{\overline{T}_{40}} \tag{5.5}$$

$$LRTDF'(r) = \frac{\langle T_{40}(r)\rangle_\theta}{\overline{T}_{40}} \tag{5.6}$$

For example, fig.5.1 shows the $LOTDF' = T/\overline{T}_{40}$ measured in a Rolls Royce engine, ranging from 0.68 to 1.21.

As mentioned in § 1.3, the radial and circumferential variations are strongly dependent on the degree of swirl of the mainflow, the presence/absence of dilution jets and also on the point in the engine cycle. As a consequence, the modifications in the combustion chamber layout switching from RQL to Lean-Burn combustors deeply alter the aerothermal flow field approaching the HP turbine. Mainly, two aspects are responsible of the major differences between the *ITD* of two combustor architectures:

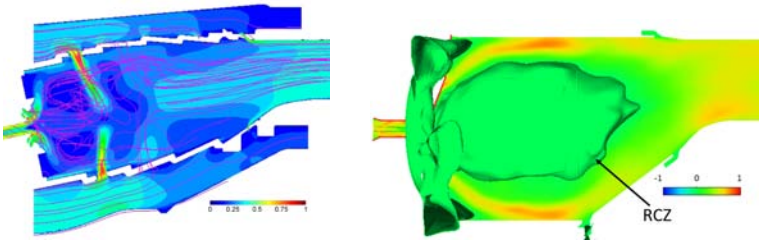

(a) RQL combustor [98] (b) Lean-Burn combustor [99]

Figure 5.2: Evolution of the flow field in the combustor chamber: comparison between RQL and Lean-Burn arrangements

- *Dilution holes*: the strong mixing between the mainstream and the dilution jets in RQL combustors smooth the velocity and thermal gradients before the outlet section, resulting in quite flat profiles at the turbine inlet. An example of the impact of the dilution jets on the combustor flow field in depicted in figure figure 5.2(a), which shown the CFD prediction obtained by Cha et al. [98] of normalized velocity magnitude for a RQL combustor. On the other hand, the swirling mainflow in Lean-Burn combustors reaches plane 40 almost undisturbed, except for the presence of the central recirculation zone generated by the vortex breakdown of the jets coming from the swirler. Therefore, the tangential momentum of the mainstream, and the resulting swirl angle distribution, is definitely higher at the combustor exit with respect to RQL. As an example, figure 5.2(b) shows the axial velocity field and the recirculation zone found by Wankhede et al. [99] in their numerical analysis on a swirl-stabilized lean-burn combustor (liner cooling flows are absent). The behaviour of the flow field directly impacts the temperature distribution in plane 40, whose profiles are much more marked at mid-radius for a chamber without dilution holes.

- *Liner cooling flows*: temperature distortion in Lean Burn combustor are much more emphasized not only because of the hotter cen-

tral core of non-diluted burning gases, but also due to the colder flows close to the liners: in fact, cooling arrangements such as effusion systems generate a layer of coolant that increases row by row along the chamber without a significant mixing with the mainflow. Therefore, the thick inner and outer coolant layers at the combustor exit enhance the temperature difference between the walls and the center of the gas flow path, enforcing the non-uniformities at the turbine inlet.

To clarify the impact of then dilution jets on the thermal field at the combustor exit, an example of real temperature profiles (using eq. 5.6) measured in aero-engines are shown in fig. 5.3: plots, issued from the work of Goebel et al. [100], shows the effect of the swirl degree and dilution flows on the radial temperature profile of a small scale combustor. The degree of non-uniformity of the temperature field is clearly visible in the plots, ranging from very stretched profiles for high swirl-no dilution and both the low swirl cases, to pretty flat profiles resulting from a signifying

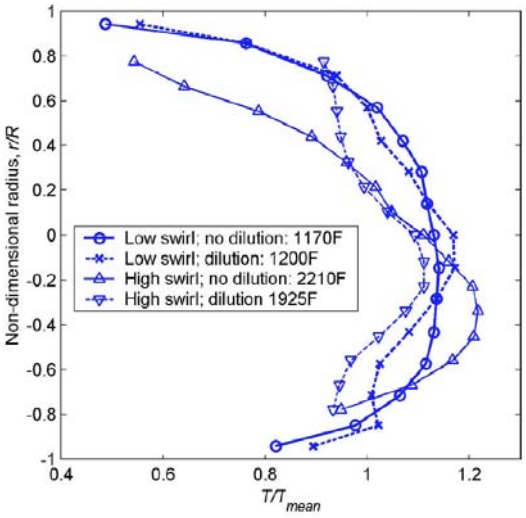

Figure 5.3: Measured combustor radial exit temperature profiles [12]

intense mixing between high swirling flow and dilution jets.

5.2 Review of the Hot Streak Research Facilities

Povey and Qureshi [12] recently have made an exhaustive review of the hot streak simulators for turbine testing. Their work, along with further literature reviews (e.g. Dorney *et al.* [101]) shows that no less than ten rigs devoted to hot streak study have been created from the 80's. The majority of the known and reported facilities are located in the USA. It's only recently that interesting facilities were created in Europe such as the ILPF (UK), and the one under development within the FACTOR project.

The very first facilities, built in the early 80's, were designed for proof-of-concept investigations, [12]. The three rigs that will be presented here are:

The Warm Core Turbine Test Facility at the Nasa Lewis Research Center, Cleveland, Ohio (1983), shown in figure 5.4. It has been described by Stabe, Whitney, and Moffitt in [102, 103]. The experimental results were also recently used a basis for numerical studies by Dorney and Gundy-Burlet [104].

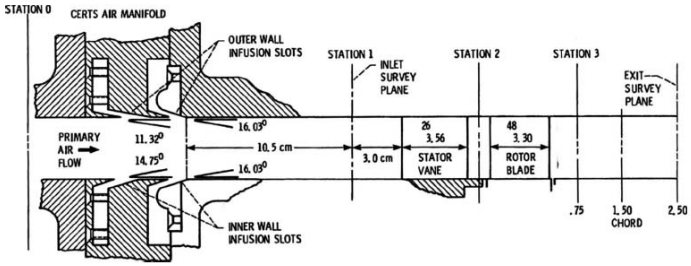

Figure 5.4: Flow path through the Warm Core Turbine Test Facility [102]

The Large Scale Rotating Rig at the United technologies Research

Center, East Hartford (1985). It was mainly studied by Joslyn and Dring [105, 106, 107], Butler *et al* [108] and Roback and Dring [109, 110].

The Rotating Blow-Down Facility at the Massachusetts Institute of Technology (MIT), Cambridge (1989).The rig was developed by Shang for his MSc thesis [111]. Shang *et al* reported experimental results [112], and CFD simulations (using Euler equations) based on the rig configuration [113].

The first results obtained with these facilities allowed for a better understanding of the flow and heat transfer dynamics in HP turbines. More complex and heavily instrumented rigs were then designed to get a deep insight on hot streak interaction with turbines:

The Isentropic Light Piston Facility at QinetiQ, Hamphsire, UK in 2002 (figure 5.5). This test rig comprised either one turbine stage or one stage and a half. The rig is described by Hildith *et al* [115] and Chana *et al* [116]; and test results can be found in Povey *et al* [95, 97]. As part of the Brite-Euram Turbine Aerothermal External Flows programme (TATEF II), the facility was recently upgraded

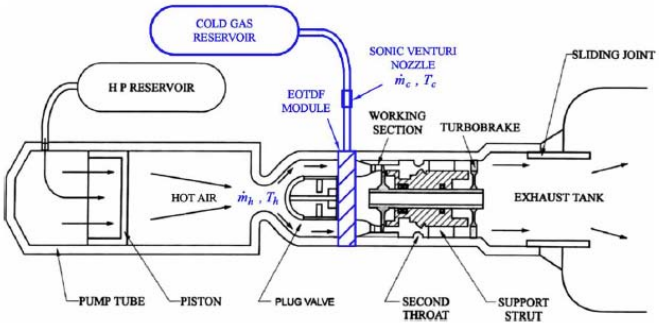

Figure 5.5: Sketch of QinetiQ Enhanced Isentropic Light Piston Facility rig [114]

[12, 114] to get a strong, well-defined temperature profile and to study hot-streak-vanes clocking effect. Studies on this new version can be found in Salvadori et al. [117] and Qureshi *et al* [118].

The Turbine Research Facility at the Air Force Research Laboratory, Wright-Patterson Air Force Base, Dayton, (2004), depicted in figure 5.6. It is a fully controllable inlet profile generator, both in terms of pressure and temperature, which geometry mimics a typical gas turbine combustor. It was studied by Barringer, Thole and Polanka [119, 120, 121] and described in details by Barringer *et al* [122].

The Turbine Test Facility at Ohio State University (2004). This heavily instrumented rig (more than 800 measurements) features a realistic recent turbine stage with cooled vane, rotor blade and purge flows. It was developed by Haldeman, Dunn and Mathison [123, 124, 125, 126, 127]. The most complete description of the rig can be found in Mathison *et al* [125], and Haldeman *et al* [128].

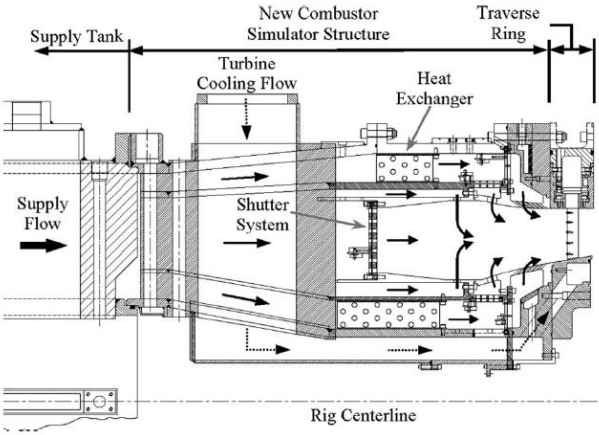

Figure 5.6: Sketch of the combustor simulator installed at the Turbine Research Facility [122]

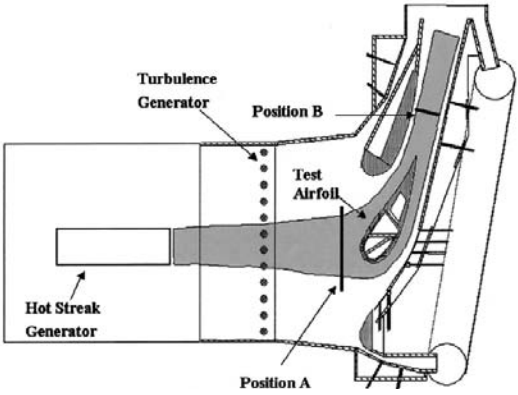

Figure 5.7: Overview of the University of Texas at Austin hot-streak rig [129]

The University of Texas at Austin published in 2004 the results of their experiments conducted by Jenkins and Bogard [129, 130]. Their work aimed at reducing the hot spot strength by adequate positioning of the hot streak and use of film cooling. Therefore, this rig is smaller than the previous ones: it only features a hot streak generator and three realistic film cooled HP *NGV*, as sketched in figure 5.7.

European project FACTOR is the latest project on the topic: this rig, still under development, will be installed at DLR Gottingen in Germany. A specific section will be dedicated to this project and its test facility in § 5.5.

The main characteristics of each test facility previously mentioned are summarized in table 5.1.

Table 5.1: Summary of the main features of the major hot streak rigs [131]

Facility	**Rig elements**	**Fluid and mainstream test conditions**	**Hot streak (HS) chics**	**Temperature range at vane inlet (design point)**
Warm Core Turbine Test Facility (Nasa Lewis Research Center) - 1983	Scale $\times 0.77$ subsonic HP turbine stage (26 NGV and 48 rotor blades) Cumulated run time 200hrs	Air and Natural gas $P \simeq 3.1bar$; $\overline{T} = 672K$	Annular can combustor and cooling air from 4 infusion slots. Circular or elliptical HS. HS/vane count 1:1	$\frac{T_{max}}{\overline{T}} = 1.05$ $\frac{T_{min}}{\overline{T}} = 0.875$
Large Scale Rotating Rig (United technologies Research Center) - 1989	Scale $\times 1.0$ low speed 1.5 turbine stage with TE cooling	Air and $C0_2$ (HS tracking) $\simeq$ ambient P, T	HS simulated by density ratio (isoP flow). Hot streak or (*cold streak* $\star$).	$\frac{T_{max}}{\overline{T}} = \frac{\overline{p}}{\rho_{max}} = 2.0$ *(1.0* $\star$*)* $\frac{T_{min}}{\overline{T}} = \frac{\overline{p}}{\rho_{min}} = 1.0$ *(0.67* $\star$*)*
Rotating Blow-Down Facility (MIT) - 1989	Scale $\times 0.75$ RR transonic core HP turbine stage (36 vanes, 61 rotor blades) Blow-down 300ms	Argon-freon-12	Tube-bundle heat-exchanger to generate four HS. HS/vane count 1:3	$\frac{T_{max}}{\overline{T}} = 1.04$ 12 acl upstream $\frac{T_{min}}{\overline{T}} = 0.88$
Isentropic Light Piston Facility (QinetiQ) - 2002 *(Enhanced version in 2008* $\triangle$*)*	Scale $\times 1.0$ HP turbine stage and 1.5 stage (32 HP vanes, 60 rotor blades, 26 LP vanes) Blow-down $500ms$	Air $P = 4.6bar$; $\overline{T} = 444K$	Air compressed and heated by piston for hot streak; cooling air (ambient T) introduced from 32 annular slots. HS/vane count 1:1	$\frac{T_{max}}{\overline{T}} = 1.07$ *(1.12* $\triangle$*)* $\frac{T_{min}}{\overline{T}} = 0.91$ *(0.72* $\triangle$*)*
Turbine Research Facility (Air Force Research Lab) - 2004	Scale $\times 1.0$ Turbine stage Run time $1 - 5s$	Nitrogen $P = 2.1 - 5.52bar$	Heated and pressurized supply tank feeding mainstream and cooled stream (primary and secondary dilution holes + film cooling). Lots of HS shapes are possible. HS/vane count 1:1	$Max\left(\frac{T_{max} - T_{min}}{\overline{T}}\right) = 0.1$ $Min\left(\frac{T_{max} - T_{min}}{\overline{T}}\right) = 0.01$
Turbine Test Facility (Ohio State University) - 2004	Scale $\times 1.0$ 1.5 HP Turbine stage (Cooled vane/uncooled rotor with purge flow/LP vane) Run time $\simeq 10ms$	Air	Controllable heater rods inserted in Inconel honeycomb cells to generate HS. HS/vane count 1:1	$\frac{T_{max}}{\overline{T}} = 1.21$ $\frac{T_{min}}{\overline{T}} = 0.75$
University of Texas at Austin - 2004	Three scaled-up film cooled NGVs Low speed wind tunnel	Air	Electrical resistance heaters in a metal duct, surrounded by ambient temperature mainstream ($T_\infty = 300K$). Cryogenic NGV cooling ($187K$). HS/vane count 1:3	$\frac{T_{max}}{T_\infty} = 1.1 - 1.25$
FACTOR - 2014	Scale $\times 1.0$ 1.5 HP Turbine stage (40 film cooled NGVs, 60 rotor blades with purge flow and 20 LP struts) Run time hrs	Air $P \simeq P_{atm}$; $\overline{T} = 450K$	Combustor simulator with axial swirler for hot air stream and cold air from film cooling. HS/vane count 1:2 (LE or mid-pitch centered)	$\frac{T_{max}}{\overline{T}} = 1.1$ $\frac{T_{min}}{\overline{T}} = 0.75$

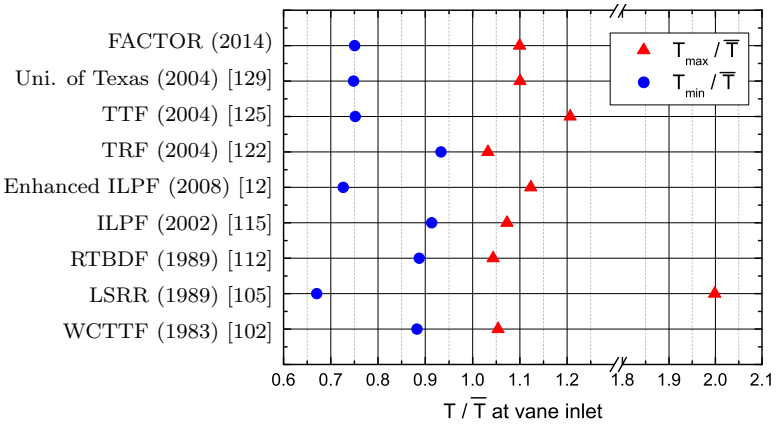

Figure 5.8: Maximum and minimum temperature relative to the mean temperature at vane inlet (or upstream when data are not available)

The maximum and minimum temperature ratio at the vane inlet from the last column of table 5.1 are plotted in fig. 5.8 for all the facilities. Note that the relative position of the measurement plane with the vane LE is not always given and vary between all the cases.

The main instrumentation devices installed on each rig are summarized in table 5.2. The measurements focused on the turbine stage, i.e. that the monitoring probes (rig feeding lines, exhaust, heat exchangers etc.) are not indicated here. Finally note that the instrumentation devices were not necessarily installed all together during a measurement campaign. It results from a stack-up of different tests performed on each facility.

Table 5.2: Summary of the overall instrumentation of the major hot streak rigs [131]

Facility	**HP NGV**		**HP rotor**		**LP vane**
	Inlet	Vane	Inlet	Blade	
Warm Core Turbine Test Facility (Nasa Lewis Research Center) - 1983	Five P_s taps on inner/outer walls P_t, T_t radial rack at inlet (19 radial points)	Seventeen P_s tapings on inner/outer walls	T_t radial rack 0.75 and 1.5 chord downstream TE	Three touch probe clearance measurement devices Ten P_s tapings over vane span	
Large Scale Rotating Rig (United technologies Research Center) - 1989	T_t, P_t and $[CO_2]$ radial rack		$[CO_2]$ radial rack at rotor inlet and outlet.	154 $[CO_2]$ sampling sites on vane surface, and 28 on hub endwall.	
Rotating Blow-Down Facility (MIT) - 1989	P_t profile 12 acl upstream LE			Surface-bonded heat flux gauges.	
Enhanced Isentropic Light Piston Facility (QinetiQ BRITE project) - 2009	T_t, P_t rack 9 radial $\times$ 19 circumferential positions = 171 points	Three P_s tapings over span Vane surface and endwall heat flux (thin film platinium resistance gauges)			
Turbine Research Facility (Air Force Research Lab) - 2004	Three T_t rack (3/7/9 thermocouples $\varnothing 25\mu m$) and two P_t rack (9/9 pressure transducers) used at vane inlet and outlet. HWA (two hot-film probes)	Two P_s transducers over span Three vane surface and seven endwall heat transfer gauges (Oxford technique)			
Turbine Test Facility (Ohio State University) - 2004	One P_t, two T_t and three P_s racks used at eight circumferential positions	140 double-sided KApton heat-flux gauges	Seven T_t thermocouples at blade LE ($\varnothing 1.27mm$) Purge flow T_t (butt-welded thermocouple), P_t (Kulite pressure transducer) and heat transfer (Pyrex gauge)	Flush-mounted Pyrex heat flux gauges on vane surface (> 60), blade hub platform (12) and blade tip Unshrouded thermocouple on platform and angel wing ($\varnothing 25\mu mm$)	Same P_t, T_t racks as NGV inlet
University of Texas at Austin - 2004	Six E-type thermocouple on radial rack and Twenty two K-type thermocouple on circumferential rack at mid-span	Measurements at 0.21 chord upstream LE, 0.32 chord downstream TE and in vane passage			

5.3 Review of Past Studies on the Combustor-Turbine Interaction

Many numerical and experimental studies deal with the hot streaks an with the interaction between the HP turbine and the temperature and pressure distortions from the combustor. However, it is important to underline that these works are mainly conceived for RQL architectures, and therefore only some general results can be extended to lean combustion systems.

An exhaustive review is behind the aim of this section; in this context, only a brief overview of literature studies concerning the influence of the turbine on the flow field inside the combustor is provided. However, for sake of completeness, a more detailed literature review on the effects of hot streaks on the first stage of the high pressure turbine can be found in Appendix B.

5.4 Influence of Turbine Flow on the Combustor

Historically, the combustor and turbine communities are two distinct entities. As described in the previous section 5.2, the influence of combustor exit conditions on the turbine has been numerically and experimentally investigated since the 80's, whereas the influence of the HP NGV on the combustor flowfield is a very recent field of research. So-far, only numerical investigations were performed on this topic. Nevertheless, even CFD simulations on this interface are challenging because of the very different nature of the flow field in the combustor (unsteady mixing, high swirl, combustion processes, low-Mach flow) and within the turbine (highly compressible, near-wall and boundary layer flow).

Most of the simulations used during the combustor design process use a uniform static pressure at outlet. It is however inaccurate because of the potential effect induced by the NGV. The pressure field (and thus velocity field) in the combustor exit region are modified by presence of the turbine.

One of the only available simulation of the NGV action on the combustor flowfield was performed by Roux et al. [132]. They run reactive LES simulations (AVBP solver) on a periodic sector of a real annular gas turbine, including (or not) two NGVs. Results indicate significant changes of the flow field especially in the rear part of the combustor. The primary zone is mostly unchanged. As shown in figure 5.9 the temperature distorsion at turbine inlet is significantly changed, with local difference up to $+130K$ with NGV, near the hub. The major difference results in the unsteadiness of the flow field: the velocity rms values are multiplied by 5 to 10 with the NGV, in the rear part of the combustor. The rms temperature field shown in the bottom part of figure 5.9 indicates the flow perturbation induced by the NGV: changing from a very uniform field (no NGV) to more coherent structures (with NGV).

Klapdor [94, 133] performed steady-state simulations of the Rolls-Royce engine BR710 with and without NGV (2 vanes): deviations up to $\pm 30\%$ on the velocity magnitude were found at 25% axial chord length

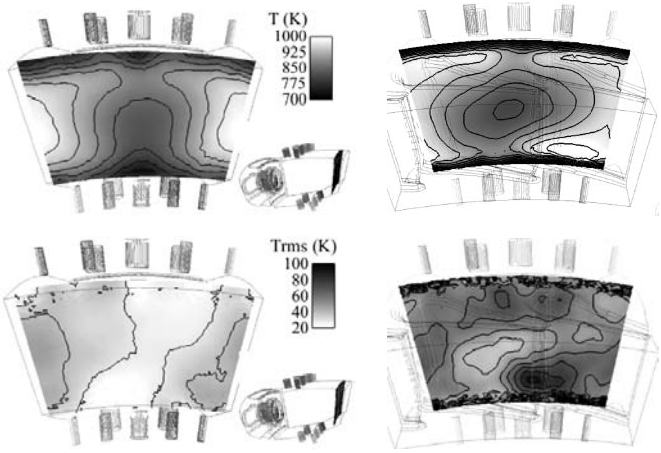

Figure 5.9: CFD Mean temperature field (top) and rms temperature (bottom) at combustor exit, with NGV (left) and without NGV (right) [132]

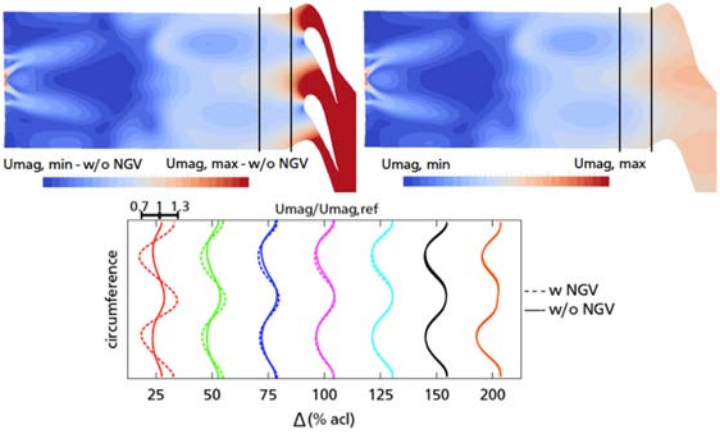

Figure 5.10: Velocity magnitude field at midpsan with (left) and without NGV (right), and velocity profiles at different acl, from CFD [94]

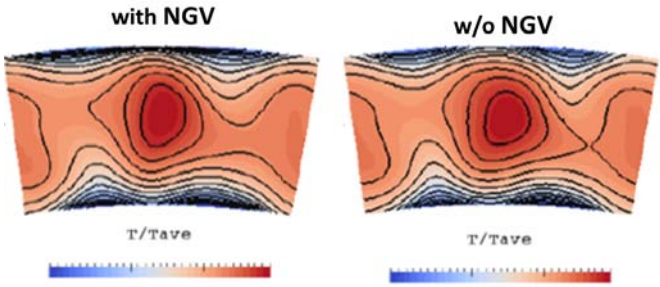

Figure 5.11: Temperature field at 25% acl upstream the LE, with and without NGV, from CFD [94]

(*acl*) upstream the vane LE, as illustrated in fig. 5.10. The potential effect of the NGV of course lead to higher velocities in front of the vane passage, and therefore less mixing compared with the no-NGV case. However, above 75% *acl* distance upstream the LE, no difference was visible.

The temperature fields upstream the NGV were found to be very sim-

ilar as shown in fig. 5.11: the OTDF and LRTDF are almost identical for the two cases. This result is in contradiction with the strong differences highlighted by Roux *et al.* [132], possibly because of the mixing/smoothing created by RANS models, and its inability of capturing unsteady phenomena.

5.5 FACTOR Project Overview

At the status of the art, there is currently no experimental test infrastructure in Europe dedicated to advanced measurements of a turbine operated together with a realistic lean burn combustor simulator. Many European projects have investigated combustor technologies to improve combustor technologies, cooling, emissions and exit temperature profiles (e.g. INTELLECT and NEWAC) and others addressed to understand the behaviour of hot flow structures in the HP turbine (e.g. TATEF2 and AITEB2). These projects gave a better understanding of the characteristic phenomena of combustors and turbines, and allowing to improve their design and development.

However industrial experience demonstrates that the separate optimisation of the two modules - combustor and turbine - does not necessarily ensure that the system in which they are embedded will also be optimum. Therefore, the understanding of their mutual interaction is fundamental, especially for the development of new combustion technologies (e.g. lean burn combustion) where, in addition, there is also a lack of industrial experience.

The tight link between the combustor and the turbine in an engine is driving engine manufacturers to put a strong effort to master this interface: extremely hot gases, variable boundary layers, turbulence effects and inherent unsteadiness are some of the phenomena making this region of the engine a difficult interface. Furthermore, this interface still requires strong improvements as gas turbine designers are lacking the experimental data needed to optimise the design.

Within this context, a new continuous flow facility hosted by DLR

(Gottingen, Germany) is under development within the European project FACTOR[3] (*Full Aerothermal Combustor-Turbine interactiOn Research*). The research center will host a modern aero-engine combustor simulator and a 1.5 high pressure turbine stage, operating at realistic Reynolds and Mach numbers. The main objective of the project is to set up an experimental test infrastructure to perform measurements by means of the most advanced techniques; measurements techniques will be adapted to FACTOR rig specific requirements and they will be combined to ensure that an all-encompassing and comprehensive experimental database will be gathered, respecting exactly the same boundary conditions. The wide database obtained with different techniques will be finalized to set up boundary conditions and make comparison with numerical simulations performed with conventional and advanced CFD techniques: in view of a designing more efficient and low cost engines, this effort will deepen the knowledge of the combustor-HP turbine interaction and moreover it will draw the guidelines on how to numerically model this interaction.

5.5.1 FACTOR Test Facility

To get a detailed understanding of the combustor-HP turbine interactions, an experimental test infrastructure made up of a full annular modern aero-engine combustor simulator and a 1.5 high pressure turbine stage will be set up, operating at realistic Reynolds and Mach numbers: the combustor simulator, fed by hot and cold air flows, will supply realistic flow field to the downstream HP stage and the following LP strut, enabling experimentalists to explore the aerodynamic and thermal interactions between combustor and turbine. A sketch of the test rig is depicted in figure 5.12.

Each module of the continuous turbine test rig is designed following the state-of-the-art major trend of development for aeroengine gas turbines:

[3] *http://www.factor-fp7.eu/*

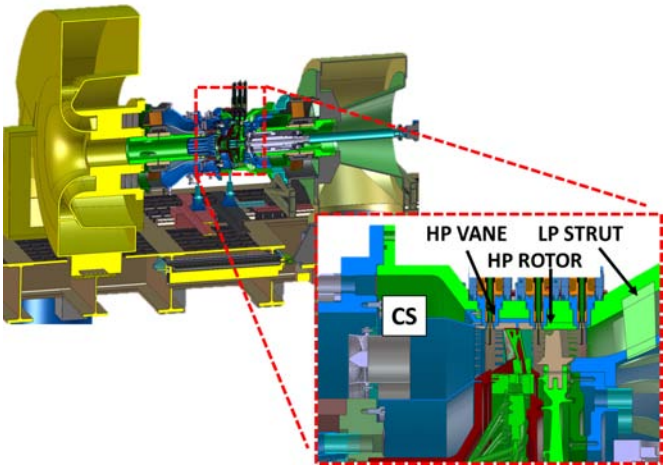

Figure 5.12: Test section of the FACTOR test rig - Draft version

- air flow split in the combustor simulator (*CS*) is representative of a lean burn arrangement; liners are equipped with an effusion cooling system;
- the combustor allows the investigation of the effects of swirler/vane clocking on the aerodynamics and heat transfer of the HP stage;
- HP stage is characterized by an aggressive turbine duct with an aerodynamic loaded (turning) structural vane, blade and strut;
- vane and blades are provided with engine-representative shower head and film cooling holes to have a realistic heat transfer on the surfaces of the airfoils;
- the rig is provided with all the typical features of a real gas turbine, such as disks and the related secondary air system, squealer at the blade tip to control the clearances, etc.

To date, many measurement methods for turbine specific applications have been investigated in great detail. The challenge of the project is to

adapt several different advanced experimental techniques to the difficult-to-access areas of the rig bed without perturbing the test itself. Additionally, the expected high temperatures coming from the combustor simulator will be challenging for the use of some instrumentation (probes, sensors, etc.). To ease the task, the different techniques will be developed by several European academic and industrial partners, that will then alternate to perform measurements on the same test rig. The planned measurements, adapted and further developed to fulfil the specifications of the rig, are listed in table 5.3: recalling table 5.2, it is clear that the goals set by the project are quite ambitious with respect to previous campaigns on analogous test rigs, but only through such kind of massive investigations a deep improvement in the knowledge of this complex system and its related physical phenomena will be possible. A complete overview on the FACTOR test rig and the foreseen experimental and numerical campaigns can be found in the paper of Battisti et al. [134].

Table 5.3: Measurement techniques planned in the FACTOR rig

<table>
<tr><th></th><th>Combustor</th><th>HP-NGV</th><th>HP-ROTOR</th><th>LP-STRUT</th></tr>
<tr><td>Velocity and Turbulence</td><td>PIV-Probes</td><td colspan="3">PIV</td></tr>
<tr><td>Gas Temperature,
Pressure and Density</td><td colspan="3">Laser Vibrometry
Probes - Raman Scattering</td><td></td></tr>
<tr><td>Surface Pressure</td><td></td><td colspan="3">Pressure Taping</td></tr>
<tr><td>Surface Temperature</td><td></td><td colspan="3">Infrared Thermography - Thermocouples</td></tr>
</table>

Chapter 6

Development of an Annular Combustor Simulator for Aerothermal Investigations on Hot Streaks

"It cost much labour and many days
before all these things were brought to perfection"
D. Defoe, Robinson Crusoe

Within the context of the FACTOR European research project, a annular three sector test rig was manufactured and instrumented to deepen the investigation on hot streaks generation and transport. The rig reproduces the geometry of a lean combustor chamber (1:1 scale), provided with an effusion cooling system and without dilution holes; thanks to the three sector arrangement, detailed measurements can be performed on the mixing phenomena between the hot mainflow and the coolant and on the aerothermal field at the combustor exit.

This chapter will present an overview of the main features of the combustor simulator, as well as the design and the numerical validation pro-

cedure of the three sector rig; afterwards, the facility will be described, providing details on the integration of the instrumentation and on the planned experimental test matrix. Finally, a macro-analysis of the governing parameters of the rig will be provided, in order to identify the relation between the control variables and the non-dimensional numbers and thus to have a full characterization of its operating conditions.

6.1 FACTOR Combustor Simulator Specifications

The design of of the non-reacting combustor simulator (CS) was one of the major task of the FACTOR project. Special efforts were made to closely mimic a recent lean burn engine configuration to capture all physical scales at the combustor-turbine interface. Therefore, the design of the module was commissioned to *Turbomeca*[1] and *Avio Aero*[2], as partners of the project, due to their wide experience in gas turbine combustor development and manufacturing.

As it will be explained in the next section, a three annular sector combustor simulator was designed starting from the specifications of the combustor chamber provided by the two industrial partners mentioned above. The test rig was aimed at characterizing the mixing between the hot and the cold flows inside the chamber, to study the generation and the transport of hot streaks through the combustor. Further in the FACTOR project, a full annular combustor with the same geometry of the three sector rig will be manufactured and installed in the facility at DLR (§ 5.5) to investigate the impact of the hot streaks on the HP turbine.

To ease operability and to allow the use of different measurement techniques, no combustion is enforced in the chamber and the temperature profile is obtained only by mixing hot and cold air streams.

The main features of the combustor simulator can be described as follows:

- Full annular axial combustor;
- Equipped with 20 swirlers, leading to 18° of tangential extention for each sector;
- Single vane-swirlers;
- Pressure drop across swirler of ≈3.5%;
- The combustor is producing a targeted temperature profile by mixing two different air flows: cold air will be issued at ≈300K, while

[1] *http://www.turbomeca.com/*
[2] *http://www.avioaero.com*

hot mainstream temperature will be $\approx 530K$. Mainstream temperature was set taking into account that going beyond this level would lead to different technological difficulties concerning gaskets, insulation, thermal stress, instrumentation, etc.;

- Turbulence intensity between 10% and 20% at combustor outlet.

Combustor simulator key features are representative of a lean burn technology. The main functional impacts of the lean burn technology on the design of the module are the following:

- a flow split with around 2/3 of air mass flow going through the swirlers and 1/3 of air mass flow used for cooling;
- liners are provided with an effusion cooling system, and no dilution holes are inserted;
- the angle of inner liner is 35° (measured with horizontal axis).

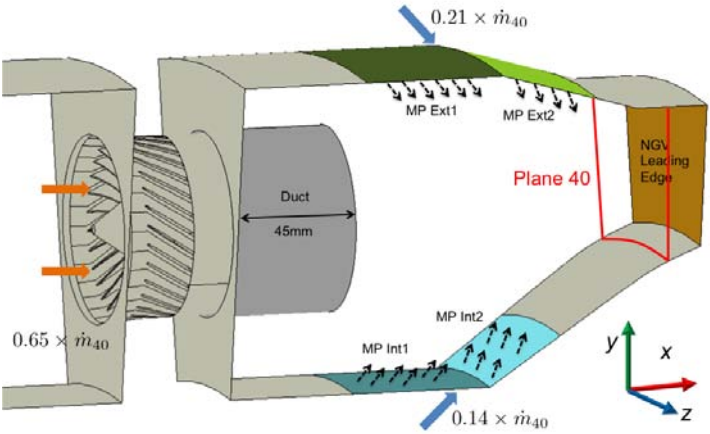

Figure 6.1: Sketch of the CS: multiperforated liners are shown in color (inner and outer feeding cavities are not shown) [135]

The generic design of the *CS* is schematically shown in figure 6.1; the picture indicates also the position of "*Plane 40*" (*P40*), which represents the combustor-turbine interface and it is one of the main focus of attention of the experimental investigations. The sketch illustrates one of the so called "ducted configuration": a duct is placed at the swirler exit to confine and preserve the hot swirling flow, and thus strengthen the hot streak at the *CS* exit. Even if such a configuration is clearly non representative of a real engine, it was introduced as an easy solution to test different velocity distributions of the mainflow in the chamber, and therefore to analyse how they affect the mixing with the coolant from the effusion system and the resulting hot streaks generation.

The total air mass flow of the combustor is split into 65% through the swirlers and 35% for effusion cooling; considering this flow split and the reference temperature indicated above, the mean adiabatic temperature at the combustor-turbine interface is $450K$. The inner and outer liners (respectively light blue and green in Fig. 6.1) are multiperforated with different patterns of effusion holes, aligned with the streamwise direction (no compound angle) in a staggered configuration; the main characteristics of each patch, two for each liner, are summarized in table 6.1. The geometry of the chamber is not scaled with respect to a real engine (1:1 scale); the main difference concerns the feeding system of cooling air: two dedicated supply lines, separated from the mainstream one, discharge coolant in

Table 6.1: Main features of the different patches of the effusion cooling

Patch	**d [mm]**	**L/d [-]**	α **[deg]**	$\mathbf{S}_x$**/d [-]**	$\mathbf{S}_y$**/d [-]**	**Porosity [%]**
MP Ext1	0.50	3.5	30	3.8	2.0	6.69
MP Ext2	0.50	2.0	60	4.0	2.0	5.74
MP Int1	0.50	3.5	30	4.8	2.0	8.31
MP Int2	0.50	2.0	60	3.2	2.0	5.20

Figure 6.2: Sketch of a swirler of FACTOR combustor simulator

an inner and an outer plena (*cavities*) by means of several pipes; each supply line has its own valve to control the cooling mass flow rate. With respect to an engine-like configuration, where the two cooling annuli and the mainstream are fed by the same "pipe", i.e. the diffuser at the compressor exit, the selected arrangement facilitates the operability of the rig, allowing to easily set the desired temperature ratio and flow split between the mainstream and the cooling flows.

The axial swirlers, depicted in figure 6.2, were designed by *Aero Avio* and contains 30 flat vanes disposed around a central hub. The swirlers were manufactured with a Direct Metal Laser Sintering (DLMS) Rapid Manufacturing process[3]: components are formed layer by layer using local melting by applying a laser on metal powders. This technology allows the creation of complex geometries using CAD data automatically. The impact of the manufacturing technique has been taken into account since the early stages of the design of the swirlers.

[3] *http://www.avioaero.com*

The design of the combustor simulator and its swirlers was carried out starting from the specifications mention above and from target profiles set within the project at the combustor exit. Standard industrial steady RANS simulations were employed for this process of reverse engineering. The target profiles, depicted in figure 6.3, are more clearly defined than typical distributions measured in literature (for instance, see [95]): even if, from this point of view, they are less engine representative, this choice was

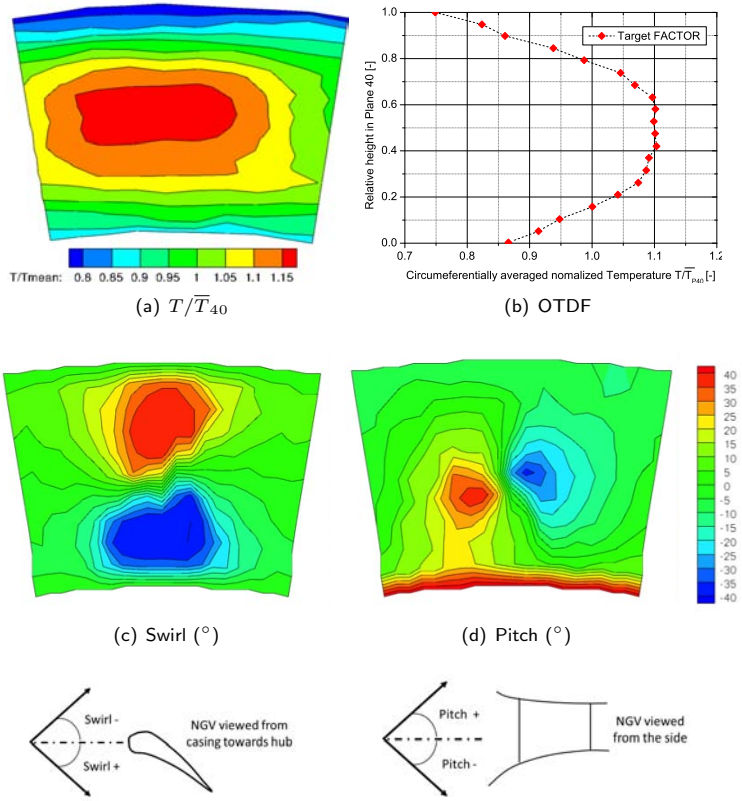

(a) $T/\overline{T}_{40}$ (b) OTDF

(c) Swirl (°) (d) Pitch (°)

Figure 6.3: FACTOR target fields in Plane 40 (view from upstream)

made to have well defined and well characterized inlet conditions for CFD validations. The target, defined in *Plane 40*, shows a well marked central hot spot (fig. 6.3(a)-6.3(b)), while the velocity angle fields (fig. 6.3(c)-6.3(d)) indicates a strong rotating flow coming from the injectors. These target profiles have to be intended as an ideal term of comparison.

6.2 Sector Test Rig

Starting from the given specifications of the combustor chamber, representative of a lean burn engine, a three annular sector combustor simulator was designed; the purpose of this facility, named *Sector rig*, was the investigation, by means of an extensive experimental campaign, of the hot streaks generated by the mixing inside the chamber, as well the characterization of the aero-thermal field at the outlet section (*Plane 40*). Details on the campaign will be given in § 6.4.

The use of a non-reactive three-sector arrangement is often adopted in open literature; for instance, Wurm et al. [136] and Andreini et al. [137] use three-linear sector rigs to study the interaction of an engine-representative flow field with different cooling systems, while Spencer et al. [138] use a three-annular sector rig to investigate the flow field and the turbulence in a combustor chamber. These rigs are operated at ambient temperature and pressure. On the other hand, the Sector rig will operated in a relevant environment: the pressure will be around $\approx 170kPa$, and an engine-representative density ratio will be obtained by heating the mainflow at about $530K$. In the author's knowledge, the test rig developed within this work is the unique annular lean burn combustor simulator with such features.

The adoption of a three sector arrangement can reasonably ensure that the actions of the lateral swirlers on the central one are representative of the full 360° configuration. However, this assumption was confirmed by numerical simulations performed by *CERFACS/Turbomeca*, as partners of the project: here, only a brief overview of the main outcomes of the study will be provided. Details on this exhaustive analysis can be

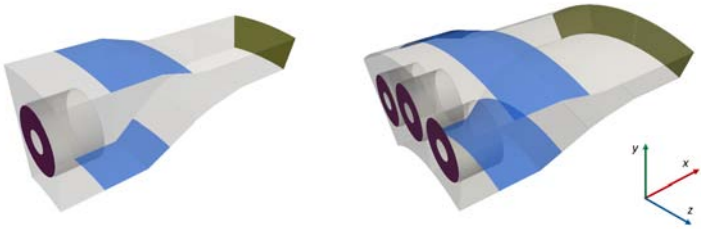

Figure 6.4: Domain of the monosector and trisector simulations [135]

find in in the work of Koupper et al. [135].

Large Eddy Simulations of a single sector with axi-periodicity along the azimuthal direction, representative of a full annulus, and of the Sector Rig with lateral walls were performed by means of the parallel code AVBP [139]; computational domains, which include a $45mm$-duct at the exit of the swirles, are sketched in figure 6.4. Despite an increased computational cost, the choice of using the LES approach guarantees a dynamic representation of the large scale motions, whose contributions are critical in complex geometries with mixing flows such combustor chamber [140, 141].

The time-averaged solutions show that the flow field of the central sector is very similar in the two cases under investigation. As an example, figure 6.5 shows the good agreement in terms of normalized axial velocity field at the central plane of the mono and the three sector; the reference velocity is the mean axial velocity at the swirler exit (U_{ref}). The only difference between the two simulations is the presence of a second central recirculation zone for the trisector and that disappears for the monosector. However, this negative axial velocity zone is very small, and does not impact the mixing process and the flow in plane 40.

Regarding the combustor exit, the mean solutions are circumferentially averaged in plane 40 and the radial profiles of swirl and pitch angles are shown in figure 6.6. The pitch angles are identical, while the swirl

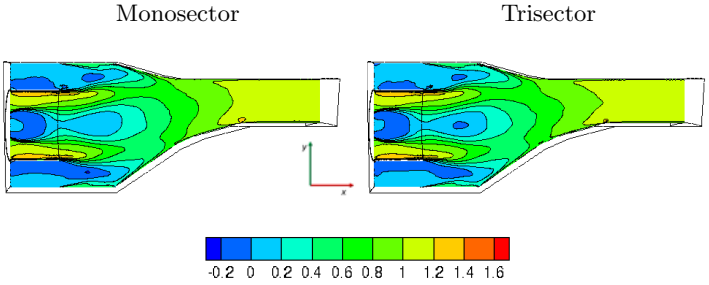

Figure 6.5: Normalized axial velocity U/U_{ref} in the central plane (time-averaged LES results from [135])

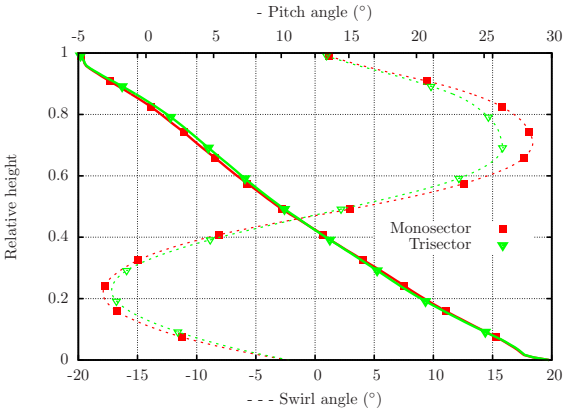

Figure 6.6: Radial profiles of swirl and pitch in plane 40 (time-averaged LES results from [135])

angle presents only a small reduction of about 3° in the upper part of the channel for the trisector.

As far as the hot streaks are concerned, figure 6.7 shows the thermal field in plane 40. An overall transport of hot fluid is noticeable for the trisector (see Fig.6.8): hot air is blocked in the top left corner (D) and

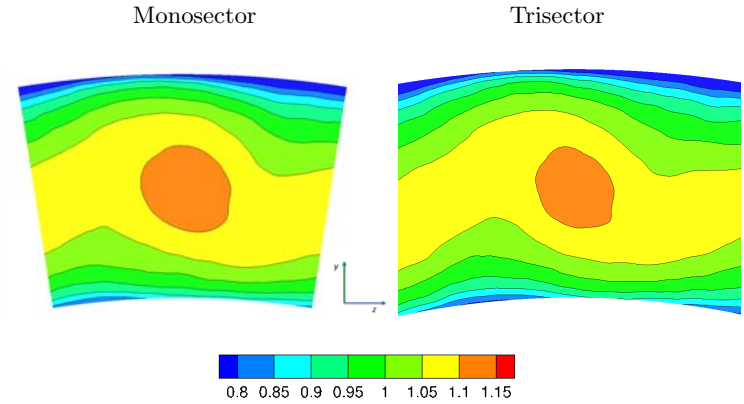

Figure 6.7: $T/\overline{T}_{40}$ in plane 40 (time-averaged LES results from [135])

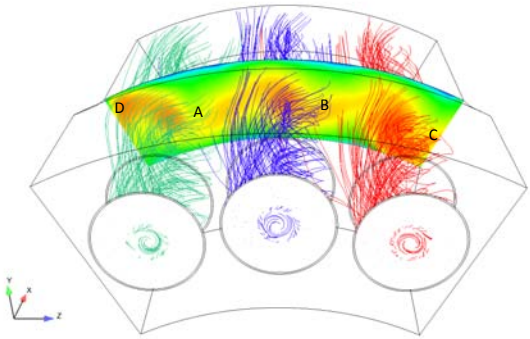

Figure 6.8: Streamlines emitted from each swirler towards plane 40 in the trisector (time-averaged LES results from [135])

in the bottom right corner (C). Because of the overall swirl (clockwise when looking downstream), a small part of each swirler stream is convected towards the adjacent sector on the right (A $\rightarrow$ B $\rightarrow$ C) . In the case of a full annulus (periodic simulation), this effect is balanced by the periodicity of the configuration, resulting in a centered hot spot for each

sector. For the trisector configuration, the effective confinement tends to reduce the strength of the left hot spot while emphasizing the right one. The central sector seems however not affected. This is confirmed by locally calculating the temperature difference $(T_{mono} - T_{tri})/T_{tri}$ which is mostly below 1%, and at maximum is 4%.

Sumamrizing, the numerical simulations showed how the effects of the lateral walls on the central sector are negligible; therefore, measurements on the central sector are actually representative of the full annular arrangement.

In the next paragraph, a detail description of the Sector Rig will be presented.

6.2.1 An Overview of the Sector Rig

The numerical analysis of the combustor simulator presented above confirmed that the influence of the lateral walls on the central sector are small and thus the measurements in the central pitch of the trisector layout are representative of full annular rig; these results supported the design for the Sector Rig, and allowed to proceed to rig manufacturing, assembly and commissioning at the University of Florence.

The Sector Rig reproduces 54° of the geometry of the full annular combustor that will be installed further in the project at DLR. The Sector rig includes all the features of the combustor simulator: three swirlers, the multiperforated liners, the inner and outer cavities and the shape of the outlet duct which will house the stator and rotor blades in the DLR rig; the curvatures of the surfaces and the overall geometry of the liner and of the cavities were exactly reproduced in order to guarantee that the combustor flow path of DLR is accurately reproduced. Vanes and blades are not included and, thus, the potential effects on the flow field due to the presence of the HP stage will not be reproduced; however, as it was shown in § 5.4, these effects are small and the outcomes obtained in the Sector rig can be extended to the DLR rig.

A sketch of the rig is displayed in figure 6.9: different colours indi-

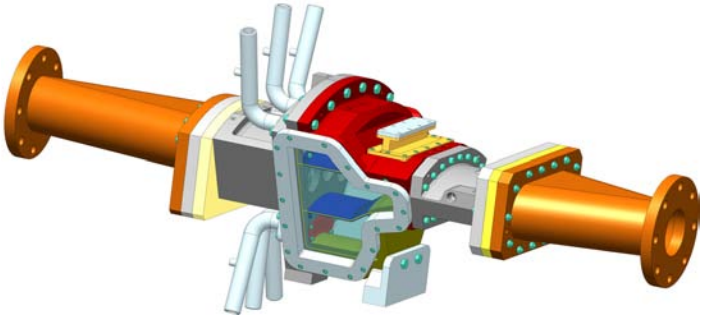

Figure 6.9: Sketch of the Sector Rig

cate the different components that are assembled in the rig, like the outer (red) and inner (yellow) casings, provided with the coolant feeding pipes (light grey), the inner and outer shaped liners, provided with laser-drilled effusion holes (blue), and the inlet and outlet ducts (orange) that connect the annular sector to the cylindrical pipes coming from the compressors and going towards to the stack (see next section). Special graphite gaskets able to bear up to $300°C$ were employed to avoid leakages.

A special attention was dedicated during the design phase to optical accesses: in order to perform optical measurements, such as Particle Image Velocimetry (PIV), three large windows were included in the rig. As shown in figure 6.9, the test rig includes two wide lateral windows, located at sides of the combustor simulator, and a further window placed in the area of Plane 40 (not visible in the picture). Windows were manufactured with the same shape of the lateral walls to be fully integrated with the geometry of the Sector rig; they were designed to guarantee the suitable accesses for a deep investigation of the flow field both in the combustor chamber and at its outlet section. With respect to the full annular configuration the sealing between the liners and the lateral sides must be guarantee to avoid air leakages from the coolant cavities to the combustor chamber: this issue was solved introducing a local thickening of the lateral sides of the liners, which allowed to gain enough room to place a gasket between them and the lateral windows.

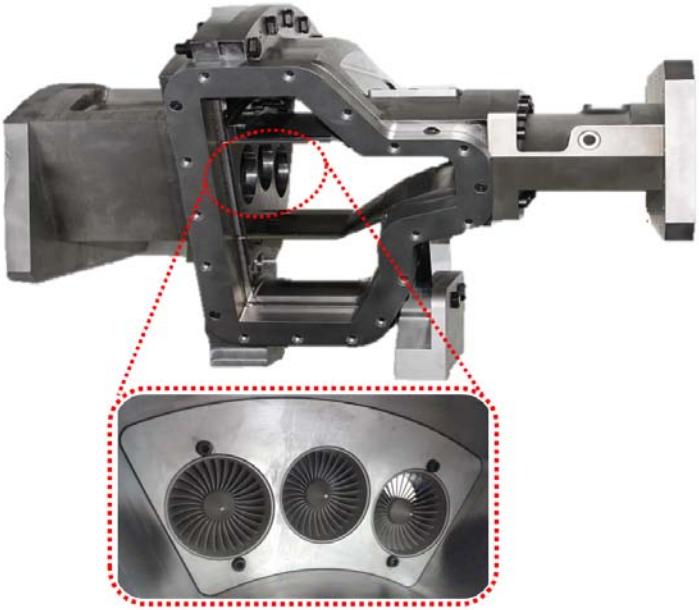

Figure 6.10: View of the test rig and detail of the swirlers (upstream view) [135]

A picture of the rig is shown in figure 6.10: it is possible to observe the two annular multiperforated liners and the housing of the three swirlers, here mounted without ducts. The final arrangement of the test rig was strongly influenced by demands of the planned measurement techniques. In addition to several pressure taps and thermocouples dedicated to monitor the behaviour of the fluid and of the liner walls, measurements will be focused on the investigation of the aerothermal field at *Plane 40* and *Plane 40+* (*P40+* is located $20mm$ downstream *P40*, in correspondence of the vane leading of the DLR rig). As it will be explained in § 6.4, data will be obtained using different probes mounted on an automatic traverse system; the system can be fixed on the outer casing by means of an adaptive flange (yellow part on the outer casing in figure 6.9) that allows

the coincidence between the machine axis and the center of rotation of the azimuthal motion. In addition, this flange can be substituted with a further shaped window to allow optical measurements at the combustor exit; to minimize the influence on the flow field, both the flange for the traverse system and the window reproduce the internal surface at the exit of the rig without modifying the flow path.

6.3 Rig Environment

The test section is operated in a hot wind tunnel, whose layout is sketched in Figure 6.11: compressed air, discharged by two screw compressors, crosses a chiller, which cools the mass flow down to room temperature and removes the humidity. Compressors deliver a mass flow rate of $\approx 1kg/s$ at a maximum pressure of $10bar$; the desired mass and pressure conditions for the tests are set up throttling several valves located along the lines: one modulating valve at the intake of each compressor, one globe valve for the control of the mainstream, one globe valve on each coolant lines and one final vee-valve at the rig exit. During the tests, valves are automatically driven through a PID control system to keep constant operating conditions; in particular, the control system, developed in-house with LabVIEW®, can act simultaneously on all the valves to reach the desired set point of pressure or mass flow in few seconds.

Along the line a $2m^3$ vessel dumps pressure fluctuations. Mass flow is then divided into two different lines, the mainstream and the coolant,

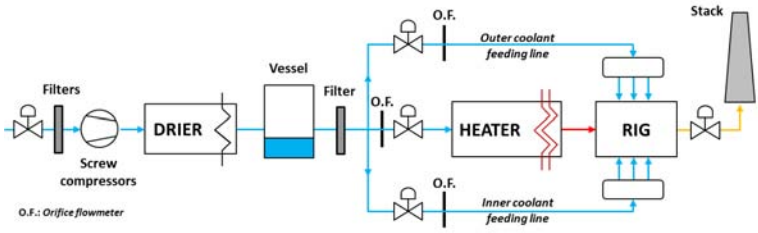

Figure 6.11: Sketch of the test facility [135]

Figure 6.12: View of the Sector rig test cell

which are independently operated by means of the three electronically controlled globe valves mentiones above. Mainstream mass flow rate is measured by means of a calibrated orifice (standard EN ISO 5167-1) and then sent to a $600kW$ electric heater, which rises temperature up to the target value. The heater is automatically controlled by means of a PID system which keeps constant temperature at the inlet of the test rig. Coolant is delivered to the rig through two separated lines: each line discharges air in a plenum, which is connected with the test article through three pipes. The pipes drive the coolant in a cavity, which works as a feeding plenum for the multiperforated liner. Before reaching the stack, the overall mass flow crosses a final vee-ball valve able to sustain high temperature conditions; this valve is automatically controlled and it is aimed at setting the desired pressure level inside the test section. A picture of the test cell is displayed in figure 6.12: the Sector rig and the outlet valve are visible in the foreground, while the electric heater and the coolant lines, provided with the orifice flow meters and the control

valves, are in the background.

6.3.1 Commissioning of the test rig

Several preliminary tests were carried out to check the operability of the entire test facility and moreover to verify that long-term stable conditions were guaranteed.

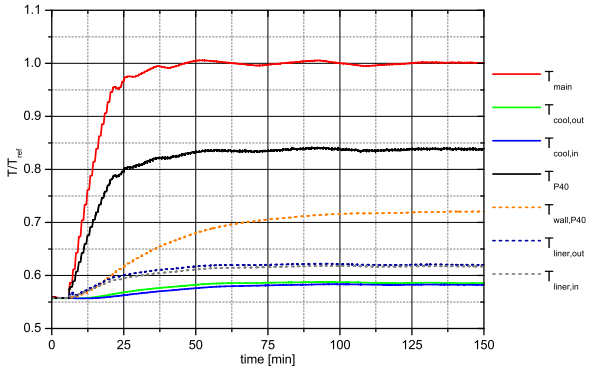

(a) Fluid and metal temperatures.

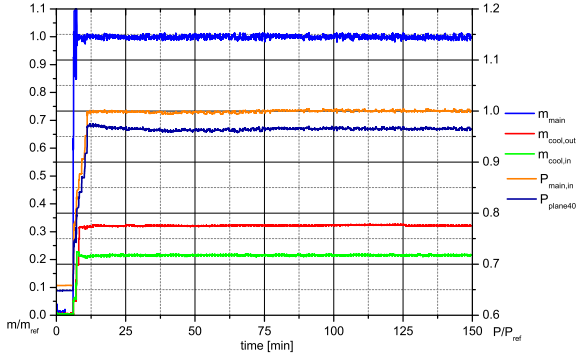

(b) Mass flow rates and pressures across the swirlers.

Figure 6.13: Preliminary test: warm up of the test rig [135]

The test rig was equipped with several static pressure taps and thermocouples; a custom-tailored LabVIEW®-based application developed in-house provided accurate monitoring and recording of the conventional data from measurement data scanners. A pressure scanner NetScanner^{TM} System 9116 with temperature compensated piezoresistive relative pressure sensors is employed to measure static pressure in 16 different locations inside the rig; the maximum uncertainty is $\pm 52Pa$ with a level of confidence of approximately 95%. A HP/Agilent® 34972A data acquisition/switch unit is used to monitor the flow temperature measured by means of several T-type thermocouples ($\pm 0.5K$ uncertainty, 95% level of confidence). In addition, two thermocouples are welded on each liner and further three of them are located inside the metal, close to the location of *Plane 40*; metal temperatures are used also to assess when the thermal steady state conditions are reached. Mass flow rates were measured by means of calibrated orifices; they are affected by an error of 2-3% according to the standard ANSI/ASME PTC 19.1 [87] based on the Kline and McClintock method [88].

Figure 6.13 shows the behaviour of the main measured quantities in the rig during a warm up sequence: each quantity is normalized using the nominal value at the inlet of the swirlers. The warm up sequence is concluded when the metal temperatures (dashed lines in Fig. 6.13a) reach an asymptotic value, roughly 125 minutes after the starting of the test. It is possible to appreciate how the PID control system of the valves and of the heater keep stable the operation of the facility once the steady state conditions are reached: the maximum oscillation of mass flows is $\pm 1.5\%$, while for pressures and temperatures is $\pm 0.5\%$.

6.4 Test Matrix and Operating Conditions

The main purposes of the experimental campaign in the Sector rig are directly linked to the objectives of the FACTOR project:

- to investigate the aerothermal behaviour of the combustor simulator, with a special attention to the resulting mixing between coolant and mainstream at the combustor exit;
- to provide a wide experimental database to carry out comparisons with advanced CFD codes and to assess their accuracy and reliability;
- to provide information about the hot streaks generation and transport through the combustor simulator in view of the measurements on the HP turbine in the full annular rig at DLR.

The test rig was adapted in order to perform an exhaustive experimental survey both at the combustor outlet and inside the chamber; position of the static pressure taps and thermocouples and the location

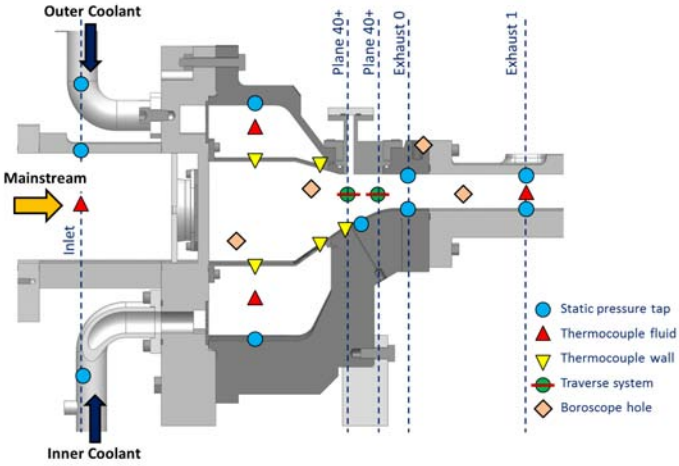

Figure 6.14: Locations of the probes and the measuring planes

of the main instrumentations is depicted in figure 6.14. Initially, the flow field inside the chamber will be investigated by means of the Particle Image Velocimetry (*PIV*) technique; despite the several optical accesses integrated in the rig, the use of boroscopes is necessary. As an example, the sketch in figure 6.14 indicates the position of some of the accesses for the boroscope integrated in the rig. PIV will be used to measure the flow field inside the combustor simulator both in isothermal and nominal conditions, providing the only experimental data in this area of the whole FACTOR project. PIV will be employed in *Plane 40*, too.

Afterwards, measurements will be focused at characterizing the aerothermal flow field in *Plane 40*, where an automatic traverse system will be installed: the investigation will be performed by means of a 5-hole probe provided with a thermocouple and it will allow to obtain detailed measurements of the temperature, pressure and velocity profiles at the combustor outlet. As mentioned in § 6.1, several configurations of the swirler will be tested: ducts with different lengths will be placed at the swirler exit to modify the strengthen of the swirling flow in the chamber and, therefore, to investigate its impact on the mixing with the coolant from the liner effusion systems. Even if such a configuration is non representative of a real engine, it was introduced as an easy solution to analyse the effects of different velocity distributions in the combustor on the generation of the hot streaks. Results will be compared with the target of the project to check the reliability of the numerical tools employed during the design phase of the combustor.

Further investigations will provide more details on the flow field: the automatic traverse system will be employed to perform measurement with a fast response thermocouple, that will be used both in *Plane 40* and *Plane 40+*. This probe will give more information on the hot streaks and above all on the temperature fluctuations; moreover, measurements in *Plane 40+* will give an idea of the hot streaks evolution towards the HP nozzle.

Plane 40 and *Plane 40+* will be studied also by means of hot wire anemometry (*HWA*): these measurements will provide information on

the flow field in terms of turbulence levels and length scales. However, this technique is based on the estimate of the quantity of heat convected away by the fluid and thus it requires the flow under investigation to be isothermal; therefore, when HWA is used, the rig must be operated under isothermal conditions and, to obtain valid experimental data, the isothermal working point must be representative of the nominal one. The procedure adopted to select the isothermal point will be discussed in § 6.4.1.

Details on the different instrumentations and measurement techniques will be given in the chapter 7.

6.4.1 Isothermal Operating Point

As explained in the previous section, the test campaign of the trisector rig includes turbulence and velocity measurements at the exit of the combustor simulator by means of HWA; such measurement technique requires the flow to be isothermal, as the velocity is determined based on the quantity of heat convected away by the fluid. Therefore, an isothermal operating point representative of the nominal conditions has to be selected.

The following study intends to propose a macro-analysis of the governing parameters of the Sector rig aimed at identifying how the working conditions have to be changed in order to keep the non-dimensional parameters unchanged. In the cases of very simple geometries and flow configurations, evaluating the action of the control parameters on the non-dimensional ones is straightforward. However, as it will be shown in the following, the combustor simulator features three feeding lines at different temperature and mass flow, and involves six control parameters and (at least) height dimensionless parameters which are linked by nonlinear equations. In this context, an algebraic representation of the test rig conditions is introduced with the aim of proving a vast diagnostic of the possibilities.

This work was developed within the design phase of the Sector rig and it was carried out in collaboration with *Cerfacs/Turbomeca*; the al-

gebraic representation is based on the formalism proposed by Champion [142], who directly gave his contribute and reviewed the whole work.

6.4.1.1 Control and Non-Dimensional Governing Parameters

The test rig operating point is established and controlled based on the following parameters; values at the design point (DP) are indicated in bracket):

- Mainstream [0]
  - Temperature ($T_0 = 530K$)
  - Pressure ($P_0 = 153kPa$)
  - Mass flow ($m_0 = 0.468K$)
- Outer Coolant [1] / Inner Coolant [2]
  - Temperature ($T_1 = T_2 = 300K$)
  - Pressure ($P_1 = P_2 \approx 153kPa$)
  - Mass flow ($m_1 = 0.151kg/s$; $m_2 = 0.101kg/s$)

The configuration of the rig allows to reduce the number of degrees of freedom, as the two cooling cavities feeding the multiperforated plates share the same pressure and temperature: $P_1 = P_2$ and $T_1 = T_2$. Moreover, the pressure drop created by the swirler and the liner are almost identical (around 3.5%), therefore one can reasonably assume that $P_0 = P_1 = P_2$=P. Finally, the test section is governed by six control parameters: $m_0, P, T_0, m_1, T_1, m_2$. These parameters are bounded by the rig constraints: for example the exit pressure has to be above the atmospheric pressure ($P > 120kPa$); the maximum mainstream temperature is limited by the heater capacity ($T_0 < 800K$); the total mass flow can not exceed the compressor capacity ($m_0 + m_1 + m_2 < 1.0kg/s$); air temperature on the coolant lines temperature is roughly equal to the room temperature ($T_1 \approx T_{amb}$) because of the absence of a cooler or a heater.

As far a the non dimensional parameters are concerned, lots of combinations of them can be found to describe the physics of the flow in the combustor simulator; however, as a first approach, the flow can be represented by a central hot flow surrounded by two colder cross-flows. The hot mainstream is described by its Reynolds number Re_0 and Mach number at swirler exit M_0. In the two cooling cavities, the Mach number is expected to be very low (effect of the plenum), and subject to very minor modifications, therefore it is not very meaningful; so, only the Reynolds number is used in each cavity: Re_1 and Re_2. Moreover, the multiperforated plates can be characterized by the blowing ratio $BR_i = \frac{\rho_i V_i}{\rho_0 V_0}$ and the momentum flux ratio $I_i = \frac{\rho_i V_i^2}{\rho_0 V_0^2}$.

It is not intended to add dimensionless parameters at the outlet of the combustor simulator (e.g. Re in plane 40) as they result from the mixing of the three streams and so depend on too many parameters. Only first-level, inlet non-dimensional parameters will be considered.

Summarising, the obtained 6 control parameters and 8 non-dimensional numbers are shown in figure 6.15 in black and red respectively.

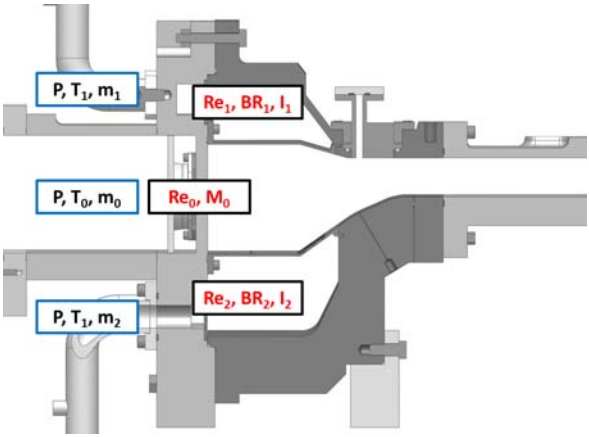

Figure 6.15: Sketch of the rig showing the control (black) and non-dimensional (red) parameters

6.4.1.2 Relation Between Control and Non-Dimensional Parameters

The selected non-dimensional parameters have to be expressed as a function of the control parameters of the rig.

Starting from the Mach number:

$$M = \frac{V}{\sqrt{\gamma RT}} \propto \frac{m\sqrt{T}}{P} \tag{6.1}$$

Note that the ratio of specific heat (γ) is assumed to be constant because of the limited temperature and pressure variations.

$$Re = \frac{\rho V L}{\mu} = \frac{mL}{A\mu} \tag{6.2}$$

L is a characteristic length, while A is a reference surface used to define the mass flow rate.

Due to the moderate temperature involved in the Sector rig, the air viscosity is assumed to follow a power law:

$$\mu = \mu_0 \left(\frac{T}{273}\right)^{2/3} \tag{6.3}$$

Therefore Eq. 6.2 turns into:

$$Re = \frac{mL}{A\mu_0 \left(\frac{T}{273}\right)^{2/3}} \propto \frac{m}{T^{2/3}} \tag{6.4}$$

The blowing ratio is easily expressed as a function of the mass flow:

$$BR_i = \frac{\rho_i V_i}{\rho_0 V_0} = \frac{m_i A_0}{m_0 A_i} \propto \frac{m_i}{m_0} \tag{6.5}$$

Finally the momentum flux ratio is expressed as:

$$I_i = \frac{\rho_i V_i^2}{\rho_0 V_0^2} = BR_i^2 \frac{\rho_0}{\rho_i} \propto \left(\frac{m_i}{m_0}\right)^2 \frac{T_i}{T_0} \tag{6.6}$$

The non-dimensional parameters can be written as a function of the

rig control parameters:

- Mainstream

$$M_0 \propto \frac{m_0\sqrt{T_0}}{P} \tag{6.7}$$

$$Re_0 \propto \frac{m_0}{T_0^{2/3}} \tag{6.8}$$

- Outer Coolant

$$Re_1 \propto \frac{m_1}{T_1^{2/3}} \tag{6.9}$$

$$BR_1 \propto \frac{m_1}{m_0} \tag{6.10}$$

$$I_1 \propto \left(\frac{m_1}{m_0}\right)^2 \frac{T_1}{T_0} \tag{6.11}$$

- Inner Coolant

$$Re_2 \propto \frac{m_2}{T_1^{2/3}} \tag{6.12}$$

$$BR_2 \propto \frac{m_2}{m_0} \tag{6.13}$$

$$I_2 \propto \left(\frac{m_2}{m_0}\right)^2 \frac{T_1}{T_0} \tag{6.14}$$

Observing these parameters, it is worth noting that:

- The blowing ratios are unchanged if the slow split between the different lines is kept constant;
- The momentum flux ratio is directly related to the temperature ratio between the hot and the cold stream (1.77 at design point)

6.4.1.3 Algebraic Representation

The relations between the 8 non-dimensional parameters and the 6 control variables previously identified are governed by non-linear equations 6.8- 6.14; therefore, identifying the action of a single control parameter on the dimensionless ones is not trivial. It is proposed here to

linearise the equations using a logarithmic formulation, so that one gets the following algebraic relation:

$$K \cdot \vec{C} = \vec{S} \tag{6.15}$$

$$K = \begin{pmatrix} 1 & -2/3 & 0 & 0 & 0 & 0 \\ 1 & 1/2 & -1 & 0 & 0 & 0 \\ 0 & 0 & 0 & 1 & 2/3 & 0 \\ 0 & 0 & 0 & 0 & -2/3 & 1 \\ -1 & 0 & 0 & 1 & 0 & 0 \\ -2 & -1 & 0 & 2 & 1 & 0 \\ -1 & 0 & 0 & 0 & 0 & 1 \\ -2 & -1 & 0 & 0 & 1 & 2 \end{pmatrix} \vec{C} = \begin{pmatrix} log(m_0) \\ log(T_0) \\ log(P) \\ log(m_1) \\ log(T_1) \\ log(m_2) \end{pmatrix} \vec{S} = \begin{pmatrix} log(Re_0) \\ log(M_0) \\ log(Re_1) \\ log(Re_2) \\ log(BR_1) \\ log(I_1) \\ log(BR_2) \\ log(I_2) \end{pmatrix}$$

K is the matrix of a linear application $f : \Re^6 \rightarrow \Re^8$. The reference design point is established by 6 control parameters $\vec{C}_{DP}$ such as the DP non-dimensional parameters are given by $\vec{S}_{DP} = K \cdot \vec{C}_{DP}$.

Knowing the relations f that allow to act on the set of control parameters without alter the non-dimensional numbers, it is interesting to search for the kernel of f, which is a vector of control parameters whose image by f is $\vec{0}$ (i.e. $log(1)$ because of the linearisation by logarithm). Any vector $\vec{u}$ of $\Re^6$ is part of the kernel of f if $K \cdot \vec{u} = \vec{0}$. This system is solved and the kernel of f is any colinear vector of :

$$\vec{u} = \begin{pmatrix} 1 \\ 3/2 \\ 7/4 \\ 1 \\ 3/2 \\ 1 \end{pmatrix}$$

This means that the dimensionless parameters $\vec{S}$ are all unchanged if all the control parameters belong to the kernel, i.e. if they obey the following

definition:

$$
\begin{aligned}
m_0 &\times a^* \\
T_0 &\times a^{*3/2} \\
P &\times a^{*7/4} \\
m_1 &\times a^* \\
T_1 &\times a^{*3/2} \\
m_2 &\times a^*
\end{aligned}
$$

with a^* any scalar, which value is only determined by the rig constraints. The evolution of the control parameters as a function of a is illustrated in figure 6.16. The design point is obtained for $a^* = 1$; the green and blue hatch zone show values of a^* that are not feasible to achieve because of too high mass flow rate or too low values of pressure. In between these two zones, pressure and mass flow conditions are achievable and an operating point can be selected based only on the possible values for the

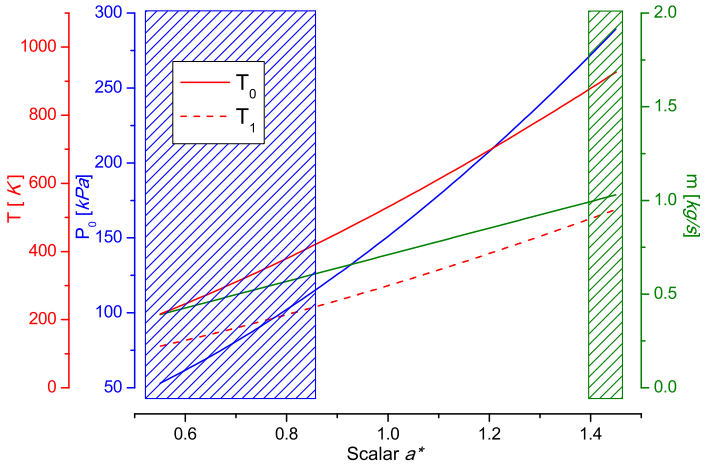

Figure 6.16: Evolution of the control parameters as a function of the scalar a it the non-dimensional number are conserved

swirler and cooling lines temperatures.

6.4.1.4 Selection of the Operating Point

The previous analysis provided a deep overview about how to operate on the control parameters of the rig to keep the fluid dynamic similitude unchanged. Unfortunately, the current layout of the test facility imposes a strong constrain on the coolant temperature: in fact, it cannot be controlled but it set equal to room temperature by the chiller at the compressor outlet. Therefore, since T_1 of figure 6.16 is fixed, it is clear that the non-dimensional parameters cannot be kept constant all at the same time.

The choice of the isothermal point for HWA was performed starting from the plot of figure 6.17: it indicates how the non-dimensional quantities change in relation to the design point (DP) varying the inlet pressure P and the overall mass flow rate ($m_0 + m_1 + m_2$). Isolines are drawn assuming the inlet temperature of the three flows are equal

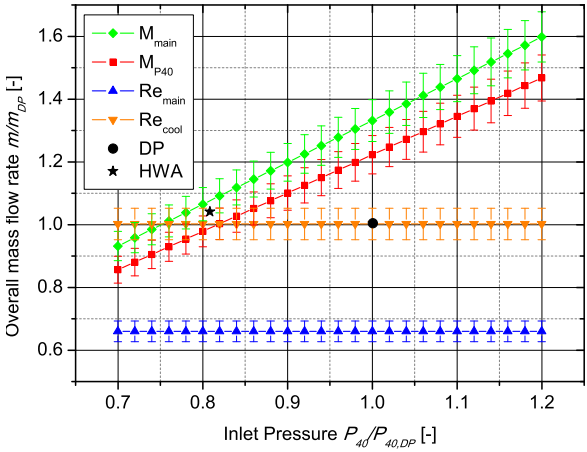

Figure 6.17: Mass flow, pressure map with lines conserving the non-dimensional parameters of the test rig [135]

to room temperature ($T_0 = T_1 = T_2 = 300K$); moreover, a $\pm 5\%$ error bar is included for each point. As stated in the § 6.4.1.2, blowing ratios are conserved just keeping the flow split unchanged; consequently, the velocity ratio between coolant and mainstream at isothermal conditions increases by a factor $T_0/T_1 \simeq 1.77$ versus nominal conditions. An accurate evaluation of the BR and VR of the effusion holes in the combustor simulator is quite difficult because of the complex flow field structures due to the recirculation zones; however, an overall estimate based on the numerical calculations performed by *Cerfacs/Turbomeca* (§ 6.2) indicates values of velocity ratio within the range VR$\approx 2.5 - 3$. Therefore, since the effusion holes work within the penetration regime (VR>0.8) [30], it was assumed that the modification in the behaviour of the cooling jets due to this changes on VR does not alter significantly the mixing process in the chamber and the resulting flow field at the outlet section.

Design Point is shown for reference in figure 6.16 (•); Reynolds numbers are unaffected by pressure (e.g., see equation 6.4), and thus only one

Table 6.2: Isothermal (HWA) and nominal (DP) operating conditions

	DP	*HWA*
Normalized total mass flow	1	1.04
Flow split: mainstream	65%	65%
Flow split: cooling cavities	35%	35%
Normalized chamber pressure	1	0.81
Swirler inlet temperature	531 K	300K
Cooling cavities temperature	300K	300K
Swirler Reynolds number Re_{sw}	111 000	175 500
Swirler Mach number M_{sw}	0.112	0.108
Effusion cooling Reynolds Re_{col}	2350	2440
Plane 40 Mach number M_{40}	0.104	0.109
Normalized Effusion VR	1	1.77

value of mass flow allows to conserve the Reynolds numbers. According to this chart, an isothermal operating point (HWA) is selected ($\star$) within the rig domain of operability, at a reduced pressure and slightly increased mass flow, as detailed in Table 6.2.

Chapter 7

Sector Rig: Instrumentation and Measurement Techniques

"If you cannot measure it
you cannot control it "
J. Grebe, The Freedom to Be Creative

The previous chapter presented the Sector rig and the planned measurements for the investigation of the aerothermal flow field in the combustor simulator. Several different techniques will be used with the aim of providing a wide database of experimental data on the combustor that will be further exploited to validate advanced CFD code and design tools.

In this works only part of the wide test matrix planned for the Sector will be presented and discussed in details. This chapter will give an overview of the experimental techniques employed in this work: multiholes pressure probes, fast response thermocouples and Particle Image Velocimetry (PIV) will be briefly introduced to support a general understanding of basic principles; however, this chapter is not intended to provide an exhaustive description.

7.1 Measurements at the Combustor Outlet

The first measurements in the *Sector rig* are aimed at characterizing the aerothermal flow field at the combustor simulator outlet with the use of several different probes: measurements are performed in correspondence of *Plane 40*. Probes are mounted on an automatic traverse system (*TS*), fixed on the outer casing by means of adaptive flanges; through 3 stepper motors the traverse system, developed in *Turbomeca*, is able of azimuthal and radial displacements, in addition to the probe angulation; the positioning accuracy is less than $0.1mm$ in both directions.

Unfortunately, the center of rotation of the azimuthal motion of the *TS* is different from the center of the annular outlet duct of the Sector rig and therefore an investigation of the whole central sector is not feasible. An example of a 600-points mesh that can be performed using a 5-hole probe is depicted in figure 7.1(a): the red external borders represent the area corresponding to the central sector in *P40*, while the circle is the projection of the swirler outer diameter on the measurement plane. The picture highlights that the center of the circumferences of the mesh is different from the one of the annular sector; moreover, it displays the

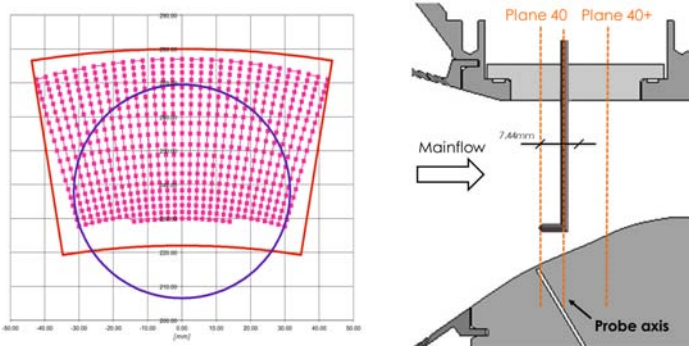

(a) Example 600-points mesh (b) Position of the 5-hole probe

Figure 7.1: Set up of the TS for the 5-hole probe

limits of the area that can be investigated: the mesh is bounded on the sides by the maximum azimuthal displacement of the *TS*, while the lower and upper limits depends on the dimension of the probe itself. In fact, as illustrated in figure 7.1(b), measuring closer to the inner wall is not feasible due to both the converging shape of the liner and the elbow of the 5-hole probe. However, despite previous consideration, measurements can be carried out in most of the central sector.

7.1.1 Five Hole Pressure Probe

A five hole pressure probe is constructed by surrounding a central pressure port with 4 equally spaced ports. The central port is on the axis of the probe, while the peripheral ports are drilled in the lateral surface of a cone typically angled between 25° and 35° to the central port. A typical probe tip is shown in figure 7.2.

Multi-hole pressure probes have been extensively studied in literature, and standard methods of calibration and implementation exist and are well documented. The accepted approach that is widely in use today was first proposed in the 70's by Bryer and Pankhurst [143] and Treaster and Yocum [144]: authors introduced the concept of dimensionless directional pressure coefficients that could be used to represent the angularity of a

Figure 7.2: Typical 5-hole probe tip

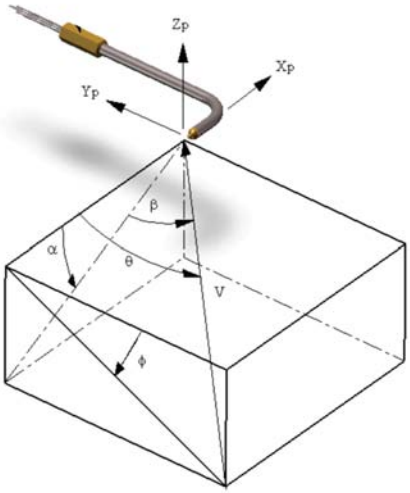

Figure 7.3: Flow angles and coordinate system conventions

flow over a large range of flows. Despite this method has been improved in the past years (for instance, see Paul et al. [145]), the principle of non dimensional coefficient is still at the basis of the calibration and the data analysis of multi-hole pressure probes. Generally speaking, when a 5-hole probe is used to measure an arbitrary flow, the pressures in the five ports are measured simultaneously: using the known relative positions of the holes, dimensionless pressure coefficients, that represent the direction of flow, can be defined starting from the difference in measured pressure across diametrically opposite holes. These directional coefficients can then be correlated to exact flow angles, and the direction of flow can be established. As far as the flow magnitude and pressure are concerned, they can be approximated using the dimensionless coefficients derived from the raw pressure data; however, for a more accurate estimate, dimensionless coefficients should be correlated to a correction factor that, applied to the pressure magnitude coefficients, allows calculate the exact flow pressure and magnitude. More details on the calibration and the

post processing procedure can be found, for instance, in the works mentioned above.

The flow angle relative to the probe tip can be defined using two coordinate systems, as depicted in figure 7.3. The pitch and swirl coordinate system defines two flow angles that are referenced to the probe's Y_p and Z_p axis; pitch and swirl (yaw) angle are called respectively β and α in the picture. The cone and roll coordinate system is a polar coordinate system: the cone angle (θ) is the total angle of attack to the probe axis, while the roll angle (ϕ) is a rotation angle that is referenced to a fixed probe axis.

The probe used in this work was manufactured and calibrated by *Aeroprobe*[1] a two different Mach number ($Ma = 0.1; 0.2$), to cover the whole velocity range expected in the rig. According to the manufacturer,

Figure 7.4: 5-hole probe installed in the outlet section of the CS

[1] *http://www.aeroprobe.com/*

the averaged magnitude error on the measured angles is $<0.1 deg$.

The probe is installed in the rig through and adaptive flange so that the tip of the probe is exactly in correspondence of Plane 40, as depicted in figure 7.1(b). A picture of the probe inserted in the rig is displayed in figure 7.4. During the tests, data are acquired by means of a piezoresistive pressure transducer, synchronized with the motion system of the traverse system. For each point of the mesh, pressure data where acquired for $2s$ at $2kHz$; averaged values were then post processed using the probe calibration files.

In addition, the probe is equipped with a thermocouple mounted in correspondence of its elbow, $7.44mm$ downstream the probe tip, that allows to acquire the flow temperature with at same rate of the pressure transducer. The measured temperature is partially biased by the presence of the 5-hole probe itself; however, it can be considered a good estimate of the real flow temperature and the obtained data will be used to identify the best duct length in relation to the target thermal field. More accurate measurements of the flow temperature are carried out using the fast response thermocouple.

7.1.2 Fast Response Thermocouple

The fast response thermocouple (FRT) consists of two fine wire, $120\mu m$ in diameter, placed inside a ceramic barrel inserted within a metallic tube; the external diameter of the probe is $3mm$. A picture of the probe is shown in figure 7.5 (on the left side of the image one of the swirler ducts is visible). The probe was developed and manufactured in *Turbomeca* to acquire temperature data at high frequency: in fact, thanks to the small inertia of the wires, this thermocouple allows to gather data at a maximum frequency of $2kHz$.

Through a dedicated flange, the probe is inserted exactly in correspondence of *Plane 40*; in addition, the small dimension of the tip of the thermocouple permits to extend the measurement mesh much closer to the inner wall with respect to the 5-hole probe. The fast response

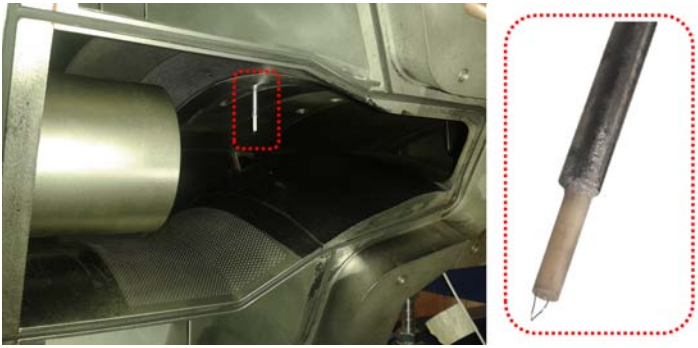

Figure 7.5: Fast response thermocouple installed in the rig (swirler duct visible on the left side)

thermocouple is directly connected to the acquisition board and it is synchronized with the motion system; data are acquired for $4s$ at $5kHz$.

7.2 PIV Measurements

As mentioned in § 6.2, during the design phase of the Sector rig special efforts were dedicated to have large optical accesses to the combustor simulator in order to perform optical measurements. In particular, the planned experimental campaign includes the characterization of the flow field inside the chamber by means of Particle Image Velocimetry technique.

With respect to the probes mentioned above, PIV is a "whole field technique" that allows to provide detailed information on the velocity field in the investigated area, i.e. *Plane 40*, all at once. This characteristic is exploited to measure the flow field both at the combustor exit, and inside the chamber: through this technique, the main feature of the flow structures generated by the swirlers and their interaction with the coolant flows are pointed out.

The possibility of using PIV inside the combustor simulator is given by the three-sector arrangement: in fact, as indicated in chapter 6, the

lateral walls of the Sector rig are made up of shaped windows that permit a wide field of view in the chamber. Such kind of measurements are not feasible in the facility at DLR due to the difficulties in integrating large optical accesses in the full annular rig; therefore, outcomes from the investigation in the Sector rig will be the only experimental data of the project about the flow field inside the combustor.

In the next paragraph an overview of the PIV technique will be provided; following, the attention will be focused on the PIV arrangement that will be adopted in the Sector rig, which is based on the use of boroscopes both for the camera and the laser: details will be given about the main features of the boroscopes and how they were adapted to fulfil the rig specifications.

7.2.1 Fundamentals of PIV

In this section the main features of the PIV technique will be briefly described to support a general understanding of basic principles; however, it is not intended to give an exhaustive overview. Further details on this technique can be found in the comprehensive work of Raffel et al. [146].

PIV is a measurement technique for obtaining instantaneous whole-field velocities; a sketch of a basic arrangement is depicted in figure 7.6. This technique is based on the well-known equation:

$$speed = \frac{distance}{time} \tag{7.1}$$

In PIV the property actually measured is the distance travelled by particles in the flow within a known time interval. These particles, known as seeding, are added to the flow; in this respect, seeding particles can be considered to be the actual velocity probes. Therefore, fluid-mechanical properties of the tracking particles must be accurately checked in relation to the nature of the flow under investigation to avoid significant discrepancies between the measured velocity, i.e. the particles velocity, and the actual velocity of the flow (ideally, the particles should also be neutrally buoyant in the fluid).

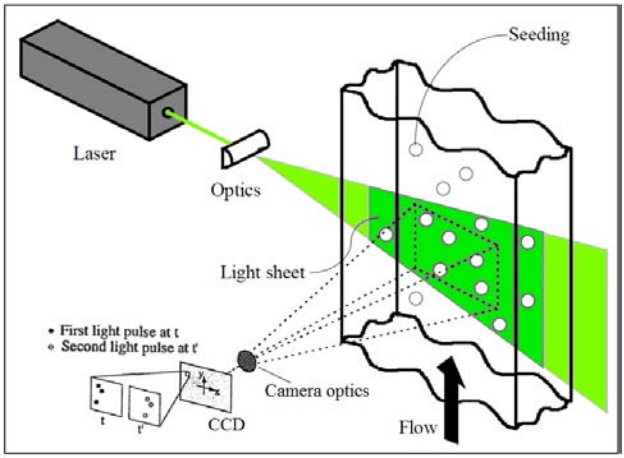

Figure 7.6: Basic principles of PIV

In order to detect the movements of the particles, the area under investigation is illuminated by a light sheet; the light sheet, generated by a laser and a system of optical components, is not continuous, but pulsed to produce a stroboscopic effect, freezing the movement of the seeding particles. The time between the light pulses is the denominator in the equation above. To detect the position of the illuminated seeding particles, a CCD-camera (CCD = Charge Coupled Device) is positioned at right angles to the light-sheet to record the light scattered by the particles on a sequence of frames: particle positions will appear as light specks on a dark background on each camera frame.

The pulsing light-sheet and the camera are synchronised so that particle positions at the instant of light pulse number 1 are registered on frame 1 of the camera, and particle positions from pulse number 2 are on frame 2. The camera images are divided into rectangular regions called *interrogation areas* or *interrogation regions*, and, for each of them, the images from the first and the second pulse of the light-sheet are cross-correlated to produce an average particle displacement vector. Doing this for all interrogation regions produce a vector map of average particle

displacements.

Dividing with the known time between the two images captured, the displacement vectors are converted into a map of so-called raw velocity vectors. To speed up the calculation of correlations, FFT-processing is used. One conceptual difference between the FFT-processing in Particle Image Velocimetry compared to laser-Doppler anemometry is that in laser-Doppler anemometry signal conditioners are essentially used to ensure there is a meaningful input. This is possible because it is a time based measurement technique and so you can wait for the input. However, since PIV is an instantaneous measurement technique, all spatial information is sampled at the same time and there is a finite statistical probability there will be some regions where there is really no meaningful input [147]. Therefore, it is necessary to subsequently validate the PIV vector map through dedicated algorithms that detect and remove erroneous vectors called "outliers".

Based on the notes of Raffel et al. [146], the main advantages and drawbacks of Particle Image Velocimetry can be drawn:

- **Advantages**:
  - *Non-intrusive technique*: in contrast to techniques for the measurement of flow velocities employing probes as pressure tubes or hot wires, the PIV technique, being an optical technique, works non-intrusively; this allows the application of PIV in flow that must not be disturbed by the presence of probe itself, like in high speed flows with shocks or in boundary layers close to the wall.
  - *Whole field technique*: PIV allows to measure the flow field in large areas with a single acquisition; moreover, thanks to the instantaneous image capturing and high spatial resolution, it enables the detection of spatial structures even in unsteady flow fields. In addition, recent upgrades of cameras and lasers have led to the development of advanced PIV techniques, such

as Sterographic PIV, Tomographic PIV and PIV time-resolved; these methods are based on a sterescopic camera recording or on a very high acquisition rates respectively and they allow the full characterization of a 3D flow field.

- *Wide operability range*: PIV is suitable to perform measurements on a wide range of different operating conditions: if the right kind of seeding particles are chosen, many different fluid types can be investigated, from liquids, to gases to burning gases. Furthermore, if the right time interval between the two laser pulses is selected, there are not theoretical limits to the velocity range that can be investigated with the same set up, from very slow flows close to the wall to supersonic flows.
- *Advanced data post process*: commercial codes for PIV data recording are usually integrated with post process algorithms that, starting from a validated velocity vector map, allow to carry on further advanced post process, such as vorticity, streamlines and so on.

- **Drawbacks**:

  - *Indirect measurement*: through this technique, the velocity of a fluid element is measured indirectly by means of the estimate of the velocity of tracer particles injected the flow; therefore, in relation to the flow madia and to the flow conditions, the choice of the right seeding is fundamental in order to minimize inertial effects.
  - *Complex experimental set up*: PIV requires quite a complex hardware set up, which consist in selecting the right seeding dimension and concentration, a suitable laser-camera layout and a "smart" time interval between the two laser pulse to minimize loss-of-pair; moreover, the set up requires suitable optical accesses in the area under investigation.
  - *Consequences of using seeding particles*: introducing foreign particles in the flow under investigation may not be feasible

due to some external constrain of the test facility: for instance, solid particles are usually not allowed in close-loop wind tunnel not to damage the compression unit. Furthermore, the cleaning of the optical accesses has to be taken into account.

7.2.2 Endoscopic PIV

Despite the large lateral optical accesses, the layout of the Sector rig does not allow to perform PIV measurement by means of a standard arrangements, but it imposes the use of boroscopes.

Rigid endoscopes, called borescopes, are rigid or flexible tube with an eyepiece on one end, an objective lens on the other linked together by a relay optical system in between; usually they are used for inspection works in areas with narrow optical accesses, such as strokes engines or turbines. With respect to modern flexible-fiber endoscopes often used in medicine, these devices allow the suitable spatial resolution which is required for PIV recording: the boroscope is provided with a special optical lens and it is connected directly to the camera, as shown in figure 7.7. The camera boroscope that will be employed for inspections in the Sector rig allows to look perpendicular to the probe axis ("side looking"); the orientation of the lens located at the tip of tube can be adjusted within an angle of more than 180°.

Boroscopes are used also to deliver the laser light in investigation areas with low optical access. Likewise the camera boroscopes, a set of lens drive the laser light inside a straight rigid pipe; located at the tip of

Figure 7.7: Rigid boroscope mounted on the PIV camera

the boroscope, a mirror prism deflects the light to an angle of 90° from the endoscope's axis, and forms a light sheet at a specific focal distance from the axis. The orientation of the light sheet can be adjusted from parallel to perpendicular to the endoscope axis, covering a wide range of orientation angles.

The use of boroscopic PIV in turbomachinery has brought very interesting results, even if its implementation into the test facilities is challenging. Among others, successful approaches to transonic turbomachinery can be found in Lang et al. [148], Voges et al. [149], Wheeler et al. [150] and Kegalj and Schiffer [151].

Several premises have to be fulfilled to collect valuable data. Major issues are the optical access, vibrations, reflections, seeding the flow, cleanliness of optics, etc. The main critical aspects that characterize the use of boroscopes in PIV are briefly listed below:

- *Image distortion*: images captured through boroscopes are affected by strong distortion, mainly the so called "fish eye" effect; this aspect has to be taken into account during the image processing and a suitable dewarping model has to be applied during the calibration process. Figure 7.8 shows an example of a calibration pattern before and after the dewarping.

- *Reduced field of view*: since the boroscope substitutes the camera (or laser) optics, the focal point of the camera field of view is almost fixed and cannot be changed (actually it can be adjusted in a narrow range). This aspect constrains the position of the boroscope with respect to the location of the measurement plane. In addition, when the camera is equipped with the endoscope, its distance from the investigation area must be quite short to have enough resolution in the CCD to capture the small seeding particles and estimate their displacement to subpixel accuracy [146]. The request for a small distance can lead to insertion the prove very close to the measurement area, which may cause disturbances of the flow field.

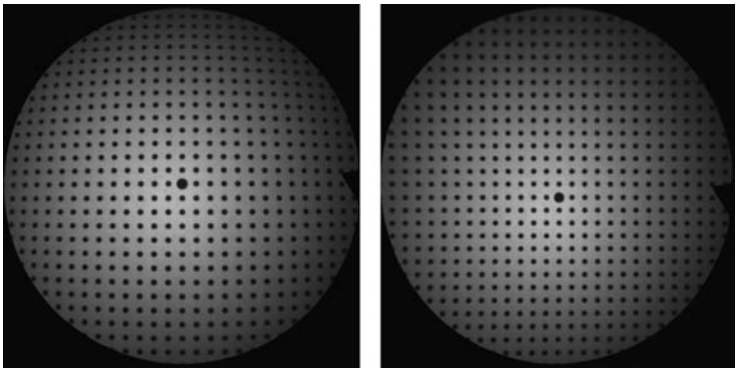

Figure 7.8: Calibration target before and after the dewarping process

Moreover, camera boroscopes drastically reduce the light sensitivity and, depending on the configuration, they require more powerful laser compared with standard camera lens.

- *Boroscopes need to be cooled and kept clean*: the use of this tool imposes severe constrain on the maximum operating temperature due to the presence of the optical lens. This maximum temperature is around $390K$; in case of harsh working conditions, these instruments need to be cooled. An example of the adaptation of a boroscope for an application inside a furnace can be found in Rottier et al. [152]. In addition, boroscope optics needs to be kept clean from the seeding particles during its operation.

7.2.3 PIV set up

Measurement of the flow field are performed using a Dantec Dynamics PIV system. The system consists of a $120mJ$ New Wave Solo Nd:YAG pulsed laser operating with a wavelenght of $532nm$ and a FlowSense 2Mpixel camera operating at a data rate of $15Hz$. All devices are controlled via the commercial software Dantec FlowManager®, which allows the synchronization of the system and moreover the collecting and the

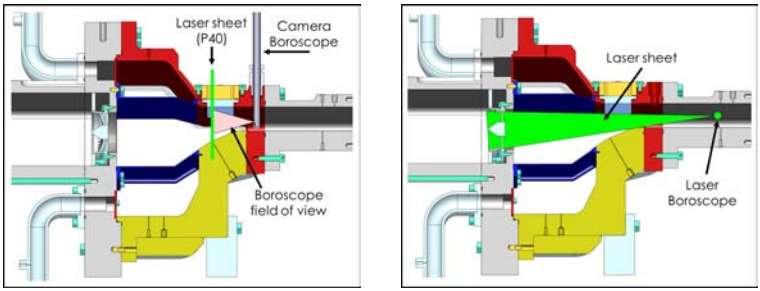

(a) Example of set up "C" (b) Example of set up "L"

Figure 7.9: Schematic view of the PIV the two set up

processing of the data. When boroscopes are employed, a flexible light guide system is used to connect the laser to its boroscope, while the camera is directly mounted on the rigid endoscope.

Investigations in the rig are carried out by means of two different PIV set up, sketched in figure 7.9 and named "C", when camera boroscope is used, and "L", when the laser boroscope is employed. In the "C" set up, the laser sheet enters the rig through the window located in correspondence of *Plane 40*, while the camera boroscope has dedicated holes drilled downstream the window. This configuration, depicted in figure 7.9(a) allows to measure the flow field in Plane 40. As shown in figure 7.9(b), in the "L" set up the laser sheet enlightens the rig in the symmetry plane while the camera focuses the investigation area through one of the wide lateral windows. To have a complete analysis of the combustor simulator, one of the lateral glass windows can be replaced with a metal one provided with several holes for the boroscope: these holes allow to overcome some geometrical costrains of the rig (e.g., laser sheet in figure 7.9(b) cannot illuminates the area close to the inner liner due to its shape near the exit of the chamber) and therefore to deepen the investigation inside the chamber.

To map the whole *Plane 40* and the entire combustor chamber, several framing must be taken for both the measurement planes and, to avoid

loss of information, each camera framing is slightly overlapped with the neighbouring ones. For each camera position, 480 image pairs were taken; the time delay between two laser pulses was adjusted depending on the local averaged velocity, from about $15\mu s$ for the frames next to the swirler, up to $40\mu s$ close to *Plane 40*. The laser sheet thickness was set to about $1mm$ to keep the number of loss of pair due to out of plane motions as low as possible.

Each set of image pairs were post processed using an adaptive grid iterative method [146]. The fundamental principle of adaptive correlation relies an iterative procedure based on the shift of the interrogation windows (i.e. the interrogation area is not locked in the space): from an initial guessed shift value, a shift is introduced from the first window (the interrogation area in the image frame from laser pulse one) to the second window (the interrogation area in the image from laser pulse two). The obtained movement vector calculated trough standard cross correlation algorithm is used as a new estimate for the window shift in the second iteration. From the results of the previous iterative process a new run is made, but this time with a refinement of the size of the interrogation area. Using Adaptive correlation helps in two ways: first, the signal strength is raised due to the capture of the in-plane dropout; secondly, a refinement of the interrogation area is possible because an adaptive window offset is applied, increasing the resolution of results and decreasing the number of erroneous vector [153].

The approach adopted in this work starts from a 256x256 pixel initial windows size, which is reduced in three steps to 64x64 final size; two iterations were chosen for the initial step, while three iterations for the following steps to achieve maximum displacement accuracy. The resulting velocity field contained 49x36 vectors for each camera framing.

These raw vector maps were validated and filtered using in succession two approaches: peak-height validation and moving-average validation [147]. The first method validates or rejects individual vectors based on the values of the peak heights in the cross correlation plane; the second method validates or rejects vectors based on a comparison between

neighbouring vectors and assuming the continuity of the flow field. Finally, an average vector map for each camera framing was computed and all post processed images were composed in a single vector map using MatLab®.

As far as the selection of the seeding material is concerned, nominal operating conditions are quite critical in relation to the layout of the FACTOR rig at DLR: in fact, mainstream temperature ($\approx 530K$) advises against liquid seeding, which would evaporate too fast, whereas the closed loop wind tunnel layout prevents the use of solid particles to avoid the damage the compressors. This aspect would not concern the Sector rig since it is installed in an open loop facility; however, in view of the measurement in the full annular rig, liquid particles have to be employed.

Among the liquid materials, silicon oil and DEHS (Di-Ethyl-Hexyl-Sebacat) have the highest evaporating temperature, even if, in the author's knowledge, none of them are used for such high temperature applications in open literature. Silicon oil (XIAMETER®PMX-200 Silicone Fluid, 100 CS, flash point $\approx 600K$) will be tested in the Sector rig and results, available before the test campaign in the full annular rig, will give indications on this issue.

The seeding necessary for the PIV measurements is introduced upstream the swirler by means of a Laskin nozzle [146]. Particles with a mean diameter of about $\approx 1\mu m$ are injected in the mainstream through a pipe as long as the height of the inlet section; the pipe was drilled with several holes of $\approx 1mm$ in diameter to allow a sufficient mixing between air and seeding before entering the test section. Coolant flow is not seeded.

7.2.4 Boroscope Cooling System Design

As indicated in section 7.2.2, the maximum operating temperature of a boroscope is around $390K$, quite below the mainstream nominal temperature of the Sector rig. Therefore, both the camera and the laser

boroscopes need to be cooled during the PIV measurements to guarantee the integrity of the optical lens.

The design of the cooling system was carried out starting from the configuration of commercial high temperature endoscope. The final configuration adopted in this work consists of an external stainless steel cylindrical housing which contains the boroscope; cooling air is fed in the proximity of the camera (or laser) connection and it is discharged in correspondence of boroscope optics directly in the mainflow of the rig. This configuration allows to prevent the deposition of seeding particles on the optics itself. Finally, a thermocouple is included to monitor the temperature of the probe. A sketch of the cooled boroscope is depicted in figure 7.10.

The cooling system was designed in-house using *Therm1D* (see chapter 3); the design was driven by the following main constrains:

- maximum temperature of the boroscope;
- diameter of the external tube (the smallest possible to reduce the interaction with the flow);
- amount of cooling air (the smallest possible to reduce its the impact on the flow field).

Therm1D was employed to set up the flow network of the cooling system and perform a fluid-metal analysis: on the hot gas side, boundary conditions were set up considering the inlet temperature, pressure and mass

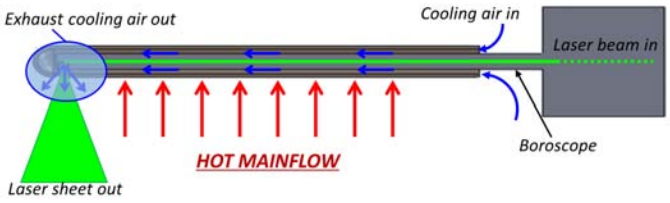

Figure 7.10: Sketch of the cooling system of the boroscope

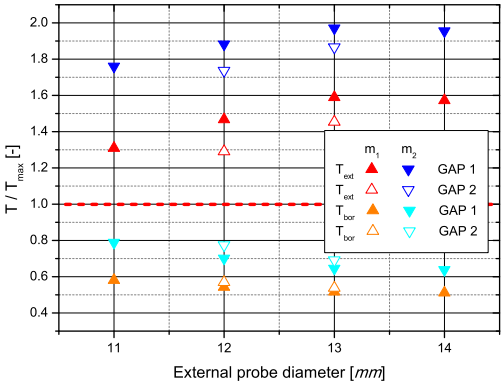

(a) External and boroscope temperature

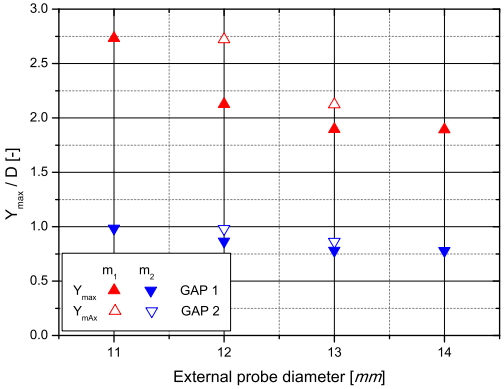

(b) Penetration length of the discharge jet

Figure 7.11: Main output of the boroscope cooling design process

flow rate of the mainstream and imposing a heat transfer coefficient distribution analogous to that on a cylinder body inside a free stream [154]. Runs were carried out keeping constant the boroscope diameter ($8mm$) and varying the mass flow rate of coolant, the external probe diameter and the passage gap for the coolant. The maximum temperature of both the external tube and the boroscope were monitored to find the more

Figure 7.12: Camera boroscope provided with the cooling system and installed on Sector rig

efficient cooling configuration.

Figure 7.11 illustrates the main results of some representative runs: figure 7.11(a) shows the temperature of the external cylinder (T_{ext}) and of the boroscope wall (T_{bor}) varying the overall probe diameter, the gap between the external cylinder and the boroscope (GAP1-GAP2) and the coolant mass flow rate ($m_2 \approx 2 \cdot m_1$). The final configuration was chosen taking in account also the standard dimension of tubes available on sale: external probe diameter $12mm$, internal diameter $11mm$. Figure 7.11(b) displays the jet penetration length (Y_{max}) estimated though the correlation suggested by Lefebvre [1]: results of this analysis, together with previous considerations, led to the definition of the requested cooling mass flow rate.

Finally, an image of the cooled boroscope installed on the rig is displayed in figure 7.12 (here mounted on the camera).

Chapter 8

Sector Rig: Experimental Results

"A theory is something nobody believes,
except the person who made it.
An experiment is something everybody believes,
except the person who made it."
A. Einstein

An extensive experimental survey was carried in the Sector rig, adopting several measurement techniques to have an accurate characterization of the hot streaks generated in an engine-like lean burn combustor. In this chapter, the attention is focused on testing several geometrical configurations of the swirlers and different effusion cooling working conditions, in order to highlight how they impact the aerothermal field at the combustor exit.

Initially, outcomes from preliminary flow checks aimed at characterizing some aerodynamic features of the rig will be shown. Afterwards, the analysis will be focused on the combustor: PIV results inside the chamber will be illustrated, followed by a detailed description of the aerothermal field at the combustor outlet (*Plane 40*) obtained by means of a 5-hole

probe and a fast response thermocouple.

Results will show the effects of the mixing between the effusion flow and the mainstream on the generation and the transport of the hot streaks. In addition, some tests will be dedicated to highlight the effects of different effusion cooling mass flow rate on the resulting temperature and velocity non-uniformities at the combustor exit.

Further investigations concerning the transport of the hot streaks between *P40* and *P40+*, as well as HWA turbulence measurements, will be performed in later stages and they are not included in this study.

8.1 Preliminary Flow Checks

The first measurements performed on the Sector rig were aimed at characterizing the aerodynamic features of both the swirlers and the effusion cooling holes. These preliminary results were aimed at verifying the manufacturing capability of these two critical part of the combustor simulator with respect to the theoretical design: concerning the swirlers, the objective was the estimate of the flow function and the effective area, while the evaluation of the permeability of each different patch was the focus of interest of the laser drilled multiperforated liners. In fact, the good manufacturing of laser drilled holes is quite dependent from several parameters of the process, and even if the discrepancy from the nominal diameter on the single hole is almost negligible, such discrepancy may lead to large changes in the overall permeability due to the huge amount of holes (5164 holes/sector).

Actually, to know these aerodynamic characteristics of the combustor

Figure 8.1: View of the swirler from the second plenum of the rig dedicated to the flow checks

is fundamental for an accurate numerical modelling of the chamber and, therefore, their estimate was of great interest in view of further comparison with CFD calculations.

The flow check of the swirlers were carried out in a dedicated test facility before installing them in the Sector. Each swirler was individually mounted on a flange that connected two plena in an open-loop suction type wind tunnel. The vacuum system was made up of two rotary vane vacuum pumps with a capacity of $900 m^3/h$ each dedicated to the extraction of the air flow; the mass flow rate was set up by guiding the speed of the pumps and using a calibrated orifice located downstream the two plena. Tests were carried out at room temperature, varying the pressure drop across the swirler and measuring the pressure inside the two chambers and the mass flow rate. Figure 8.1 shows the flange that connects the two cavities: the picture is taken from the second plenum and it displays the outlet section of the swirler.

The flow function of one of the swirlers is shown in figure 8.2 (■): as expected, the plot displays the linear relation between the reduced mass

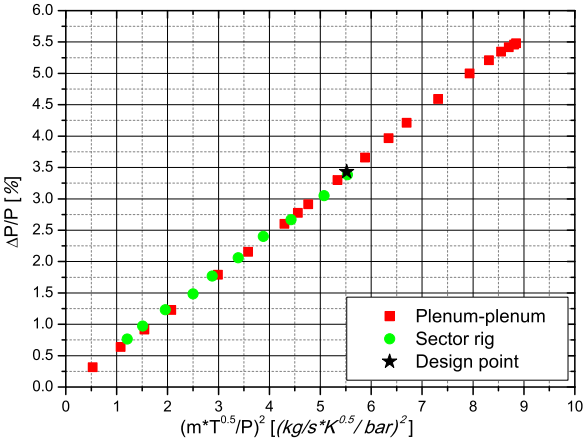

Figure 8.2: Flow function of the swirlers

flow (m_r) and the pressure drop ($\Delta P/P$), defined as:

$$m_r = \frac{m\sqrt{T}}{P_{up}} \tag{8.1}$$

$$\frac{\Delta P}{P} = \frac{P_{up} - P_{dw}}{P_{up}} \tag{8.2}$$

where P_{up} and P_{dw} are respectively the measured pressure in the upstream and downstream plena. Afterwards, swirlers were mounted in the Sector and the flow check was repeated directly inside the rig: in this case, P_{up} and P_{dw} were the static pressure measured upstream the swirler plate and in *Plane 40* (due to the low Mach number in these two locations, the static pressure can be used as an approximation of the total pressure). Tests were carried out for a reduced pressure range due to rig constrains; an equal split of the mainflow among the three swirlers was supposed during the data reduction.

Results are displayed in figure 8.2 ($\bullet$): the trend is in very good agreement with data obtained from the plenum-to-plenum measurements. Plot indicates also the position of the design point ($\star$): as expected, the pressure drop is around 3.5% for the nominal mass flow rate.

Finally, data of each measured point were exploited to estimate the effective area of the swirler, defined as the area through which the actual mass flow rate (m_{act}) flows isoentropically:

$$A_{eff} = \frac{m_{act}}{\rho_{is} \cdot V_{is}} \tag{8.3}$$

Results indicate an average effective area of $1545mm^2$, affected by an averaged relative error of 2.6%: the agreement with numerical data is very good, being below the 3% the discrepancy with the value considered during the design phase of the swirler.

The permeability of the multiperforated liners is defined as the ratio between the overall passage area of the effusion holes and the surface of the liner without holes; the four patches that cover the liners are quite different one from the others, in terms of effusion angles, L/D and

streamwise pitch, therefore they were individually checked.

As explained above, using the nominal hole diameter may introduce large errors in the estimate of the overall permeability. Therefore, the procedure employed for the flow check of the swirlers was applied patch by patch, while the remaining ones were closed with duct tape: varying the pressure drop between the coolant feeding cavity and *Plane 40*, the flow function and the effective area was calculated for each patch of the liner. To go back from the effective area to the actual geometrical area, necessary for the calculation of the permeability, a representative value of the effusion hole discharge coefficient was assumed ($C_d = 0.70$, [68]).

Results, summarized in table 8.1, are quite in good agreement with the target values.

Table 8.1: Outcomes of the estimate of the multiperforated liner permeabilities

Patch name	**Ext1**	**Ext2**	**Int1**	**Int2**
Target	6.68%	5.75%	8.30%	5.20%
Exp ($C_d = 0.70$)	6.70%	6.10%	8.05%	4.58%

8.2 Preliminary PIV Results

Preliminary PIV measurements were performed inside the combustor chamber to point out the characteristic flow structures generated by the swirlers and by the interaction between the mainflow and the coolant. At this early stage of the survey, measurements were performed only in isothermal condition, i.e. the reference condition for the hot wire anemometry: in fact, this condition simplified the operability of the rig and the absence of high temperature allowed to easily use the boroscopes.

To analyse how different velocity distributions of the mainflow affect the mixing with the coolant from the effusion system, and therefore the resulting hot streaks, different "ducted" configurations were investigated; as mentioned in § 6.1, the effect of the duct is that of conserving the hot swirling flow in the chamber and moving the beginning of the interaction with the coolant closer to the exit of the combustor. Several ducts of different lengths were installed at the swirler exit and were individually tested: the different configurations are named *D35*, *D45* and *D55*, where the digits correspond to the length of the duct in *mm*. Following this convention, the configuration without duct was named *D00*.

Preliminary PIV measurements were carried only on the basic configuration (*D00*) and on the one with the longest duct length (*D55*); these experimental investigations were performed in the central X-Y plane of the combustor simulator, adopting the "L" configuration indicated in figure 7.9(b)).

Figure 8.3 illustrates the characteristics of the flow field generated by the central injector for the *D00* configuration; the image reports the magnitude of the velocity normalized with respect to the maximum (V_{ref}). A full investigation of the chamber was not feasible because of the difficult optical access; therefore, to clarify the position of the measuring area in the chamber, the vector map was included within cross section of the combustor simulator.

Measurements highlight some typical flow structures of a modern

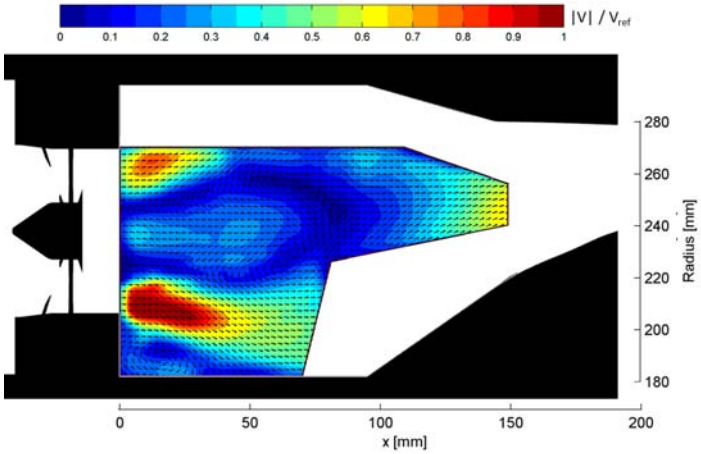

Figure 8.3: Normalized velocity magnitude in the combustor simulator (D00)

swirl-stabilized combustor, which are the corner vortex (under the inner jet) and the central recirculation zone (RCZ) generated by the vortex breakdown. The two high momentum jets exiting the swirler seems to be quite imbalanced: in fact, the velocity magnitude of the core of the inner jet is roughly 20% greater than the outer jet. A more deep analysis of the PIV images acquired during the tests pointed out the presence of a glare in correspondence of the outer radius of the swirler, which slightly biased the local measured velocity. From a comparison with images not affected by this glare, an error of about 12-15% was estimated on the evaluation of the velocity of the outer jet. However, including also this uncertainty range, a slightly imbalance between the two jet is still present and it is related to the shape of the RCZ (see below).

With respect to radial swirlers (for instance, see the work of Sedalor et al. [155] or Andreini et al. [137]), the axial swirler impresses a small radial momentum to the jets, which exit the injector with a low angle with respect to the axial direction; consequently, the impingement phenomenon of the jet on the liners, typical of the radial swilers, is not

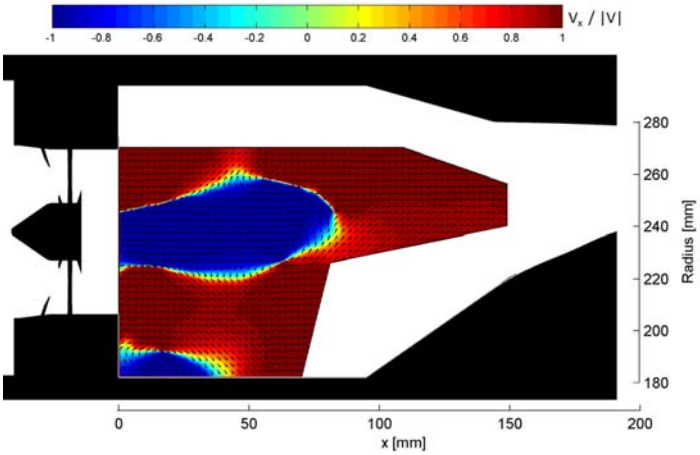

Figure 8.4: Normalized axial velocity in the combustor chamber (D00)

present. Furthermore, focusing on the inner jet, a rapid deceleration of the mainflow can be observed, which starts around the first row of effusion holes, $45mm$ downstream the swirler plate.

Keeping the focus on fig. 8.3, the central recirculation zone is well defined around the axis of the swirler; immediately downstream the swirler exit, roughly between the two jets, measurements show a reverse flow acceleration bubble: this acceleration, due to the passage area reduction caused by the jets, indicates that the closure of the RCZ is very close to the swirler itself, inside the small room between it and the "actual" inlet of the combustor chamber. Finally, an acceleration of the flow is visible also at the outlet of the chamber: it is caused by both the presence of the outer and inner cooling flows, and the vena contraction caused by the shape of the inner liner.

Figure 8.4 shows the axial velocity component (V_x) normalized with the local value of velocity magnitude: this picture highlights the extension of the central and the corner recirculation zones. The central RCZ is slightly lifted off by the presence of the inner coolant injections and the convergent inner liner: this phenomenon is probably the reason that

explain the slight imbalance of the two jets from the swirler. The image indicates also that the flow is mainly axial, except for a small area between the two RCZ and the region close to the inner wall, in correspondence of the convergent section at the combustor exit.

The flow field obtained with the *D55* is displayed in figure 8.5 in terms of normalized velocity module; the two jet coming from the duct are still imbalanced, but, differently from the *D00* configuration, the outer one is the more intense. On the other hand, the inner jet is smaller and, due to the presence of the liner, seems more pressed to the duct; moreover, it is early deviated towards the acceleration zone, visible roughly in the center of the vena on the right side of the measuring area.

The central recirculation zone is highlighted in figure 8.6, which shown the normalized axial velocity component: the central RCZ is completely de-attached from the duct and it is quite small with respect to the no-duct configuration. However, it is reasonable to suppose that a larger recirculation zone is located inside the duct, downstream the swirler exit.

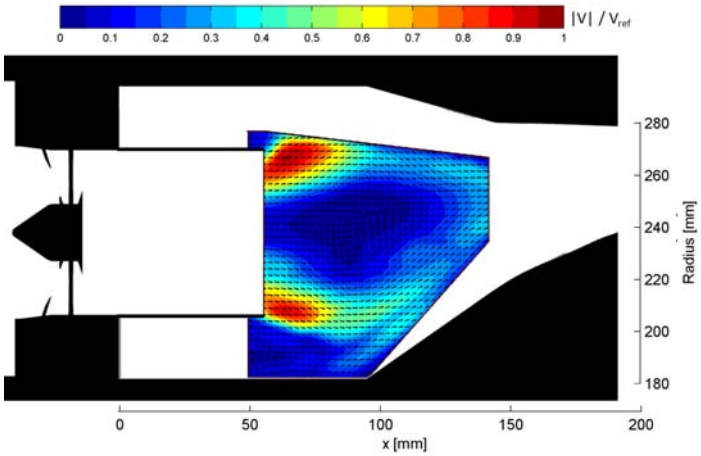

Figure 8.5: Normalized velocity magnitude in the combustor simulator (D55)

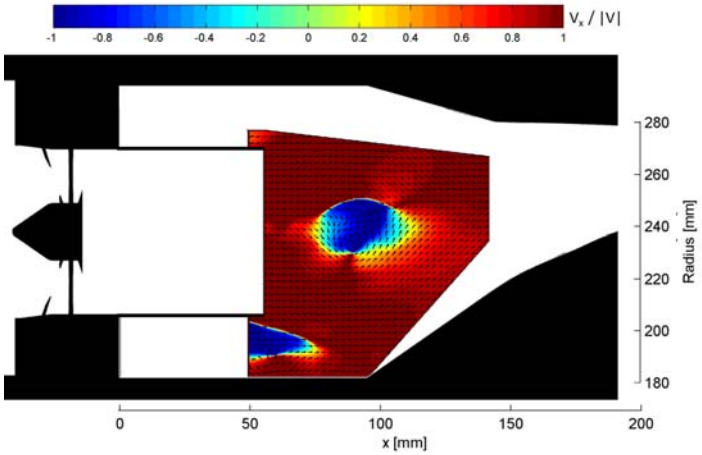

Figure 8.6: Normalized axial velocity in the combustor chamber (D55)

In addition, the last portion of a further RCZ is confined between the duct and the inner liner. Finally, the image shows the mainstream lift off close to the inner liner due to the coolant injection and the shape of the wall.

As mentioned above, this preliminary investigation will be completed in later stages of the experimental campaign: further measurements will be carried out imposing the design working conditions, and a comparison with the isothermal results presented here will highlight the impact of coolant-to-mainstream density ratio on the mixing of the two flows and on the evolution flow field.

8.3 Aerothermal Flow Field at the Combustor Exit

The previous session showed that, as expected, the addition of a duct at the swirler exit deeply alters the flow field inside the combustor chamber. In this section, the effects of the different duct lengths on the aerothermal field at the combustor exit (*Plane 40*) will be pointed out by the use of a 5-hole probe and a fast response thermocouple. Four different duct lengths will be testes: *D00*, *D35*, *D45* and *D55*. Results will be compared also with the reference target temperature and flow angle profiles set within project.

8.3.1 Thermal field

Figure 8.7 shows the temperature field measured in *Plane 40* for all the tested configurations, together with the target; temperature are normalized with the mean adiabatic temperature in *P40* ($\overline{T}_{P40}$=450K). From an overall point of view, experimental data highlights that the hot spot is definitively less marked than the target: in fact, to point out the differences among the tested configurations, the scale of the color bar of the picture was quite resized with respect to previous visualizations (see fig. 6.3(a)). This first general results indicates that the fidelity of the computational techniques adopted for the design of the combustor simulator are not adequate. The marked hot spot predicted by steady RANS calculations, not visible in the experiments, points out that such numerical approach is not suitable to accurately reproduce the intense mixing inside a combustor chamber. On the other hand, preliminary LES calculations performed by *Cerfacs/Turbomeca* (not shown here), are much more in agreement with experiments, highlighting that advanced unsteady computational tools must be use to have a reliable predictions of the turbulent mixing of the swirled flow in a lean combustor chamber.

The thermal field resulting from the *D00* configuration (fig. 8.7(b)) is characterized by a thin strip of hot flow, located around the middle radius, that crosses the entire tangential extension of the central sector area and it is not bounded on the lateral sides. This is a consequence of

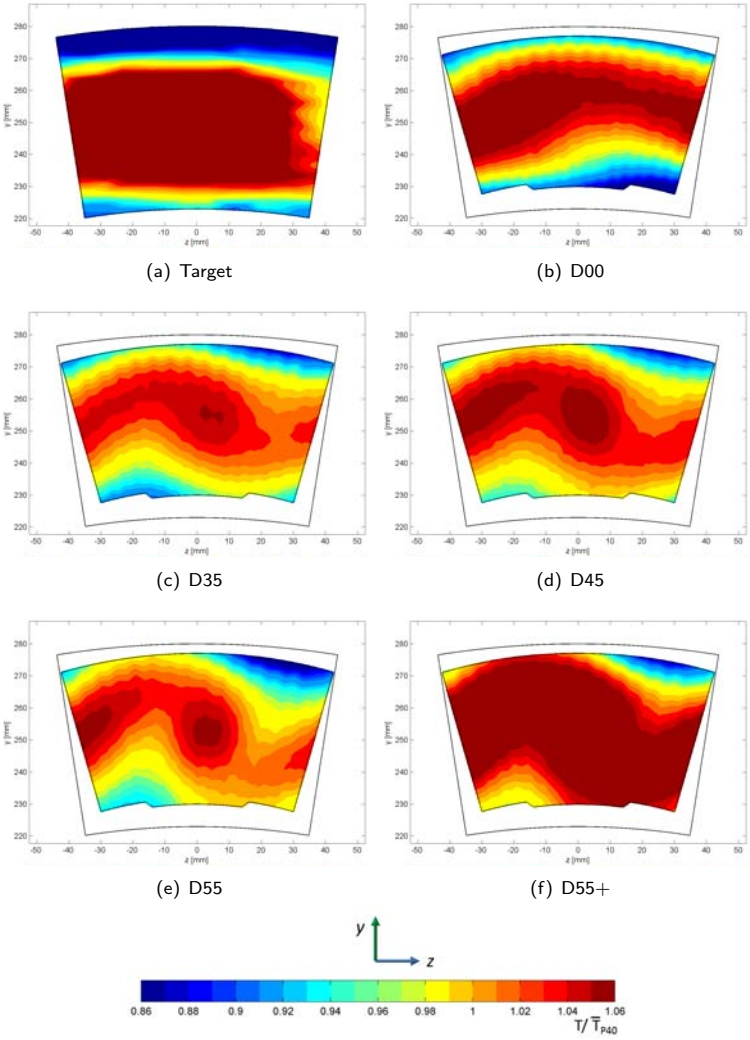

Figure 8.7: Normalized temperature field in Plane 40

the development of the flow field in the combustor chamber, whose main characteristics were highlighted by the PIV measurements and confirmed by CFD calculation performed by *Cerfacs/Turbomeca* for the nominal condition: the wide jet opening at the swirler exit generates a large hot zone which covers, in the proximity of the swirler plate, almost the whole chamber heigh. In correspondence of the first rows of effusion cooling, located roughly at one third of the chamber length, the hot flow rapidly becomes confined in the central area of the chamber due to the coolant injection. Actually, in the first part of the chamber, the swirling flow dissipates a great part of its tangential momentum: therefore, the closure of the hot recirculation zone is quite far from *P40*, and the strong mixing with the coolant, which starts downstream the RCZ closure, quickly lowers down the temperature of the mainflow. This phenomenon is sketched in figure 8.8(a). Numerical calculations indicated that this behaviour is almost the same in the planes between two adjacent sectors, which justifies the presence of a hot streak unconfined on the lateral sides.

In addition, experimental data point out that the impact of the coolant on the temperature distribution is pretty marked, especially in the inner side: considering that the 5-hole probe does not allow to measure too close to the wall (see § 7.1.1), the extension of the cooling layer is quite large, as indicated by the dark blue area appearing on right corner. Fi-

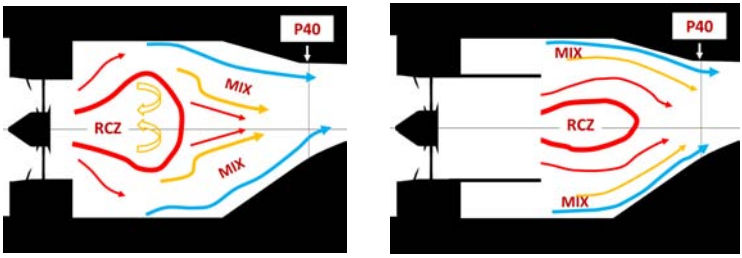

(a) D00 (b) D55

Figure 8.8: Sketch of the evolution of the mainflow in the combustor for two different swirler configurations

nally, the wavy shape of the hot streak is due to the interaction between the high-momentum coolant layer and the swirling mainflow, which is rotating clockwise with respect to the pictures. This wavy shape of the hot flow, ascribable to the rotation impressed by the swirler, is definitively much more "physical" with respect to the flat hot spot of the target; it important to recall that, as indicated in § 6.1, the aim of the target was just to set a reference for the design process of the combustor simulator.

The thermal fields resulting from the ducted configurations, displayed in figures 8.7(c) - 8.7(e), show a hot spot which is more marked with respect to the *D00*, even if it is still quite smaller if compared with the target. This is due to a different development of the flow field in the chamber, described in § 8.2 and sketched in figure 8.8(b): due to the presence of the duct, the RCZ is narrower in comparison with the one without duct, but it closure is nearer to the combustor exit. Consequently, the hot swirling flow is conserved up to the measurement plane, while the region of mixing with the coolant is more bounded, and the coolant layer in *P40* is more confined as well.

The temperature fields generated by all the tested ducts have the same main features, which are a central "circular" spot within a wavy hot region around the middle radius: even if the differences between the three configurations are not that marked, results confirms that the effects of a longer duct are: the hot spot is more marked and the temperature level in the central area is higher; the tangential momentum of the mainflow is more conserved, resulting in a more cambered hot flow; the mixing with the effusion flow is more intense and less bounded in the regions close to the liners.

A further test was carried out to assess the impact of the mainflow temperature: keeping the same flow split and the longest duct, mainstream temperature was increased of $30K$. Results of this configuration, named *D55+*, are displayed in figure 8.7(f): mainstream temperature does not affect the flow field, whose structure remains unchanged, while, as expected, the temperature of the central hot region is raised up.

The representation of the temperature field adopted in figure 8.7 is

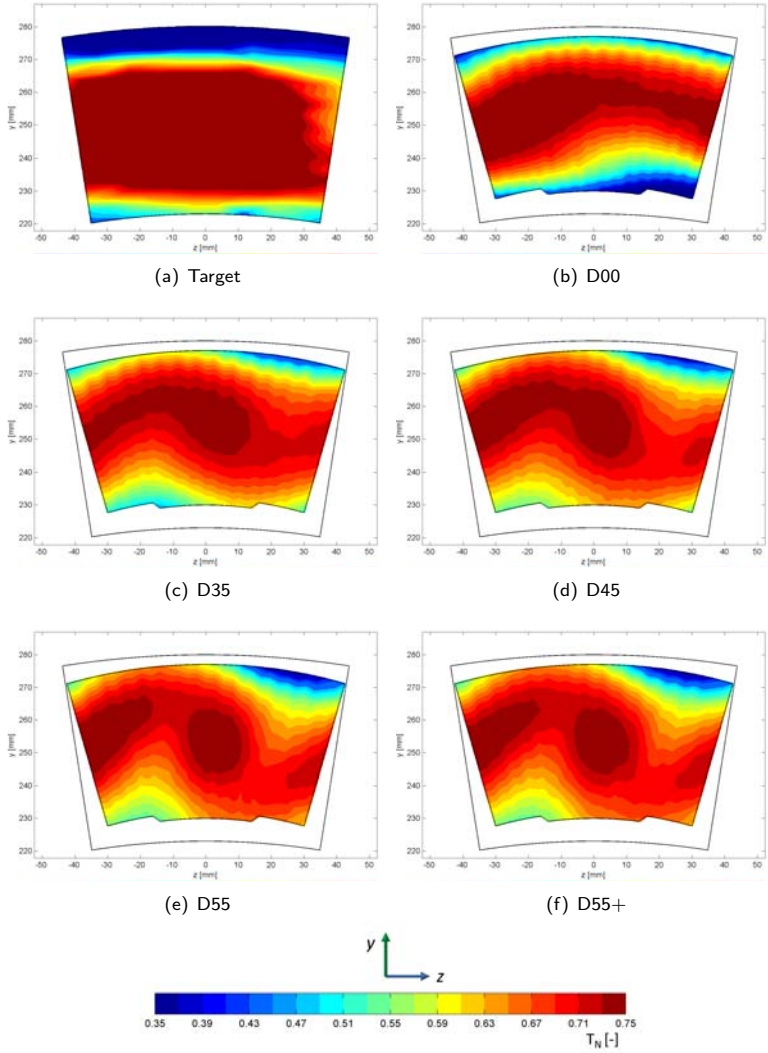

Figure 8.9: Non-dimensional temperature (T_N) field in Plane 40

slightly biased by a limit of the test facility: the chiller installed at the compressor exit delivers air at room temperature, precluding the possibility to set its value at the desired level. As a consequence, the coolant temperature depends on the ambient temperature and it was not exactly the same in all the tests. To overcome this limit, a further normalized temperature is defined as:

$$T_N = \frac{T - T_{cool}}{T_{main} - T_{cool}} \tag{8.4}$$

where T_{main} and T_{cool} are measured respectively upstream the swirlers and inside the coolant cavities. Figure 8.9 shows the temperature distributions obtained introducing this new variable: maps point out that the topology of the non-dimensional thermal fields obtained by the three ducted configuration and the *D55+* is almost the same (exactly the same for the two working conditions of *D55*).

Temperature data were circumferentially averaged and results are shown in figure 8.10 in terms of T_N along the relative radius in *Plane 40*: as highlighted by the 2D maps (fig. 8.7), the thick layer of inner

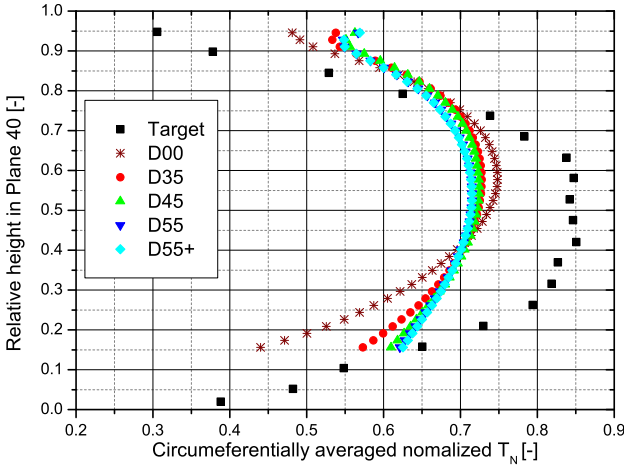

Figure 8.10: Trends of normalized temperature

coolant push the peak temperature towards the 60% height of the outlet section rather than in the center (as in the target profile), which roughly correspond to the axis of the swirler. Moreover, the impact of the mixing with cooling flows causes both lower peak values and a general shifting of the curves towards colder temperatures, which is more emphasized in the area close to the hub.

Plot shows that the *D00* configuration presents the highest peak value: looking at the 2D maps, it is clear that this is a consequence of a non-bounded hot spot that covers the whole tangential extension of the investigation plane. Averaged temperature profiles of the ducted configurations are almost the same; slight difference can be observed for the *D35*, which presents lower temperatures close to the inner liner: as indicated by the maps, the mixing obtained with the shorter duct is less intense and the resulting coolant layer is more bounded.

Finally, figure 8.11 displays the temperature profiles extracted along some investigation lines, whose positions are depicted in fig. 8.11(a). Pitch angles (β) indicated in the picture represent the two swirlers/vanes clocking positions that will be investigated in the full annular rig: hot spot aligned with the vane leading edge ($\beta = 0°$) and with the centre of the vane passage ($\beta = |4.5|°$). Plots highlight the radial and tangential normalized temperature distortions for the *D00* and the *D55* configurations. Focusing on the tangential profiles, *D00* results (fig. 8.11(b)) point out that the thermal distortion at 50% height of *Plane 40* is almost zero, while it is more defined close to the outer wall; moving to the lowest radii, temperature profiles drops quickly, especially in correspondence of the positive β angles. Temperature levels for the *D55* (fig. 8.11(c)) are higher, even close to the inner wall, and the distortion at half channel is more pronounced with respect to the previous configuration. Distributions close to the walls are coherent with the wavy shape of the hot flow indicated by the 2D maps. Moving to the radial profiles, trends of *D00* (fig. 8.11(d)) indicate that the peak value moves radially but, as mentioned before, its value remains almost constant. Concerning *D55* (fig. 8.11(e)), the differences among the profiles are more marked: peak

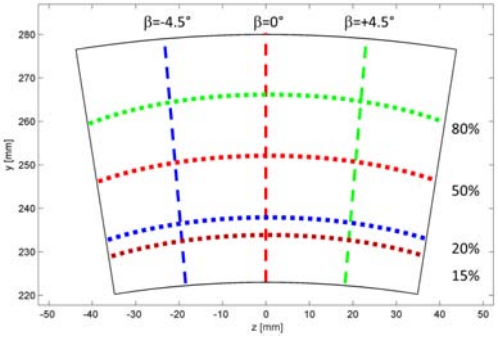

(a) Positions of the investigation lines

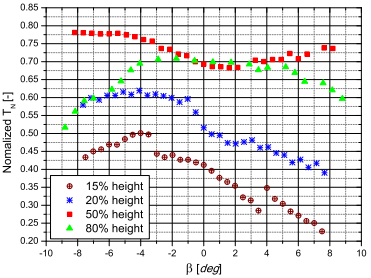

(b) D00 - T_N tangential profiles

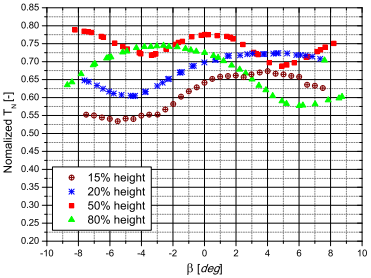

(c) D55 - T_N tangential profiles

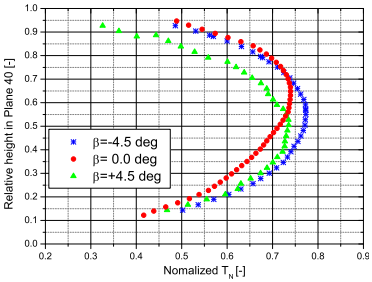

(d) D00 - T_N radial profiles

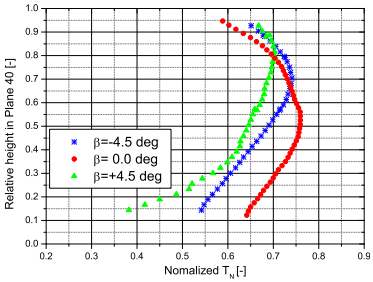

(e) D55 - T_N radial profiles

Figure 8.11: Radial and tangential normalized temperature distortions

value in front of the swirler (β=0°) is more emphasized with respect to lateral ones both at mid height of the channel, and close to the inner walls.

8.3.2 Aero field

The focus will be moved to the aero-field in *Plane 40* measured by means of the 5-hole probe. One of the aims of the FACTOR project is to test the HP stage subjected to an aggressive swirled flow coming from the combustor, in order to simulate realistic operating conditions at the turbine inlet. Consequently, special attention is paid to the flow angle distributions in *Plane 40* and, similarly to the thermal field, the terms of comparison will be the target profile set in the early stages of the project.

Figure 8.12 shows the measured Mach number and the velocity vectors in *Plane 40* for the *D00* and *D55* configuration; results for the remaining ducted cases are analogous to the latter one. Maps indicate that Mach is quite low in the entire investigation area and, recalling fig. 8.7, its distribution can directly related to the temperature field: the lowest values are located in correspondence of the hotter zones, which are the central

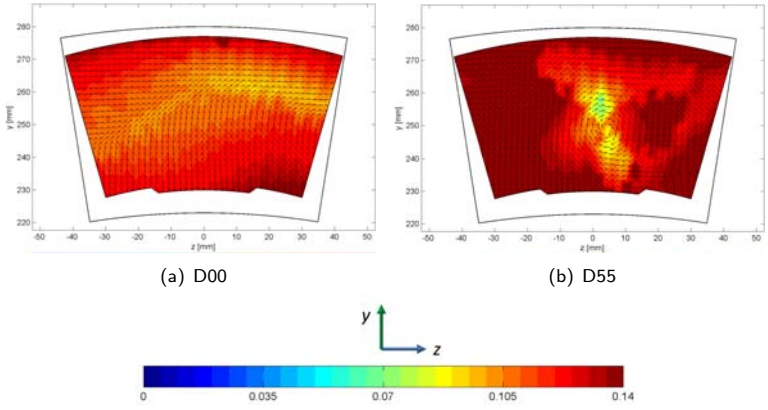

(a) D00 (b) D55

Figure 8.12: Mach number distributions in Plane 40

band crossing the whole tangential extension for the no-duct case, and the central hot spot for the 55*mm* duct configuration. Even if the differences between the lower and the higher Mach are small, maps indicate that the flow downstream the hot recirculation zone is slower that close to the walls; this is probably due to an acceleration of the coolant and the nearest flow due to the area reduction close to the combustor outlet and to the blockage made by the bulk flow coming from the swirler. In addition, velocity vectors point out that without duct, the mainstream dissipates most of the tangential momentum in the combustor chamber and it conserves only a residual overall rotation towards the right side; on the other hand, the duct preserves the rotating core of the mainstream up to the combustor exit, visible in correspondence of the area with the lowest Mach numbers.

Circumferentially averaged trends of Mach number are shown in figure 8.13: *D00* presents a quite sharper profile with respect to the ducted configurations, which instead are characterized by small variation along the radius. As it will be pointed out by the maps of swirl and pitch angles, low Mach in the at mid radius indicates a scarce remaining inertia

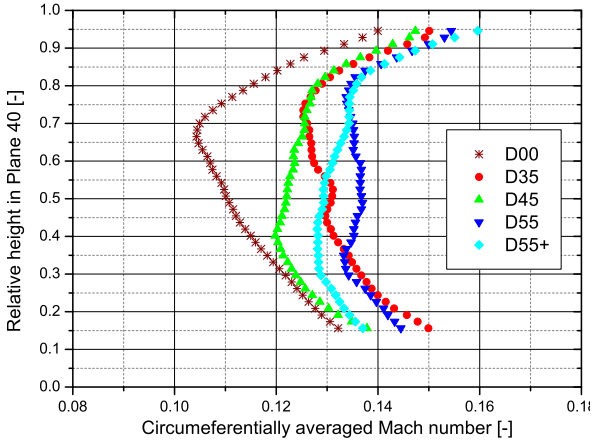

Figure 8.13: Averaged distribution of Mach number in Plane 40

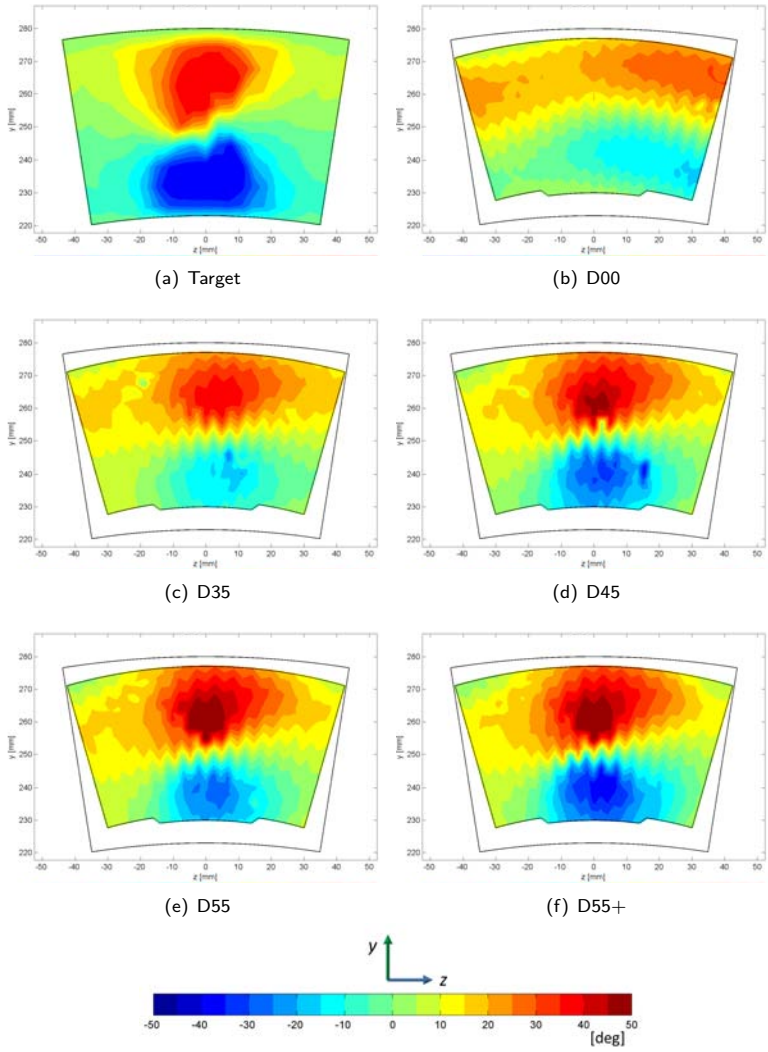

Figure 8.14: Swirl angle maps in Plane 40

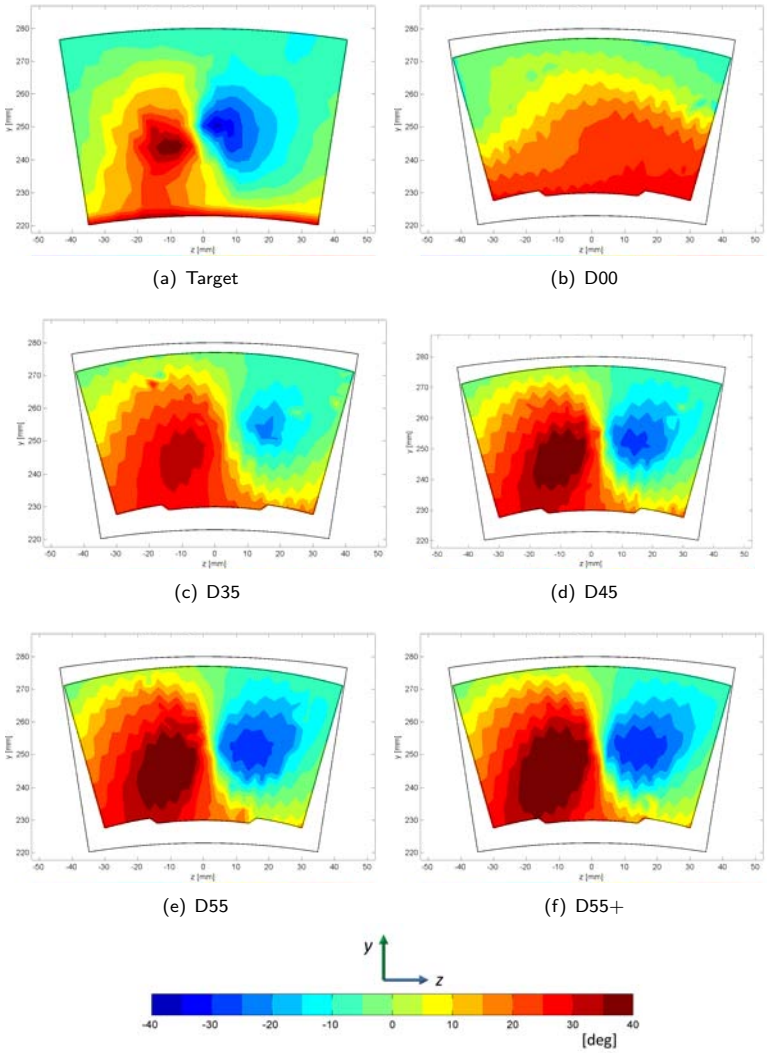

(a) Target (b) D00

(c) D35 (d) D45

(e) D55 (f) D55+

Figure 8.15: Pitch angle maps in Plane 40

of the mainflow in correspondence of the chamber outlet, which causes a more homogeneous flow field.

Figures 8.14 and 8.15 show respectively the swirl and pitch angles distributions for the target of the project and for all the tested configurations. Maps confirm the outcomes from the investigation of the thermal field: without the duct, the interaction with the coolant for the multi-perforated plate dissipates the rotating mainflow from the swirlers and it obstacles the development of a marked central region of hot rotating flow. On the other hand, the introduction of the duct reduces this effect, and the longer the duct, the more the tangential momentum of the mainflow is conserved at the chamber exit. Furthermore, these results confirms that the effect of an increase of $\approx 10\%$ of the mainstream temperature (*D55+*) alters only marginally the resulting flow field.

Finally, swirl angle radial profiles for *D00* and *D55* are shown in figure 8.16: trends are displayed for $\beta = 0°$ (swirler aligned with vane leading edge) and for $\beta = |4.5|°$ (swirler aligned with vane passage). These information are very useful for the design of cooling system of the NGV leading edge, since the swirler profile directly affects the position and the

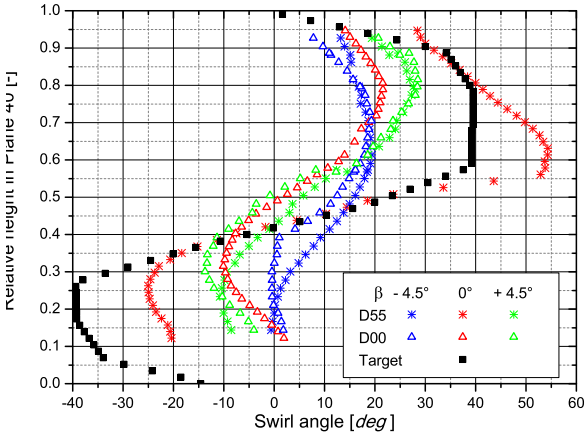

Figure 8.16: Swirl angles radial distributions

inclination of the stagnation line, and hence the pressure distribution, on the first vane row. Results indicate that the swirl angle distribution for $\beta = |4.5|^\circ$ is almost symmetric in both the configurations and that the centre of rotation of the flow (zero swirl angle) is close to the mid-radius. On the other hand, as expected from the maps, profiles for $\beta = 0^\circ$ are pretty different between the two configurations: for the *D00*, the trend is quite symmetric, centred on the mid-radius and swirl angles almost equal to the lateral profiles. *D55* presents a sharper trend, with very high swirl angles close to the outer wall, roughly doubled with respect to the inner side; the position of the center of rotation is close to half of the channel, in agreement with the target profile.

8.3.3 Fast Response Thermocouple Analysis

The fast response thermocouple (FRT) was employed only for the investigation of the thermal fields generated by $D00$ and $D55$; for each measuring point, temperature data were acquired for $4s$ with a sampling frequency of $5kHz$.

Figure 8.17 shows the field of mean normalized temperature T_N measured with the FRT: distributions appear much smoother with respect to those obtained with the 5-hole probe because of both the reduced disturb of FRT probe on the flow, and the larger amount of data to average; moreover, thanks to the little dimension of the probe, it was possible to measure very close to the inner wall.

Temperature fields measured with the two probes are in very good agreement, as indicated by the circumferentially averaged values of figure 8.18. Slight discrepancies are visible at the lowest radii, which are probably ascribable to the different position of the two probes: indeed, as indicated in § 7.1, the thermocouple of the 5-hole probe is located downstream $P40$, and the lower measured temperatures are compatible

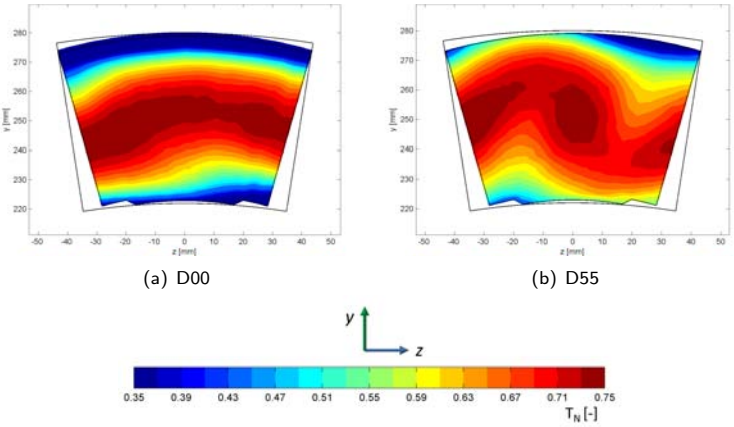

Figure 8.17: FRT analysis: mean normalized temperature field

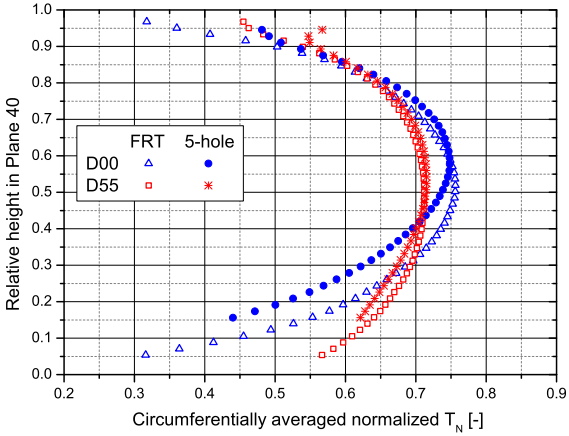

Figure 8.18: Comparison between the temperature profiles measured with the FRT and the 5-hole probe

with the progression of the mixing between coolant and mainflow, which is promoted at the inner radii by the shape of the liner.

The main purpose of using the *FRT* was measuring the temperature fluctuations: in fact, exploiting the small thermal inertia of the thermocouple, it was possible to catch flow oscillations up to $2kHz$. First of all, the areas with the largest fluctuations were identified through the estimate, for each measured point, of the maximum temperature difference, defined as:

$$\Delta T_{max} = T_{max}|_{98\%} - T_{min}|_{98\%} \tag{8.5}$$

$T_{max}|_{98\%}$ ($T_{min}|_{98\%}$) indicates that the 98% of the measured temperature are lower (higher) than this value, so that outliers are discharged; the temperature differences were normalized with the local mean values. The distributions of $\Delta T_{max}/T_{mean}$ for the two investigated configurations are displayed in figure 8.19: both the duct and unducted case show that the highest temperature fluctuations are located close to the inner wall, in correspondence of the mixing layer between the coolant and the mainstream. Here, fluctuations are around 8%-10%, roughly doubled

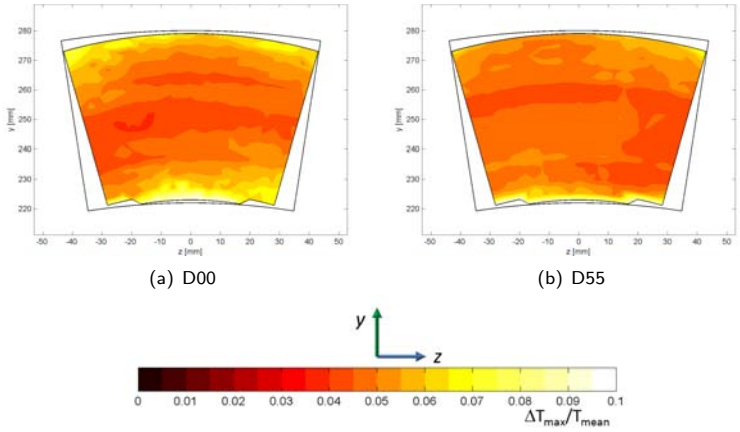

(a) D00 (b) D55

Figure 8.19: FRT analysis: non dimensional ΔT_{max} maps

with respect to the centre of the rotating flow. *D00* presents high level of temperature oscillation also close to the outer wall, which are not visible for *D55*.

Previous outcomes are proved by maps displayed in figure 8.20, which represent the root mean square deviation (T_{RMSD}) normalized with ΔT_{max}; root mean square deviation is defined as:

$$T_{RMSD} = \sqrt{\frac{\sum_i^n (T_i - T_{mean})}{n}} \tag{8.6}$$

As a statistical measure of the magnitude of a varying quantity, non-dimensional T_{RMSD} maps confirm that the main temperature variations with respect to the mean are close to the walls, especially for the *D00*.

Circumferentially averaged distributions of normalized ΔT_{max} are illustrated in figure 8.21(a): trends are analogous for *D00* and *D55*, which present the lowest value around the mid radius and the highest value at the walls; concerning the T_{RMSD} (fig. 8.21(b)), *D00* shows values roughly 25% greater than the ducted configuration.

Once assessed the presence and the location of relevant temperature-

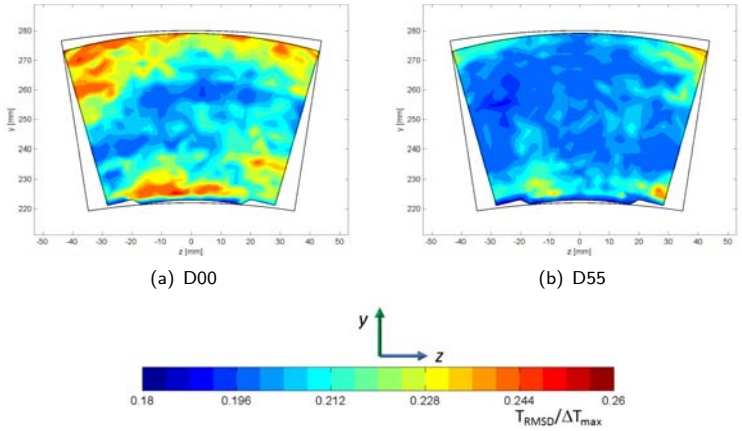

(a) D00 (b) D55

Figure 8.20: FRT analysis: normalized T_{RMSD} maps

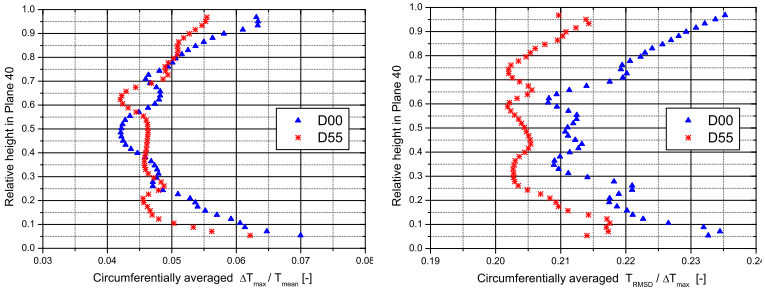

(a) $\Delta T_{max}/T_{mean}$ (b) $T_{RMSD}/\Delta T_{max}$

Figure 8.21: Estimate of temperature fluctuations: circumferentially averaged distributions

fluctuation zones, the signals acquired for some point near the inner wall were post processed by means of the discrete Fourier transform (DFT) to identify the main characteristic frequencies. An example of a measured signal is displayed in figure 8.22(a) for a point close to the wall ($D00$, $\beta = 0°$): most of the temperature fluctuations around the mean

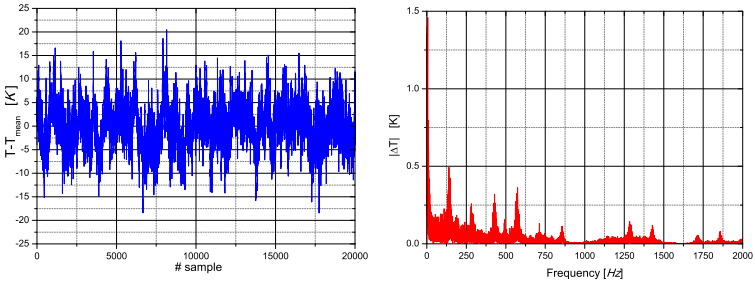

(a) Measured $T - T_{mean}$ (b) Spectrum of temperature oscillations

Figure 8.22: Temperature fluctuations analysis for a measured point close the inner wall (D00)

value lay between $5K$ and $10K$. However, the *DFT* analysis shown in fig. 8.22(b) does not highlight any characteristic frequency of the phenomenon. This result indicates that the mixing process between the coolant and the mainstream ends upstream *Plane 40*, and thus the flow close to the wall is already well mixed when it reaches the combustor outlet: in fact, despite the relevant temperature fluctuations measured in this area, the *DFT* analysis showed that these fluctuation just comes from just random oscillations of the flow.

8.4 Influence of Effusion Cooling Flow on Hot Streaks

The previous sections showed the effects of different rotating strengths of the mainflow on the generation of the hot streak and on the consequent temperature and velocity non-uniformities at the combustor exit. In this section the configuration of the swirler is kept unchanged, while the attention is focused on the effects of varying the effusion cooling mass flow rate on the hot streaks.

For this analysis, tests were performed with the *D55* configuration since, among the others, it generates the most bounded hot streak as well as high swirl angle non-uniformities in *Plane 40*. Test conditions are

Table 8.2: Effects of effusion cooling on the hot streaks: test conditions (mass flow rate are expressed in percentage of the total flow in P40)

Test name	m_{main}/m_{cool}	$m_{cool,out}$	$m_{cool,inn}$	BR_{out}	BR_{inn}
Out+20%	0.65/0.35	0.280	0.070	7.3	2.2
Out+10%		0.245	0.105	6.5	3.3
Des. Point		0.210	0.140	5.5	4.5
Out-10%		0.175	0.175	4.6	5.5
Out-20%		0.140	0.210	3.7	6.7

summarized in table 8.2: the overall flow split between the mainflow and the coolant was kept constant and equal to the design conditions: 65% mainflow, 35% coolant (Outer + Inner). Keeping this split unchanged, the Outer coolant flow rate was increased (decreased) of a certain percentage of the total cooling mass flow, while the Inner coolant was decreased (increase) of the same percentage. As an example, test named "*Out+20%*" indicates that the 20% of the overall cooling flow rate of the design point (35%·0.2=7%) was shifted from the Inner to the Outer liner: Inner coolant was decreased from 14% to 7%, while the Outer was increased from 21% to 28%. Temperatures of the two fluids were kept equal to the design conditions: in this way, the averaged adiabatic temperature in *P40* is the same for all the tests. Measurements were performed using only the 5-hole probe provided with its thermocouple.

Table 8.2 includes also the averaged blowing ratios for each test conditions: this parameter was calculated using the effective area of each effusion patch estimated during the preliminary flow checks (§ 8.1) and the measured cooling flow rates. As far as the mainstream conditions are concerned, the reference axial velocities were extracted from the numerical simulations performed by *Cerfacs/Turbomeca*. Test named "*Out-10%*" is characterized by the same mass flow on the two sides; however, the effusion blowing ratios are not the same because of the different porosity of the two liners. The range of BR under investigation indicates that the effusion jets always work in penetration regime, and it recalls the analy-

sis performed in Chapter 4: while in the former part of this research the effusion cooling was studied in details, the purpose of this survey is to highlight how it affects the hot streaks at the combustor exit varying the operative conditions.

Figure 8.23 shows maps of non-dimensional temperature T_N (eq. 8.4) measured in *Plane 40* for the design point and the four tested conditions of table 8.2. From an overall point of view, the dependency of the shape and of the extension of the hot streak from the coolant distribution is well marked and, as a general results, the hot core moves towards the liner with the smaller cooling flow.

Focusing on the tests *Out+20%* and *Out+10%* (figures 8.23(b) and 8.23(c)), it is possible to observe how the high penetration of the effusion jets and the resulting large amount of outer cooling flow at the combustor exit "push" the hot swirling flow to the inner liner. The extension of the hot spot is definitively enlarged and, furthermore, the interaction of the outer coolant and the mainflow is well marked, especially in the right corner: here, a low temperature area, which extends almost up to the mid radius, is caused by the drawing of the coolant by the swirling flow. In addition, similarly to the design conditions, the cold "compact" layer close to the outer liners indicates that the mixing between the two flows is only marginal in the proximity of the wall. Concerning the inner side, the use of the 5-hole probe does not allow to measure too close to the liner; however, it is reasonable to suppose that due to the low-penetration of the jets and the reduced mass flow rate, the coolant is bounded in a thin layer very close to the inner surface.

As far as tests *Out-10%* and *Out-20%* are concerned (figures 8.23(d) and 8.23(e)), results confirms that increasing the inner coolant, the hot spot moves radially towards the outer liner. However, the hot streak is not enlarged as the two previous tests: even if the outer coolant is less penetrating, it remains much more compact due to the small curvature of the outer liner, and the resulting hot streak is more bounded in the centre of the channel. For these tests, the interaction between the inner coolant

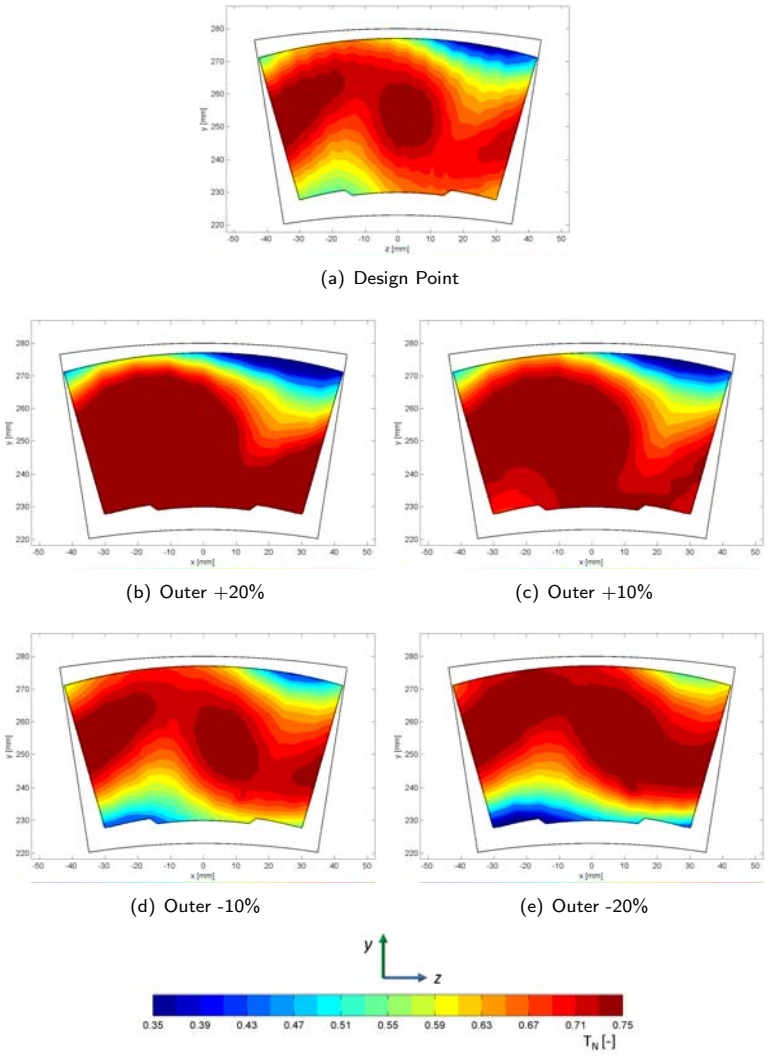

(a) Design Point

(b) Outer +20%

(c) Outer +10%

(d) Outer -10%

(e) Outer -20%

Figure 8.23: Effects of different effusion cooling regimes on the hot streaks: non dimensional temperature (T_N) fields in Plane 40 (D55)

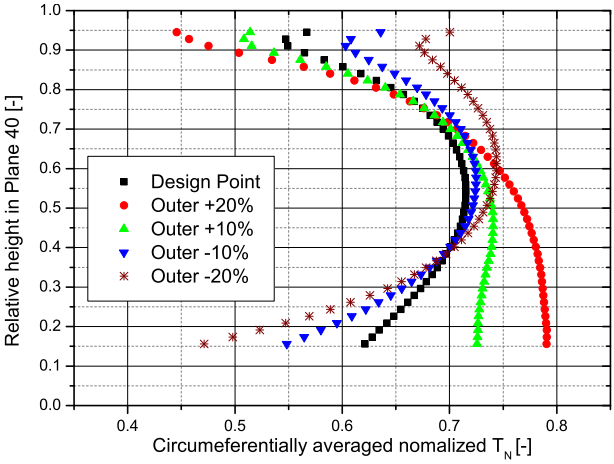

Figure 8.24: Effects of different effusion cooling regimes on the hot streaks: circumferentially averaged profiles of T_N

and the mainstream is visible on the left side; moreover, maps point out that the inner cooling layer is quite thick, since it covers roughly 1/5 of the channel height.

Figure 8.24 shows the circumferentially averaged values of T_N along the relative hight of the channel: the plot highlights that, when the outer coolant is increased, the temperature profile close to the inner wall is almost flat, set around the highest temperature values. On the other hand, trends confirms that the behaviour of the outer region is less sensitive to the flow split changes. Finally, the plot remarks that the position of the hot core moves radially towards the highest radii if the inner cooling flow rate is increased.

Figure 8.25 shows the swirl angle distributions measured in *Plane 40* for the operating conditions mentioned above. Maps confirm the behaviour of the system already pointed out by the themal fields: the rotating core moves outwards increasing the inner coolant; the outer side is less sensitive to variations of the flow split, while the inner part of the

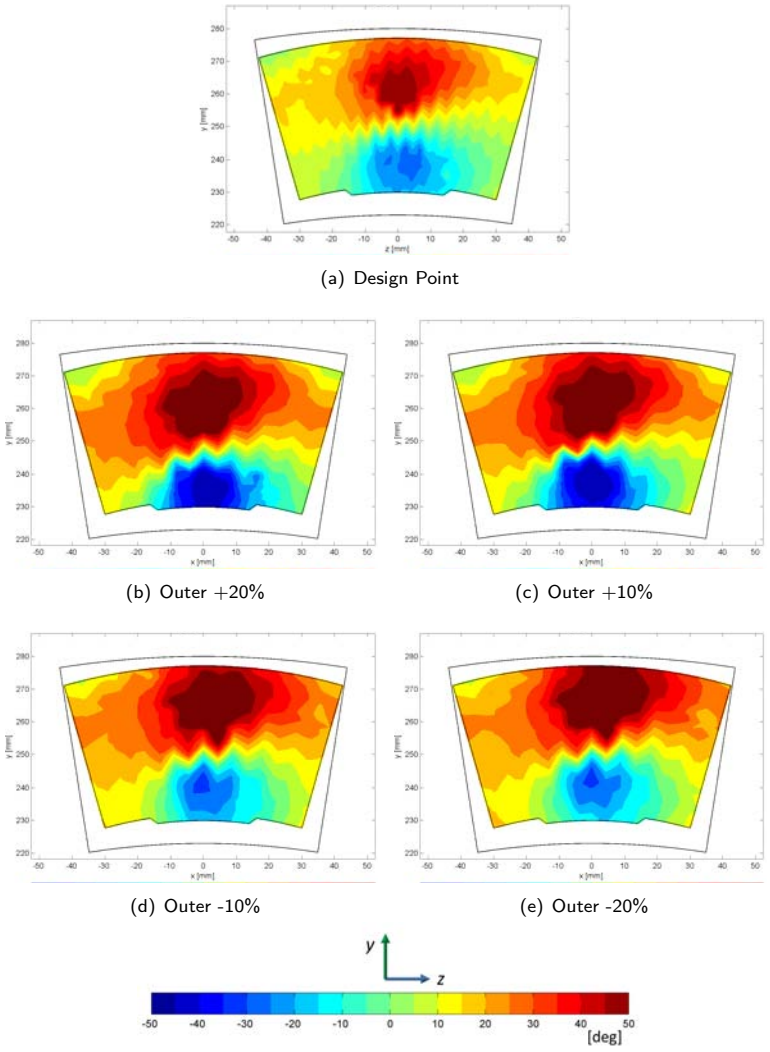

(a) Design Point

(b) Outer +20%

(c) Outer +10%

(d) Outer -10%

(e) Outer -20%

Figure 8.25: Effects of different effusion cooling regimes on the hot streaks: swirl angle contours in Plane 40 (D55)

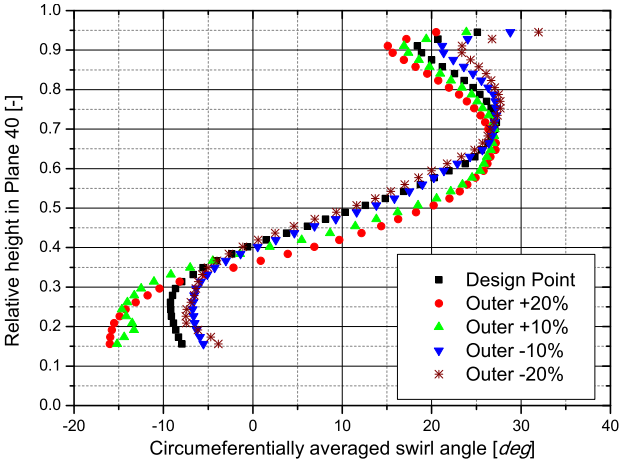

Figure 8.26: Effects of different effusion cooling regimes on the hot streaks: swirl angle circumferentially averaged profiles

swirling flow is quite damped by the combined effect of the curvature of the liner and the substantial thickness cooling layer and (e.g. fig. 8.25(e)).

Circumferentially averaged trends are displayed in figure 8.26: differences among the Design Point and the *Outer+20%* - *Outer+10%* are significant only very close to the liners, where the effect of the penetration of the jets and interaction between the coolant layer and the mainstream is more intense. On the other hand, the influence of an increase of the inner cooling flow is more important: focusing on *Outer-20%*, swirl profile is shifted of about $\approx 6^\circ - 7^\circ$ around the central radius, while this difference grows up to $\approx 10^\circ$ close to the inner liner. As mentioned above, such changes have a strong impact on the resulting pressure distribution, and hence on the design, on the NGV of the high pressure turbine.

8.5 Concluding Remarks

This chapter presented the experimental survey carried out in the Sector rig, an annular three sector combustor simulator which reproduces a

lean burn combustor chamber cooled by an effusion system. The rig, 1:1 scaled and operated in engine-representative conditions, was aimed at the characterization of the mixing between the hot swirling mainflow and the coolant, and the resulting generation of hot streaks at its outlet section. Several geometries of the swirlers were tested in order to analyse the impact on the hot streaks of different intensities of the mainstream tangential momentum, i.e. rotation of the main flow; moreover, several operating regimes of the effusion cooling were investigated to assess the effects of varying the effusion blowing ratio on the aerothermal field at the exit of the chamber.

Initially, the flow field inside the chamber was investigated by means of endoscopic PIV; measurements highlighted the characteristic flow structures of a modern swirl-stabilized combustor, which are the high momentum jets exiting the swirlers and the central recirculation zone generated by the vortex breakdown. The effects of the coolant injection on the flow field are visible in last part of the chamber, close to its exit, where the coolant layer becomes thicker.

The investigation on the hot streaks was focused on the outlet section of the combustor chamber; measurements in *Plane 40*, which represents the combustor-HP turbine interface, were carried out by means of a 5-hole probe and a fast response thermocouple; the aim was the analysis of the temperature and the aero fields resulting from the mixing between the mainstream and the coolant from the effusion system.

In the first part of the survey, several geometries of the swirler were tested. Detailed results pointed out that an increase in the tangential momentum of the mainflow generates more bounded hot streaks; measurements indicated also that, due to the absence of the dilution holes, that usually promote the mixing in the chamber, the coolant layer from the effusion system remains packed close to the liner, and the interaction with the mainstream is not extended to the whole passage area. This causes a well marked temperature profile at the combustor exit, especially if compared with typical “flat” profiles of RQL combustors. Concerning the flow field, measurements highlighted that the tangential momentum

of the mainstream impressed by the swirler is weakly dissipated by the interaction with the coolant, resulting in a highly rotating flow at the combustor exit.

Afterwards, the attention was focused on the investigation of the effects of effusion cooling flow on the hot streaks: temperature and swirl angle distributions at the combustor exit were measured varying the flow split (i.e. effusion blowing ratio) between the outer and the inner coolant. Results pointed out that the inner cooling flow rate has a strong impact on the resulting thermal field: increasing this coolant flow rate, the hot streak moves radially outwards and it becomes more bounded in the radial direction. On the other hand, the behaviour of outer side was shown to be less sensitive to variations of the flow split. Concerning the swirl angle, measurements indicated that an increase of the inner cooling flow, i.e. more penetrating jets, damps the rotation of the hot streak at the combustor exit. Similarly to the temperature field, the behaviour of the outer side is less affected by these changes in the operative conditions.

The information collected in this survey allowed to increase the knowledge on the hot streak in an engine-representative lean burn combustor and, moreover, on the effects of effusion cooling flow on the resulting combustor exit non-uniformities. Although the outcomes of the investigation cannot directly be used for the combustor design, the obtained wide database is valuable in benchmarking computational predictions, especially for advanced CFD techniques such as LES. Anyhow, these first results highlighted that the standard industrial steady-RANS approach, used for the design of the combustor simulator, is not suitable to predict with sufficient accuracy the mixing process inside the chamber: in fact, experiments indicated that the hot streak is definitively less marked and intense than the one estimated by the numerical simulations.

In later stages, results presented in this work will be further deepen and extended with new investigations and using different measurements techniques, such as hot wire anemometry.

Conclusions

The research activity presented in this dissertation was set up to deepen the knowledge and draw guidelines for the design of combustors for ultra-low NO_x aeroengine. Indeed, the development of high-efficiency low-emission gas turbines for aircraft propulsion is an up-to-date topic in which all engine manufacturers are putting strong efforts in view of the demanding legislation limits set by ICAO-CAEP.

In the current scenario, lean combustion systems are considered the most effective technology for a significant reduction of polluting emissions in future aeroengines, especially as far as NO_x are concerned. In order to meet the new requirements introduced by these innovative systems, a complete review of the combustor architecture and of its main features is of outstanding importance.

In particular, to obtain a lean combustion, up to 70% of the overall air mass flow is utilized for fuel preparation and the initiation of lean combustion, at the expense of cooling air, which is severely reduced. Furthermore, cycle parameters as overall pressure ratio and turbine inlet temperature are continuously rising to improve the engine performance, which leads to an increase of the thermal load at the combustor wall. For that reason lean combustors require very efficient cooling schemes to cope life targets. In addition, lean combustor liners do not have any additional mixing ports downstream of the fuel injectors and, consequently, the resulting aerothermal field which develops inside the chamber is completely changed with respect to current RQL combustor. Indeed, temperature and velocity non-uniformities at the combustor exit have a sensitive im-

pact on the high pressure stage, since they directly affect the turbine life and performance, and thus a deep understanding is necessary when optimising the design of new HP turbines and combustors of lean burn engines.

The design of efficient and reliable lean burn combustors requires very detailed knowledge about parameters influencing new cooling system performance and, moreover, about the hot streaks exiting the combustor chamber. Furthermore, it is necessary to fulfil the lack of experimental data on these innovative combustors, in view of validating advanced computational modelling and of increasing the industrial experience. Meeting these needs represents the objectives of the investigations carried out in this work, which was aimed at deepening the understanding of some phenomena involved in the lean combustor and at collecting new detailed experimental data. The test rigs and the experimental procedures developed in this work, as well as their integration with numerical activities, were directed to provide useful information for the design of a low emission combustor, as well as to indicate general guidelines to update the current design tools.

Initially, the focus of attention was dedicated to effusion cooling systems; indeed, this innovative technology is becoming the standard choice for lean burn combustion thanks to its promising cooling capabilities with reduced coolant consumptions. The analysis was carried out by both numerical tools and experimental tests. A one-dimensional thermal procedure, dedicated to the conjugated fluid-metal calculation for combustor cooling systems, was enhanced to easily manage the geometrical modelling of a combustor; the procedure was then applied to a real engine effusion-based cooling scheme in order to assess, through a comparison with available experimental data, its reliability in predicting the performance of an effusion cooling system.

The modelling of the effusion cooling and the improvements made on the procedure were further tested later in the work, exploiting the experimental data collected during an extensive investigation on an effusion

cooling system integrated in a typical modern combustor cooling layout. The survey was performed on a simplified effusion geometry, 3:1 scaled, provided with other typical elements of a liner, that were a slot cooling system and a dilution hole. The geometry under investigation was tested under a wide range of working conditions, in order to point out the effects of several operating parameters and to provide useful information for the design of an effusion system. The survey was motivated from a lack of experimental data available in literature concerning the effects on the effusion cooling performance of: coolant-to-mainstream density ratio; high values of blowing ratio, i.e. high penetration of the cooling jets; interaction among the effusion system and other typical features of a combustor liner. Measurements were performed by means of Thermochromic Liquid Crystals and were aimed at estimating the heat transfer coefficient and the adiabatic effectiveness of both the effusion alone and entire cooling system.

Experiments highlighted the high overall efficiency of the effusion system, especially when it is coupled with the slot cooling; moreover, results indicated that the presence of a dilution jet deeply affects the film cooling distribution, i.e. the adiabatic effectiveness, but without having a strong impact on the heat transfer. In addition, the survey allowed to point out how the cooling performance of the system are driven by different operating parameters, mainly blowing, velocity and density ratios, and how changes in these parameters affect the behaviour of the system.

Afterwards, the wide obtained experimental database was exploited by the previously mentioned one-dimensional thermal procedure to validate the correlations available for effusion cooling and to deepen the analysis on the system. Using the measured experimental values of heat transfer coefficient and adiabatic effectiveness, the behaviour of the cooling arrangement was simulated under realistic engine operative conditions, in order to estimate further performance parameters such as the NHFR and the overall effectiveness.

The extensive analysis allowed to point out the effects of different operating parameters on the behaviour of the system; in addition, it high-

lighted that the combined effusion and slot system is very effective and robust from a cooling point of view for a wide range of operative conditions. These outcomes, as well as the collected experimental database, are valuable to update the design tools and to draw guidelines for the development of this system in the lean combustor environment. Furthermore, the investigation pointed out a good flexibility of effusion: consequently, this allows, during the design phase, to focus its optimization taking into account other requirements, like combustion issues, aeroacoustic or simply off-design working conditions.

Such kind of investigation, which included an effusion system integrated with realistic supporting elements tested under representative working conditions, especially in terms of density ratio, represents an innovative contribution to the research on this cooling technology. However, it is important to underline that the results are obtained with simplified mainstream conditions and without taking into account the effects of turbulence, whose level was rather lower than a real combustor; actually, recent studies showed that the presence of a highly swirling mainflow deeply affects the film cooling distribution, and hence significantly bias the performance of the effusion system. Nevertheless, the outcomes of this work provided some general information on the effusion cooling behaviour which are valid independently from the specific geometry of the injection device.

After having assessed the efficiency and the reliability of the effusion cooling and, more generally, having increased the overall fidelity on this technology, this system was integrated in the combustor and the focus was moved to the entire combustion chamber. More specifically, the analysis was aimed at investigating the mixing process between the mainstream and coolant and the generation of temperature and velocity non-uniformities (hot streaks) at the combustor exit. In order to obtain engine-representative data, such kind of analysis required that the geometry of the test rig was close to a real combustor and tested in a relevant environment; therefore, with respect to the analysis on the effusion cool-

ing geometry, an important step in TRL (Technology Readiness Level) of the experiment was necessary, which was raised from ≈ 3 to ≈ 4.

A three annular non-reactive combustor simulator was designed and instrumented for an in-depth analysis on the transport of hot streaks through the combustor chamber. The rig, 1:1 scaled, reproduced a engine-representative chamber for modern lean burn combustors, provided with liner effusion cooling; moreover, it was operated in a relevant environment to have a representative mixing between the hot swirling mainflow and the coolant. In the author's knowledge, the test rig developed within this work is the unique annular lean burn combustor simulator with such features. In accordance with the objectives outlined at the beginning of the work, this facility allowed to perform extensive investigations of the aerodynamic and thermal fields in the combustor chamber. Moreover, being a non-reactive rig, the facility allowed the use several experimental techniques in order to perform detailed measurements: within this work, endoscopic PIV was employed to investigate the flow field inside the chamber, while a 5-hole probe and a fast response thermocouple were used to explore the temperature and the velocity fields at the combustor exit. Several geometries of the swirlers were tested in order to analyse the impact of different intensities of the mainstream tangential momentum, i.e. rotation of the main flow, on the mixing. As a general results, the temperature and the velocity profiles observed at the outlet section are definitely far from the "flat" profiles of current RQL combustor: the absence of the dilution holes reduces the mixing between the hot and cold flows, resulting in a central hot core which keeps a significant part of the tangential momentum impressed by the swirler, and a bounded coolant layer which mainly remains close to the liner.

Furthermore, recalling the first part of the research, the attention was focused also on the effects of the effusion cooling flow on the hot streaks: the impact of the cooling system on the aerothermal field at the exit of the chamber was investigated varying the operating regime, i.e. the blowing ratio, of the effusion jets. Results pointed out that the extension and the position of the hot streak is deeply affected by the working condi-

tions of the inner liner cooling system; on the other hand, the behaviour of outer side was shown to be less sensitive to such kind of variations.

The information collected in this survey allowed to increase the knowledge on the hot streak in an engine-representative lean burn combustor and, moreover, on the effects of effusion cooling flow on the resulting combustor exit non-uniformities. Although the outcomes of the investigation cannot directly be used for the combustor design, the obtained wide database is valuable in benchmarking computational predictions, especially for advanced CFD techniques such as LES. Anyhow, these first results highlighted that the standard industrial steady-RANS approach is not suitable to predict with sufficient accuracy the mixing process inside the chamber and the behaviour of the resulting hot streaks at its outlet.

In accordance with the current scenario of modern aeroengine combustors and with objectives outlined at the early stages of this work, the extensive investigation led in this study contributed to increase the comprehension of the effusion cooling behaviour and of the mixing process inside a lean burn combustor; moreover, the survey extended the available experimental data of such type of low emission combustors. Clearly, the analysis on these system is not concluded; a deeper understanding is necessary to increase the confidence and to proceed to a reliable design. However, in this context, the facility set up within this work can be further exploited to increase the database both by means of investigations in the combustor chamber, and through dedicated analysis of the effusion system integrated in a realistic lean combustor environment.

In the short term, new tests are planned in the test rig: to have a close comparison with advanced LES codes, new experiments will be carried out to perform unsteady measurements such as hot wire anemometry and time-resolved PIV.

Appendix

Appendix A

Therm1D Analysis on the MobRig combustor

A.1 Geometry of the MobRig

The analysis carried out on the NEWAC combustor cooling system (§ 3.2.1) was aimed at assessing the capability of the new features of the revised procedure, especially in terms of handling the combustor geometry. Following the obtained good results, *Therm1D* was employed to study a test case characterized by a more complex geometry, named *MobRig*. The tubular test rig was developed by *Avio Aero* to test burners for aeroengine annular combustor; most of the tests were carried out using innovative injectors based on the PERM technology. In addition, the rig is equipped with several pressure and temperature probes to gather data during the experiments: beyond monitoring the system, experimental data are used also as a comparison to assess the reliability and the performance of numerical CFD codes in predicting the combustor behaviour.

First developed within the European project LOW NOx II, the test rig has been recently upgraded within the European project TECC-AE. The major changes concerns the cooling arrangement, which now includes a modern effusion system. A sketch of the test rig is depicted in figure A.1. Air enters the test rig from a feeding pipe located in correspondence of the

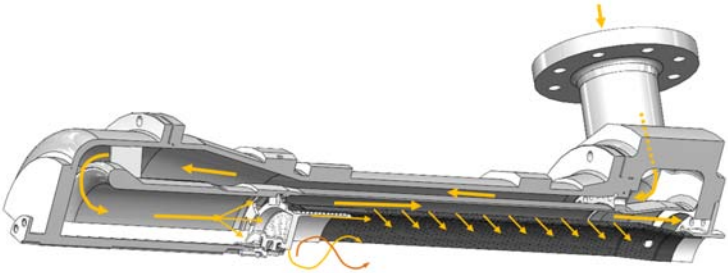

Figure A.1: Sketch of the MobRig

burnt gas outlet section; after crossing a calibrated orifice, air accesses into a "first" annulus, aimed at delivering the flow at the opposite side of the rig; after a 180° bend, air reaches a plenum where it is split into three streams: one feeds the injector, the other feeds the dome cooling system and the third is dedicated to the liner cooling. The dome cooling system is made up of an impingement array; similarly to the NEWAC combustor, exhaust air is collected and directed towards the liner with the aim of generating a slot film cooling to protect its first part. The passage between the heat shied and the liner is quite longer than in NEWAC combustor and it is provided with ribs: this solution helps the cooling of the heat shield in this area which is far from the impingement plate and that, otherwise, would have been cooled only by forced convection. The remaining mass flow is dedicated to liner cooling: air crosses a calibrated orifice and enters a "second" annulus, coaxial with the first one, which feeds the effusion array, made up of by 70^{th} rows with L/d = 6 and $\alpha = 30°$. A row of dilution holes is located in the last part of the liner; in addition, a further calibrated orifice is placed at the end of the annulus to simulate a bleeding port.

The complex geometry of test rig represented a severe test to assess the capability of the new version of the procedure in terms of geometry management; in fact, while it would not have been easily reproduced with the previous version of the code, the new code allows an accurate and

simple representation of the rig with the help of a its cad model.

Figure A.2 sketches the flow network of the MobRig: the main models employed to represent the flow path are here briefly listed:

- models to reproduce smooth channels (*TCL*), ribbed channel (*TCR*) and smooth channel with mass subtraction due to effusion holes (*SC1*);
- a model representing the impingement system for the dome cooling (*JET*);
- a model to represent the slot film cooling at the exit of the dome cooling system (*FCS*);
- several models to take into account pressure losses due to bends, sudden area changes (*BVS*), orifices (*CDP*), etc.

Once the geometrical representation of the metal parts of the combustor is completed, and consequently the fluid paths do, managing the placement of the network models comes as a result.

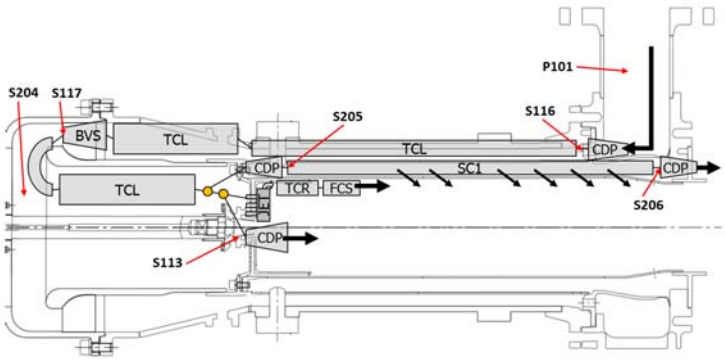

Figure A.2: Network modelling of MobRig cooling system and position of the pressure probes

A.2 Aerothermal Analysis of the MobRig

The procedure was first employed to perform an aerodynamic analysis of the rig and to compare results with a non reactive experimental test; an adiabatic run was carried out with the aim of tuning the flow network, especially in terms of discharge coefficients of the orifices located along the flow path. Concerning the C_d of effusion holes, they were estimated using the correlation proposed by Andreini et al. [68]; figure A.3 shows the trend of the discharge coefficients given by the correlation: they decrease almost linearly with the decrease of the mass flow in the annulus. Boundary conditions were given by the experimental data; in addition, experimental tests provided several pressure measurements obtained in different position of the rig, as it is depicted in figure A.2 (P# and S# correspond to total pressure and static pressure probes respectively). Data were used to check the tuning of the network; results, shown in figure A.4, indicate a very good agreement between experiments and *Therm1D*; in correspondence of the end of the flow path, this agreement is even better then that resulting from the simulation of the system by means of a

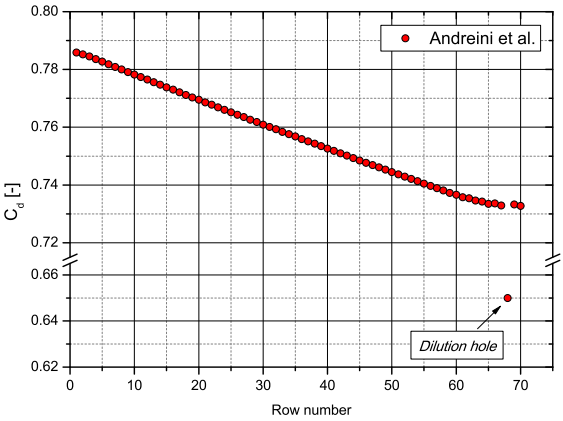

Figure A.3: Discharge coefficients of the effusion holes

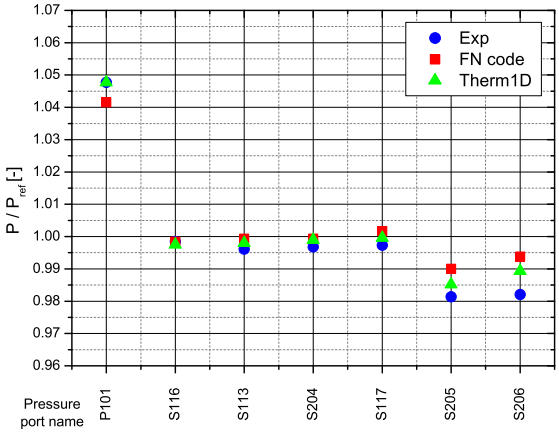

Figure A.4: Pressure distribution on the MobRig: exp. vs 1D codes

commercial fluid network solver.

Once the flow network was tuned, the procedure was employed for a thermal analysis of the whole test rig. As far as the film cooling is concerned, the correlation proposed by L'Ecuyer and Soechting [30] was selected for the estimation of the adiabatic effectiveness of the effusion holes. Regarding the slot film cooling, Goldstein's correlation [71] was chosen due to the high value of BR (≈ 5.0); similarly to the NEWAC setting (§ 3.2.1), film cooling superposition was activated up to the dilution row.

Hot gas boundary conditions are set by means of a one-dimensional distribution of pressure, temperature, velocity, FAR, etc., that describe the flame behaviour along the liner. These boundary conditions are quite difficult to be set with high accuracy since the complex flow and thermal fields within the combustor chamber are strongly three-dimensional and non uniform; furthermore, the combustion process introduces unsteady effects and the resulting flow can hardly be represented through a one-dimensional distribution without using further numerical tools. Concerning this analysis, RANS calculation were made to extract 1D

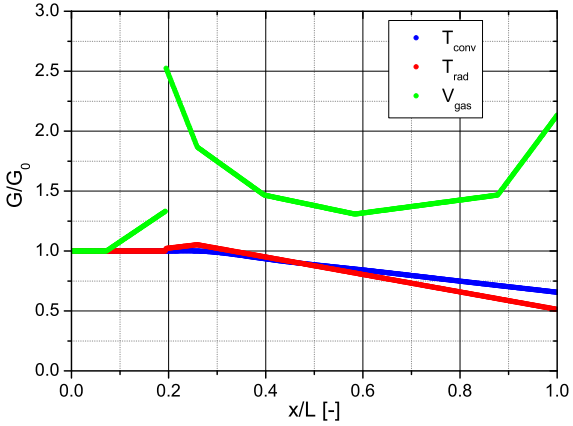

Figure A.5: Hot gas side boundary conditions

distributions of interest along the combustor. Some data are shown in figure A.5 (T_{rad} and T_{conv} is used to compute the radiative and convective loads respectively; V_{gas} is the velocity of hot gases): values are normalized with the value at the inlet of the chamber. Temperature distributions decreases towards the end of the combustor because of the mixing with the cooling air coming from the slot and the effusion holes; velocity increases in proximity of the slot coolant injection ($x/L = 0.2$) due to the interaction between the impinging jet coming from the burner, the resulting recirculation zone and the coolant injection itself. The velocity augmentation near the exit of the combustor is caused both by the increase of mass flow inside the chamber, due to the coolant injections along the liner, and by a slight reduction of the passage area in the flame tube.

Figure A.6 displays a comparison between the metal temperature distribution obtained with *Therm1D* and the experimental data measured by means of thermocouples welded on the walls; it is possible to notice a very good agreement between numerical and experimental results, except

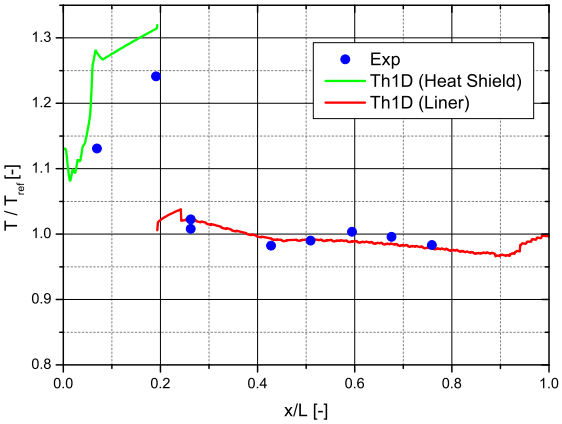

Figure A.6: MobRig metal temperature: exp. vs Th1D

a slight overestimate of *Therm1D* the end of the heat shield (in term of absolute values of temperature, it is $\approx 5\%$): this can be ascribed to a non accurate representation of the hot gases by means of a 1D trend, since in this area the heat loads are quite sensitive to the three-dimensional recirculating flow structures generated by the injector.

Appendix B

Effects of Hot Streaks on the HP turbine

This section provides a brief literature review of the effects of hot streaks on the first stage of the high pressure turbine, as well as the main secondary flows generated by the turbine inlet pressure and temperature distortions.

B.0.1 Hot Streak Migration

The preferential migration of the hot streak on the rotor pressure side was one of the first important findings. Roback and Dring [109] at LSRR studied cold and hot streak migration through a rotor passage by means of density ratio changes. The hot streak was reproduced with CO_2 and located at vane mid pitch. They observed a strong accumulation of the hot streak on the blade PS, whereas the cold streak (lower temperature than the core flow) moved towards the blade SS. The accumulation of the hot streak on the blade PS is clearly visible in figure B.1, especially if compared with a neutral profile.

The principal effect of this migration was firstly linked by Butler *et al.* [108] to the Kerrebrock-Mikolajczak effect [156]. They stated that Mach number and flow angles are roughly uniform at NGV exit, leading to a

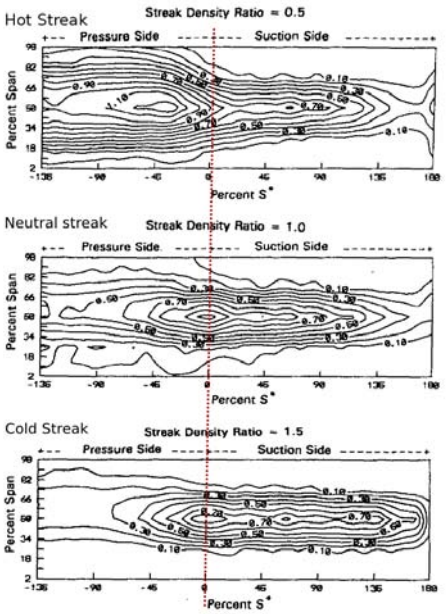

Figure B.1: Trace concentration of the hot (top), neutral (center) and cold (bottom) streak on the rotor blade SS and PS (adapted from [109])

higher absolute velocity for the hot streak as $V = M\sqrt{\gamma r T_s}$. Then, in the relative frame of reference of the rotor, the velocity of the hot streak is oriented toward the PS compared to the cooler fluid. Therefore, this preferential migration of the HS is explained by a change in incidence angle induced by the temperature difference.

Shang *et al.* [113] performed 2-D and 3-D multiblade row unsteady Euler computation on fully structured meshes, based on the MIT rig configuration described previously. The hot streak contour at midspan is shown in fig. B.2, clearly highlighting the HS path.

Roback and Dring [109] also studied the influence of the hot streak position on the span. When it is injected at mid pitch and 75% span, i.e. close to the blade tip, the authors observed an important radial shift,

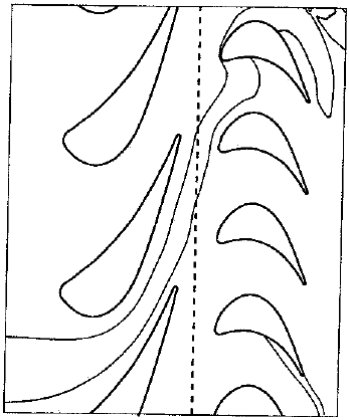

Figure B.2: Hot-streak calculation in the turbine (2D Euler code), using entropy as a flow marker [113]

showing a flow deflection towards the tip. When injected at 25% span, the flow field disturbance was less, but the accumulation on the hub endwall was four times more important compared to a mid span hot streak. This is an important information, as the convection of hot fluid towards the endwall can create important local heat flux, which may reduce the lifetime of the turbine.

The hot streak radial displacement within the rotor passage is attributed by Prasad and Hendricks [157] to the relative magnitudes of the total pressure gradient and the buoyancy force. Therefore, no general rule can be drawn, as the hot streak may migrate towards the hub (like Shang at MIT [111]) or casing (like Roback and Dring [109] at LSRR).

Shang *et al.* [113] were the first to report the action of unsteady blade-row interaction on the hot streak. Indeed, the stator-rotor interaction results in a fluctuating NGV exit flow angle, which cause the hot streak to wobble at the rotor blade passing frequency. This generates nonuniformity in the time-averaged rotor inlet temperature, as significant as $\pm 100K$ for $\pm 3^{\circ}$ swing in NGV exit angle.

B.1 Heat Transfer on Vane Surface and Endwall

The clocking effect between hot streak injector (i.e. fuel injector in real engine) and turbine rows was studied by many authors. Roback and Dring [109] found that the hot streak is less likely to affect the inner/outer endwall if it's directed on the NGV leading edge. The hot streak is supposed to be driven on the NGV SS, and then conducted toward midspan by the secondary flows. When it finally reaches the rotor blade, its radial extent is much smaller.

At the ILPF rig, Povey *et al.* [95] and Qureshi *et al.* [118] carried out deeper observations on the injector-NGV clocking. The latter performed RANS 3-D calculations on the turbine HP vane, using the compressible code *HYDRA*. They shown that circulation effects in the approach to the vane leading edge induces a shift in the location of the hot streak peak with respect to the LE. For a hot streak aligned with the HP vane mid-passage, this results in a preferential motion of cold flow towards the SS (hot flow towards PS), and thus a reduction in the driving gas temperature (see left side fig. B.3). On the other hand, a hot streak aligned with the vane LE would lead to higher heat transfer on the vane SS. The impact on the vane surface Nusselt number was measured to be as high as ±20% on the SS, [95]. On the pressure side, the heat transfer variations induced by the clocking between the hot streak and the NGV

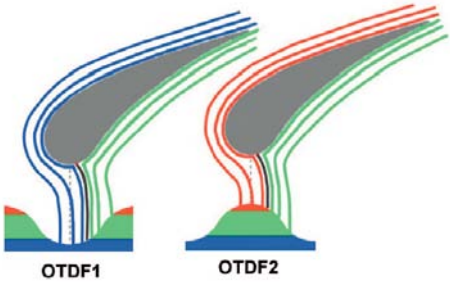

Figure B.3: Schematic of typical NGV midspan streamlines emitted from the hot streak located at different position of the vane passage [95]

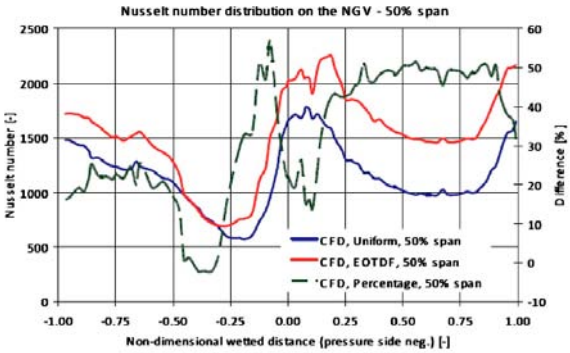

Figure B.4: Nusselt number distribution on the NGV at midspan, for non-uniform and uniform inlet temperature profiles [117]

were found to be small.

Salvadori et al. [117] recently performed RANS 3D simulations with the *HybFlow* CFD code on the MT1 turbine stage investigated at ILPF. Their work allows to highlight the HS preferential migration on SS when plotting the evolution of the Nusselt number on the vane surface (PS and SS), as shown in fig. B.4. Compared to uniform inlet temperature profile, the heat transfer is increased up to +50% on the SS whereas the augmentation is limited to +20% on the PS when using EOTDF.

Finally, Povey *et al.* [97] conducted the same kind of experiments on a low pressure vane. They also observed a migration of the HS towards the pressure side when aligned with NGV mid-passage, but leading to a significant increase in heat transfer to the vane ($Nu + 10 - 20\%$ vs. uniform profile). The authors assumed that this migration was mainly due to secondary flows within the vane passage, along with an incidence angle segregation as cited previously (Kerrebrock-Mikolajczak effect).

As far as endwalls are concerned, Colban *et al.* [158, 159] conducted experiments on a scaled-up ($\times 9$) NGV at Virginia Tech with a combustor simulator (with film cooling and slots). They observed that the cooling fluid tends to accumulate on the NGV suction side, as well as on the platform endwalls, resulting in adiabatic wall effectiveness close

to $\eta = 1$. However, they observed that increasing the coolant mass flow doesn't result in a continual increase of the effectiveness: the increase in total pressure modifies the secondary flow pattern, and the cooling flow is driven towards midspan.

Povey *et al.* [95] reported significant reduction in endwalls Nusselt number when using a non-uniform vs. uniform temperature profile (-30 to -50% at hub and -25 to -35% at casing endwall). The authors estimate that this decrease is mostly driving-temperature induced rather than caused by a change in heat transfer coefficient because the aerodynamic flow field suffers very little change between uniform/non-uniform temperature. This trend was confirmed by CFD simulations by Qureshi *et al.* [118].

B.2 Pressure Profiles and Secondary Flows

At combustor exit, the profile non-uniformities usually are generated by the combustor features (film cooling and dilution holes, slots, etc.) and they roughly span in the $10 - 15\%$ regions close to the inner and to the outer radii. It is commonly agreed that the total pressure is the governing parameter for secondary flows in the turbine stage, [119, 158, 160]. Secondary flows are characterized by the non-alignment of the velocity components with the inviscid flow through the passage, [158]. These flows are usually generated near the platform: Povey *et al.* [95] reported about 10% of span from hub and 30% from casing. They modify the flow vorticity, vortex size and trajectory, leading to local modifications of the vane-endwall heat transfer, [120].

The development of turbine secondary flows is highly complex. However, the leading mechanisms as presented in the work of Hermanson and Thole [96], Colban *et al.* [158, 159], and Barringer *et al.* [120] are shown here.

Barringer *et al* [119, 122] introduced a pressure coefficient defined as:

$$C_p = \frac{P_t - P_{t,midspan}}{(0.5\rho V^2)_{vane\ inlet}} \tag{B.1}$$

Depending on the pressure coefficient, authors identified three main flow regimes: *(i)* uniform profile, leading to reduced secondary flows; *(ii)* turbulent boundary layer (*BL*) profile, i.e. low total pressure at endwalls $c_p < 0$; *(iii)* boundary layer profile with an inflection point close to the root: $c_p > 0$. See left side of fig. B.6 for an example of *(ii)* and *(iii)* profiles. Depending on the total pressure field, different structures may develop within the vane passage:

- *Horse Shoe Vortex (HSV)* forms at the vane leading edge.
- *Passage Vortex (PV)* forms near both endwalls when the pressure profile is not uniform. It is considerably larger than the *CV*. The *PV* passes over top of the horse-shoe vortex on the PS before combining with it, and finally reaching the adjacent vane SS.
- *SS Corner Vortex (CV)* forms at both inner and outer corner between vane SS and platform, when the pressure profile is not uniform. Both *PV* and *CV* convect fluid from endwalls towards midspan.
- *Counter Rotating Vortex (CRV)* forms in the specific case of an inlet total pressure profile containing an inflection point near the vane root ($c_p > 0$). This counter-rotating vortex is larger is size than the *PV*.

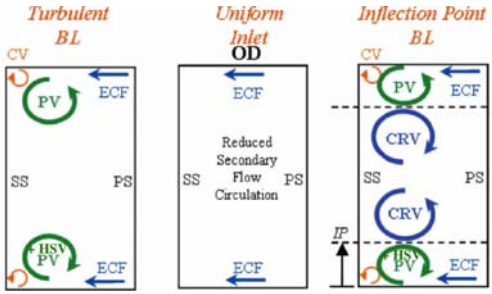

Figure B.5: Secondary flows developing within a vane passage: cross-passage view near midaxial chord looking downstream (adapted from [120])

An illustration of these flow vortices proposed by Barringer *et al.* [120] is shown in fig. B.5 for the three inlet pressure profiles.

Velocity arrows shown in figure B.6 are extracted from experiments of Colban *et al.* [159] using a turbulent *BL* (profile A) and an inflection point *BL* (profile B). The *PV* is clearly visible in both cases, as well as a very small *CV*. The large *CRV* appears only for profile B, and the tangency plane between *PV* and *CRV* roughly matches the profile inflection point.

Barringer *et al.* [119, 120] studied the influence of the combustor exit pressure profile on the heat transfer and aerodynamic loading of a turbine stage, using a great variety of pressure profiles. They observed that non-uniform pressure distributions can lead to ±10% in the *NGV* surface pressure (loading), especially at endwalls (root and tip) on the SS. Regarding heat transfer, they showed that low Nusselt number values can be obtained by a higher total pressure near the endwall relative to midspan. Indeed, the induced high pressure fluid buffers away the hot fluid from midspan and breaks-up the passage vortex. Such a pressure distribution is consistent with a profile with an inflection point *BL*, as shown in figure B.6. The authors suggest the existence of an ideal pro-

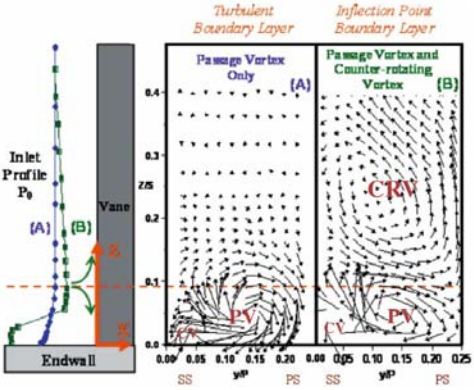

Figure B.6: Velocity arrows within the vane passage from experiments [159]

file $P = P(r)$ (no circumferential variation), with $c_p \simeq 1.0$ allowing for reduced secondary flows and thus heat transfer.

Bibliography

[1] Lefebvre, A. H. *Gas Turbine Combustion*. Taylor & Francis, 1998.

[2] Han, J. C, Dutta, S., and Ekkad, S. V. *Gas Turbine Heat Transfer and Cooling Technology*. Taylor & Francis, first edition, 2000.

[3] Mellor, A.M. *Design of Modern Gas Turbine Combustors*. Academic Press, 1990.

[4] Rolls-Royce. *The Jet Engine*. Rolls-Royce plc, 5th edition, 1996.

[5] Lefebvre, A.H. and Noster, E.R. The influence of fuel preparation and operating conditions on flame radiation in a gas turbine combustor. *ASME, (72-WA/HT-26)*, 22:463–473, 1972.

[6] Lefebvre, A. The role of fuel preparation in low emission combustion. *J ENG GAS TURB POWER*, 117, 1995.

[7] Wulff, A. and Hourmouziadis, J. Technology review of aeroengine pollutant emissions. *Aerospace Science and Technology*, 8:557–572, 1997.

[8] Correa., S.M. Carbon monoxide emissions in lean premixed combustion. *Journal of Propulsion and Power*, 8(6):1144–1151, 1992.

[9] Combustor technology: present and future - The need for future combustor technology to meet environmental constraints. *TLC: Towards Lean Combustion - EU research project*, *http://gfn.unizar.es/tlc/?q=background*, 2005.

[10] Wilfert, G., Sieber, J., Rolt, A., Baker, N., Touyeras, A., and Colantuoni, S. New environmental friendly aero engine core concepts. *Proceedings of the 18th ISABE conference*, (ISABE-2007-1120), 2007.

[11] Behrendt, T., Hassa, C., and Gerendas, M. Characterization of advanced combustor cooling concept under realistic operating conditions. *ASME Conference Proceedings*, (GT2008-51191), 2008.

[12] Povey, T. and Qureshi, I. Developments in hot-streak simulators for turbine testing. *Journal of Turbomachinery*, 131(3):1–15, 2009.

[13] Technology Readiness Assessment (TRA) guidance. Technical report, United States Department of Defense, 2011.

[14] Behrendt, T. and Hassa, C. A test rig for investigations of gas turbine combustor cooling concepts under realistic operating conditions. *J. Aerospace Engineering*, 22:169–177, 2008.

[15] Florschuetz, L., Truman, C., and Metzger, D. Streamwise flow and heat transfer distributions for jet array impingement with crossflow. *ASME Journal of Heat Transfer*, 103:337–342, 1981.

[16] Surace, M. *Investigation of impingement systems for gas turbine combustor cooling*. PhD thesis, University of Florence, Energy Engineering Department, 2004.

[17] Hebert, R.T. Innovative cooling configurations for low emission gas turbine combustors. Master's thesis, Faculty of the Louisiana State University, 2004.

[18] Esposito, E.I. Jet impingement cooling configurations for gas turbine combustion. Master's thesis, Faculty of the Louisiana State University, 2006.

[19] Stollery, J.L. and El-Ewany, A.A.M. A note on the use of boundary-layer model fo correlating film-cooling data. *International Journal of Heat Transfer*, 8:55–65, 1965.

[20] Yang, C.S., Kung, T.L., and Gau, C. Heat transfer process under a film-cooled surface with presence of weak swirling flow in the mainstream. *Experimental Thermal and Fluid Science*, 32:632–640, 2007.

[21] Simon, F.F. Jet model for slot film cooling with effect of freestream and coolant turbulence. Technical Report 2655, NASA, 1986.

[22] McNally, C.A., Pashby, I.R., and Folkes, J. Laser drilling of cooling holes in aero-engines: State of the art and future challenges. *Materials Science and Technology*, 20(7):805–816, 2004.

[23] Andrews, G. E., Bazdidi-Tehrani, F., Hussain, C. I., and Pearson, J. P. Small diameter film cooling hole heat transfer: The influence of hole length. *ASME Conference Proceedings*, (91-GT-344), 1991.

[24] Andrews, G. E., Khalifa, I. M., Asere, A. A., and Bazdidi-Tehrani, F. Full coverage effusion film cooling with inclined holes. *ASME Conference Proceedings*, (95-GT-274), 1995.

[25] Kretschmer, D. and Odgers, J. A simple method for the prediction of wall temperatures in gas turbines. *ASME Conference Proceedings*, (78-GT-90), 1978.

[26] Fric, T.F. and Roshko, A. Vortical structure in the wake of a transverse jet. *J. Fluid Mechanics*, 279:1–47, 1994.

[27] Acharya, S. Numerical modeling methods for film cooling. In *Film Cooling Science and Technology for Gas Turbine: State-of-the-Art Experimental and Computational Knowledge*, volume 06 of *Lecture Notes in Computer Science*, 2007.

[28] Andreopoulos, J. On the structure of jets in a cross-flow. *J. Fluid Mechanics*, 157:163–197, 1985.

[29] Walters, D. K. and Leylek, J. H. A detailed analysis of film-cooling physics: Part I-streamwise injection with cylindrical holes. *J. Turbomach.*, 122(1):102–112, 2000.

[30] L'Ecuyer, M.R. and Soechting, F.O. A model for correlating flat plate film cooling effectiveness for rows of round holes. In *AGARD Heat Transfer and Cooling in Gas Turbines 12p (SEE N86-29823 21-07)*. sep 1985.

[31] Goldstein, R.J. Film cooling. *Advances in Heat transfer*, 7:321–379, 1971.

[32] Eckert, E.R.G. Analysis of film cooling and full-coverage film cooling of gas turbine blades. *J. Eng. Gas Turbines Power*, 106:206–213, 1984.

[33] Zhao, L. and Wang, T. An investigation of treating adiabatic wall temperature as the driving temperature in film cooling studies. *ASME Conference Proceedings*, (GT2011-46012), 2011.

[34] Kelly, G. B. and Bogard, D. G. An investigation of the heat transfer for full coverage film cooling. *ASME Conference Proceedings*, (GT2003-38716), 2003.

[35] Sen, B., Schmidt, D. L., and Bogard, D. G. Film cooling with compound angle holes: Heat transfer. *J TURBOMACH*, 118:800–806, 1996.

[36] Andrews, G. E., Asere, A. A., Gupta, M. L., and Mkpadi, M. C. Effusion cooling: the influence of number of hole. *Journal of Power and Energy*, **204**, 1990.

[37] Bunker, R. *The Gas Turbine Handbook - Cooling Design Analysis*. US Department of Energy NETL, 4th edition, 2006.

[38] Wurm, B., Schulz, A., and Bauer, H.J. Cooling efficiency for assessing the cooling performance of an effusion cooled combustor liner. *ASME Conference Proceedings*, (GT2013-94304), 2013.

[39] Martiny, M., Schulz, A., and Wittig, S. Full-coverage film cooling investigations: adiabatic wall temperatures and flow visualization. *ASME Conference Proceedings*, (95-WA/HT-4), 1995.

[40] Martiny, M., Schulz, A., and Wittig, S. Mathematical model describing the coupled heat transfer in effusion cooled combustor walls. *ASME Conference Proceedings*, (97-GT-329), 1995.

[41] Scrittore, J. J., Thole, K. A., and Burd, S. W. Investigation of velocity profiles for effusion cooling of a combustor liner. *ASME Conference Proceedings*, (GT2006-90532), 2006.

[42] Kumada, M., Hirata, M., and Kasagi, N. Studies of full-coverage film cooling. II - Measurement of local heat transfer coefficient. *ASME, Gas Turbine Conference and Products Show*, 1981.

[43] Schulz, A. Infrared thermography as applied to film cooling of gas turbine components. *Meas. Sci. Technol.*, 11:948–956, 2000.

[44] Scrittore, J. J., Thole, K. A., and Burd, S. W. Experimental characterization of film-cooling effectiveness near combustor dilution holes. *ASME Conference Proceedings*, (GT2005-68704), 2005.

[45] Metzger, D.E., Takeuchi, D.I., and Kuenstler, P.A. Effectiveness and heat transfer with full-coverage film cooling. *ASME Journal of Engineering for Power*, 95:180–184, 1973.

[46] Crawford, M. E., Kays, W. M., and Moffat, R. J. Full-coverage film cooling-Part 2. Heat transfer data and numerical simulation. *Journal of Engineering for Power*, 102(4):1006–1012, 1980.

[47] Martinez-Botas, R. F. and Yuen, C. H. N. Measurement of local heat transfer coefficient and film cooling effectiveness through discrete holes. *ASME Conference Proceedings*, (2000-GT-243), 2000.

[48] Ceccherini, A., Facchini, B., Tarchi, L., and Toni, L. Adiabatic and overall effectiveness measurements of an effusion cooling array

for turbine endwall application. *ASME Conference Proceedings*, (GT2008-50826), 2008.

[49] Facchini, B., Maiuolo, F., Tarchi, L., and Coutadin, D. Combined effect of slot injection, effusion array and dilution hole on the heat transfer coefficient of a real combustor liner - part 1 experimental analysis. *ASME Conference Proceedings*, (GT2010-22936), 2010.

[50] Facchini, B., Maiuolo, F., Tarchi, L., and Coutandin, D. Experimental investigation on the effects of a large recirculating area on the performance of an effusion cooled combustor liner. *J. Eng. Gas Turb. Power*, 134, 2012.

[51] Toni, L. *Gas Turbine Aero-Engines Effusion Cooling Systems*. PhD thesis, University of Florence, Energy Engineering Department, 2009.

[52] Ceccherini, A. *Design of Innovative Cooling Systems for Aero-Engine Combustion Chambers*. PhD thesis, University of Florence, Energy Engineering Department, 2009.

[53] Ligrani, P., Goodro, M., Fox, M., and Moon, Hee-Koo. Full-coverage film cooling: Film effectiveness and heat transfer coefficients for dense and sparse hole arrays at different blowing ratios. *J TURBOMACH*, 134(6):061039, 2012.

[54] Martin, A. and Thorpe, S. J. Experiments on combustor effusion cooling under conditions of very high free-stream turbulence. *ASME Conference Proceedings*, (GT2012-68863), 2012.

[55] Ekkad, S. V., Zapata, D., and Han, J. C. Film effectiveness over a flat surface with air and co2 injection through compound angle holes using a transient liquid crystal image method. *ASME Journal of Turbomachinery*, 119:587–593, 1997.

[56] Ekkad, S. V., Zapata, D., and Han, J. C. Heat transfer coefficient over a flat surface with air and co2 injection through compound

angle holes using a transient liquid crystal image method. *ASME Journal of Turbomachinery*, 119:580–585, 1997.

[57] Lin, Y., Song, B., Li, B., Liu, G., and Wu, Z. Investigation of film cooling effectiveness of full-coverage inclined multihole walls with different hole arrangements. *ASME Turbo Expo*, (GT2003-38881), 2003.

[58] Lin, Y., Song, B., Li, B., and Liu, G. Measured film cooling effectiveness of three multihole patterns. *ASME Journal of Heat Transfer*, 128:192–197, 2006.

[59] Andreini, A., Ceccherini, A., Facchini, B., and D.Coutandin. Combined effect of slot injection, effusion array and dilution hole on the heat transfer coefficient of a real combustor liner - Part 2 numerical analysis. *ASME Conference Proceedings*, (GT2010-22937), 2010.

[60] Andreini, A., Soghe, R. Da, Facchini, B., Mazzei, L., Colantuoni, S., and Turrini, F. Local source based CFD modeling of effusion cooling holes: Validation and application to an actual combustor test case. *J. Eng. Gas Turb. Power*, 136(1), 2013.

[61] Kretschmer, D. and Odgers, J. A simple method for the prediction of wall temperatures in a gas turbine combustor. *ASME, (78-GT-90)*, 1972.

[62] De Champlain, A., Gosselin, P., and Kretschmer, D. Prediction of wall heat transfer for a gas turbine combustor. *Proc. Instn. Mech. Engrs.*, 213:169–180, 1999.

[63] Facchini, B., Surace, M., and Zecchi, S. A new concept of impingement cooling for gas turbine hot parts and its influence on plant performance. *ASME Conference Proceedings*, (GT-2003-38166), 2003.

[64] Facchini, B., Surace, M., and Tarchi, L. Impingement cooling for modern combustors: experimental analysis and preliminary design. *ASME Conference Proceedings*, (GT2005-68361), 2005.

[65] Arcangeli, L., Facchini, B., Surace, M., and Tarchi, L. Correlative analysis of effusion cooling systems. *J. Turbomach.*, 130(011016), 2008.

[66] Andreini, A., Carcasci, C., Ceccherini, A., Facchini, B., Surace, M., Coutandin, D., Gori, S., and Peschiulli, A. Combustor liner temperature prediction: a preliminary tool development and its application on effusion cooling systems. *First CEAS European Air and Space Conference Century Perspectives*, (Paper n.026), 2007.

[67] Andreini, A., Ceccherini, A., Facchini, B., Turrini, F., and Vitale, I. Assesment of a set of numerical tools for the design of aeroengines combustors: study of a tubular test rig. *Proceedings of ASME Turbo Expo*, (GT2009-59539), 2009.

[68] Andreini, A., Bonini, A., Caciolli, G., Facchini, B., and Taddei, S. Numerical study of aerodynamic losses of effusion cooling holes in aero-engine combustor liners. *J. Eng. Gas Turb. Power*, 133(2) (021901), 2011.

[69] Andreini, A., Facchini, B., Mazzei, L., Bellocci, L., and Turrini, F. Assessment of aero-thermal design methodology for effusion cooled lean burn annular combustors. *ASME Conference Proceedings*, (GT2014-26764), 2014.

[70] Hay, N. and Lampard, D. Discharge coefficient of turbine cooling holes: a review. *ASME Turbo Expo*, (96-GT-492), 1996.

[71] Rohsenow, W. M., Hartnett, J. P., and Ganic, E.N. *Handbook of Heat Transfer Applications.* McGraw Hill, second edition, 1985.

[72] Ballal, D.R. and Lefebvre, A.H. Film-cooling effectiveness in the near slot region. *ASME J. Heat Transfer*, 95:256–266, 1973.

[73] Lakshminarayana, B. *Fluid Dynamics and Heat Transfer of Turbomachinery.* John Wiley & Sons, Inc., 1996.

[74] Andreini, A., Carcasci, C., Gori, S., and Surace, M. Film cooling system numerical design: Adiabatic and conjugate analysis. *Proceedings of HT2005*, (HT2005-72042), 2005.

[75] Stasiek, J. A. and Kowalewski, T.A. Thermochromic liquid crystals applied for heat transfer research. *OPTO-ELECTRONICS REVIEW*, 10, 2002.

[76] Camci, C. Liquid crystal thermography. In *Temperature Measurements*, Von Karman Lecture Series, 1995.

[77] Sage, I. Thermochromic liquid crystals. *Liquid Crystals*, 38:1551–1561, 2011.

[78] Chan, T. L., Ashforth-Frost, S., and Jambunathan, K. Calibrating for viewing angle effect during heat transfer measurements on a curved surface. *International Journal of Heat and Mass Transfer*, 44:2209–2223, 2001.

[79] Hay, J.L. and Hollingsworth, D.K. Calibration of microencapsulated liquid crystals using hue angle and a dimensionless temperature. *Experimental Thermal and Fluid Science*, 18:251–257, 1998.

[80] Hay, J.L. and Hollingsworth, D.K. A comparison of trichromic systems for use in the calibration of polymer-dispersed thermo-chromic liquid crystals. *Experimental Thermal and Fluid Science*, 12:1–12, 1996.

[81] Farina, D.J., Hacker, J.M., Moffat, R.J., and Eaton, J.K. Illuminant invariant calibration of thermochromic liquid crystals. *Experimental Thermal and Fluid Science*, 9:1–12, 1994.

[82] Roach, P. E. The generation of nearly isotropic turbulence by means of grids. *Heat and Fluid Flow*, 8(2):83–92, 1987.

[83] Byerley, A.R. *Heat transfer near the entrance to a film cooling hole in a gas turbine blade.* PhD thesis, Merton College, Oxford, 1989.

[84] Andreini, A., Caciolli, G., Da Soghe, R., Facchini, B., and Mazzei, L. Numerical investigation on the heat transfer enhancement due to coolant extraction on the cold side of film cooling holes. *ASME Conference Proceedings*, (GT2014-25460), 2014.

[85] Andreini, A., Da Soghe, R., Facchini, B., and Mazzei, L. Heat transfer enhancement due to coolant extraction on the cold side of effusion cooling plates. *ASME Conference Proceedings*, (GT2014-25393), 2014.

[86] Jones, T. V. Theory for the use of foreign gas in simulating film cooling. *International Journal of Heat and Fluid Flow*, 20:349–354, 1999.

[87] ASME. Measurement uncertainty. In *Instrument and Apparatus*, volume ANSI/ASME PTC 19.1-1985 of *Performance Test Code*. ASME, 1985.

[88] Kline, S. J. and McClintock, F. A. Describing uncertainties in single sample experiments. *Mechanical Engineering*, 75:3–8, Jan 1953.

[89] Scrittore, J. J., Thole, K. A., and Burd, S.W. Experimental characterization of film-cooling effectiveness near combustor dilution holes. *ASME Conference Proceedings*, (GT2005-68704), 2005.

[90] Caciolli, G., Facchini, B., Picchi, A., and Tarchi, L. Comparison between psp and tlc steady state techniques for adiabatic effectiveness measurement on a multiperforated plate. *Experimental Thermal and Fluid Science*, 48:122–133, 2013.

[91] Baldauf, S., Scheurlen, M., Schulz, A., and Wittig, S. Correlation of film-cooling effectiveness from thermographic measurements at enginelike conditions. *J. Turbomach.*, 124(4):686–698, Nov 07, 2002.

[92] Piggush, J. D. and Simon, T. W. Measurements of net change in heat flux as a result of leakage and steps on the contoured endwall

of a gas turbine first stage nozzle. *Applied Thermal Engineering*, 27:722–730, 2007.

[93] Wurm, B., Schulz, A., Bauer, H.J., and Gerendas, M. Impact of swirl flow on the cooling performance of an effusion cooled combustor liner. *ASME Conference Proceedings*, (GT2012-68972), 2012.

[94] Klapdor, E. V. *Simulation of combustor - turbine interaction in a jet engine.* PhD thesis, Technischen Universität Darmstadt, 2010.

[95] Povey, T., Chana, K. S., Jones, T. V., and Hurrion, J. The effect of hot-streaks on hp vane surface and endwall heat transfer: An experimental and numerical study. *Journal of Turbomachinery*, 129 (1):32–43, 2007.

[96] Hermanson, K. S. and Thole, K. A. Effect of nonuniform inlet conditions on endwall secondary flows. *Journal of Turbomachinery*, 124(4):623–631, 2002.

[97] Povey, T., Chana, K. S., and Jones, T. V. Heat transfer measurements on an intermediate-pressure nozzle guide vane tested in a rotating annular turbine facility, and the modifying effect of a non-uniform inlet temperature profile. *Proceedings of the Institution of Mechanical Engineers, Part A: Journal of Power and Energy*, 217 (4):421–432, 2003.

[98] Cha, C.M., Hong, S., Ireland, P.T., Denman, P., and Savarianandam, V. Experimental and numerical investigation of combustor-turbine interaction using an isothermal, nonreacting tracer. *J. Eng. Gas Turb. Power*, 134, 2012.

[99] Wankhede, M.J., Bressloff, N.W., Keane, A.J., Caracciolo, L., and Zedda, M. An analysis of unstable flow dynamics and flashback mechanism inside a swirl-stabilised lean burn combustor. *ASME Conference Proceedings*, (GT2010-22253), 2010.

[100] Goebel, S. G., Abuat, N., Lovett, J. A., and Lee, C. P. Measurements of combustor velocity and turbulence profiles. In *American Society of Mechanical Engineers (Paper)*, 1993.

[101] Dorney, D. J., Gundy-Burlet, K. L., and Sondak, D. L. A survey of hot streak experiments and simulations. *International Journal of Turbo and Jet Engines*, 16(1):1–15, 1999.

[102] Stabe, R. G., Whitney, W. J., and Moffitt, T. P. Performance of a high-work low aspect ration turbine tested with a realistic inlet radial temperature profile. Technical Report NASA-TM-83655, AIAA PAPER 84-1161, NASA Glenn Research Center, 1984.

[103] Whitney, W. J., Stabe, R. G., and Moffitt, T. P. Description of the warm core turbine facility and the warm annular cascade facility recently installed at nasa lewis research center. Technical Report 81A34158, NASA Glenn Research Center, 1980.

[104] Dorney, D.J. and Gundy-Burlet, K.L. Effects of hot streak shape on rotor heating in a high-subsonic single-stage turbine. *International Journal of Turbo and Jet Engines*, 18(1):15–29, 2001.

[105] Joslyn, H. D. and Dring, R. P. A trace gas technique to study mixing in a turbine stage. *Journal of Turbomachinery*, 110(1):38–43, January 1988 1988.

[106] Joslyn, D. and Dring, R. Three-dimensional flow in an axial turbine: Part 1—aerodynamic mechanisms. *Journal of Turbomachinery*, 114 (1):61–70, January 1992 1992.

[107] Joslyn, D. and Dring, R. Three-dimensional flow in an axial turbine: Part 2—profile attenuation. *Journal of Turbomachinery*, 114(1):71–78, January 1992 1992.

[108] Butler, T., Sharma, O., Joslyn, H., and Dring, R. Redistribution of an inlet temperature distortion in an axial flow turbine stage. *Journal of Propulsion and Power*, 5(1):pages 64–71, 1989.

[109] Roback, R. J. and Dring, R. P. Hot streaks and phantom cooling in a turbine rotor passage: Part 1—separate effects. *Journal of Turbomachinery*, 115(4):657–666, October 1993 1993.

[110] Roback, R. J. and Dring, R. P. Hot streaks and phantom cooling in a turbine rotor passage: Part 2—combined effects and analytical modeling. *Journal of Turbomachinery*, 115(4):667–674, October 1993 1993.

[111] Shang, T. Influence of inlet temperature distortion on turbine heat transfer. Master's thesis, Department of Aeronautics and Astronautics, 1995.

[112] Shang, T., G.R., Guenette, Epstein, A.H., and Saxer, A.P. The influence of inlet temperature distortion on rotor heat transfer in a transonic turbine. *AIAA Paper No. 95-3042*, 1995.

[113] Shang, T. and Epstein, A.H. Analysis of hot streak effects on turbine rotor heat load. *Journal of Turbomachinery*, 119(3):544–553, 1997.

[114] Povey, T. and Qureshi, I. A hot-streak (combustor) simulator suited to aerodynamic performance measurements. *Proceedings of the Institution of Mechanical Engineers, Part G: Journal of Aerospace Engineering*, 222(6):705–720, 2008.

[115] Hilditch, M. A., Fowler, A., Jones, T. V., Chana, K. S., Oldfield, M. L. G., Ainsworth, R. W., Hogg, S. I., Anderson, S. J., and Smith, G. C. Installation of a turbine stage in the pyestock isentropic light piston facility. In *American Society of Mechanical Engineers (Paper)*, pages 1–9, 1994.

[116] Chana, Kam S., Hurrion, James R., and Jones, Terry V. The design, development and testing of a non-uniform inlet temperature generator for the qinetiq transient turbine research facility. *ASME Conference Proceedings*, 2003(36894):273–280, January 1, 2003 2003.

[117] Salvadori, S., Montomoli, F., Martelli, F., Chana, K. S., Qureshi, I., and Povey, T. Analysis on the effect of a nonuniform inlet profile on heat transfer and fluid flow in turbine stages. *Journal of Turbomachinery*, 134(1), 2011.

[118] Qureshi, I., Beretta, A., and Povey, T. Effect of simulated combustor temperature nonuniformity on hp vane and end wall heat transfer: An experimental and computational investigation. *Journal of Engineering for Gas Turbines and Power*, 133(3), 2011.

[119] Barringer, M. D., Thole, K. A., and Polanka, M. D. Effects of combustor exit profiles on vane aerodynamic loading and heat transfer in a high pressure turbine. *Journal of Turbomachinery*, 131(2):1–10, 2009.

[120] Barringer, M. D., Thole, K. A., and Polanka, M. D. An experimental study of combustor exit profile shapes on endwall heat transfer in high pressure turbine vanes. *Journal of Turbomachinery*, 131(2): 1–10, 2009.

[121] Barringer, M. D., Thole, K. A., Polanka, M. D., Clark, J. P., and Koch, P. J. Migration of combustor exit profiles through high pressure turbine vanes. *Journal of Turbomachinery*, 131(2):1–10, 2009.

[122] Barringer, M. D., Thole, K. A., and Polanka, M. D. Experimental evaluation of an inlet profile generator for high-pressure turbine tests. *Journal of Turbomachinery*, 129(2):382–394, 2007.

[123] Mathison, R. M., Haldeman, C. W., and Dunn, M. G. Heat transfer for the blade of a cooled stage and one-half high-pressure turbine-Part I: Influence of cooling variation. *Journal of Turbomachinery*, 134(3), 2011.

[124] Mathison, R. M., Haldeman, C. W., and Dunn, M. G. Heat transfer for the blade of a cooled stage and one-half high-pressure turbine—Part II: Independent influences of vane trailing edge and purge cooling. *Journal of Turbomachinery*, 134(3):031015, May 2012 2012.

[125] Mathison, R. M., Haldeman, C. W., and Dunn, M. G. Aerodynamics and heat transfer for a cooled one and one-half stage high-pressure turbine-Part I: Vane inlet temperature profile generation and migration. *Journal of Turbomachinery*, 134(1), 2012.

[126] Mathison, R. M., Haldeman, C. W., and Dunn, M. G. Aerodynamics and heat transfer for a cooled one and one-half stage high-pressure turbine-Part II: Influence of inlet temperature profile on blade row and shroud. *Journal of Turbomachinery*, 134(1), 2012.

[127] Mathison, R. M., Haldeman, C. W., and Dunn, M. G. Aerodynamics and heat transfer for a cooled one and one-half stage high-pressure turbine-Part III: Impact of hot streak characteristics on blade row heat flux. *Journal of Turbomachinery*, 134(1), 2012.

[128] Haldeman, C.W., Mathison, R.M., and M.G., Dunn. Design, construction, and operation of a combustor emulator for short-duration high-pressure turbine experiments. *AIAA Paper No. 2004-3829*, 2004.

[129] Jenkins, S., Varadarajan, K., and Bogard, D. G. The effects of high mainstream turbulence and turbine vane film cooling on the dispersion of a simulated hot streak. *Journal of Turbomachinery*, 126(1):203–211, 2004.

[130] Jenkins, S. C. and Bogard, D. G. The effects of the vane and mainstream turbulence level on hot streak attenuation. *Journal of Turbomachinery*, 127(1):215–221, 2005.

[131] Koupper, C. QUAL Cerfacs 2012. 2012.

[132] Roux, S., Cazalens, M., and Poinsot, T. Outlet-boundary-condition influence for large eddy simulation of combustion instabilities in gas turbines. *Journal of Propulsion and Power*, 24(3), 2008.

[133] Klapdor, E. V. Towards investigation of combustor turbine interaction in an integrated simulation. Number GT2010-22933. ASME Turbo expo 2010, ASME, 2010.

[134] Battisti, C., Kost, F., Atkins, N., Playford, W., Orain, M., Caciolli, G., Tarchi, L., Mersinligil, M., and Raffel, J. Full aerothermal combustor turbine interaction research. *Proceedings of the EASN workshop on Flight Physics and Propulsion*, 2012.

[135] Koupper, C., Bonneau, G., Caciolli, G., Facchini, B., Gicquel, L. Tarchi L., and Duchaine, F. Development of an engine representative combustor simulator dedicated to hot streak generation. *ASME Conference Proceedings*, (GT2014-25120), 2014.

[136] Wurm, B., Schulz, A., and Bauer, H.J. A new test facility for investigating the interaction between swirl flow and wall cooling films in combustors. *ASME Conference Proceedings*, (GT2009-59961), 2009.

[137] Andreini, A., Caciolli, G., Facchini, B., and Picchi, A. Experimental investigation of the flow field and the heat transfer on a scaled cooled combustor liner with realistic swirling flow generated by a lean-burn injection system. *ASME Conference Proceedings*, (GT2014-25643), 2014.

[138] Spencer, A., Hollis, D., and Gashi, S. Investigation of the unsteady aerodynamics of an annular combustor using PIV and LES. *ASME Conference Proceedings*, (GT2008-50277), 2008.

[139] Schoenfeld, T. and Rudgyard, M. Steady and unsteady flows simulations using the hybrid flow solver AVBP. *AIAA Journal*, 37(11): 1378–1385, 1999.

[140] Poinsot, T. and Veynante, D. *Theoretical and numerical combustion - Third Edition.* 2011.

[141] Sagaut, P. *Large Eddy Simulation for Incompressible Flows: An Introduction.* Scientific Computation. Springer, 2006.

[142] Champion, J.L. *Etude expérimentale des films parétaux de refroidissement produits par une paroi multiperforée - cas des con-*

ditions de fonctionnement des chambres de combustion de moteurs aéronautiques. PhD thesis, Poitiers, 1997.

[143] Bryer, D.W. and Pankhurst, R.C. Pressure-probe methods for determining wind speed and flow direction. *London: Her Majesty's Stationary Office*, 1971.

[144] Treaster, A.L. and Yocum, A.M. The calibration and application of five-hole probes. *ISA Transactions*, 18:23–34, 1979.

[145] Paul, A.R., Upadhyay, R.R., and Jain, A. A novel calibration algorithm for five-hole pressure probe. *International Journal of Engineering Science and Technology*, 3:89–95, 2011.

[146] Raffel, M., Willert, C.E., and Kompenhans, J. *Particle Image Velocimetry - A Pratical Guide.* Springer, 2nd edition, 2007.

[147] Dynamics, Dantec. *FlowManager software and Introduction to PIV Instrumentation.* 5th edition, 2000.

[148] Lang, H., Morck, T., and Woisetschlager, J. Stereoscopic particle image velocimetry in a transonic turbine stage. *Experiments in Fluids*, 32:700–709, 2002.

[149] Voges, M., Beversdorff, M., Willert, C., and Krain, H. Application of particle image velocimetry to a transonic centrifugal compressor. *Experiments in Fluids*, 43:371–384, 2007.

[150] Wheeler, A.P.S., Miller, R.J., and Hodson, H.P. The effect of wake induced structures on compressor boundary-layers. *J. Turbomach*, 129:705–712, 2007.

[151] Kegalj, M. and Schiffer, H.P. Endoscopic PIV measurements in a low pressure turbine rig. *Proceedings of the 14th Int. Symp. on Applications of Laser Techniques to Fluid Mechanics, Lisbon*, 2008.

[152] Rottier, C., Godard, G., Corbin, F., Boukhalfa, A.M., and Honoré, D. An endoscopic particle image velocimetry system for

high-temperature furnaces. *Measurement Science and Technology*, 21, 2010.

[153] Gnirss, M. and Tropea, C. Simultaneous PIV and concentration measurements in a gas-turbine model. *Exp Fluids*, 45:pp. 643–656, 2008.

[154] Kreith, F., Manglik, R.M., and Bohn, M.S. *Principles of heat transfer*. Cengage Learing, 7th edition, 2011.

[155] Sedalor, STeddy, Patil, Sunil, Ekkad, Srinath, Tafti, Danesh, Kim, Yong, Moon, Hee-Koo, and Srinivasan, Ram. Study of flow and convective heat transfer in a simulated scaled up low emission annular combustor. *ASME Conference Proceedings*, (GT2010-22986), 2010.

[156] J.L., Kerrebrocke and A.A., Mikolajczak. Intra stator transport of rotor wakes and its effect on compressor performance. *Journal of Engineering for Power*, 92, 1970.

[157] Prasad, Dilip and Hendricks, Gavin J. A numerical study of secondary flow in axial turbines with application to radial transport of hot streaks. *Journal of Turbomachinery*, 122(4):667–673, 2000.

[158] Colban, W. F., Thole, K. A., and Zess, G. Combustor turbine interface studies - Part 1: endwall effectiveness measurements. 2003.

[159] Colban, W. F., Lethander, A. T., and Thole, K. A. Combustor turbine interface studies - Part 2: flow and thermal field measurements. 2003.

[160] Stitzel, Sarah and Thole, Karen A. Flow field computations of combustor-turbine interactions relevant to a gas turbine engine. *Journal of Turbomachinery*, 126(1):122–129, January 2004 2004.